UNIVERSITÀ DEGLI STUDI DI PAVIA

—— o ——

SCIENTIFICA ACTA

QUADERNI DEL DOTTORATO

VOLUME VIII ANNO VIII NUMERO 3

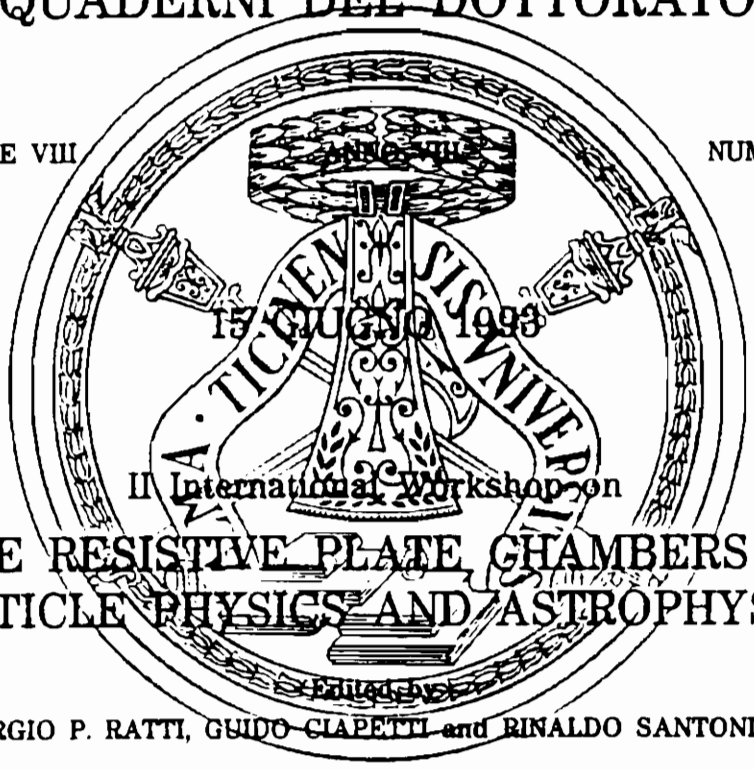

II International Workshop on

THE RESISTIVE PLATE CHAMBERS IN PARTICLE PHYSICS AND ASTROPHYSICS

Edited by

SERGIO P. RATTI, GUIDO CIAPETTI and RINALDO SANTONICO

ISTITUTO NAZIONALE DI FISICA NUCLEARE

—— o ——

CENTRO STAMPA - DIPARTIMENTI FISICI
via Bassi, 6 27100 Pavia

FOREWORD

The timing of this Workshop has been very appropriate. A large amount of experience has accumulated recently on the Resistive Place Counters [RPC] in several Countries; a good number of experiments have been completed or brought to a very advanced stage so that "second order" problems have been brought to the surface and therefore to our attention.

The RPC "technique" is relatively new and a large amount of R&D is in progress. If seen in perspective, the RPC looks like a very versatile detector well suited to cover - at reasonable cost - large areas; a detector providing large and fast signals for a moderately expensive readout electronics.

Such optimistic premises have however to face the increasingly severe environments into which the RPC's are supposed to operate: high intensities, large backgrounds, tight safety requirements, to mention only few.

This second Workshop, together with the open confrontation of experts and the comparison of different experimental results, is of great importance. Decisions are being taken for the final design of very large and complex detectors to be operated either at high energy colliders or in cosmic ray experiments of the new generation.

Thus, the efficiency variation with increasing temperature or with the presence of a uniform, diffused γ-neutron background; the effect of the particle rate on both efficiency and time response; the performances with non flammable, non ozone-depleting gases, are issues which are assuming an increasing relevance.

For all these reasons, we felt it very important to coherently collect and distribute the information and the conclusions resulting from the Workshop. Only three contributions to the Meeting are missing.

We hope that this volume may be useful to the scientific community.

Pavia, june 15th, 1993

The Editors
Sergio P. Ratti
Guido Ciapetti
Rinaldo Santonico

INDEX

RPC: STATUS AND PERSPECTIVES

Rinaldo Santonico

Universita' di Roma "Tor Vergata" and INFN Sezione di Roma 2

Via della Ricerca Scientifica - 00133 Roma, Italy

1 Historical Remarks

Most of the existing gaseous detectors are based on the electric field generated by a positively charged wire. The strong dependence of this field on the distance r from the wire $E \propto 1/r$ has basic consequences on the detector working mode:

- It limits the extension of the "multiplication region" and therefore the radial size of the discharge, to a distance of the order of the wire diameter.
- It makes the detector very stable, the field strength being very low at the cathode walls.
- It makes the detector time resolution modest due to the jitter of the electrons drift motion up to multiplication region near the wire.

The Geiger-Muller counter invented in the years '20 was the first detector which used a charged wire to produce a field inside a gas. It can be considered as the common "ancestor" of a large family of detectors which were created to fulfill specific needs of the experiments and includes multiwire proportional chambers, limited streamer tubes and also, more recently, microstrip gas counters.

The wire detectors had an impressive impact on the experimental physics.

A much higher time resolution with respect to the wire detectors can be achieved by the planar detectors which are based on the uniform electric

field generated by two parallel electrode plates. Their common ancestor is the Keuffel spark counter [1] from which Pestof counters [2] and resistive plate chambers[3] were derived. Planar detectors, except in their pulsed version of the optical spark chamber, had so far a modest impact on the experimental physics in spite of their intrinsic interest.

The RPCs have recently proven to be a detector capable of real applications to experiments demanding both space and time resolution over large detection areas [4].

The experience accumulated in the experiments that used them so far makes the RPCs a natural candidate technology for the muon detection at the future hadronic colliders and for the cosmic rays physics.

2 A simple working model

The sketch of a RPC is shown in fig. 1. Two parallel electrode plates of bulk resistivity $\rho = 10^{10\div12}\Omega\,cm$ generate a uniform, intense electric field, usually about $4KV/mm$, in a $2mm$ gas gap filled with a mixture of Argon, butane (about 60/40 in volume) and Freon $(3-5\%)$ at normal pressure.

The electrode plates are coated, on the external sides, with thin graphite layers connected to high voltage and to ground respectively. Due to their high surface resistivity of about $0.1M\Omega/\Box$, these graphite electrodes are transparent to the transients of electrical discharges generated inside the gas. The capacitive signal read out is therefore possible through virtually grounded pads which are fixed or simply pressed on the detector walls.

A PVC-Polyethylene film $0.3mm$ thick, glued on the graphite layer, is used to insulate the high voltage electrodes from the read out pads which can be arbitrarily shaped being completely independent from the mechanical structure of the detector. As an example, X and Y orthogonal read out strips are shown in fig. 1.

The RPC just described has the structure of a two dielectrics planar capacitor. A correct description of the system has to take into account the finite resistivity of the real dielectrics as in the equivalent circuit shown in fig. 2a.

Two cases have to be considered:

- The case of a non-ionized gas corresponds to an infinite gas resistivity,

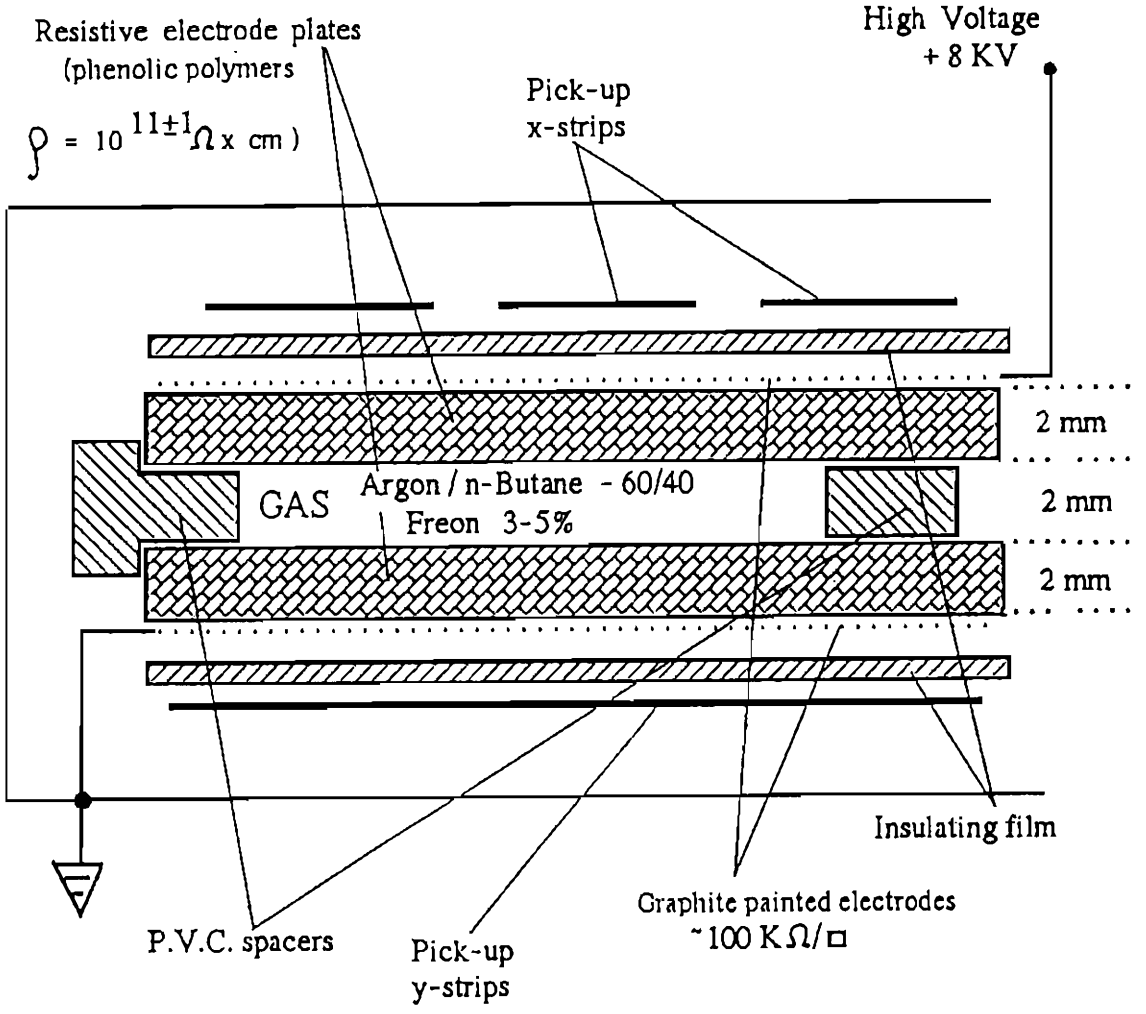

Figure 1: Sketch of a resistive plate chamber

$R_g = \infty$ in fig. 2a. Therefore in the steady situation the supplied voltage is entirely applied to the gas gap.

- When the gas is crossed by a ionizing particle, the electric discharge generated in the gas can be described by a current generator (fig. 2b) which discharges the "gas capacitor" C_g so that the voltage initially applied to the gas is transferred to the resistive plate described by the capacitor C in fig. 2b. The system goes back to the initial condition following an exponential law with a characteristic time constant τ which

is independent from the size of the capacitor:

$$\tau = R(C + Cg) = \rho\epsilon_0(\epsilon_r + 2d/g)$$

where ϵ_r is the relative dielectric constant and d is the thickness of the plates and g is the gas gap.

The above relationship gives $\tau \sim 10\,msec$ for $\rho = 10^{10}\Omega\,cm$. This characteristic time constant has to be compared with the discharge duration that, for the gas and voltage conditions that are usual for RPCs, is only $10\,ns << \tau$. In such a short time the electrode plates behave like insulators and the discharge occurring in the gas cannot be fed. This quenching mechanism is at the basis of the working principle of the detector.

It has been suggested by Pestov that a chamber with resistive electrode plates is intrinsically divided in a large number of small "discharge cells" which are to some extent independent from one another. The area of each cell is proportional to the total charge Q freeded in the gas:

$$S = \frac{Qg}{\epsilon_0 V}$$

The parameter Q is a crucial one in determining the rate capability of an RPC. The discharge occurring in the gas indeed can only be fed by a limited current that can flow across a pair of high resistivity electrode plates. A small value of Q allows therefore to keep the operating current small and the detection efficiency high, even in presence of an intense flux of ionizing particles and provided that the frontend electronics can offer enough amplification and bandwidth.

3 Signal Charge and Gas composition

RPCs can be efficiently operated even with gas mixtures containing large amounts of electronegative gases like freons. Wire detectors on the contrary require non electronegative gases for an efficient operation because free electrons can be captured in their drift motion to approach the wire. The

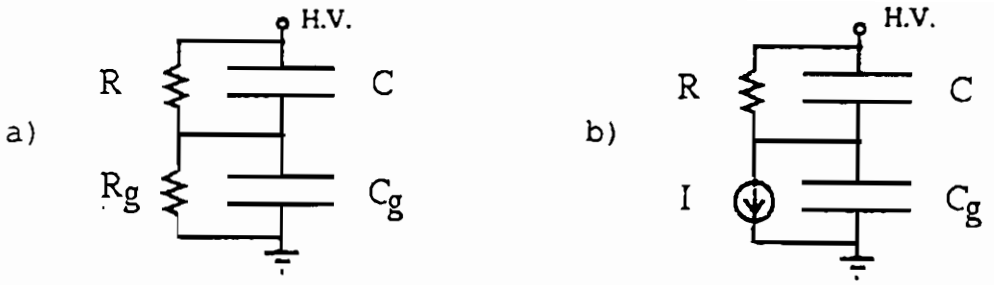

Figure 2: Equivalent circuit of the "discharge cell". The capacitors C and C_g correspond to the resistive plates and to the gas gap respectively. For a non ionized gas (figure 2a) $R_g = \infty$ and the supplied voltage is entirely applied to the gas gap. A current generator (figure 2b) describes the effect of the electric discharge. The voltage initially applied to the gas is transferred to the resistive plate

addition of relatively small amounts of some kind of freons, e.g. CF_3Br, to the RPC gas has the effect of reducing the size of the electric signal induced on the pick-up strips.

The signal charge distribution of a RPC operated with a fixed Argon/ Butane ratio of 60/40 in volume and different amounts of freon, for a $0.5\mu sec$ integration gate is shown in fig. 3.

The case of a freonless gas (fig. 3a) and of one containing 4% (fig. 3b) and 8% (fig. c) respectively are reported. The detection efficiency is approximately the same, 96%, for the three cases and the operating voltage is slightly increasing with the freon concentration. All three distributions show a sharp peak corresponding to single discharges, followed by a tail due to multiple discharges. The average of the single discharge peak decreases of about one order of magnitude, from 500 to $50\,pC$, for an increase of the freon concentration from zero to 8%. As a conclusion the freon concentration in the gas has a drastic effect of reduction on the signal charge.

As discussed above this effect improves the rate capability of the detector. But for considerably larger amounts of freon a high amplification and bandwidth frontend electronics is needed.

A RPC operating with pure CF_3Br has been successfully tested at the CERN RD5 test beam up to a maximum rate of $10KHz/cm^2$ [5]. The signal

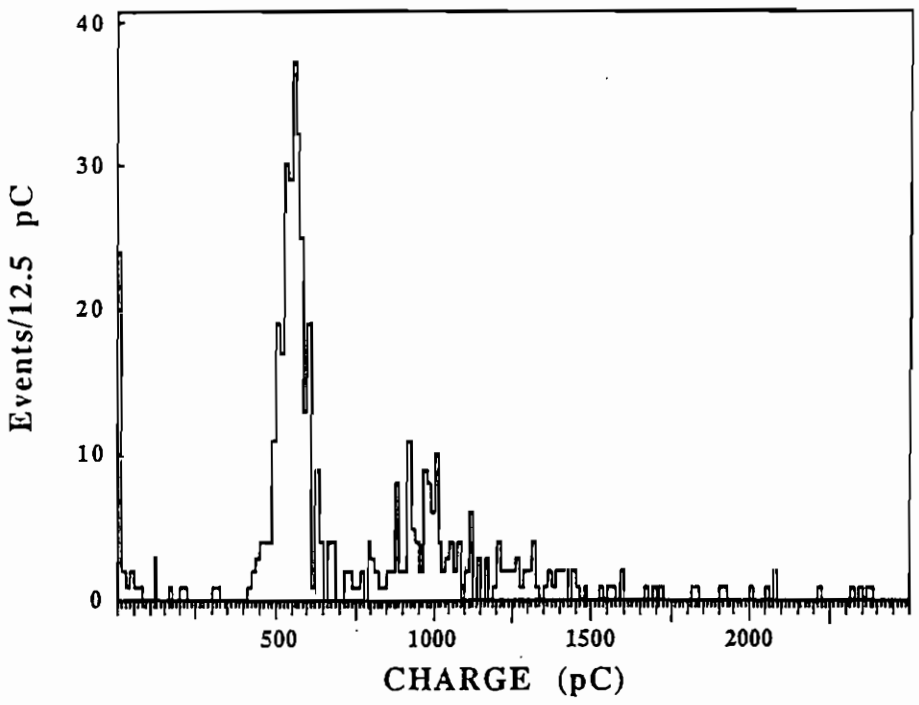
Events/12.5 pC
40
30
20
10
0
500
1000
1500
2000
CHARGE (pC)

a)

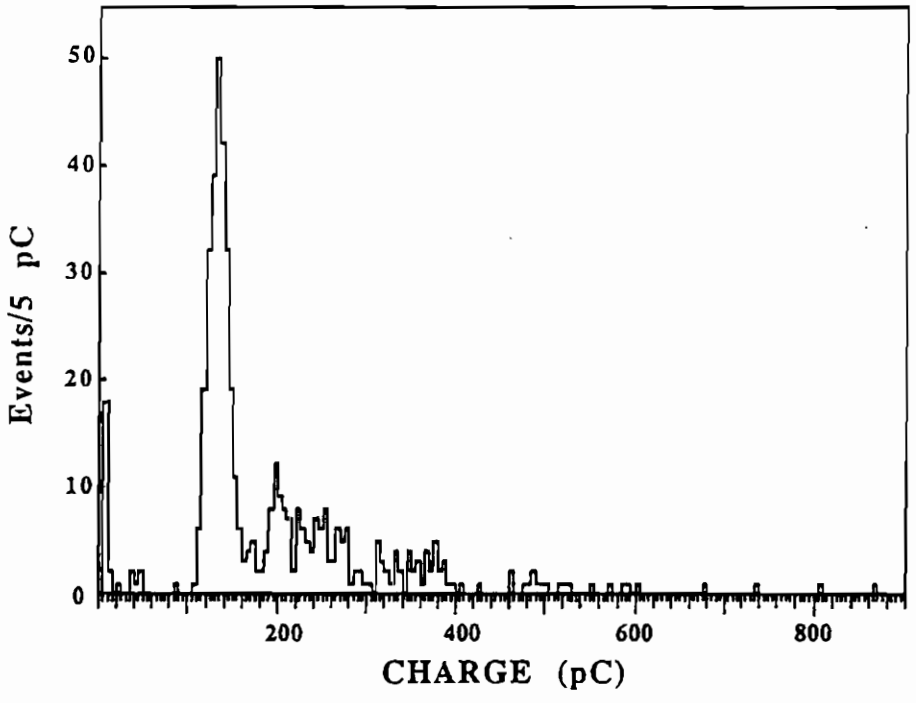
Events/5 pC
50
40
30
20
10
0
200
400
600
800
CHARGE (pC)

b)

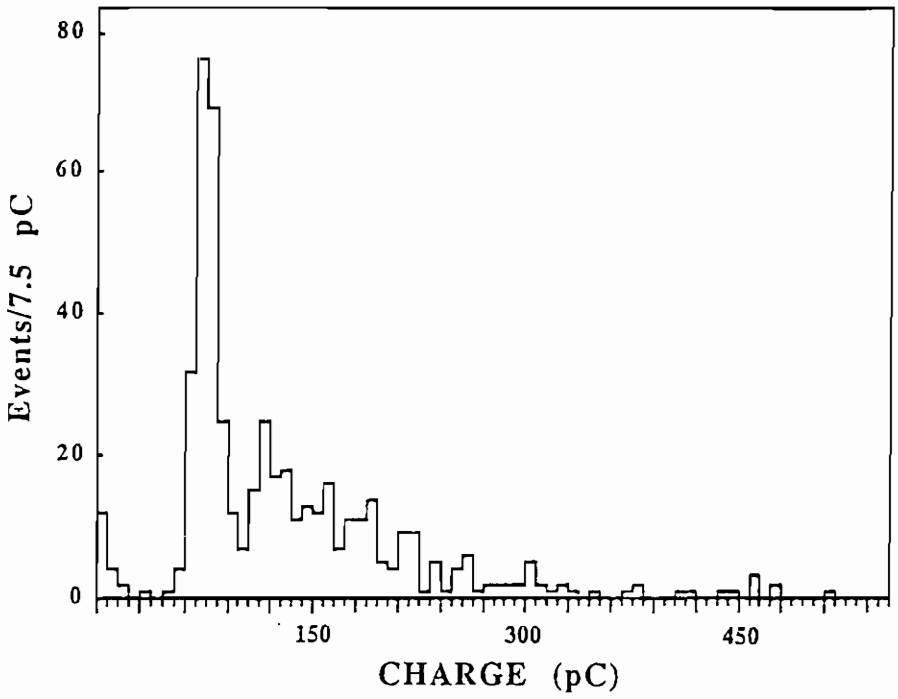

c)

Figure 3: Signal charge distribution for fixed Argon/Butane ratio (60/40 in volume) and different amounts of CF_3Br in the gas mixture: 0% a), 4% b), 8% c)

charge in this operating condition was $< 1pC$, i.e. a factor 10^2 smaller than in the usual operating condition. A similar factor is gained in rate capability.

The area of the elementary cell corresponding to this extremely small charge is of the order of $S = 10^{-2}mm^2$ and the linear dimensions are much smaller than the gas gap !.

In this condition two contiguous cells can hardly be independent and the oversimplified model of the independent discharge cells described above must be revised.

4 Signal Pick-up

The pick-up electrodes of the RPCs can be shaped as strips or squared pads. The strips have the advantage to behave as signal transmission lines of well defined impedance that allow to transmit the signals at large distance with minimal loss of amplitude and time information.

The main advantage of the squared pads is the unambiguous bidimensional localization of the particle trajectory.

The disadvantages are the higher number of frontend electronic channels and a more complicated and sometime non obvious way to connect the pads to the frontend discriminators. When a low spacial resolution is required it may be attractive the idea to use very large pads to reduce the number of frontend channels. But the following considerations show that the pad size cannot be arbitrarily large.

The current produced by the discharge in the gas induces a signal on the pick up electrode. A systematic study of the distribution of the charge induced on a small number of contiguous strips $6mm$ wide, around the discharge position, [6] [7] show that the induced charge is concentrated over a "pick up area" which turns out to be of the order of only $1\,cm^2$. The equivalent circuit of the read out electrode can be described as a current generator charging a capacitor C in parallel to a resistor R, as shown in fig. 4 where C is the electrode capacity and R the resistance connecting the electrode to ground.

Lets consider two particularly interesting cases. A long read out strip can be treated to a good approximation as a signal transmission line. The capacity C, in this case is independent from the length of the strip and, for an ideal transmission line of width greater $1\,cm$ it is proportional only to the

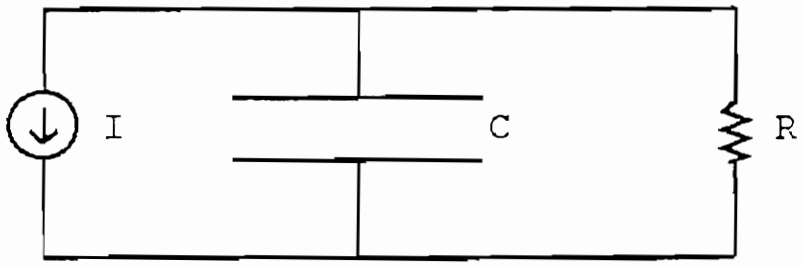

Figure 4: Equivalent circuit of the readout electrode

pick up area mentioned above, i.e. C about $1\,pC$. If Z is the characteristic impedance of the line, $R = Z/2$, as the signal propagates in both directions along the strip and, for a 50Ω line, the time constant RC is of the order of $25\,ps$ i.e. much shorter than the rise time of the signal.

In this case, according to the equivalent circuit in fig. 4, there is no signal integration. The current injected in the strip is at any instant proportional to the current of the discharge in the gas and the amplitude is $V_0 = R\,I_{max}$.

A squared pad on the contrary can be treated to a reasonable approximation as a concentrated capacitor so that $C = C_{pad}$. In this case R is the input impedance of the frontend discriminator connected to the pad and the time constant RC, for very large pads, could be much longer than the signal duration. In this condition the output signal would be strongly integrated, with an amplitude $V_0 = Q/C$ decreasing with the pad capacity and a long exponential fall time. A $30 \times 30\,cm^2$ pad connected to a 100Ω input impedance discriminator for example, would give a time constant of about $100\,ns$, a factor of 10 longer than the discharge duration with the standard gas.

This latter case would be particularly critical in connection with a pure freon operation.

5 Problems with the Neutron Background at the future Colliders

I has been recently pointed out that at the LHC experiments the rate of the detectors far away from the interaction region, like the muon detectors, will be largely dominated by the soft neutron and gamma background. At ATLAS e.g. a neutron background of $10^6/cm^2\,sec$ interesting the muon detector has been estimated [8].

This background would presumably induces in a RPCs system a much larger counting rate than that expected from the muon background.

A dedicated test to measure the neutron and gamma sensitivity, the rate capability and the ageing under neutron irradiation for RPCs, is therefore of basic importance in view of the use of RPCs as muon detectors at the future colliders.

The first test in this direction has been realized at MIT [9]. It measured a neutron sensitivity of 3×10^{-3} at a few MeV neutron energy for a standard RPC and a lifetime $> 8\,years$ at a rate of $2Hz\,cm^{-2}$.

This rate would correspond to a neutron background of $700Hz\,cm^{-2}$ according to the measured sensitivity, a value considerably smaller than the one expected now.

Nevertheless it could be extrapolated to a more realistic situation according to the following argument. As stated above the pure freon operation gives signals of charge a factor of 10^2 smaller than in the standard operation.

Therefore, as far as the ageing effects depending only on the total charge flowing in the gas are concerned, the same RPC if operated with pure freon would have the same lifetime under a neutron flux of $10^5 Hz\,cm^{-2}$.

6 Mass production

The production of very large modular detectors is a serial work particularly suited for industrial production.

RPCs are currently produced in the industry. The muon detectors of the experiments WA92 and RD5 at the CERN are realized with RPCs of industrial production.

In the next future a large system of 400 RPC modules will be constructed to upgrade the L3 experiment at LEP in the forward-backward regions [10] .

The present mass production capability is $\sim 20\,m^2/day$ for standard RPCs.

References

[1] J.W. Keuffel, Phys. Rev. 73 (1948) 531 and Rev. Sci. Instr. 20 (949) 202.

[2] Yu.N. Pestof and G.V.Fedotovich, Preprint IYAF 77-78. SLAC Translation 184 (1978);
Yu.N. Pestof, Nucl. Instr. and Meth. 196 (1982) 45; W.R. Atwood et al., Nucl. Instr. and Meth. 206 (1983) 99.

[3] R. Santonico and R. Cardarelli, Nucl. Instr. aand Meth. 187 (1981) 377;
R. Cardarelli aand R. Santonico, Nucl. Instr. and Meth. A263 (1988) 200-25.

[4] R. Santonico, Proc. Neutrino Telescopes Workshop, Venezia Nov 17-19, 1988;
F. Ceradini et al., Proc. ECFA LHC Workshop, ECFA 90-133, vol. III, eds. G. Jarlskog and D. Rein, (CERN 1990) p. 838;
C. Bacci et al., Nucl. Instr. and Meth. A315 (1992) 102.

[5] R.Cardarelli, contribution to this workshop.

[6] B.Pontecorvo, contribution to this workshop.

[7] F. Rossi, Doctoral Thesis, Universita' di Roma "La Sapienza" (1988).

[8] A.Ferrari, Communication at the ATLAS General Meeting, Feb. 4, '93.

[9] I.Pless, contribution to this workshop.

[10] S.Patricelli, contribution to this workshop.

PERFORMANCE OF E771 RPC MUON DETECTOR

(E771 Collaboration)

Presented by E. GORINI

Università di Lecce, Dipartimento di Fisica and INFN, Sezione di Lecce, Italy

The technique of Resistive Plate Counters, equipped with pad readout instead of strips, has been successfully used for the first time in a high rate environment. The performance of the muon detector of E771, based on this technique, is illustrated in detail, including the dependence of the efficiency on the local rate of incident particles.

1. Introduction

The primary objectives of experiment E771 at Fermilab [1,2] are the production of beauty particles and the study of their decays by means of a high intensity, high momentum proton beam on a silicon target. The strategy adopted to detect beauty events is to select dimuons coming from J/ψ produced at a secondary vertex.

The E771 detector is located in the High Intensity Lab at Fermilab and is an upgrade of the former E705 spectrometer. The current set-up includes a new 800 GeV/c beam line, a segmented silicon target, a silicon micro strip detector (12 planes), new drift chambers (CC/WC) with pad and strip readout and a muon detector made of Resistive Plate Counters (RPC). In addition, Fastbus readout electronics, RPC based muon triggers, and a new Data acquisition chain have also been implemented.

2. Muon detector

The muon detector consists of three planes of RPC modules separated by hadron absorbers at the downstream part of the E771 spectrometer (Fig 1).

RPCs are thin gap (2 mm) gas devices [3] operating in streamer mode in a high uniform electric field (40 kV/cm). Their main characteristics are good time resolution, low cost and large area coverage. Figure 2 shows a cross sectional view of an RPC module. The counters are filled with a mixture of 53 % Argon, 42 % Butane and 5 % Freon 13B1. The charge produced by the streamer process is picked up by external copper pads facing the high voltage side. At the nominal setting of 8.2 kV the signals range from 100 to 200 mV (depending on the pad size) with a 3-4 ns rise time and 20 ns width. An aluminum frame surrounds the counters to ensure rigidity and to support the signal connectors and gas inlets and outlets.

Ten 2×1 m^2 RPC modules are assembled together to form a detector plane. Slight overlapping of the modules is necessary to recover dead zones along the perimeter of the detector due to the supporting frame. The beam plug in the first two muon planes has forced the construction of L-shaped modules in order to have a complete coverage of the area around the plug. A standard module is used for the third plane where no plug is present. Figure 3 shows the resulting pad configuration, identical for the three planes, as seen from the beam. The different pad sizes have been chosen as a compromise between good granularity (especially in the central region) where most of the flux is impinging, and multiple scattering in the hadron absorber. The pad surface is 6×6 cm^2 for the central modules and ranges up to 12×12 cm^2 in the outer regions.

Mass flow meters control the gas mixture ensuring 1 % stability and precision. Each counter is connected to a separate gas line, to a ball flow meter and to a high precision manometer (the large area of the RPC does not allow pressures higher than 2-3 mbar). A safety system set at 3.5 mbar (including the pressure drop after 60 m nylon tubing) prevents accidental build up of over-pressure along the lines.

A computer controlled system [4], which can operate up to 15 kV with 1 mA current limit, supplies the high voltage to the RPC modules and, through a CAMAC interface, all the relevant parameters are continuously monitored. The gas and high voltage systems communicate through a custom-made interface control box [5] which operates on the high voltage when the gas mixture falls out of pre-defined limits.

3. Readout and Fastbus Front-End Electronics

A readout board [6] discriminates (at a threshold of about 60 mV) and shapes (20 ns width) the signals coming from the counters. Each board serves 16 pads and gives fast signals in ECL and TTL logic, respectively to the acquisition chain and to the trigger electronics together with the 4 additional logical OR of 2×2 adjacent pads. A crate allocates 8 boards and 16 crates serve a detector plane (for a total of 6144 channels). For the first plane all the channels are sent to the data acquisition system, while for the other two planes only the OR-*ed* signals are acquired.

The ECL signals are sent, after 20 meters of twisted pairs cables, to the Fermilab FASTBUS data acquisition system [7] which is capable of associating an event to a single Tevatron RF bucket (20 ns) and of completely recovering within one or two buckets by operating synchronously with the 53 MHz accelerator clock. A digital memory is used to provide a trigger delay, which is adjustable in one bucket steps up to a maximum of 4.8 μs.

The front end electronics system consists of a set of Fermilab FASTBUS modules which delay, encode and read the detector hit informations and requires 2 fully loaded crates for a total of 3072 channels.

4. Data Taking

The E771 detector has been exposed, during the 1991-92 running period, to the 800 GeV/c Tevatron proton beam of about 4×10^7 protons per second intensity with a spill

length of 23 seconds every 54 seconds. This corresponds approximately to 2×10^6 interactions per second on a 5% interaction length thick silicon target.

Two different, parallel triggers, both based on programmable logic arrays, have been used. The first one (1A or μ trigger) [8] used triple coincidences of the three RPC planes to define the presence of muons with momenta greater than 6 GeV/c. The second one (1B or p_T trigger) [9] used triple coincidences of the first RPC plane with two of the four upstream CC/WC's pad planes, selecting pre-defined hit patterns loaded in the trigger logic corresponding to trajectories with $p_T > 0.8$ GeV/c.

The single muon trigger rate was about 100 kHz at the maximum interaction rate, corresponding to roughly $25 \div 30$ incident particles per cm^2 averaged over the entire surface of the central RPC modules of the first plane. Figure 4 shows the trigger profile obtained in each of the 32 groups (superOR) in which the 1A trigger is subdivided.

In order to check both RPC and trigger performances, a muon trigger, similar to the one of E705, based on the coincidences of the scintillator planes placed next to the RPC planes, was set-up and used as monitor.

5. Performance of the RPCs.

The resistivity of the bakelite electrodes and the gas amplification of the mixture have been indirectly measured, for each one of the 29 RPC modules, through their voltage to current characteristics in the absence of beam (Fig. 5), by assuming that the conduction occurs only through the spacers. Figure 6 shows the relatively homogeneous value of the resistivity for the entire sample of RPCs.

The RPC have been operated at a voltage of 8.2 kV, about 200 volts above the onset of the efficiency plateau. With this setting the currents were as high as 700 μA (in the central modules of the first plane) during beam spills.

Figure 7 shows the hit distributions on the pads of the first plane and the central hole due to the beam plug. The advantages of the bi-dimensional arrangement of the pads are

evident, as well as some noise due to the spacers. The hit multiplicity per module due to crossing muons was very low. The noise (mainly due to punch-through particles) has been defined as the fraction of hits not belonging to the reconstructed muon tracks. Figure 8 shows this value for the 29 modules.

The cross-talk between adjacent pads has been carefully studied in order to understand the extent of the optimization of the pad size. The cross-talk is mainly due to the capacitive coupling between adjacent pads and is therefore dependent on the length of their perimeter. Figure 9 shows the cross-talk distribution for pads sharing a side or a corner pad, the average is about 8 %. A small contribution to the cross-talk is also due to the electronics (including cables) and is measured to be about 10% of this. Finally figure 10 shows the distribution, for the entire sample of RPC modules, of the equivalent distance from the edge of the pad below which a hit induces cross-talk on an adjacent pad. Its mean value is consistent with the size of the gap between adjacent pads.

The time resolution σ_T has been measured using TDC's installed on all the RPC modules belonging to a quadrant of the muon detector. Figure 11 shows σ_T for low rates of incident particles. The average resolution of 4 ns does not depend on the pad size because of the larger contributions due to cables, read out, and front end electronics. The intrinsic time resolution of the detector has been measured to be about 1 ns [10] and is dependent on the incident particle rate. Figure 12 shows this behavior both for the time resolution and the signal delay.

A tracking program, based on the existing muon scintillator planes, corrected for acceptance, has been used for the evaluation of the efficiencies. These are consistent with those expected and due to the spacers (about 96%) when measured at low incident rates, but decrease with beam intensity. Fig. 13 shows the average efficiency for the second plane of RPC versus the average incident rate as computed from the interaction triggers. The rate of decrease is not in agreement with the one measured in a test beam at CERN [11]. In order to fully understand this discrepancy we have computed the efficiencies by de-convoluting the timing dependence of the RPC on the incident rate. The resulting efficiency is plotted in Fig. 14. The rate dependent efficiency, corrected for this effect,

becomes thus consistent with the measurements in [11] where a much wider gate (100 ns instead of 20 ns) was applied.

6. Conclusions

Resistive Plate Counters equipped with pad readout, instead of strips, have been successfully used for the first time in a high rate environment. The technique appears to be very promising in virtue of the high stability of operation and the excellent timing properties, which makes it ideal as the active volume of muon detectors.

Cross talk between adjacent pads and noise have been measured and shown to be whitin acceptable limits. Geometric efficiency is limited by the size and the number of the gap spacers, which are also the main source of noise.

Rate dependent efficiencies have been observed at incident rates of the order of $25 \div 30$ particles per cm^2 over large surfaces and are mainly explained by timing effects.

References

[1] B. Cox at al., Fermilab Proposal P771, (April 1986).

[2] F.Grancagnolo, INFN-AE/90-07.

[3] R.Santonico et al., Nucl. Instr. and Meth., 187 (1981) 377; R.Cardarelli et al., Nucl. Instr. and Meth., A263 (1988) 20.

[4] Mod. SY127, Technical information, CAEN.

[5] M.Panareo, INFN/TC-92/12.

[6] L.Antoniazzi et al., Nucl. Instr. and Meth., A307 (1991) 312.

[7] C. Swoboda et al., IEEE Trans. on Nucl.Sci., Vol. 37, No. 2, April 1990.

[8] L. Antoniazzi et al., Nucl. Instr. and Meth., A314 (1992) 563.

[9] S. N. Zhang et al., IEEE Trans. on Nucl. Sci., 39, 1992, 814; L. Antoniazzi et al., E771 Internal Note (1990).

[10] F. Grancagnolo, INFN/AE-90/21; E. Gorini, Nucl. Phys. B (Proc. Suppl.), 23B (1991) 249.

[11] M.Bertino et al., Nucl. Instr. and Meth., A283 (1989) 654.

Figure Captions

Fig. 1. E771 Muon detector. Scale is in meters.

Fig. 2. Cross sectional view of a Resistive Plate Counter.

Fig. 3. Pad configuration.

Fig. 4. Trigger profile. Beam is coming from the top.

Fig. 5. Current-voltage characteristics for a tipical module.

Fig. 6. Distribution of resistivity.

Fig. 7. Hit distribution on first RPC plane.

Fig. 8. Distribution of the fraction of hits not belonging to a reconstructed track.

Fig. 9. Distribution of cross-talk (side and corner pads).

Fig. 10. Equivalent thickness for cross-talk.

Fig. 11. Time distribution at different rates of incident particles.

Fig. 12. Time resolution and signal delay vs. particle flux.

Fig. 13. Efficiency vs. particle rate. Measured with muon tracking.

Fig. 14. Efficiency vs. particle flux. Measured with timing distributions.

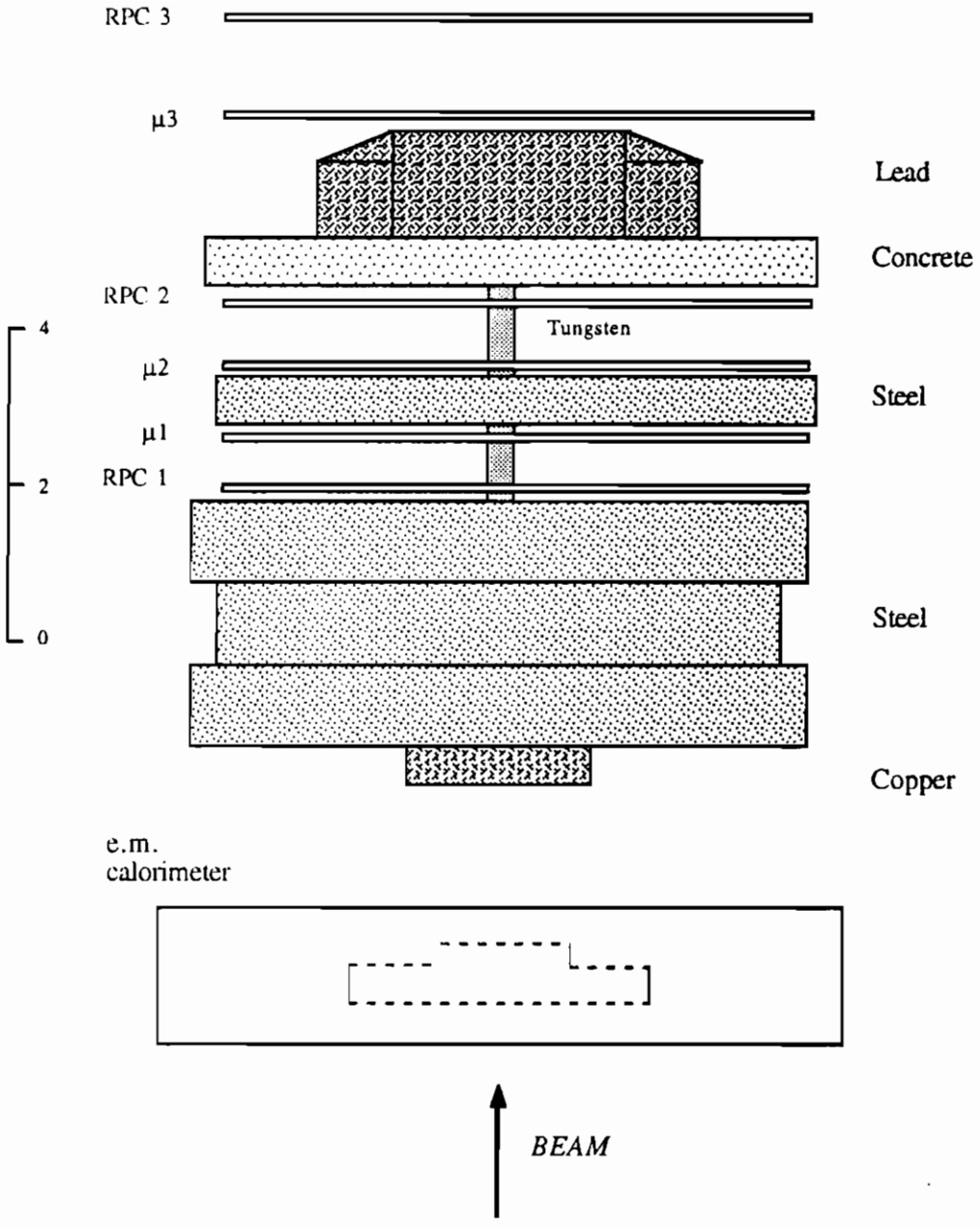
RPC 3
μ3
Lead
Concrete
RPC 2
Tungsten
4
μ2
Steel
μ1
RPC 1
2
0
Steel
Copper
e.m.
calorimeter
BEAM

Figure 1

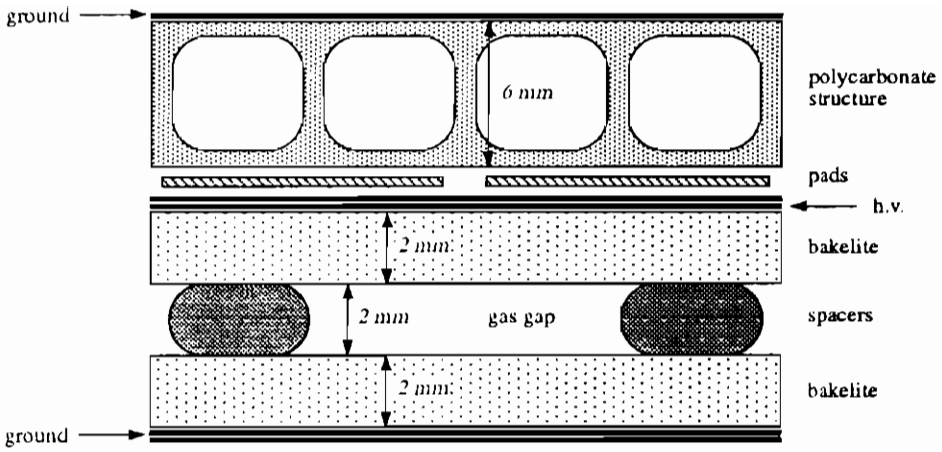

Figure 2

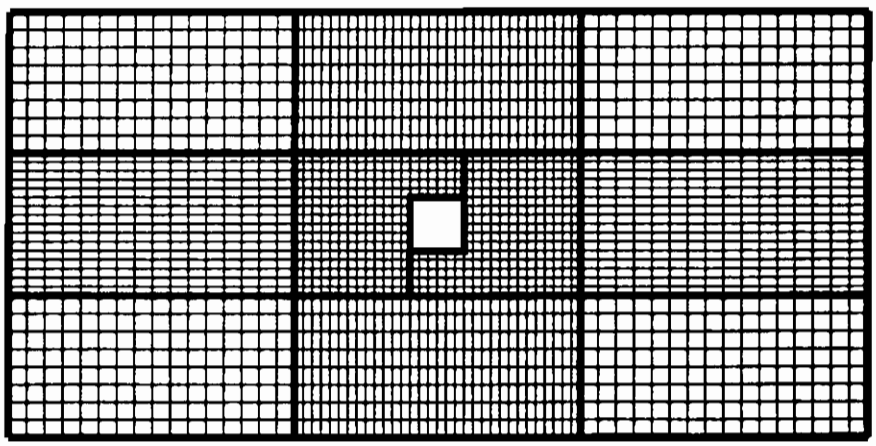

Figure 3

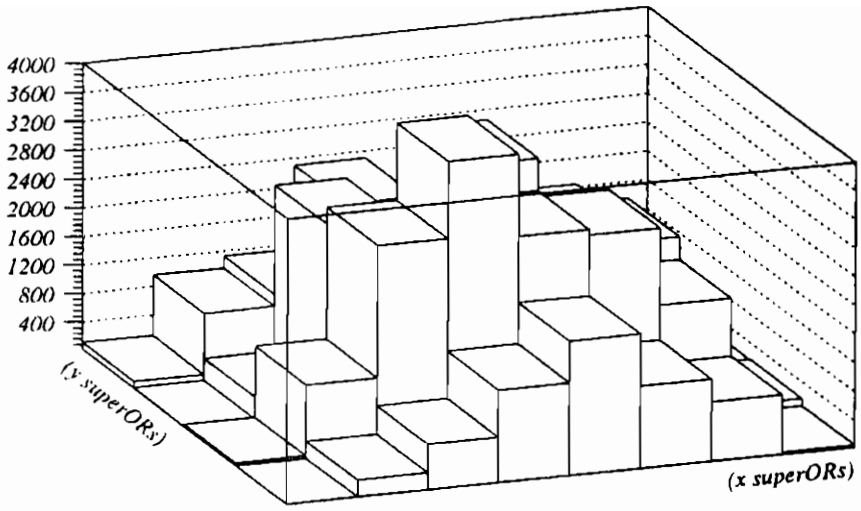

Figure 4

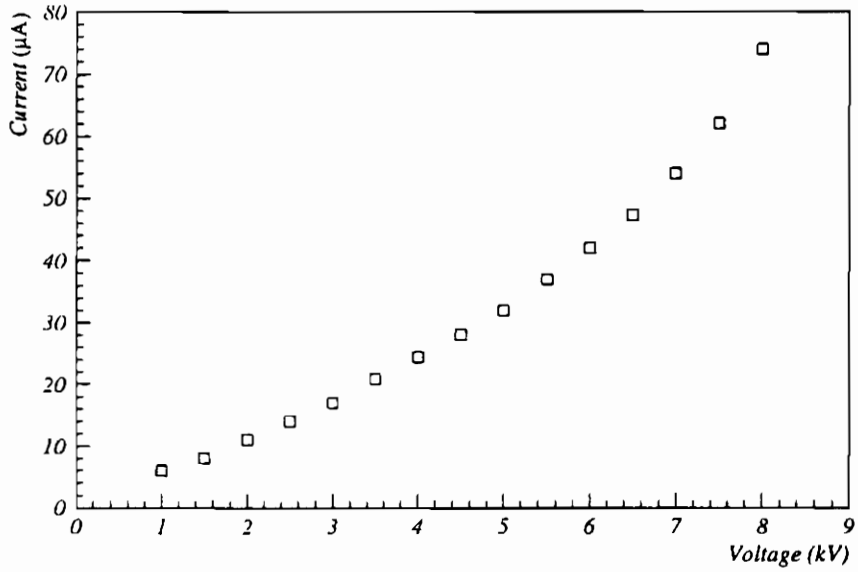

Figure 5

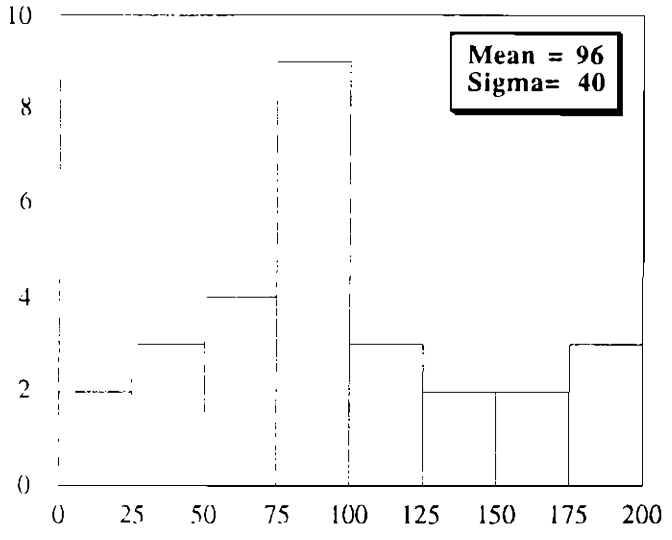

Figure 6

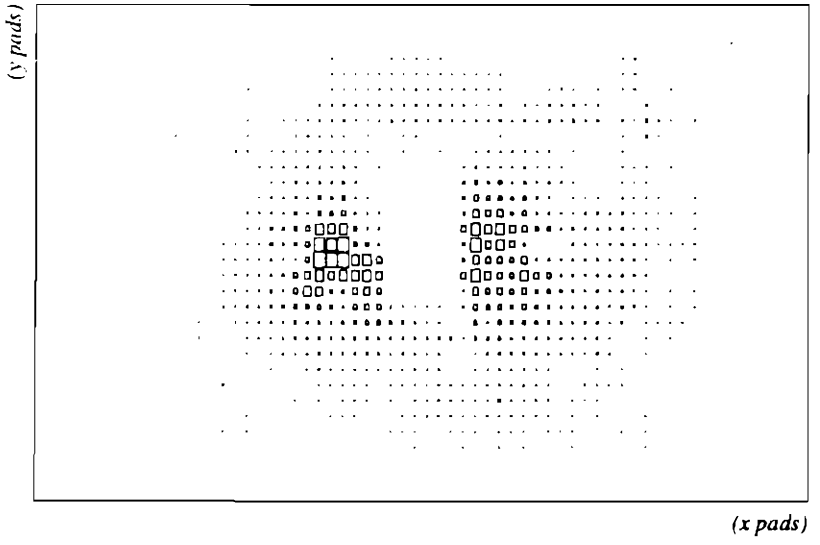

Figure 7

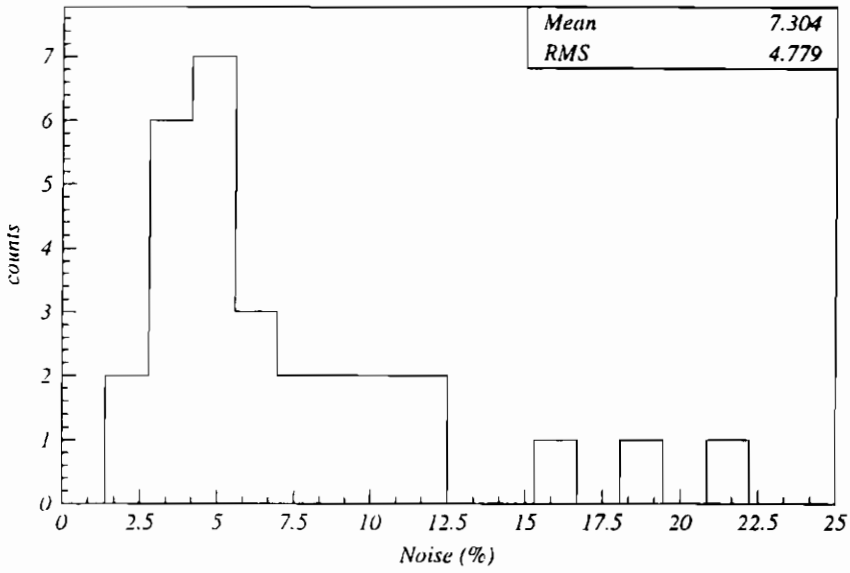

Figure 8

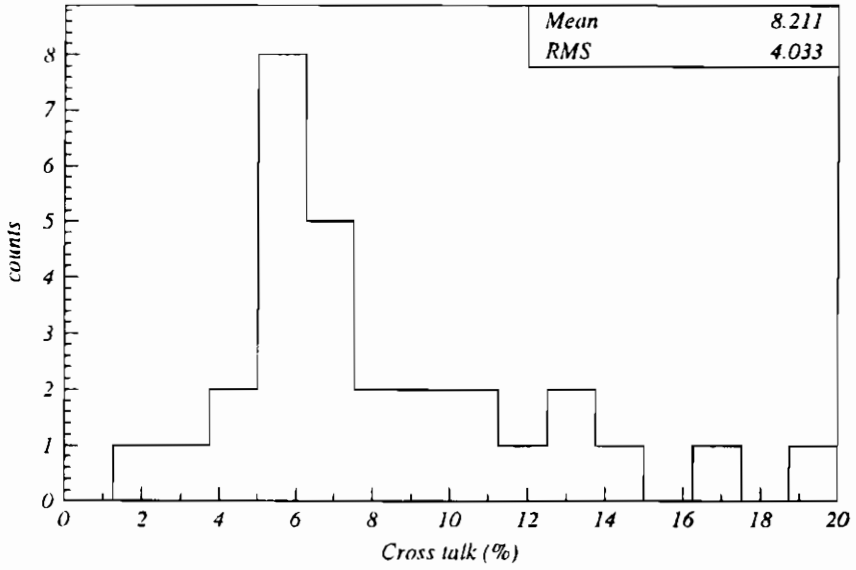

Figure 9

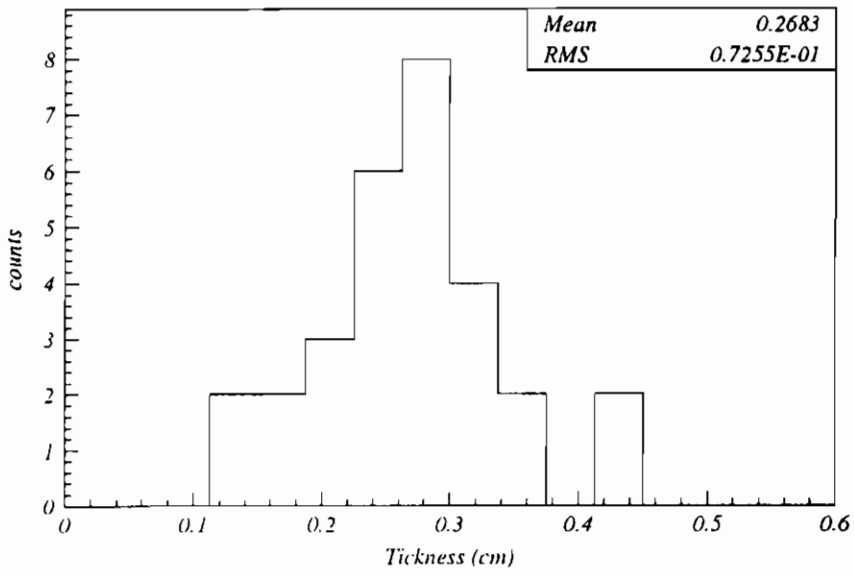

Figure 10

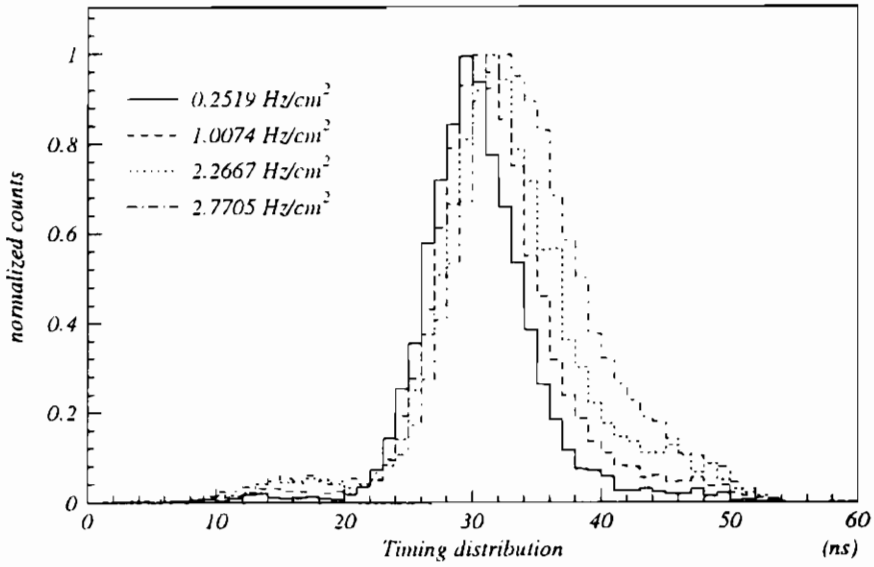

Figure 11

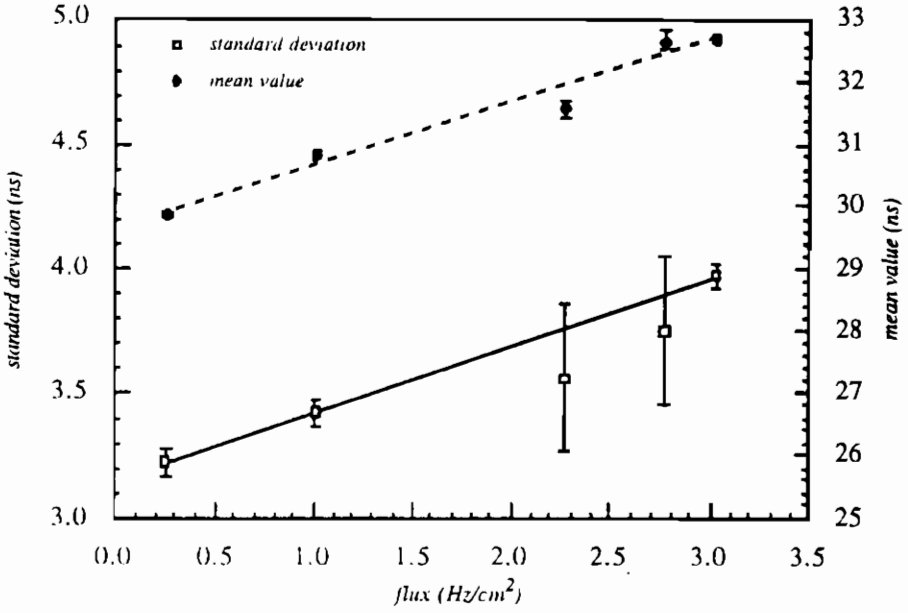

Figure 12

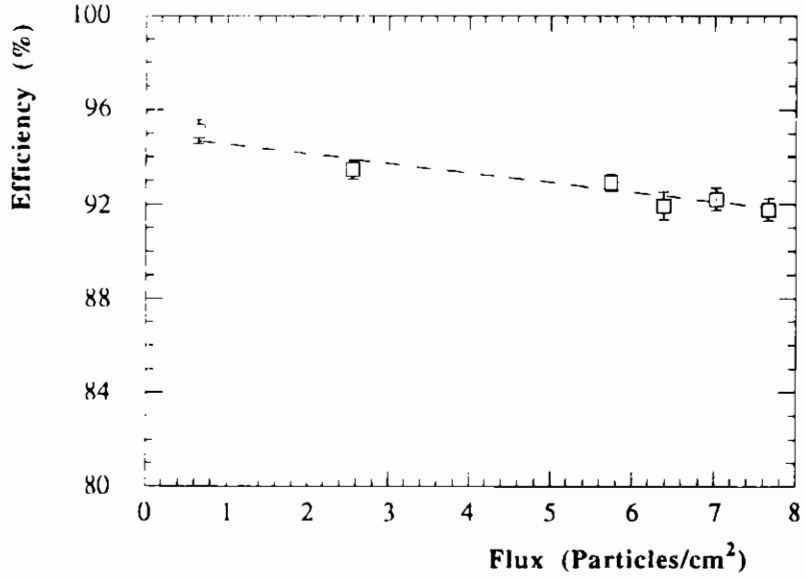

Figure 13

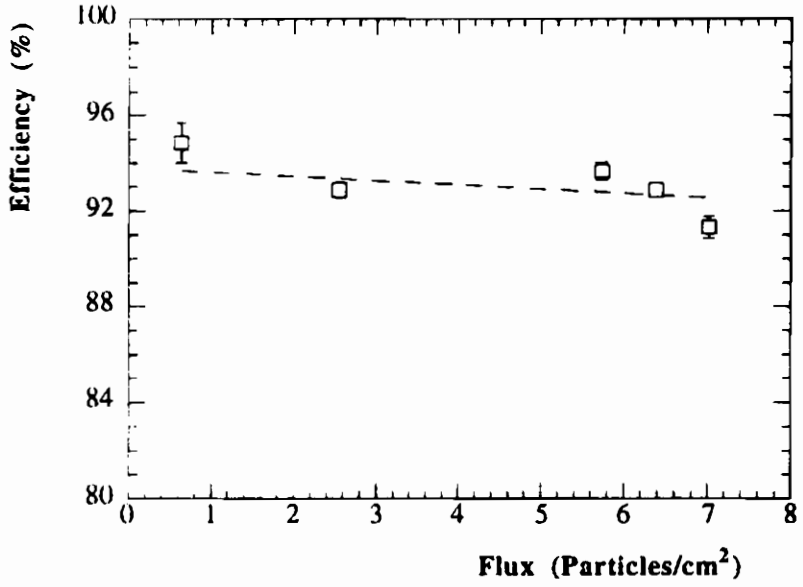

Figure 14

THE MUON TRIGGER HODOSCOPE OF THE BEAUTY HADROPRODUCTION EXPERIMENT WA92; PERFORMANCES AND PRELIMINARY RESULTS ON BEAUTY MUONIC DECAYS

G. Martellotti and D. Orestano
I.N.F.N. Sezione di Roma, Italy
The Beatrice[1] collaboration

1 Introduction

The Resistive Plate Chambers (RPCs), even if known since many years, have been used for charged particles detection and tracking in high energy physics experiments only very recently. RPCs with digital strip read-out are very well suited to build large area, high (~cm) granularity hodoscopes with comparable performances respect to scintillators hodoscopes but with big advantages in terms of cost, flexibility in segmentation, simplicity of operation and read-out, reliability.

This workshop was done with the idea of evaluating the level of maturity of the RPC technique. We thought therefore appropriate to present here the performances of a large area muon detector based on RPCs that has been used in an experiment for hadroproduction of beauty particles at the CERN SPS, with a 350 GeV/c π^- beam, WA92[1] . The preliminary results of the experiment with the identification of some beauty muonic decay candidates show that this type of detector can be used with very good performances in detecting and tracking charged particles.

2 The experimental set up

The WA92 experiment makes use of the Ω spectrometer for particles momenta measurement. The general lay-out of the experiment is shown in fig.1. The target (2 mm of copper or tungsten) is outside the magnetic field. A 17 planes high resolution silicon telescope, the *Decay Detector*[2](DD), equipped with analog read-out, is positioned immediately after the target with the aim of disentangling the complex beauty decay topologies. A second silicon telescope with larger lever arm and digital read-out for impact parameter detection, the *Vertex Detector*[3] (VD), follows the DD. At the

[1]M.Adamovich, M.Adinolfi, Y.Alexandrov, C.Angelini, F.Antinori, C.Bacci, D.Barberis, D.Barney, J.Batten, W.Beusch, C.Bruschini, R.Cardarelli, A.Cardini, V.Casanova, F.Ceradini, G.Ciapetti, M.Dameri, G.Darbo, A.Di Ciaccio, A.Duane, J.P.Dufey, V.Flaminio, A.Forino, B.R.French, A.Frenkel, R.Gessaroli, K.Harrison, R.Hurst, S.Kharlamov, A.Kirk, F.Lacava, J.C.Lassalle, C.Lasseroni, L.Malferrari, G.Martellotti, P.Martinengo, P.Massanti, J.C.McEwen, P.Nechaeva, A.Nisati, D.Orestano, B.Osculati, M.Passaseo, G.Penso, E.Petrolo, L.Pontecorvo, A.Quareni, P.Ragni, V.Rhysov, C.Roda, L.Rossi, C.Salvo, R.Santonico, G.Schuler, M.Torelli, S.Venesiano, M.Versocchi, D.Websdale, M.Weymann, L.Zanello and M.Zavertyaev

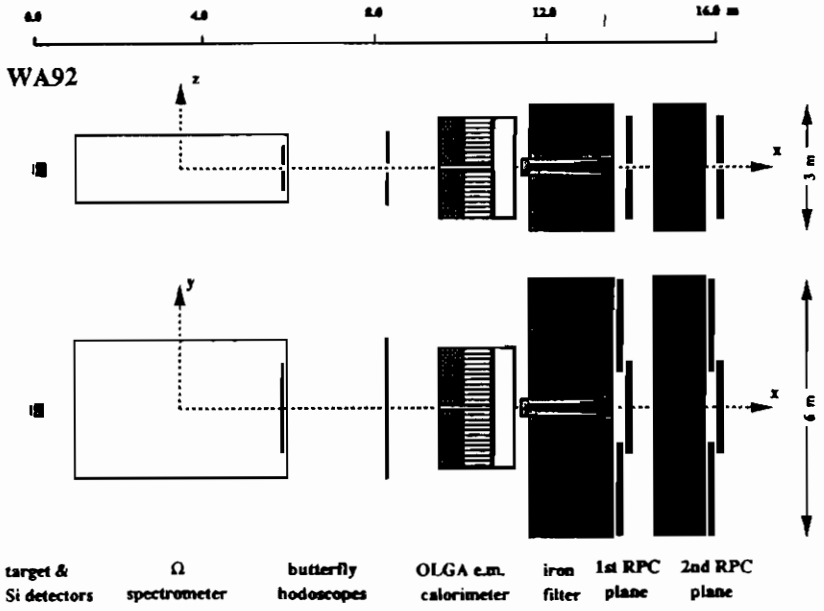

Figure 1: *Lay-out of* WA92 *experiment*

spectrometer end a lead glass electromagnetic calorimeter identifies electrons and π^0 and a large acceptance RPCs hodoscope behind two iron absorbers performs the muon identification[4].

Due to the very small beauty signal at the energies of SPS fixed target experiments, a very selective trigger based on the main features of beauty decays, keeping at the same time a large acceptance for the signal, is needed. The event selection can exploit the presence of multiple secondary vertices originated from the beauty to charm cascade decay, the large branching ratio for semileptonic decays and the emission of secondaries with large transverse momenta.

In WA92 three main triggers have been implemented: one requiring tracks with a large ($\geq$ 100 μm) impact parameter to the interaction vertex, one requiring the identification of a penetrating muon coming from the interaction region and a high P_T trigger.

The trigger on impact parameter tracks is performed by a fast processor elaborating the data of the VD. A second trigger processor makes use of the RPCs information to identify muons. Finally a two planes scintillator hodoscope with "butterfly" shape selects high P_T charged particles[5].

3 The muon trigger hodoscope

The muon trigger hodoscope consists of two detector planes at 14 and 16 m from the target, placed behind two iron absorbers of 2.0 and 1.2 m thickness respectively. The core of the first absorber is made of disks of tungsten ($\sim 21\lambda$) where the π^- beam is dumped. The thickness of the first absorber ($\sim 12\lambda$) is chosen to filter out most of the hadrons produced in the target, while keeping the multiple coulomb scattering of high energy muons at a low level to allow association of tracks measured in the hodoscope with those measured in the spectrometer. The presence of the second absorber ensures that only muons are able to reach the second plane of the hodoscope ($\sim 20\lambda$ in total).

The hodoscope is built with "standard", single gap, RPCs[6], equipped with 3 cm pitch read-out strips. These detectors provide fast response, good efficiency and uniformity of response over several square meters. Besides the requirement of a fast response at trigger level, a good time resolution is also needed to avoid accidental coincidences of beam halo muons with the interaction trigger. Each hodoscope plane is made of three detector planes, two equipped with horizontal read-out strips to measure the vertical coordinate (z-chambers) and one equipped with vertical read-out strips (y-chambers). Each detector plane is made of six chambers 1×2 m^2 slightly staggered in the y direction to avoid dead regions due to the spacers.

There are two main background components to prompt muons: the muons that originate from in-flight decays of pions and kaons and the muons that originate in hadron showers initiated in the electromagnetic calorimeter positioned upstream the first absorber. This second component has a softer momentum spectrum and a wider angular distribution: it can be strongly reduced by requiring the collinearity with the target.

The field in the Ω magnet is directed vertically and the particles with low transverse momenta are deflected horizontally close to the central plane. Thus this plane is mainly populated by decay muons that originate from parents emitted with low transverse momenta. For this reason each hodoscope plane has been divided in two halves: up and down. Each half hodoscope has an angular coverage $8 \leq \mid \theta_x \mid \leq 70$ mrad in the vertical plane and $0 \leq \mid \theta_y \mid \leq 180$ mrad in the horizontal plane. The bending power of the magnet and the requirement of penetrating through the iron filter impose a cut on muon longitudinal momentum of about 5 GeV/c. A fast processor, with a fixed processing time of 90 ns, is used to verify whether the track hits in the non bending projection (z-chambers) are collinear with the target[7]. To associate the hit pattern to the interaction vertex the processor defines roads with programmable width and inclination. These roads are mapped onto a matrix made of fast programmable logic devices. The requirement of a track pointing to the target increases the momentum cut to about 7.5 GeV/c. Due to the minimum angle covered by the hodoscope, the muon trigger condition reflects in a cut in the transverse momentum distribution at about 100 MeV/c. Table 1 summarizes the acceptance for both the signal and the background

Trigger	Beauty acceptance	trigger rate	enrichment factor
1μ	18%	2.8%	6.4
$1\mu \times 1P_t$	14%	1.3%	10.7
$1\mu \times 2$IP tracks	11%	0.25%	44.0

Table 1: *Acceptance for montecarlo beauty events (computed with PYTHIA event generator and GEANT simulation), trigger rate and enrichment, for different trigger conditions*

for the muon trigger used alone or in coincidence with other trigger requirements.

4 Operation and performance

The WA92 experiment took data in 1991 for 15 days and in 1992 for 3 months. The RPCs hodoscope performances have been stable and no serious problem arised during both the data taking periods. During these run periods the chambers were operated using a gas mixture of 55% argon, 42% n-butane and 3% freon. With this mixture they reached the efficiency plateau at an electric field of about 35 kV/cm and the efficiency was about 97%. The processor was operated with roads three strips wide: every strip of the first plane was in coincidence with three strips of the second plane. During most of the data taking periods the beam intensity was on average 1.2 MHz and the hodoscope rate, due to the halo of muons accompanying the pion beam, was 25 kHz. In these conditions the interaction trigger rate was 20 kHz and the muon trigger rate 700 Hz.

Looking for tracks reconstructed in the RPCs hodoscope, using only the z coordinate, we find at least one track in 96% of the muon triggered events. Figure 2 shows the angular difference in the non bending plane, $\Delta\theta_x$, between the tracks reconstructed in the muon trigger hodoscope and those measured in the VD, 14 m upstream, for the same event and for a different event (dashed histogram). A clear correlation is visible. The normalization of the two histograms is such that the area of their difference equals the number of reconstructed muons. The difference between the two histograms represents therefore the true correlation between tracks reconstructed in RPCs and in the VD. A fit to that distribution, removing the combinatorial background, shows that it can be explained in terms of the sum of three different contributions: muons from pions in-flight decays, having a sigma of 2.5 mrad and representing 50% of the sample, muons from kaons in-flight decays, having a sigma of 12 mrad, accounting for another 25% of the sample, and a flat component due to the absence of the muon track in the VD in 25% of the events. The last component can be explained partly by the different angular coverage of the two detectors and partly by the track reconstruction inefficiencies

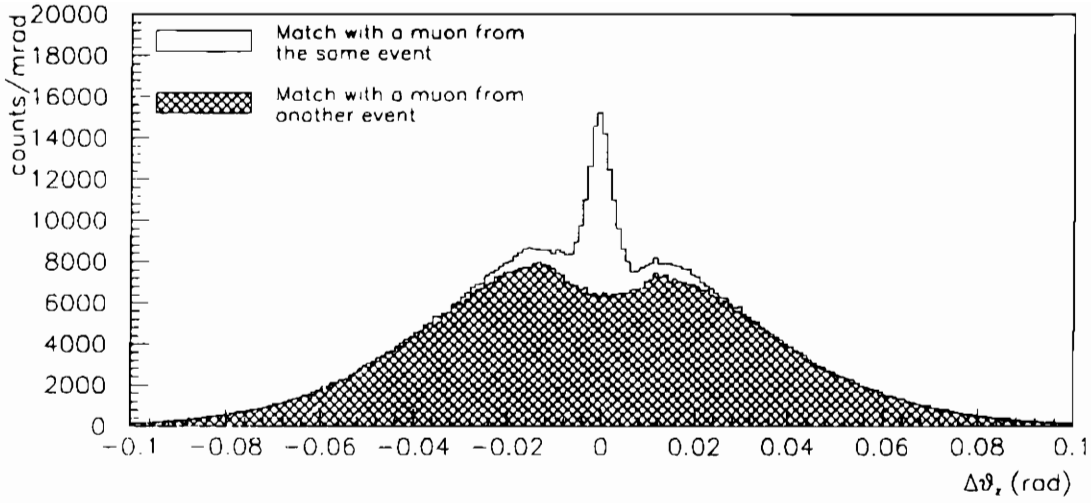

Figure 2: *Angular difference between the tracks reconstructed in the muon trigger hodoscope and those measured in the VD*

in the VD. Using both coordinates and the reconstruction in the spectrometer, which rejects tracks presenting large kinks, we find at least one fully reconstructed muon in 65% of the muon triggered events.

5 Preliminary results on the muonic decays

During the 1992 run we have collected 90 10^6 of events using a combination of the three main triggers of the experiment. The total sensitivity is 120 evts/nb([2]). Here we present the preliminary results of the analysis on a special trigger stream that required at the same time one identified muon, two impact parameter tracks (impact ≥ 100 μm) and one or two high P_T (≥ 600 Mev/c) triggers. This sample of 1.7 10^6 events, after a filter stage to remove obvious trigger pathologies, has been fully reconstructed in the spectrometer (including the silicon hodoscopes) with the additional request of at least one muon having a transverse momentum with respect to the beam axis ≥ 1 GeV/c and linked to a reconstructed secondary vertex or not pointing to the primary vertex within more than 100 μm. On the remaining 1000 events a further selection, based on the graphic analysis of the VD and DD data (including the pulse hight information coming from the DD), has been applied. In this way a large fraction of the secondary vertices has been rejected as due to interactions occuring on the silicon planes, artefacts of the vertex algorithm.... The final sample contains 72 neutral 2-prong decays (V2),

[2]we define the sensitivity as the total number of interactions analysed by the trigger divided by the interaction trigger cross section (per nucleon).

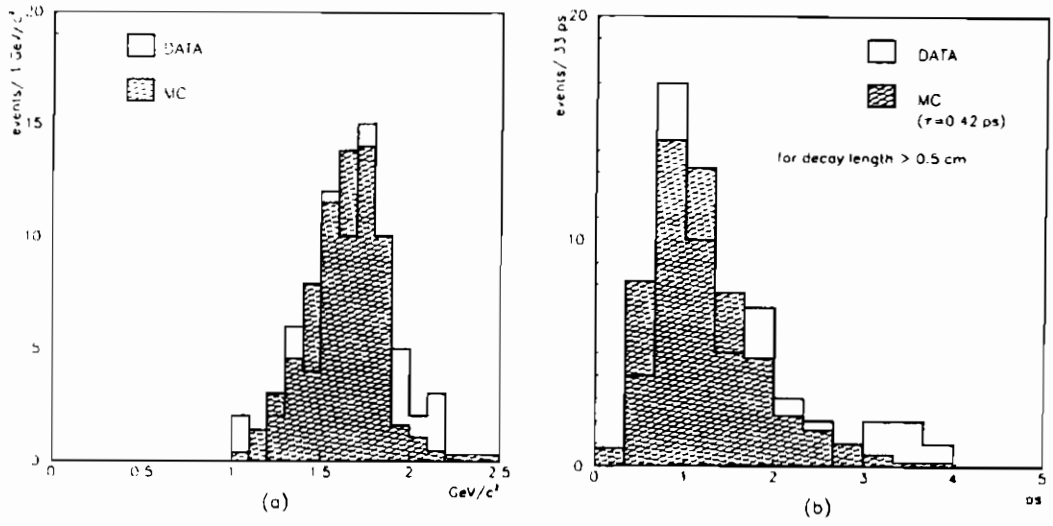

Figure 3: *a) Minimum mass and b) time "t", evaluated for V2 charm candidates and for montecarlo D^0 semileptonic decays*

17 charged 3-prong decays (C3), 1 neutral 4-prong decay (V4), and 10 chain decays. The V2, C3 and V4 are all compatible with a charm semi-leptonic decay hypothesis, as can be seen for example from fig.3 a,b where we compare the minimum mass of the V2 systems, M_{min} and the quantity $t = lM_{D^0}/P_{vis}$, where l is the decay length, with the MC expectation including all the cuts. The minimum mass is defined as $M_{min} = \sqrt{M_{vis}^2 + P_{Tmiss}^2} + P_{Tmiss}$, where M_{vis} is the invariant mass of the visible system evaluated for the μK hypothesis, and P_{Tmiss} is the missing transverse momentum, computed with respect to the line of flight. The quantity "t" is similar to the proper time τ but is calculated using the visible momentum of the system P_{vis} instead of its total momentum. Moreover in ten of these events another charm decay candidate is also visible.

In the 10 events showing a decay chain topology the first decay vertex is incompatible with a charm interpretation (charged decays in one prong with $P_T > 1.0$ GeV/c or charged/neutral multiprongs with $M_{min} > 2.0$ GeV/c^2) while the second decay is always compatible with a charm interpretation. In 2 events also a second decay chain is observed. We conclude that these events are possible candidates for beauty decays. One example of such events is shown in fig.4.

Applying the trigger and the same analysis chain to montecarlo events we expect an acceptance of 1.5 10^{-2} (about 5 events/nb of beauty cross section) for beauty and an acceptance of 10^{-4} and 3 10^{-4} respectively for the charm mesons decays $D^0 \rightarrow \mu\nu X$ and $D^{\pm} \rightarrow K^*\mu\nu$. Montecarlo evaluation of the expected background in our final sample is at present in progress.

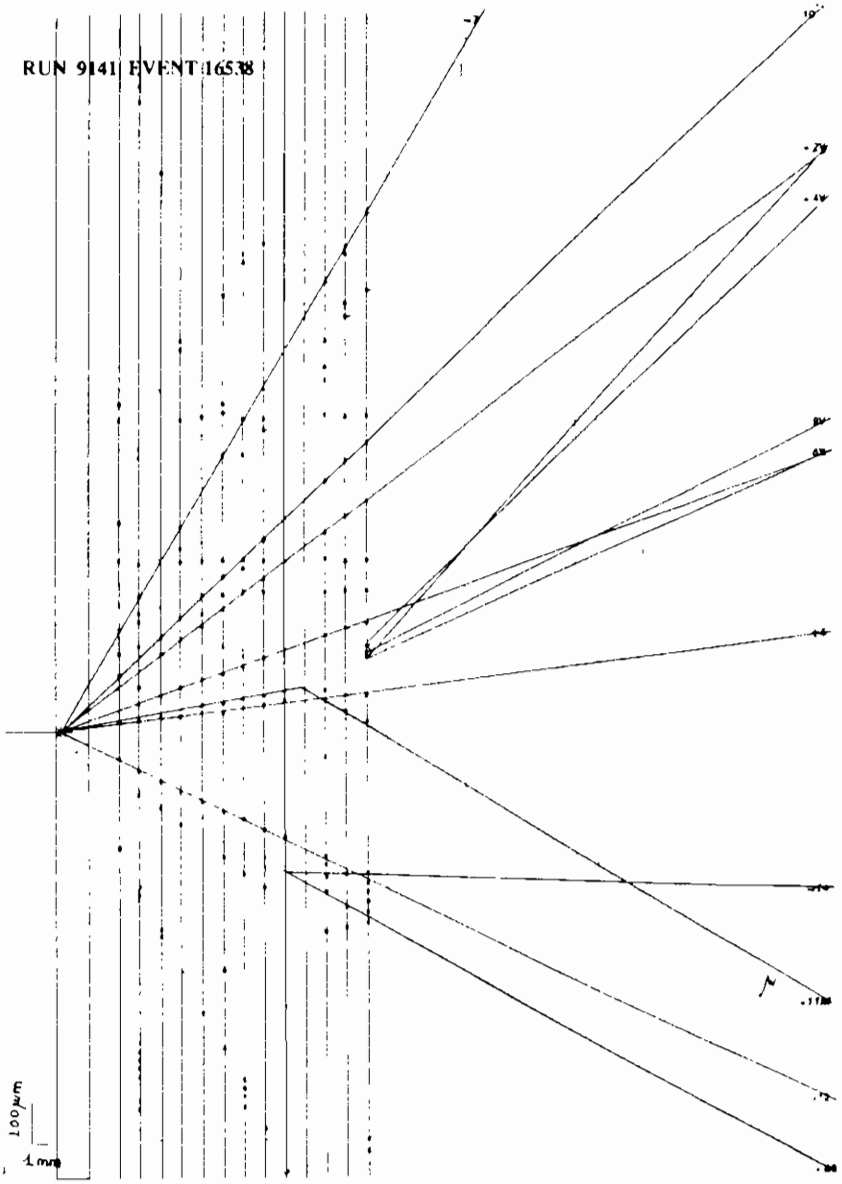

Figure 4: *DD view (xz projection) of one beauty candidate: a C1, at 1.3 cm distance from the target, with a positive muon having a P_T of 1.5 GeV/c with respect to the parent particle line of flight, followed, after 2.5 mm, by a V4 vertex. In the $K^+\pi^+\pi^-\pi^-$ mass hypothesis the invariant mass of the V4 is 1.878 GeV/c^2 and the sum of momenta points back to the C1 vertex .*

6 Conclusions

In this contibution we have described the characteristics and the performances of a large area hodoscope made with standard RPC chambers used at the CERN SPS in the exeriment WA92 for muon identification and tracking. In a two years period of operation the detector has behaved in a very reliable way and with the expected performances. The preliminary analysis of a sample of high P_T muon triggers has been able to identify 90 charm semileptonic decays and few beauty semileptonic candidate decays.

References

[1] L. Rossi et al. (BEATRICE Collaboration), proposal to SPSC, CERN-SPSC/90-10, March 1990.

[2] F. Antinori et al. , Nucl.Instr.and Meth. A288(1990)82;
M. Adinolfi et al. , CERN PPE 92-181, 30 September 1992, to be published in Nucl.Instr.and Meth.

[3] M. Adamovich et al. , Nucl.Instr.and Meth. A309(1991)401;
G. Darbo and L. Rossi, Nucl.Instr.and Meth. A289(1990)584.

[4] C. Bacci et al. , Nucl.Instr.and Meth. A324(1993)83.

[5] W. Beusch et al. , Nucl.Instr.and Meth. A249(1986)391.

[6] R. Santonico and R. Cardarelli, Nucl.Instr.and Meth. A187(1981)377;
R. Cardarelli et al. , Nucl.Instr.and Meth. A263(1988)20.

[7] E. Petrolo and S. Veneziano, Proc. 5th Pisa Meeting on Advanced detectors, La Biodola, Isola d'Elba, Italy, May 26-31, eds. A Baldini, A. Scribano and G. Tonelli, Nucl.Instr.and Meth. A315(1992)95;
E. Gennari, E. Petrolo and S. Veneziano, IEEE Trans.Nucl.Sci. 39(August 1992)821.

THE RPC TRIGGER SYSTEM FOR THE L3 FORWARD BACKWARD MUON DETECTOR

Sergio Patricelli*
Dept. of Physical Science and INFN
Pad.20 Mostra d'Oltremare 80135 Napoli, Italy

Abstract

In this paper we describe the trigger system for the L3 Forward Backward (F/B) Muon Detector which will make use of Resistive Plate Chambers. Using 192 double gas gap chambers covering an area of more than 300 m^2, this system is the largest one to be built in the following years and its operation will constitute an important test of industrially produced detectors of this kind. We also report results of tests done with these detectors both in the final experimental environment (i.e. L3 magnet door) and in our laboratory with cosmic rays.

1 Introduction

In view of the approved LEP program for the energy upgrade of the machine to $E_{c.m.s.} \approx$ 190 Gev, the L3 experiment [1](Fig. 1) will extend the polar angle coverage for muon detection lowering the minimum detection angle from 43° to 22° both in the forward and backward regions[2]. For each of these regions, muon measurement will be achieved by the addition of three planes of precision drift chambers (FI, FM, FO) and by the toroidal magnetization of the doors of the existing solenoidal magnet (Fig. 2). In the region $43° > \theta > 36°$ muons will be measured by the MI and MM chambers of the barrel system and the new forward chamber FI located inside the magnet door.

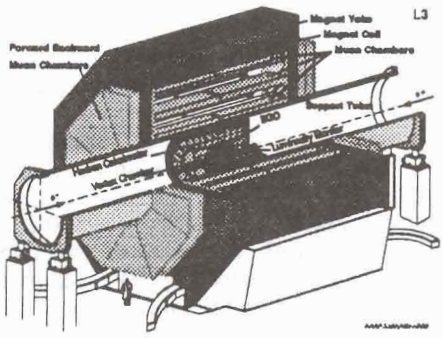

Fig. 1: The L3 Detector

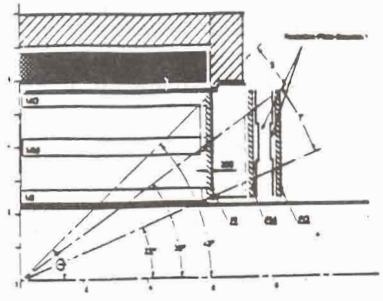

Fig. 2: Cross section of the L3 F/B muon detector.FI, FM and FO are drift chambers. RPCs are usedto trigger in the T region.

* co-authors are: A. Aloisio, M.G. Alviggi, E. Brambilla, G. Carlino, R. De Asmundis, V. Innocente, S. Lanzano, L. Lista, P. Paolucci, P. Parascandolo, G. Passeggio, D. Piccolo, C. Sciacca, V. Soulimov, N. Zaitsev.

Trigger in this region will be the one used for the barrel system. In the region $36° > \theta > 22°$ muons will be momentum analyzed by the toroidal spectrometer formed by the FI, FM and FO chambers and muon trigger in this region will be provided by separate fast detectors, also essential for cosmic rays rejection since no scintillation counters are present in F/B regions.

The new muon detection system will increse the acceptance for Higgs detection up to 90 Gev mass limit by a factor 2 (Fig.3) in the channel $e^+e^-\rightarrow Z°H° \rightarrow \mu^+\mu^- H° \rightarrow \mu^+\mu^-$ *+hadrons* and improve the measurement accuracy of the asymmetry in the angular distribution of the reaction $e^+e^- \rightarrow W^+W^-$ to determine the triple gauge boson coupling constant g_{ZWW}.

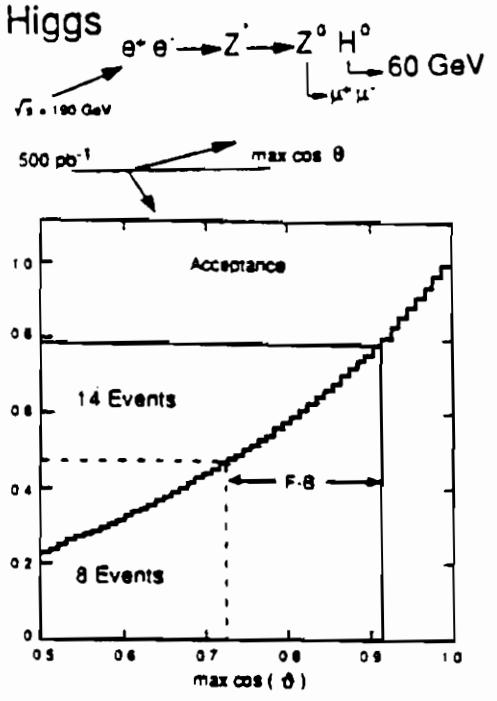

Fig. 3: Acceptance for Higgs detection with new F/Bdetector.

2 Resistive Plate Chambers.

Resistive Plate Chambers have been chosen for their fast time response, relative low cost and possibility of large scale industrial production. We have chosen RPCs of proven technology developped by Santonico et al.[3] with small modifications.

The sensitive volume of these detectors is a 2 mm thick gas layer operated under a steady electric field of 3.5 - 4.0 kV/mm. Free electrons generated by ionizing particles induce an avalanche -> streamer process and the resistive high-voltage electrodes, transparent to the pulses originated in the gas volume, allow a capacitive readout through external pickup electrodes

Fig. 4 shows the schematics of a double layer RPC of the type that will be used in the system. It consists of two counters mounted in the same mechanical structure, with independent H.V. but read by a single pickup plane.

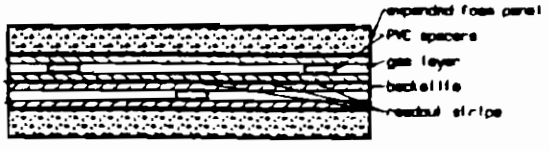

Fig. 4: Cross section of a double gas gap RPC.

The electrode plates are made of 2 mm thick backelite (phenolic polymer) with a volume resistivity of $\approx 10^{11}\ \Omega$ cm painted on one surface with graphite covered by a 300 μm PVC insulating foil. Planarity of the two backelite planes is assured by PVC spacers (0.8 cm^2 area) glued on the inner surface and located on a grid of 10 cm side in the sensitive volume.

To reduce stocastic noise induced by field inhomogeneities near the spacers, graphite is removed at positions occupied by spacers and to avoid geometrical inefficiencies due to

spacers, the grids of the two chambers in the same mechanical assembly are shifted by 5 cm in one direction.
The sensitive volume is filled with a gas mixture of argon, isobutane and freon (58:38:4) at atmospheric pressure and the discharge generated by ionizing particles is quenched by the following mechanisms:

- UV photon absorption by isobutane.
- Capture of outer electrons by freon. This reduces the size of the discharge.
- Switching off of the electric field around the discharge point. In fact the duration of the discharge is ≈ 10 ns while the relaxation time of the resistive electrodes is $\tau = \rho\varepsilon \approx 10^{-1}$ sec, so that during the discharge the electrode plates behave like insulators and a small area around the impact point shows a dead time of the order of τ.

Induced pulses are collected on aluminum strips, 29 mm wide separated by 2 mm, located between the two counters. The induced charge is of the order of 100 pC and the pulse has a rise time of ≈ 2 ns and a fwhm of ≈ 10 ns.
The two counters are enclosed in two panels of expanded foam previously preformed which assure mechanical stiffness to the assembly.

3 System layout.

In the L3 F/B muon system, each drift chamber of the FM and FO planes will be equipped with one layer of double gas gap Resistive Plate Counters. The two drift chambers are joined by a truss structure and the RPCs will be located on the inner surfaces of the chambers (Fig. 5). Drift chambers, frames and RPCs will be prepared as one rigid unit in production and as such mounted on the magnet door. The total number of these sectors (half octants) will be 32. Each layer of RPCs (Fig. 6) is composed of three trapezoidal units: L (Large), M (Medium), S (Small).To avoid dead areas due to mechanical constraints in the construction of one unit, the Medium RPC is at a different z position and partially overlaps the Large and Small ones. Distance between the strip planes for the two Large and Small RPCs is Δz = 56 cm, while distance for the two Medium RPCs is Δz = 46 cm. Readout strips are perpendicular to the octant center line; each RPC chamber has 32 readout strips and their lenght varies from 98 cm to 216 cm. The total number of RPC counters is 192 for a total of 6144 readout strips. The resulting total area of bigap RPC is > 300 m^2.

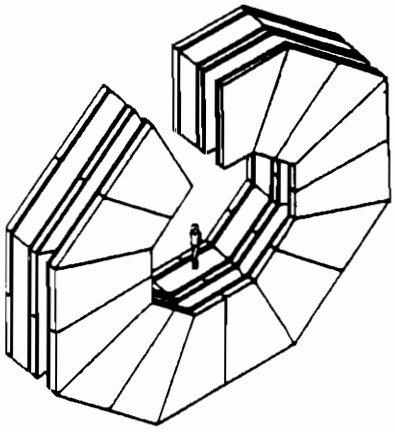

Fig. 5: Expanded view of the F/B muon system.

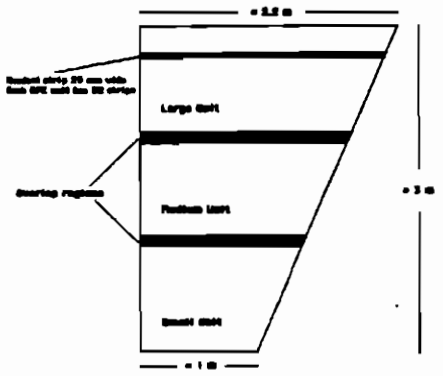

Fig. 6: RPC chambers covering one drift chamber.

Induced pulses on readout strips are discriminated and amplified by fast transistors whose output drives directly TTL electronics. Front-end boards are mounted on the detector: each board accepts inputs from 16 adjacent strips and produces shaped (150 ns differential TTL) outputs for fired strips. The board also provides a fast OR signal of the 16 strips. This signal has a fan-out of three: one output is sent directly to an 1875 Le Croy TDC channel for time measurement, another is used to generate an early signal for the trigger processor and the last one is used for monitoring purposes.A test input will permit the injection of a test pulse on all input channels to test the full readout chain and to allow a zero time calibration.

4 Trigger generation.

RPCs will provide a level-1 muon trigger in the forward-backward region by searching for particles traversing the 1 m thick magnetized iron magnet doors and pointing to the interaction vertex. A muon generated at the interaction point and which traverses the magnet door, will move on a straight line in the space between the two RPC planes. The slope of its trajectory depends on the polar angle θ at the origin, charge sign and momentum (through magnetic deflection in the toroidal field and multiple scattering experienced in the various absorbers, mainly in the hadron calorimeter and in the iron of the magnet door). We can therefore associate to each readout strip in the FM plane a limited number of strips in the FO plane. In a 96 x 96 coincidence matrix (Trigger Matrix), muons coming from the interaction point will populate a "road" whose "width" is dependent on their momentum. Fig. 7 shows the Trigger Matrix obtained by Monte Carlo simulation for muons of different momenta at the vertex; Fig. 8 shows trigger efficiency when "roads" of different "width" (i.e. number of strips) are used in the trigger (z displacement of Medium RPC with respect to Small and Large ones is not taken into account).

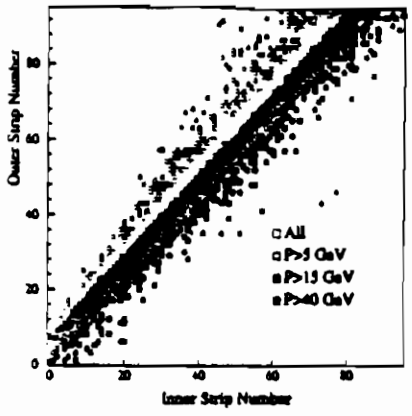

Fig. 7: MonteCarlo simulation of Trigger Matrix.

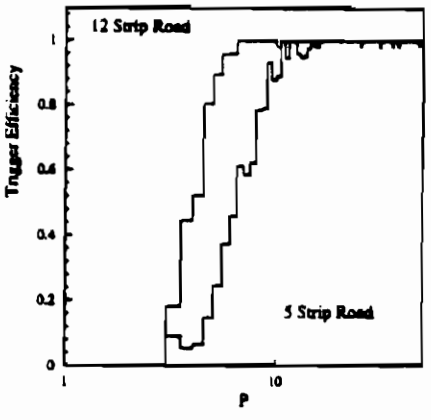

Fig. 8: Trigger efficiency for different road cuts.

Fig.9 shows the schematic of trigger logic for one of the sixteen octants of the detector.Both for FM and FO planes, strips of equal lenght of the same octant are locally ORed in order to have one Trigger Matrix for every octant. For each of the 32 sectors, Fast Or signals from all front-end boards in a FM (FO) layer are ORed to generate a fast signal for particles passing the layer. The ORed signal of 96 strips in a FM (FO) layer is thenORed with the same signal of the contiguous layer of the same octant.

The coincidence of the full FM and FO planes in an octant is used to strobe, in presence of a beam pick-up signal, the operation of the relative trigger processor. The expected jitter of the strobe signal is low enough to separate random triggers associated with the halo of the "incoming" beam (see results of test performed on L3 magnet door.).
96 logical OR signals from strips in one plane (FM, FO) in one octant are sent to one Zero Suppressor and Encoder Module. 32 of such modules will be used in the trigger system: 8 for FM and 8 for FO planes for both the forward and backward regions. Output of this module consists of n 8 bits words, one for each hit strip, containing encoded information of its number , transmitted to the following module via a dedicated bus. Zero suppression of input data and trasmission of output data to the subsequent module are done in parallel and the total processing time is less than 1 μs. The module will be connected to a VME backplane to implement many auxiliary functions such as: masking of input sparking channels, application of predefined input patterns to test the trigger processor, readout of data via VME backplane for debugging.

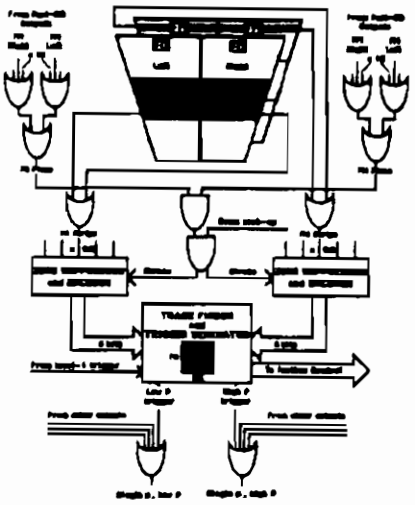

Fig. 9: Trigger schematics for one octant.

The two Zero Suppressor and Encoder Modules for FM and FO planes of the same octant will transmit their output data to a Track Finder and Trigger Generator Module. This module is responsible for detecting a coincidence between two strips in the two planes which is included in regions (e. g. "roads") of the Trigger Matrix which are user programmable. Sixteen of such modules are connected to a VME backplane and will process data in parallel for all octants in the Slave and Master wheels. Each cell of the Trigger Matrix is mapped into one of 96 x 96 locations of a 2 bit RAM. Roads for muons coming from the interaction vertex can be programmed by filling the appropriate locations of the RAM and the use of two bits will allow the definition of two different "roads" in the same matrix, corresponding to different momentum cuts. Track finding starts when all data have been received from the Zero Suppressor and Encoders: if n and m are the numbers of hit strips respectively on the FM and FO planes, the system will scan through the n x m possible search addresses which can be formed using data received from the Zero Suppressor and Encoders and a "track found" signal will be generated when a coincidence is found within the pre-defined range. Time required to scan all search addresses (n x m x 100 ns) depends on the number of hit strips in the two planes and if this is greater than the maximum allowed for level-1 trigger generation, a timeout condition is set and the corresponding octant is unconditionally set to "track found". High and low momentum triggers for all octants are ORed to generate the level-1 trigger of the FB muon detector. Information with the encoded numbers of hit strips of all 16 octants, will be transferred to tape via the Fastbus data readout system when an event is accepted by the complete L3 level-1 trigger.

5 Test results.

During the past year, various RPCs of the same type that will be used in the trigger system of the FB muon detector have been extensively tested in our laboratory in Naples using

cosmic rays tracked by a 1 x 1 m^2 telescope.The tracking telescope (Fig.10) consists of two drift chambers of the kind used for the longitudinal coordinate measurement in the L3 muon barrel system and two planes of scintillator counters. Each chamber is formed by two staggered x planes and two staggered y planes; total number of drift cells is 96. The two chambers are separated by 1.6 m, leaving space for many RPC simultaneously under test. All relevant informations for tracks are recorded on disk to allow subsequent off-line analysis: in particular, time masurement for RPCs is done with a Fastbus 1875 LeCroy TDC of the same kind that will be used in the experiment, and drift times are measured with 1879 LeCroy TDC.

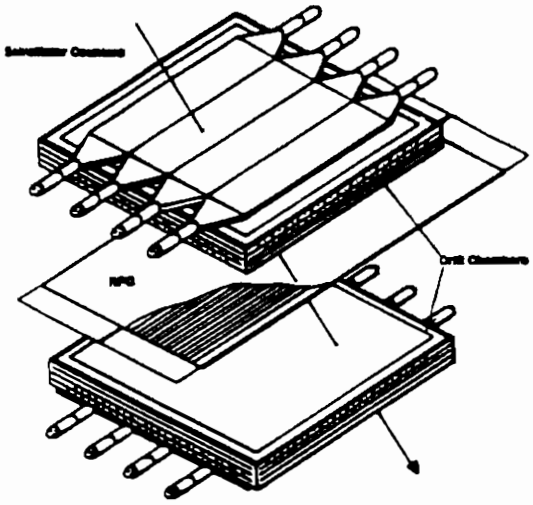

Fig. 10 Cosmic ray telescope used for test

The single rate of a double gas gap RPC of trapezoidal shape and 1.6 m^2 area vs the applied voltage is shown in Fig. 11 while Fig. 12 shows the coincidence rate of two equal chambers.The detection efficiency of one RPC has been measured using tracks reconstructed by drift chambers and its dependence on the applied high voltage is shown in Fig. 13. The efficiency at the plateau is $\varepsilon > 99\%$. Fig. 14 shows the distribution of the relative delay between Fast Or signals, which groups 16 readout strips, from two RPCs placed one on top of the other, crossed by cosmic rays seen by two planes of scintillator counters (1 x 1 m2 area, separated by 180 cm with the two RPCs in the center).

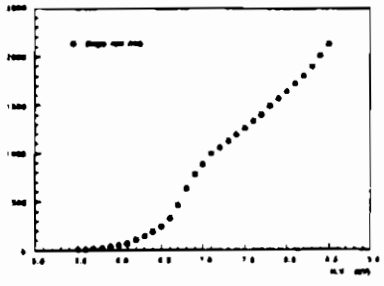

Fig. 11 Single rate vs. H.V.

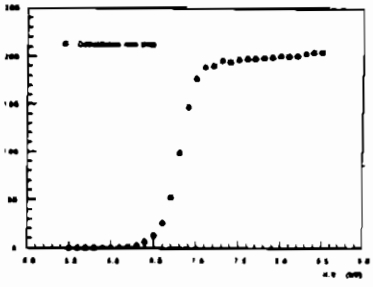

Fig. 12 Coincidence rate of two RPCs.

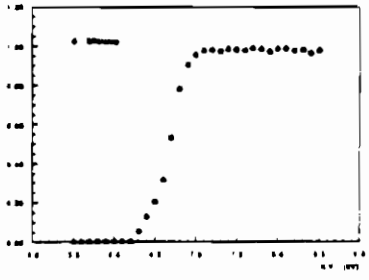

Fig. 13 Efficiency of a bigap RPC vs. H.V.

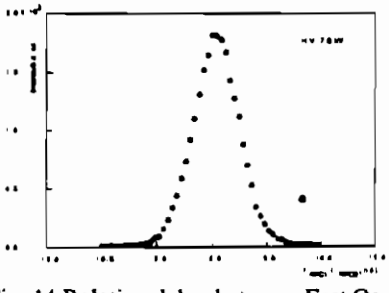

Fig. 14 Relative delay between Fast Or of two RPCs

The σ of the above distributions vs the applied high voltage is shown in Fig. 15 where it can be seen that the time resoultion of one counter $\Delta t=\sigma/\sqrt{2}$ is less than 1.5 ns for applied high voltages > 7.7 kV.
By selecting cosmic rays crossing the RPC in correspondence of the same pickup strip but along its entire length, we have measured the difference of the arrival times of the signals at the opposite ends of the readout strip line. Fig. 16 shows the resulting distributions, with each peak grouping events hitting the RPC in $\Delta x=5$ cm. (x axis is defined parallel to the pickup strips). The measured delay of the strip line is 5.4 ns/m and the longitudinal resolution obtained is about +/- 2.4 cm. All measurements have been done using as gas mixture Argon 58%, Isobutane 38%, Freon 4%.

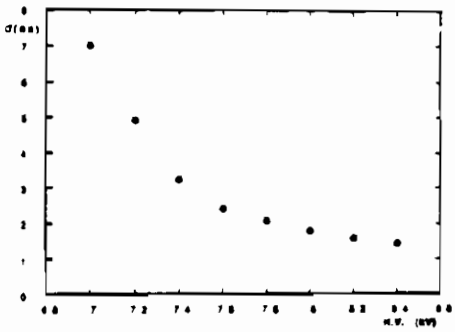

Fig. 15 σ of distribution of fig.14 vs. H.V.

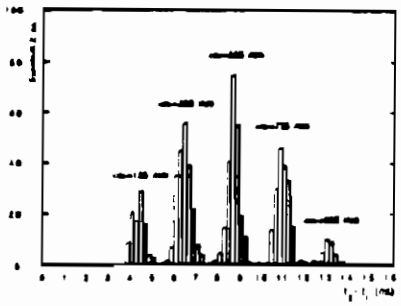

Fig. 16 Distributions of the differences of arrival times of the signal at opposite ends of pickup strips. Each strip groups events hitting the RPC in $\Delta x=10$ cm.

During the 1992 LEP run, two RPCs have been installed on the magnet door of L3 on the orbit plane and close to the support tube where the background associated with LEP beams is expected to be higher. The purpose of the test has been to verify if the background rate in the experimental environment is compatible with the maximum rate allowed for RPCs of the present type and to estimate the foreseen level-1 trigger rate. The area of the two chambers (one with a single gas gap and the other with a double gas gap) was 1.8 m^2 and data have been collected with the the two chambers separated by 5 and 60 cm.
Time distribution of particles in the background associated with beam crossing shows two separate peaks: one due to the "incoming" beam (e^- in this case) and the other due to the "outgoing" beam (e^+) (Fig. 17).

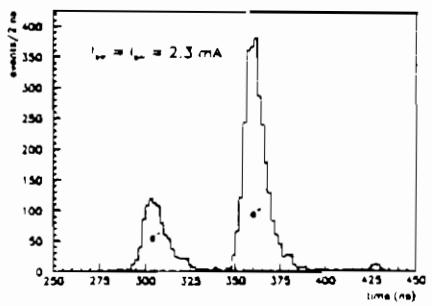

Fig. 17 Time distribution of background particles

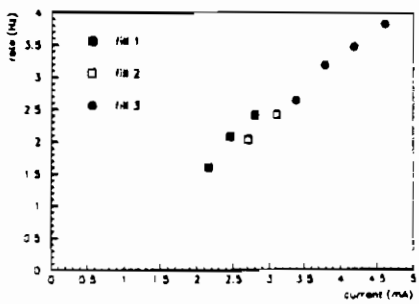

Fig. 18 Coincidence rate vs. total LEP beam current.

The coincidence rate of the two counters depends on beam currents as shown in Fig. 18 and the single background rate is negligible with respect to the one allowed for a good functioning of the chambers. The rate of coincidences decreases when moving radially out from the support tube with ≈ 75% of the total rate confined in the closest 50 cm (Fig. 19).

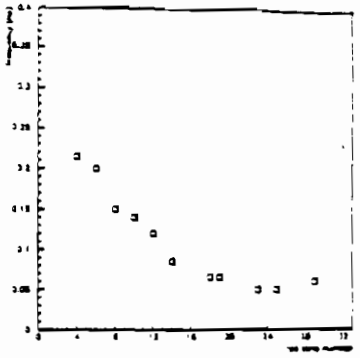

Fig. 19 Radial dependence of coincidence rate.

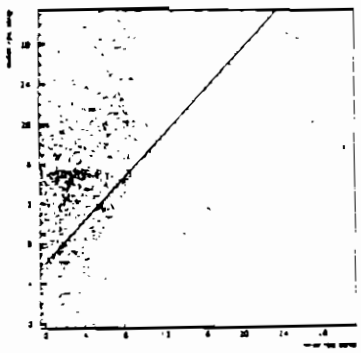

Fig. 20 Distribution of 5000 background events in the trigger matrix.

Each RPC was equipped with 32 readout strips of the same width of the ones which will be used in the final system, running in a direction perpendicular to the orbit plane. With the chambers at 60 cm distance this has allowed to study the distribution of background coincidences in the trigger matrix and estimate the trigger rate. Fig. 20 shows the distribution of 5000 events on the trigger matrix; the superimposed straight line represents the ideal "road" for particles of infinite momentum originating from the interaction vertex and without multiple scattering in the detector and magnet door. The rates, extrapolated to the complete detector surface, assuming (pessimistically) that all octants experience the same rate, and surviving after the application of cuts with "roads" of 5 and 13 strip width centered on the ideal one are respectively 28 and 68 Hz at beam currents of 2+2 mA. Since the time separation of events associated with the incoming and outgoing beams is > 50 ns, the use of a fast coincidence from the two RPC planes will allow to strobe the Zero Suppressor and Encoder Module only for events in time with the outgoing beam. This will reduce the total single μ trigger rates to 20 and 50 Hz for the two different cuts, assuming that the total current is equally divided between the two beams.

1) L3 Collaboration : NIM A289 (1990) 35.
2) L3 Forward-Backward Muon Detector. Dec. 3 1991 L3 Internal Note
3) R. Santonico and R. Cardarelli : NIM 187 (1981)377.
   R. Cardarelli et al. : NIM A263 (1988) 20.

Results from the RD5 Experiment at CERN

A. Di Ciaccio
University of Roma 'Tor Vergata' and INFN sezione di Roma II
The RD5 Collaboration

1 Introduction

The RD5 collaboration[1] at CERN [1] was formed to study topics related to muon detection at future hadron colliders. These topics include: measurement of the total punchthrough probability of hadronic showers, the angular and momentum distributions of punchthrough particles produced in an absorber with and without a magnetic field, trigger and muon momentum measurement studies, and tests of various types of large area muon detectors.

In this paper I present the first RD5 measurements of the total punchthrough probability of hadronic showers originating from negative pions incident on a stainless steel/gas tracking calorimeter as a function of penetration depth in equivalent iron as well as results on muon trigger studies and on the rejection power of these triggers on punchthrough particles. These measurements are from data taken in 1991 and 1992.

2 The RD5 detector

A schematic view of the RD5 detector [2], located in the CERN North Area H2 beam, is shown in figure 1. It consists of two magnets, a superconducting magnet (M1) [3] with a 3 Tesla field and an absorber magnet with a 1.5 Tesla field (M2) [4]. This setup can simulate a solenoidal detector with its return yoke or a toroidal spectrometer. Only M2 was powered in 1991.

The RD5 trigger in 1991 was based on 7 sets of scintillation counters marked S1 to S7 in figure 1. The beam is defined by a coincidence of S1 (10 x 15 cm^2) and S5 (15 x 15 cm^2). Whenever the rate is high enough - mainly with high momentum hadron beams - S4 (4 x 4 cm^2) is added to the trigger. In order to select muons, the counter S6 (70 x 100 cm^2) behind the calorimeter is also added to the coincidence.

[1] Aachen, Amsterdam(NIKHEF-H), Boston , BNL, Budapest, CERN, Helsinki, Madrid(CIEMAT), Nijmegen, Padova, Roma I, Roma II, Turku, UCLA, UC Riverside, Vienna(HEPHY), Warsaw.

A stainless steel/gas tracking calorimeter (TRACAL) is installed inside M1. TRACAL consists of stainless steel plates interleaved with Honeycomb Strip Chambers (HSC)[7], which can measure tracks accurately. Each chamber has an active area of 61 x 80 cm^2, with 2.6 cm gaps between the absorbers. The main purpose of TRACAL is to identify muon contamination in the hadron beam. The total absorption power of TRACAL is about 9λ. In front of TRACAL a lead brick wall of about one interaction length (29 X_0) was installed simulating an electromagnetic calorimeter.

The absorber magnet (M2) is a 1.5 Tesla iron magnet constructed as a closed magnetic circuit, 1.8 to 2 m thick, made up of 200 mm thick steel plates. Two 8.75 cm slits are provided in the upstream section to insert Resistive Plate Chambers [8]. The 0.9 x 4.8 m^2 inner area enclosed by the iron circuit has been dimensioned to accept a muon measurement station.

In order to measure the trajectories of the muons in the RD5 spectrometer with high accuracy six muon drift chambers from the UA1 experiment [9] were installed, two in every measurement station. In each station the two chambers are mounted 60 cm apart to provide a good determination of the muon direction. Each muon station covers an area of 315 x 375 cm^2. The large area provides a measurement of the spatial distribution of hadronic showers even at large distances from the beam axis. The single point resolution of the muon chambers is on average 400 μm for tracks with the angular distribution of beam particles at RD5. The detection efficiency of each tube is about 99 % over the whole drift volume.

Resistive Plate Chambers (RPCs) are mounted on the muon drift chambers in Station 1 and Station 2 and inside the absorber magnet. They are used to study different muon trigger schemes and, together with the drift chambers, for muon track reconstruction. Each plane measures 2 x 2 m^2 and has 64 readout strips of 31 mm pitch. The planes are coupled in pairs providing one measurement in the horizontal projection, z, and one in the vertical projection, y. Station 1 (see Fig. 1) has four pairs of RPCs with two $y-z$ measurements before and after the muon drift chambers. There is one $y-z$ pair in each of the two slots in the iron toroid. Station 2 has two $y-z$ pairs with one measurement on either side of the drift chambers. The RPC efficiency was measured to be higher than 95 % [2].

3 Punchthrough data analysis

During 1991 data were taken in three run periods with negative muon and pion beams. In both cases the beam momenta were 30, 40, 50, 75, 100, 200 and 300 GeV/c. The muon data were used to characterize the muon contamination in the pion beam and for detector calibration.

A pion punchthrough event and a muon event in the RD5 detector are shown in figures 2 and 3, respectively. In total 1.1 x 10^6 muon events and 1.5 x 10^6 pion events

were recorded on tape. Furthermore, for detector calibration and background studies, a set of 3.6 x 10^4 events in the muon beam and 2.8 x 10^5 events in the pion beam were taken with a random trigger and written on tape.

The pion beam used by RD5 contained from 3 to 8% of primary muons depending on the momentum. This muon contamination comes from pion decays in flight upstream of the detector. While muons penetrate the whole experimental setup, hadronic showers induced by pions typically have shorter penetration depths. The high muon contamination in downstream detectors requires one to use careful background subtraction procedures.

In the following sections two independent analysis methods are described to measure punchthrough probabilities.

3.1 Analysis Method 1

We define the total punchthrough probability at a given depth x as the ratio of the number of events with at least one hit in the detector at the depth x over the total number of events. At small depths, for a given primary energy, the longitudinal shower development scales with the average hadronic interaction length. At large depths the penetrating particles in the shower are predominantly muons coming from pion and kaon decays in the shower. An accurate punchthrough measurement at large absorber depths requires the elimination of any muon contamination in the pion beam. The method described below measures punchthrough probabilities only at the absorber depths where RPC chambers are present, namely from 1.6 to 3.5 meters of equivalent iron.

The multiplicity of wires hit in the TRACAL calorimeter for 200 GeV/c muon and pion data is shown in figure 4. A clear muon contamination is present in the pion events. A cut on the hit wire multiplicity is suitable to eliminate most of these muons, but some could survive this cut, mainly muons accompanied by electromagnetic showers, producing a large number of hit wires in TRACAL. The multiplicity cut ranged from 30 hit wires at 30 GeV/c to 50 at 300 GeV/c.

All the events passing the hit wire multiplicity cut are then analyzed with a tracking algorithm that identifies tracks penetrating through all the RPC chambers. This algorithm recognizes clusters of hit RPC strips and calculates the coordinates of their midpoint. Each pair of clustered hits, separated by at least one slab of iron, defines a road, 3 strips wide, where other clusters are searched for. If three or more clusters are found in the road, a straight line fit is performed and a track is identified if the fit passes a χ^2 cut. The measured efficiency ϵ of the tracking algorithm is $\epsilon = 0.98 \pm 0.01$.

For each track, the angle α between the beam axis and the track direction in the non-bending plane is measured. While the angular distribution of the muon data peaks at small angles [Fig. 5a], the same distribution of penetrating tracks originating in pion showers is more widely spread around the beam axis [Fig. 5b]. The difference between

the angular distributions of tracks from primary muons and tracks originating from pion events is used to remove the small residual muon contamination in the pion data. Tracks identified in pion events are tagged as primary muons if the sum of hits in the RPC chambers is compatible with a muon event (namely less than a total of 15 hit strips for the 8 RPC planes[2]) and if the angle α is $< 3\sigma_{\alpha}^{\mu}$, where σ_{α}^{μ} is the r.m.s width of the distribution of α measured with muon data [Fig. 5a]. With this cut the remaining primary muon contamination (e.g. $\sim 10^{-3}$ at 300 GeV/c) is removed. Finally, punchthrough probabilities are corrected for each individual RPC chamber efficiency and noise and for the efficiency of the applied cuts. This last efficiency has been estimated by a visual scan of the events that did not pass the applied cut and is greater than 90 % for all beam momenta. The error associated with it has been evaluated from the number of ambiguous events found in the scanning. The estimated systematic error takes into account the uncertainties in chamber noise, efficiency measurements and background subtraction. The biggest systematic errors are found at the largest penetration depths. For example, at 3.5 m of equivalent iron the relative systematic error is 15% at 30 GeV/c and 3% at 300 GeV/c.

3.2 Analysis Method 2

The second method uses hits in all detectors of RD5, i.e. hits in TRACAL wires, muon drift chambers, RPCs and also in the scintillating counter S7 mounted behind the beam dump (see Fig. 1), to find the actual penetration depth of each punchthrough particle (PThP). This method consists of the following steps: measurement of the penetration depth of the PThP in each event, subtraction of the primary muons present in the pion beam and subtraction of superimposed events (namely two events occurring within the same event trigger).

3.2.1 Penetration depth

There are 31 absorber depths d in the RD5 setup, each separated by single or grouped detector elements. The sequence of absorber materials and detector elements is presented schematically at the bottom of figure 1.

Let us denote the existence of a hit in a particular detector i by h_i, where $h_i = 0$ means no hits in the i-th detector and $h_i = 1$ means at least one hit in the i-th detector. A hit in detector i is weighted appropriately, given the efficiency f_i and noise level g_i of that detector. The detector efficiencies are measured using muons from the dedicated muon runs. The detector noise levels are measured by triggering at random within the pion beam.

[2] A muon produces, on average, 1.3 hits in a RPC chamber.

For each possible penetration depth d and event j, the probability P_d^j to obtain a given hit pattern is calculated:

$$P_d^j = \prod_i [\theta(d-i)h_i f_i + \theta(d-i)(1-h_i)(1-f_i) + \theta(i-d)h_i g_i + \theta(i-d)(1-h_i)(1-g_i)]$$

where d is the absorber depth, 1 to 31, and i ranges over all detector elements (see bottom of figure 1). $\theta(y)$ is a step function defined in the following way:

$$\theta(y) = 1 \text{ for } y \geq 0$$

$$\theta(y) = 0 \text{ for } y < 0$$

This analysis allows the different types of chambers present in RD5 to be treated in a consistent way. For any given event, the depth d having the highest probability P_d^j is called the range R of the PThP. This variable is used in the analysis to separate pions from the muon contamination, but not to calculate the final punchthrough probability.

For the distribution of penetration depth the average probability $\overline{P_d}$ is calculated, where

$$\overline{P_d} = \frac{1}{N} \sum_{j=1}^{N} \frac{P_d^j}{\sum_{k=1}^{31} P_k^j}$$

and N is the total number of events. The distribution of this variable reduces the weight of ambiguous events (i.e. an event with two or more depths having similar probabilities). For example, it is possible to have the following hit pattern: 1 1 1 1 1 1 1 0 1 0 0 0 0 0 0. This pattern represents 7 hit chambers, a chamber with no hit, and then another hit chamber. The ambiguity arises if one must choose chamber number 7 or number 9 as the final hit chamber. One does not know if the hit in chamber 9 is definitely due to noise or if no hit in chamber 8 is due to an inefficiency. The penetration depth distribution weights properly all these cases thus enabling one to avoid arbitrarily choosing one penetration depth over another. Figure 6 shows the unnormalized penetration depth distributions for 100 GeV/c muons and pions. In figure 6b one sees a broad bump corresponding to pion induced hadronic showers stopping in TRACAL or inside the absorber magnet, and a peak, at penetration depth 31, containing events penetrating through the whole detector; this peak contains primary muons events, but also contains punchthrough particles from pion showers. The sharp peak at measurement point 27 occurs because the thickness of absorber materials are not uniform throughout the detector. This peak corresponds to those particles which leak out of TRACAL, thus producing a hit at point 26, but then stop in the thick iron plate at the beginning of the absorber magnet M2.

After the removal of background events due to primary muons and superimposed events, the pion penetration depth distribution [Fig. 6b] is integrated to obtain the final punchthrough probabilities.

3.2.2 Subtraction of Primary Muons

Muon events in RD5 are characterized by one clean minimum-ionizing track (see Fig. 3) penetrating the entire detector. However, there are frequently additional hits in TRACAL due to δ - ray production and other electromagnetic processes induced by the muon. This is reflected in having at least one TRACAL layer with a large hit multiplicity. In addition, there could also be random hits due to noise. In contrast, pion showers (see Fig. 2) typically have a high hit multiplicity in many TRACAL layers and a larger spread.

In order to separate the pion events from the muon contamination, an algorithm was developed which examines the array of hit TRACAL wires, and for each event, removes from the array the hits which correspond to the characteristics of a typical muon event. After this procedure, an excess of remaining hits should be characteristic of a pion shower.

The array of hit TRACAL wires, h_{ij}, is defined as follows:

$h_{ij} = 0$ means no hits in the j-th wire of TRACAL layer i

$h_{ij} = 1$ means at least one hit in the j-th wire of TRACAL layer i

The algorithm which removes hits from the TRACAL hit array consists of the following steps:

1. To account for the hits due to high-energy-loss electromagnetic processes, all hits are removed from the TRACAL layer having the highest multiplicity.

2. Accidental hits (e.g. hits due to noise) are removed from the hit array by rejecting hits in the TRACAL layer i having the largest spread, defined by $rms(i)$, where $rms^2(i) = \sum_j h_{ij}(j - \langle j \rangle_i)^2$ and $\langle j \rangle_i = \frac{\sum_j h_{ij} j}{\sum_j h_{ij}}$.
   The sum is over the wires (j) in the i-th layer.

3. To subtract the primary minimum-ionizing track, hits are removed from the cluster (up to 3 neighboring hits) closest to the beam line in each chamber.

From the remaining hits a variable called "activity" A is calculated as follows:

$$A = \sum_i rms^2(i)$$

where the sum is over all TRACAL layers. A is a measure of the shower spread and hit multiplicity.

The range R, as defined in section 3.2.1, vs. activity A are plotted in figure 7 for 100 GeV/c muons and pions. Most muon events have an activity $A = 0$ and

the maximum range $R = 31$ and are separated from the pion events which have a larger activity and shorter range. In figures 8 a and b, the activity distribution of all 100 GeV/c muons and pions are plotted. Most of the muon events are confined to the region near $A = 0$, however there is a long tail of muon events with high activity. It was found by visual scanning that these are muons accompanied by multiple δ - rays or an electromagnetic shower. In figure 8b, a peak at $A = 0$, assumed to be due to muon contamination, is clearly seen in addition to a broad peak at higher activity assumed to originate from pion showers. The origin of these two components becomes evident if one considers the activity distribution as a function of absorber depth.

In figures 8 c,d and e, the activity distribution of only those particles stopping before Station 1 ($R \leq 10\lambda$), between Station 1 and 2 ($10\lambda < R \leq 20\lambda$) and after Station 3 ($R > 30\lambda$) are plotted, respectively. Going from figure 8c to 8d the height of the histogram reduces considerably, reflecting the absorption of pion showers, while the peak presumably due to the muon contamination is absent. In figure 8e, the peak at $A = 0$ is present indicating that these events are indeed muons penetrating the entire detector; one also sees a further reduction in the peak due to pion showers. By making a cut at $A = 20$ one is able to effectively exclude the muon background. The number of additional pion events in the region $A < 20$ is estimated by first assuming that the shape of the distribution in 8e is similar to the shape of the distribution in 8d, therefore, the fraction of events with $A < 20$ should be the same in both cases. This correction factor is applied to determine the total number of pion events penetrating to this absorber depth. The number of muon events with activity $A > 20$ can be estimated by counting the fraction of muon events with $A > 20$ in figure 8a. This correction factor is also applied to the data.

For momenta less than 100 GeV/c, the pion beam also contained a small electron contamination. The amount of contamination was estimated from the number of particles which stopped in the 29 X_0 lead brick wall installed in front of TRACAL and was measured to be less than 0.05% at 30 GeV/c. The lead was not instrumented, therefore it was not possible to determine the exact nature of the particles stopping there. This uncertainty was included in the estimate of the stopping there. This uncertainty was included in the estimate of the total systematic error in the punchthrough probability.

3.2.3 Subtraction of Superimposed Events

The probability to have two events superimposed is estimated by considering runs with a random trigger and by visual scanning. It was found that these events are mainly halo muons parallel to the beam and almost uniformly distributed over the whole area of muon chambers (4 x 3 m^2). However, most of the superimposed tracks were not reconstructed by the muon drift chambers because of time misalignment. An additional opportunity to decrease this background is given by the RPCs. The RPCs see only a fraction of the superimposed tracks due to their short gate time (70 ns). Requiring

hits in both muon drift chambers and RPCs further reduces this background.

Events having at least one reconstructed track in Station 2 or Station 3 and an activity in TRACAL greater than 2 (to suppress pure muon events) were selected for visual scanning. The superimposed events were identified by having, in addition to a hadronic shower in TRACAL, a clearly visible straight track through the muon detectors parallel to the beam, but off the beam position. These events were rejected from the data sample. The estimated error of this background subtraction was determined by the number of events which were candidates for superimposed events, but could not be clearly identified. This error is included into the total systematic error of the punchthrough probability.

4 Results on punchthrough

The results of methods 1 and 2 are presented in figure 9. This figure shows the total punchthrough probability vs. meters of equivalent iron for 30, 40, 50, 75, 100, 200, and 300 GeV/c incident pions. The curves are characterized by two distinct regions, a hadronic component and a tail composed mainly of penetrating decay muons. The punchthrough probability was measured up to a depth of 5.3 m of equivalent iron. The large systematic error is dominated by the subtraction of superimposed events. In order to reduce this background, a large area veto system which covers the acceptance of the muon chambers is being installed for the 1992 runs.

In figure 9, the RD5 results have been compared with the measurements of the CCFR experiment [10] [11]. For depths <1.7 m of equivalent iron the RD5 measurements are lower than those of the CCFR. The first factor which could account for this discrepancy is the different acceptance of the two detectors. The RD5 calorimeter, TRACAL, has an active area 61 x 80 cm^2 while the CCFR calorimeter module is 300 x 300 cm^2, thus some shower particles in TRACAL produced at large angles are undetected. Secondly, the punchthrough measurement depends on the sensitive material of which the calorimeter is constructed. For example, the CCFR calorimeter, which is composed of iron plates and liquid scintillator, is more sensitive to the neutron component of the hadronic shower than TRACAL, which is a gas sampling calorimeter. The variable response to punchthrough between gas ionization detectors and scintillation counters has been reported elsewhere [11] [12].

5 Muon trigger studies

Various trigger schemes for an iron toroid spectrometer have been studied using the RPC chambers of Station 1 and Station 2. The trigger scheme presented here requires for each RPC strip hit on the first plane of Station 2 to open a window on the second

plane[3] centered on the intersection of the line joining the strip hit on the first plane and the center of the S4 (4 X 4 cm^2) trigger scintillator. A hit found in such a window selects muons with momenta larger than a threshold defined by the width of the window. The efficiency of this trigger algorithm as a function of the muon momentum is shown in figure 10 for 3 different window widths.

The rejection power of the above trigger scheme against pion punchthrough particles present at the level of Station 2 was studied. Figure 11 shows a comparison between the punchthrough probabilities in Station 2 obtained with the analysis described in the previous sections and the same probabilities after applying the trigger algorithm with 3 and 2 strip window width, corresponding to a momentum cut-off of 40 and 50 GeV/c respectively. For pions of 30 GeV/c the trigger reduces of a factor 20 the punchthrough rate assuming a 3 strip trigger road.

References

[1] M. Della Negra et al., Study of Muon Triggers and Momentum Reconstruction in a Strong Magnetic Field for a Muon Detector at LHC, **CERN/DRDC/90-36, DRDC/P7.**

[2] A. Böhrer et al., Status Report of the RD5 Experiment, **CERN/DRDC/91-53.**

[3] M. Aguilar-Benitez et al., Nucl. Instr. and Meth. in Phys. Res. **A 258** (1987) 26.

[4] J.L. Bénichou, A. Hervé, G. Waurick, RD5 Technical Note **RD5-TN 91/01**

[5] I. Hietanen et al., Nucl. Instr. and Meth. in Phys. Res. **A 310** (1991) 671.

[6] I. Hietanen et al., Nucl. Instr. and Meth. in Phys. Res. **A 310** (1991) 677.

[7] H.Van der Graaf, Nucl. Instr. and Meth. in Phys. Res. **A 330** (1993) 44.

[8] R.Santonico and R.Cardarelli, Nucl. Instr. and Meth. in Phys. Res. **A 187** (1981) 377.
R.Cardarelli et al., Nucl. Instr. and Meth. in Phys. Res. **A 263** (1988) 20.

[9] K.Eggert et al., Nucl. Instr. and Meth. **176** (1980) 217.
C.Albajar et al., Z.Phys. **C44** (1989) 15.

[10] F. S. Merritt et al., Nucl. Instr. and Meth. in Phys. Res. **A 245** (1986) 27.

[11] P. H. Sandler et al., Phys. Rev. **D 42** (1990) 759.

[12] H. Fesefeldt et al., Nucl, Instr. and Meth. in Phys. Res. **A 292** (1990) 279.

[3]The distance between the RPC trigger planes 1 and 2 is around 80 cm.

Figure Captions

Fig. 1. Schematic view of the RD5 detector in its 1991 configuration.

Fig. 2. Pion event in RD5.

Fig. 3. Muon event in RD5.

Fig. 4. Multiplicity of wires hit in TRACAL for a) 200 GeV/c muons and b) 200 GeV/c pions.

Fig. 5. Angular distribution of a) 200 GeV/c muons and b) particles originating from 200 GeV/c pion showers in TRACAL.

Fig. 6 Penetration depth distribution of a) 100 GeV/c muons and b) 100 GeV/c pions. The depth scale used is the sequence of absorber materials in RD5 and is presented schematically at the bottom of figure 1. Note that the amount of absorber material is not the same in all layers.

Fig. 7 The distribution of range R and activity A of a) 100 GeV/c muons and b) 100 GeV/c pions. The vertical dotted lines indicate the range in interaction lengths λ.

Fig. 8. The activity distribution of a) 100 GeV/c muons, b) 100 GeV/c pions.

Fig. 9 The total punchthrough probability, as a function of meters of equivalent iron, of showers produced by negatively charged pions of momenta 30, 40, 50, 75, 100, 200 and 300 GeV/c. The results of analysis methods 1 and 2 are compared with the punchthrough measurements of the CCFR collaboration. It should be noted that the RD5 30 GeV/c data are compared with CCFR 25 GeV/c data and RD5 75 GeV/c data are compared with CCFR 70 GeV/c data. All other comparisons are made with data of the same momentum.

Fig. 10. Trigger efficiencies as a function of muon momentum for a RPC trigger with roads of 2, 3 and 4 strips corresponding to a momentun cut-off of 50,40,30 GeV/c respectively.

Fig. 11. Trigger reduction of hadronic punchthrough in Station 2 as a function of pion momentum for trigger roads of 2 and 3 strips. Efficiency curves for the considered triggers are also shown.

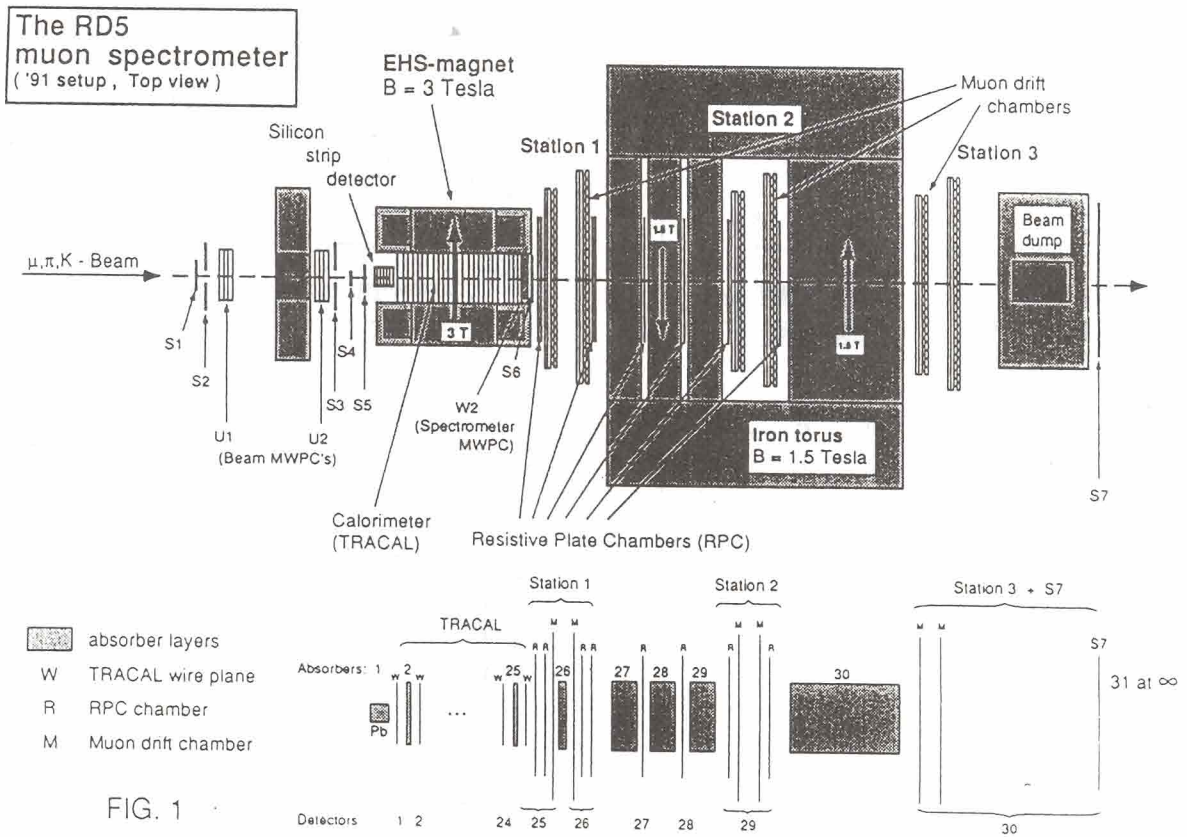
The RD5
muon spectrometer
('91 setup , Top view)
EHS-magnet
B = 3 Tesla
Silicon
strip
detector
Station 1
Station 2
Station 3
Muon drift
chambers
Beam
dump
μ,π,K - Beam
S1
S2
U1
(Beam MWPC's)
U2
S3
S4
S5
3 T
W2
(Spectrometer
MWPC)
S6
1.5 T
Iron torus
B = 1.5 Tesla
S7
Calorimeter
(TRACAL)
Resistive Plate Chambers (RPC)
absorber layers
W TRACAL wire plane
R RPC chamber
M Muon drift chamber
TRACAL
Station 1
Station 2
Station 3 + S7
Absorbers: 1
Pb
2
25
26
27
28
29
30
S7
31 at ∞
Detectors
1 2
24
25
26
27
28
29
30

FIG. 1

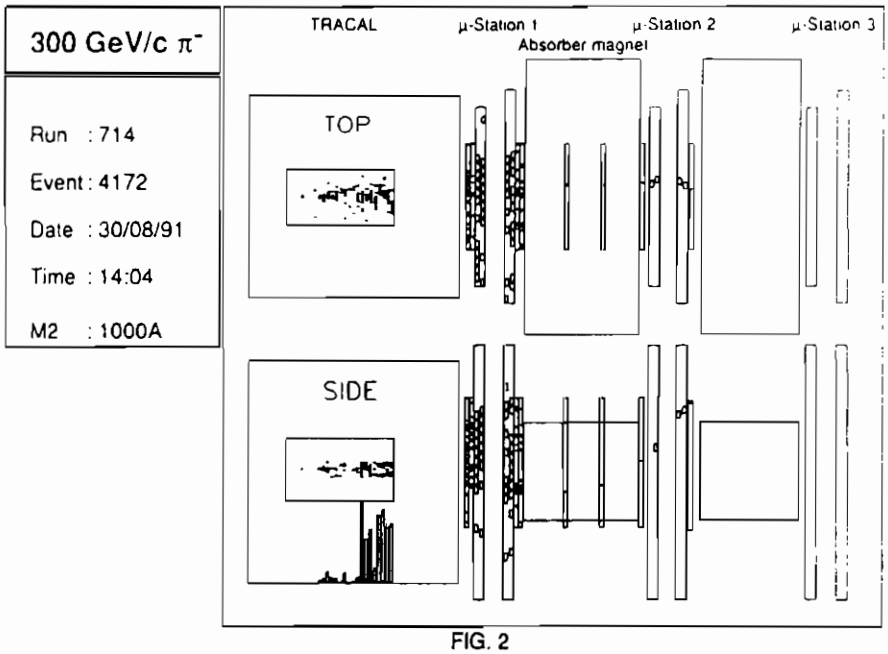
300 GeV/c π⁻
Run : 714
Event : 4172
Date : 30/08/91
Time : 14:04
M2 : 1000A
TRACAL
μ-Station 1
μ-Station 2
μ-Station 3
Absorber magnet
TOP
SIDE

FIG. 2

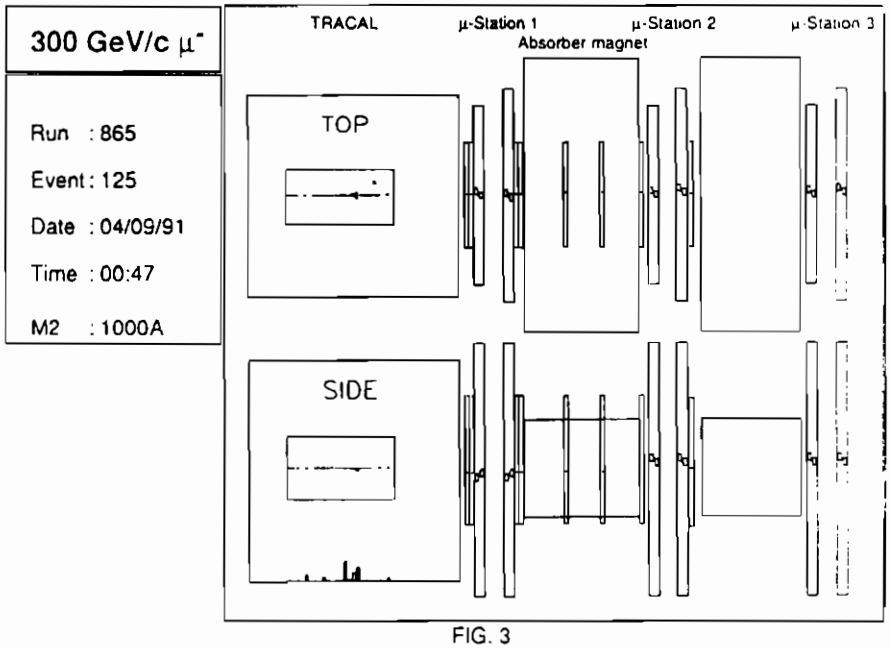
300 GeV/c μ⁻
Run : 865
Event : 125
Date : 04/09/91
Time : 00:47
M2 : 1000A
TRACAL
μ-Station 1
μ-Station 2
μ-Station 3
Absorber magnet
TOP
SIDE

FIG. 3

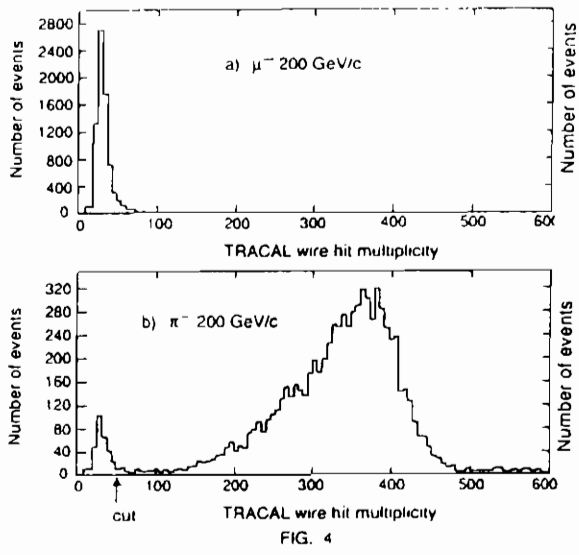

FIG. 4

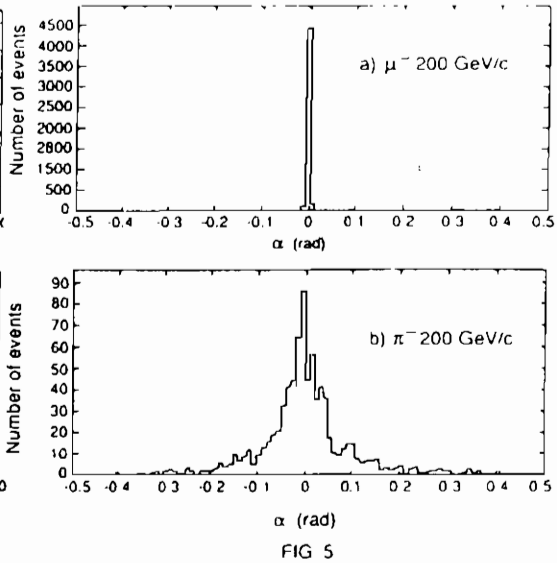

FIG 5

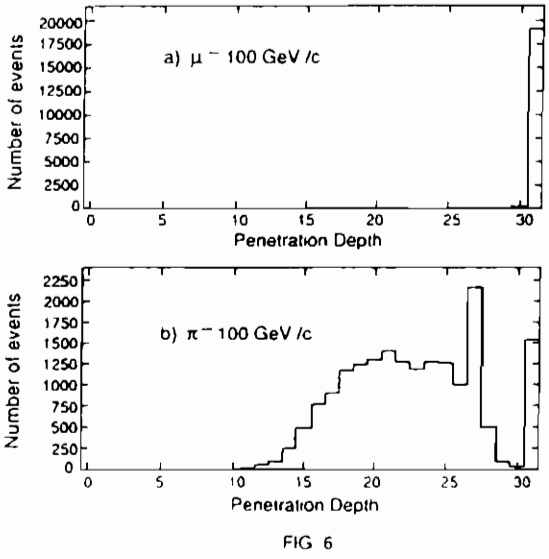

FIG 6

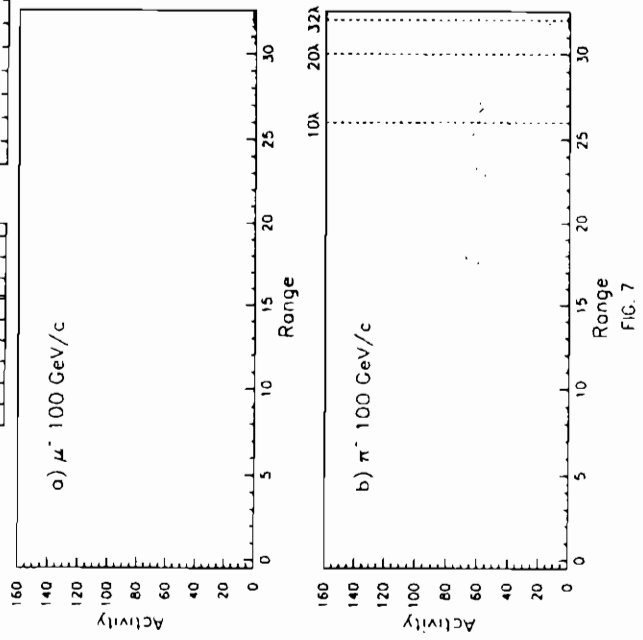

FIG. 7

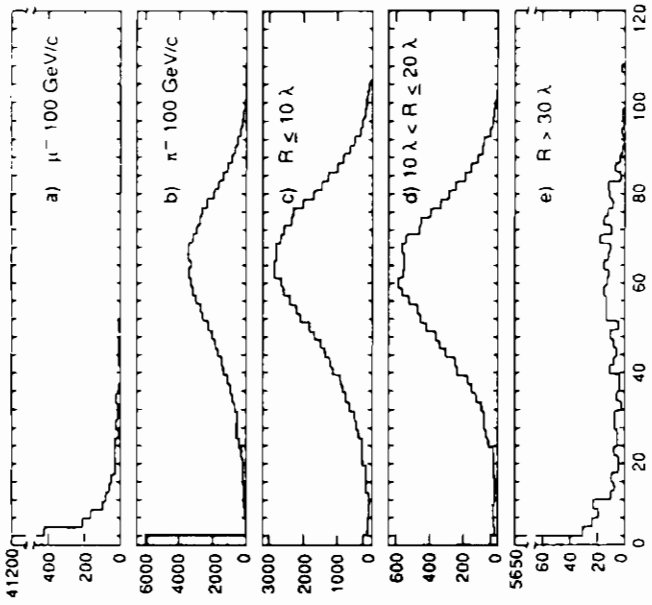

FIG 8

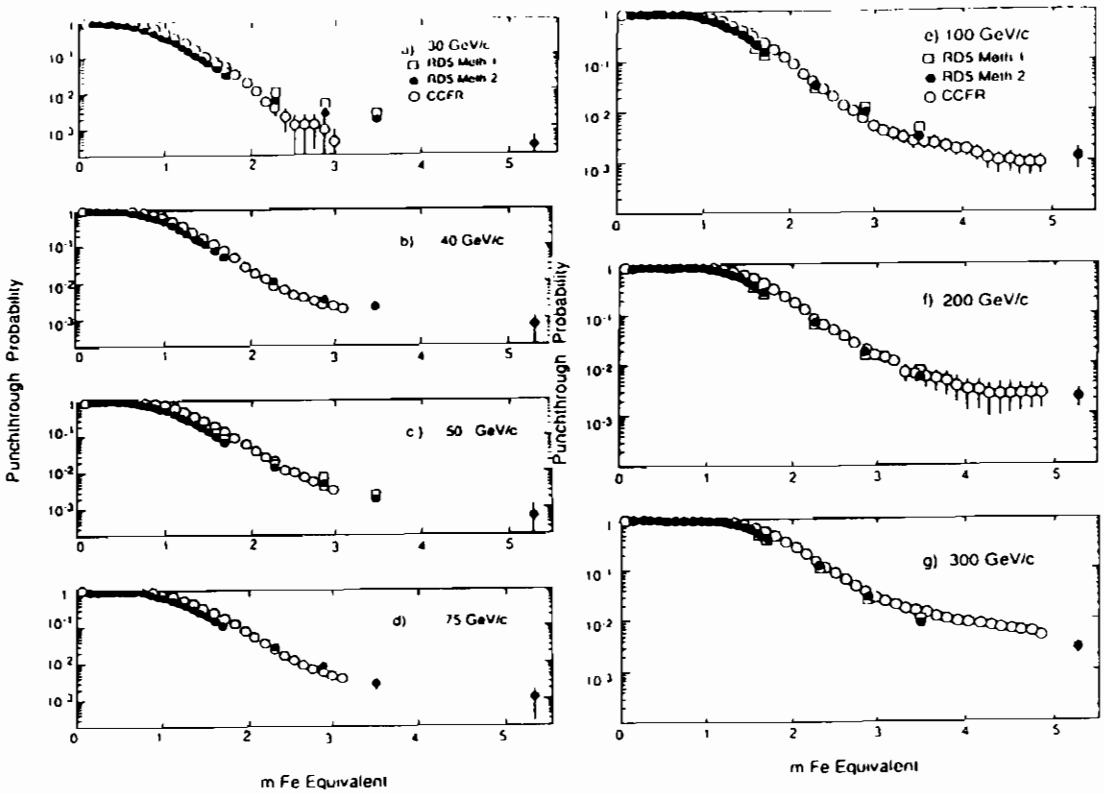

FIG 9

FIG 9

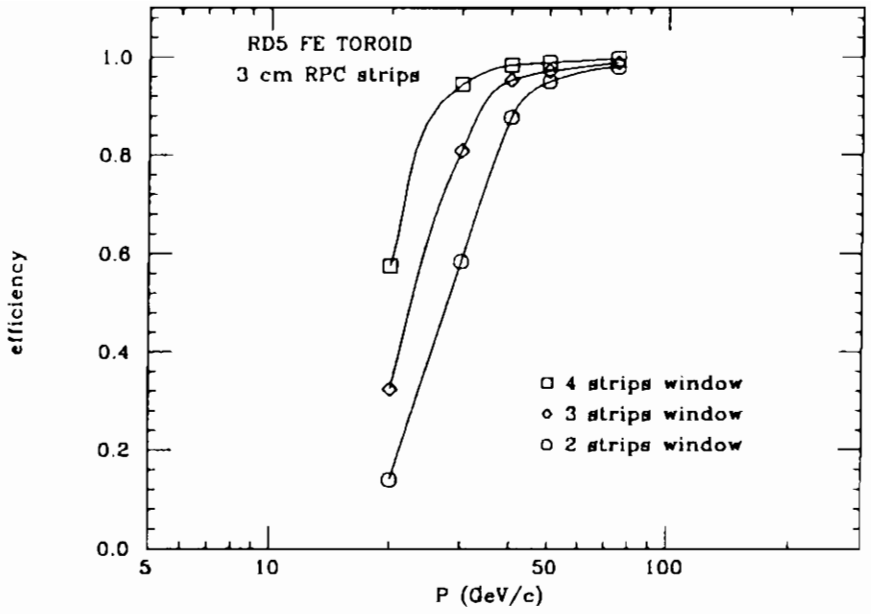
RD5 FE TOROID
3 cm RPC strips
efficiency
1.0
0.8
0.6
0.4
0.2
0.0
5
10
50
100
P (GeV/c)
4 strips window
3 strips window
2 strips window

FIG. 10

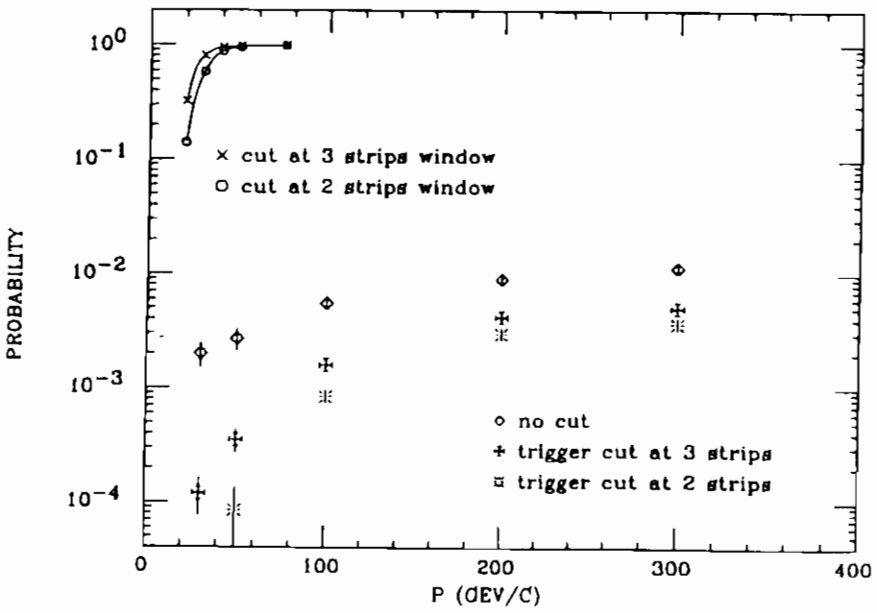
PROBABILITY
10^0
10^{-1}
10^{-2}
10^{-3}
10^{-4}
0
100
200
300
400
P (GEV/C)
cut at 3 strips window
cut at 2 strips window
no cut
trigger cut at 3 strips
trigger cut at 2 strips

FIG. 11

Level 1 muon trigger in the ATLAS experiment at the Large Hadron Collider

A. Nisati. ATLAS Collaboration

1 Introduction

Experiments at future high energy hadron colliders. LHC and SSC. will need performant triggers on high transverse momentum leptons in order to search for rare processes.

Large transverse momentum muons can be identified as penetrating particles point to interaction region. However. the muon trigger system needs to account for the large flux of very soft particles. mainly neutrons. impinging the trigger hodoscope on very large surfaces. This addresses the choice of a detector that has excellent time resolution. fine segmentation. high detection efficency. low neutron sensitivity. good rate capability and low cost.

2 The LHC project

The Large Hadron Collider (LHC) [1] is a proton-proton collider ring in the LEP tunnel with a centre-of-mass energy of $\sqrt{s} = 15.4\ TeV$. The bunch crossing frequency is 40 MHz and the nominal luminosity is $1 \times 10^{34} cm^{-2} s^{-1}$ averaged. with a peak value of $1.7 \times 10^{34} cm^{-2} s^{-1}$. We can summarize the main physics potential discovery of this machine [2] in four points:

- **the Standard Model Higgs search.** The so called "gold plated channel" for the Higgs boson discovery is the decay $H \rightarrow ZZ^{(*)} \rightarrow l^+l^-l^+l^-$; this would cover the range $130\ GeV/c^2 \leq m_H \leq 800\ GeV/c^2$. This interval can be enlarged by searching for Higgs production associated with W/Z or $t\bar{t}$ pair; in this case the lepton tagging is important and will allow to explore the range $80\ GeV/c^2 \leq m_H \leq 130\ GeV/c^2$. The decays $H \rightarrow W^+W^- \rightarrow l^{\pm}\nu\ jj$ and $H \rightarrow ZZ \rightarrow l^+l^-\ jj$ can extend the Higgs detection up to $m_H = 1\ TeV/c^2$.

- **the Supersimmetric Higgs search.** In the Minimal Supersimmetric extension of the Standard Model (MSSM) there are 5 Higgs states: 2 charged (H^+, H^-) and 3 neutral (h, H, A). Also in this case the decay $H \rightarrow ZZ \rightarrow 4l^{\pm}$ is crucial.

- **the top physics.** Hopefully the experiments CDF and D0 will give in the near future the evidence of the top quark production at the Tevatron collider. Even so only with the new supercolliders it will be possible to make precise and reliable measurement of its mass. The jets and lepton production in $t\bar{t}$ events at LHC will allow an uncertainity smaller than 5 GeV/c^2.

- **the CP-violation in B-decays.** Finally the associated production of muons with $B_d^o \rightarrow J/\Psi\ K_s^o$ can give access to CP-violation effects in the B system.

The lepton trigger and identification is then one of the most important items for the physics programme at LHC. In particular muons, with the respect to electrons, can be:

- identified after the central calorimeters of the experiment up to the highest LHC luminosities;

- identified inside jets

- triggered and measured at low transverse momenta.

3 Muon spectrometers for LHC

As we have pointed out previously, the muon trigger and reconstruction at LHC is of primary importance and therefore the design of the muon spectrometer will have the largest impact to the final performance of the whole experiment. To exploit the discovery potential at the highest luminosities the muon spectrometer should have a good performance as a stand-alone system. Namely, even at a luminosity in excess of $10^{34}\ cm^{-2}\ s^{-1}$, the charged particle rates, mainly muons, emerging from the central calorimeter do not prevent efficient muon trigger and precise momentum measurement, without need of the inner tracker that may not work satisfatorly in this extreme regime.

There are two possible designs for a stand-alone muon system:

- air spectrometer, for which the momentum resolution is such that

$$\sigma(p)/p \propto p/(BL^2) \tag{1}$$

  where L are the geometrical dimensions and B the magnetic field. This relation suggests for such a spectrometer large geometrical dimensions rather than high magnetic field intensity; this leads to a large detector. The best existing example

of this system is the L3 [3] experiment that reached a momentum resolution $\sigma(p)/p \approx 0.025$ for p=45 GeV/c [4].

In addition the air systems offer the big advantage of a trasperent spectrometer that allows an easy implementation and installation of a precise alignent devices. This is a very relevant point because the chamber alignment in the muon spectrometes is going to be the most critical issues for achieving very good momentum resolutions at the new supercollider experiments.

- magnetized iron spectrometer, for which the momentum resolution is such that

$$\sigma(p)/p \propto 1/(B\sqrt{L}) \tag{2}$$

In this case, on the contrary of the air spectrometer, is much more convenient to push the magnetic field intensity. This would lead to rather compact detector. This is the case of the CMS [5] experiment proposed for LHC.

In both cases the muon momentum resolution can be improved by including the inner tracking in the measurement. In particular this is needed to measure low momenta muons, for which the energy loss fluctuation would strongly limit the stand-alone resolution.

4 The ATLAS muon spectrometer

The ATLAS Collaboration proposes a general-purpose pp apparatus which would be operational at the startup of the LHC in order to exploit the full discovery potential [6]. The generic overall detector is shown in fig. 1. The inner tracking detector is confined to a cylinder of length 6.80 and radius 1.10 m in a field of 2 T provided by a superconducting solenoid.

The baseline technology for the electromagnetic calorimter is a highly granular LAr sampling calorimeter with Pb absorber. Iron absorbers will be used for the hadron calorimetry. The thickness is 12 i.l. at $\eta = 0$ and 14 i.l in the forward regions.

The muon spectrometer is based on a superconducting air toroid system (barrel and end-caps) which allows to achieve excellent stand-alone performances; a toroidal system offers with respect to a solenoidal magnet a good transverse momentum resolution up to $\eta = 3$. The design consists on a twelve-fold symmetry with individual coils providing a field integral of about 3 Tm. A sagitta measurement is made with three layers of chambers. The detectors proposed are high precision drift chambers: the aimed precision is $\leq 200\mu m$ per wire. The systematic error to the sagitta measurement due to the chamber misalignment should not exceed $50\mu m$.

The trigger is derived from an independent system based on the resistive plate chambers; also the possibility of triggering with the measurement chamber is considered.

5 Muon rates and background flux

In order to define the required performances of the trigger system it is important to evaluate the flux of particles impinging on the muon system of the detector. This flux is composed by:

- prompt muons, produced by semileptonic decays of heavy flavours, leptonic decays of the W and Z bosons, Drell-Yan processes;
- secondary muons, produced by the charged pion and kaon decays in flight in the central cavity or in the punchthrough of hadron showers in the calorimeter; cosmic muons.
- background particles produced in the interaction at very low angles of primary hadrons with the beam pipe, the forward and very forward calorimeters and the focusing quadrupoles. Also the beam halo of the machine contributes to this background, mainly in the forward regions of the apparatus.

The prompt single muon production cross section for the processes mentioned[7] is shown in fig. 2 as a function of the transverse momentum. The dominant contribution is due to the beauty (and charm) decays, followed by the W decay. At large p_T the top decay is competitive with the other reactions. The cross section of the pion/kaon decay in flight to muon is shown also and appears significant only at very low transverse momenta ($p_T \leq 6\ GeV/c$).

In fig. 3 is shown the dimuon production cross section. The heavy flavour decays are the dominant process at low p_T, while for $p_T \geq 20\ GeV/c$ the Z decay is the main sources of dimuons. The muon pairs due to single muon event pile up is also shown: as can be seen from the figure this contribution is negligible.

An inclusive muon trigger with $p_T^{th.} \geq 20\ GeV/c$ is adequate for the standard model Higgs search [2] and would give a rate of about 1 KHz ($L = 1 \times 10^{34} cm^{-2} s^{-1}$, $\eta \leq 3$); a dimuon trigger with the same threshold for both muons would give a rate of 15 Hz.

The background particle flux in the muon spectrometer has been calculated for hadron decays and hadron punchtrhough in the calorimeters. The results are shown in fig. 4 as a function of the pseudorapidity. The in flight decays dominates in the full interval exploited and give a flux of the order of 0.1 Hz/cm^2 in the barrel region. The rate is higher in the endcaps: 50 Hz/cm^2 at $\eta = 2$ and larger than 1 KHz/cm^2 at $\eta = 3$.

However is very likely that the noise in the muon chambers will mainly come from the huge flux of soft neutrons, electrons and hadrons produced by the primary hadron interactions at very low angle in the beam pipe wall and in the very forward devices. The Montecarlo calculation of this flux, the detector layout optmization and the necessary shielding is still under study. However preliminary results show that this flux,

of the order of $10 \div 100\ Hz/cm^2$, will dominate by order of magnitude the flux due to the in flight decays.

6 Level-1 muon trigger scheme

The muon momentum evaluation at the trigger level can be performed by measuring the difference between the incoming and outgoing particle direction in the bending plane using two detector stations, as shown in fig. 5. The bending plane in the toroidal spectrometer is defined by the beam axis and the line of flight of the particle. The first trigger station is located at the center of the air toroid at a radius $R = 750\ cm$, while the second surrounds the whole spectrometer, at a radius of $1000\ cm$. This two stations allow to measure an angle very close to outgoing muon direction, while the ingoing direction is derived by using the nominal position of the pp interaction point and the point measured in the first station. The difference of this two angles, β, is proportional to $1/p$, where p is the muon momentum.

To trigger a few tens GeV/c muons the point accuracy required is not critical and a strip detector with a few centimeters granularity can do this job. The trigger can be easily implemented with a simple coincidence logic. The fired strip on plane 1 opens a window on the plane 2. The center of this window is the extrapolation of the line defined by the nominal position of the interaction point and the point on plane 1. This extrapolation is equivalent to the line of flight of an infinit momentum muon. The size of window is defined by the transverse momentum thereshold, the magnetic field intensity and the geometry. Muons with momentum higher than the threshold will hit the second plane inside the window and then give trigger. On the contrary low momentum muons will bend more and they will miss the trigger window. The sharpness of the cut is limited by several factors:

- the stability of the pp interaction point (used in the determination of the ingoing angle). The spread of the interaction point around the nominal position is expected with a gaussian shape, with $\sigma \leq 6\ cm$;
- the inhomegeneity of the magnetic field;
- the multiple coulomb scattering in the central calorimeters;

The stripsize can be choosen such that the point measurement accuracy does not contribute significantly to the spread of the trigger window. Also the effect of the energy loss fluctuation is not important, unless the threshold is fixed to very low momenta.

In fig. 6 we show the distribution of the angle β for muons (both charges) produced at the vertex with 20 GeV transverse momentum at $\eta = 0$. This angle has been calculated with a detailed Montecarlo simulation [9] of the ATLAS detector in different conditions: a) without any smearing effect (only the magnetic field inhomegeneity is

left); b) with the pp interaction point fluctuations (gaussian shape, $\sigma = 6\ cm$) and c) with the coulomb scattering and the energy loss fluctuation also. An *ideal* strip detector with 1 cm strip size has been simulated in this study.

The fluctuation of the interaction point is the main effect to the smearing of the two peaks; the coulomb scattering, however, gives comparable effects.

The trigger window size for $p_T^{th.} = 20\ GeV/c$ ranges in the barrel from 27 cm at $\eta = 0$ to 50 cm at $\eta = 1$. In the endcaps the situation is quite different; the effect of the interaction point fluctuation is less important and the point measurement accuracy becomes more important. The trigger window size, keeping constant the p_T threshold at 20 GeV/c, decreases as η increases; at $\eta = 2$ is about 9 cm. Fig. 7 shows the trigger efficiency as a function of p_T for the 20 GeV thereshold; it dependes weekly on the pseudorapidity up to $\eta \leq 2$.

The heavy flavour muon cross section has been convoluted with this trigger efficency function calculated for a threshold $p_T^{th.} = 20\ GeV/c$. The resulting trigger rate at the luminosity $L = 1 \times 10^{34} cm^{-2} s^{-1}$ is about 4 KHz. The contribution to this rate from hadron decays, punchthrough and cosmic rays are under study. Preliminary results show a rate of a few hundred Hz.

The trigger rate for dimuon events is about 30 Hz, made by Z and heavy flavour decays in equal proportion.

7 Random trigger rate

As we have pointed out previously, the huge flux of neutrons, photons and charged particles could be the most severe problem for a muon trigger at the LHC. Namely, the random trigger rate due to this physics noise cannot be neglected and if a particular care is not taken it would dominate by far the genuine muon rate. Consequentely, since this noise in different places can be assumed completely uncorrelated, the requirement of the coincidence of several planes in one or both stations can strongly reduce the random trigger rate.

If r is the noise flux, the random trigger with n planes results proportional to $(\Delta x\ \Delta t)^{n-1}$, where Δt is the trigger time gate and Δx is the detector segmentation. This suggests the employement of a detector with very good time resolution and fine segmentation.

With a good time resolution detector it is also possible to assign correctly at the level 1 the bunch crossing identifier that has the muon trigger. This allows to send to higher level triggers only the data with bunch-id of interest, similarly to what is planned for the inner tracker and the calorimeter. In this way it is possible to reduce the requirement on the bandwidth of the online system.

8 Trigger implementation

We can summarize now the main requirement for a level-1 trigger system at the LHC:

- very good time resolution;
- fine and easy segmentation;
- high detection efficency of the chambers on a large surface;
- low sensitivity to neutrons;
- simple electronics, easy to debug;
- not expensive (large surface to be covered).

One solution could be the use of the precise measurement detector of the muon spectrometer (drift chambers). However, a dedicated trigger system would be more robust and thus would offer a more reliable work, decoupled by any other complicated measurement system. In this respect the RPC are one of the best detector candidate for a such system. The double-gap RPC has excellent time resolution ($\approx 1.5\ ns$) [10], is suitable for large area coverage and is rather compact and cheap. Two important aspects are, however, under study and need a more precise measurements:

- the detection efficiency as a function of the particle flux;
- the sensitivity of this chamber to neutrons, as a function of the neutron energy from a few MeV down to the thermal value.

9 Conclusions

The level-1 muon trigger is crucial for a large variety of physics processes search. It offers the advantage w.r.t. the electron trigger of much lower rates in the range of transverse momentum theresholds of interest. The surface to be covered by the muon trigger chambers is large and the muon system will work in an enviroment exposed to large flux of neutrons (fluxes of charged particles are considerably smaller but should not be neglected). Good time resolution, high detection efficiency, low neutron sensitivity and low cost are crucial parameters for the detector choice.

The new double-gap RPC are good candidate for this application; however the problem of rate capability and of the neutron sensitivity needs more R&D effort.

References

[1] *Design Study of the Large Hadron Collider*, CERN 91-03 (1991).

[2] Proceedings of the Large Hadron Collider Workshop, CERN 90-10 (1990), Vol. II.

[3] B. Adeva et al., *The construction of the L3 experiment at LEP*, NIM A289 (1990), pag. 35.

[4] The L3 Collaboration, *Results from the L3 experiment at LEP*, CERN-PPE/93-31 (1993), submitted to Physics Reports.

[5] *CMS*, CERN/LHCC 92-3 (1992).

[6] *ATLAS*, CERN/LHCC 92-4 (1992).

[7] A. Nisati, *Muon rates at the LHC*, Proceedings of the Large Hadron Collider, (1990) Vol. III, pag. 442.

[8] A. Ferrari, private communication.

[9] R. Brun et al., *GEANT* program V. 3.15.

[10] L. Pontecorvo, these proceedings.

Figure captions

1. The ATLAS detector
2. Integral inclusive muon cross section production in $|\eta| \leq 3$
3. Integral dimuon cross section production in $|\eta| \leq 3$
4. Charged particle rates on outer calorimeter surface; the assumed luminosity is $1.7 \times 10^{34} cm^{-2} s^{-1}$
5. level-1 muon trigger scheme; see text
6. bending angle β for 20 GeV p_T muon at $\eta = 0$
7. trigger efficiency curve for $p_T^{threshold} = 20\ GeV$ in the region $|\eta| < 2$

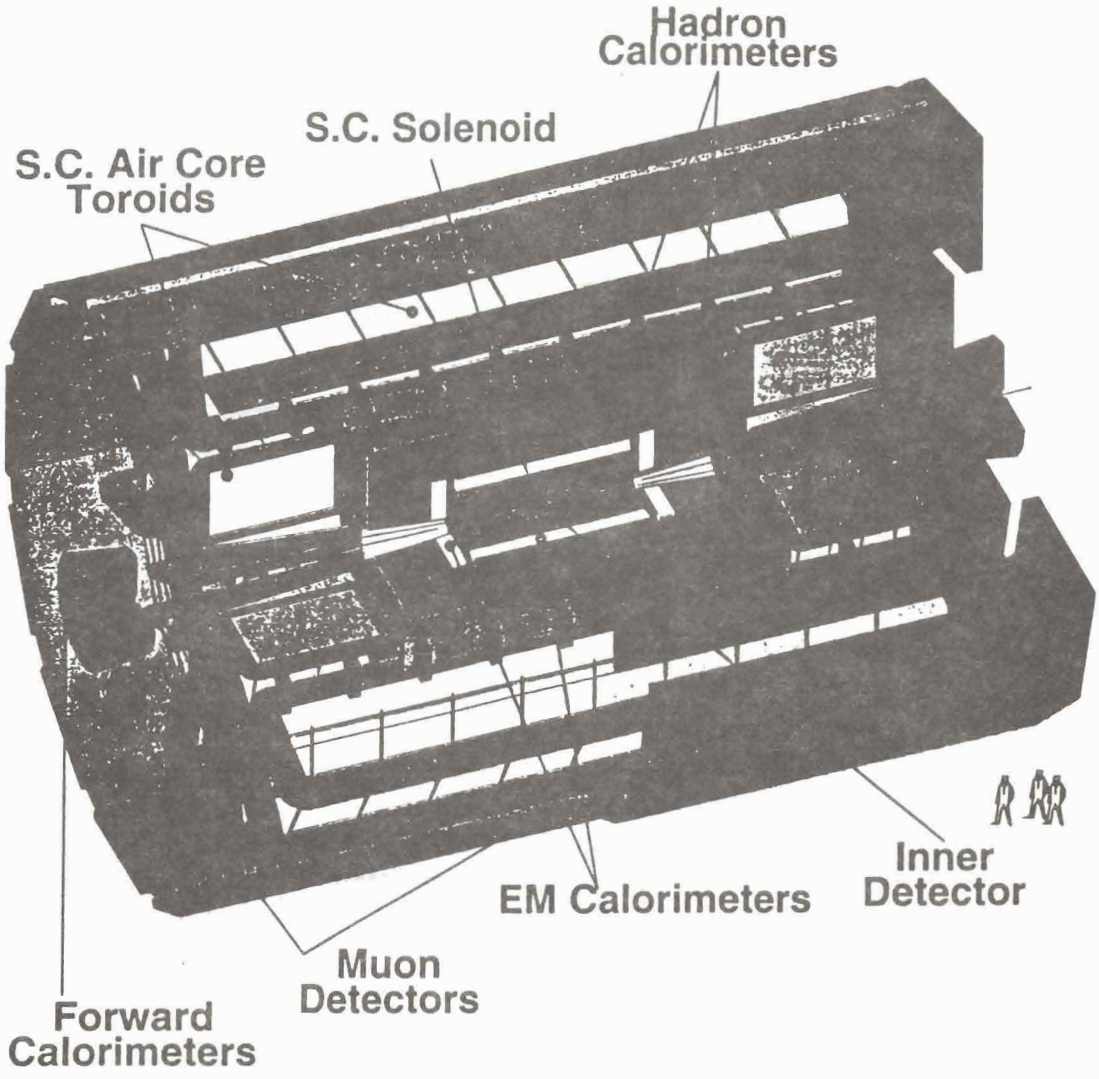

FIG. 1

The ATLAS detector

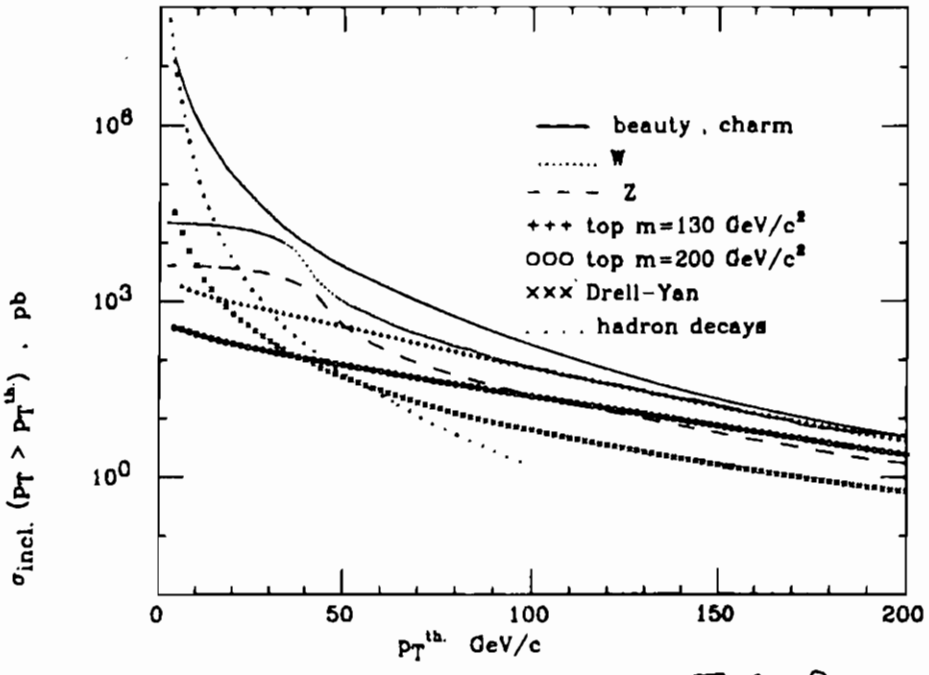
beauty , charm
W
Z
+++ top m=130 GeV/c²
ooo top m=200 GeV/c²
xxx Drell-Yan
. . . . hadron decays
$\sigma_{incl.}$ ($p_T > p_T^{th.}$) , pb
10^6
10^3
10^0
0
50
100
150
200
$p_T^{th.}$ GeV/c

FIG. 2

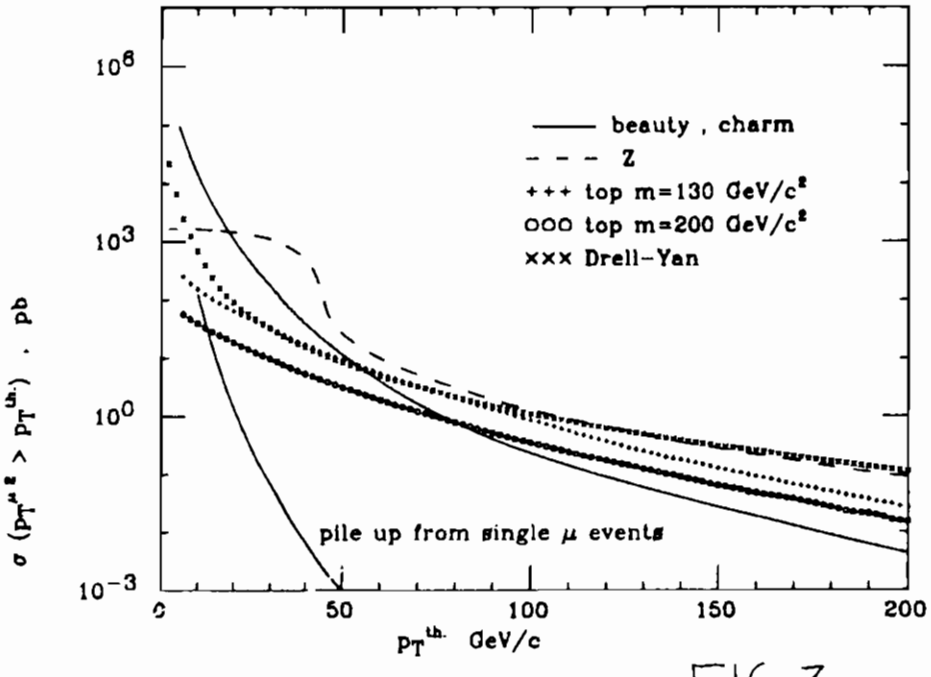
beauty , charm
Z
+++ top m=130 GeV/c²
ooo top m=200 GeV/c²
xxx Drell-Yan
pile up from single μ events
σ ($p_T^{μ}$ > $p_T^{th.}$) , pb
10^6
10^3
10^0
10^{-3}
0
50
100
150
200
$p_T^{th.}$ GeV/c

FIG. 3

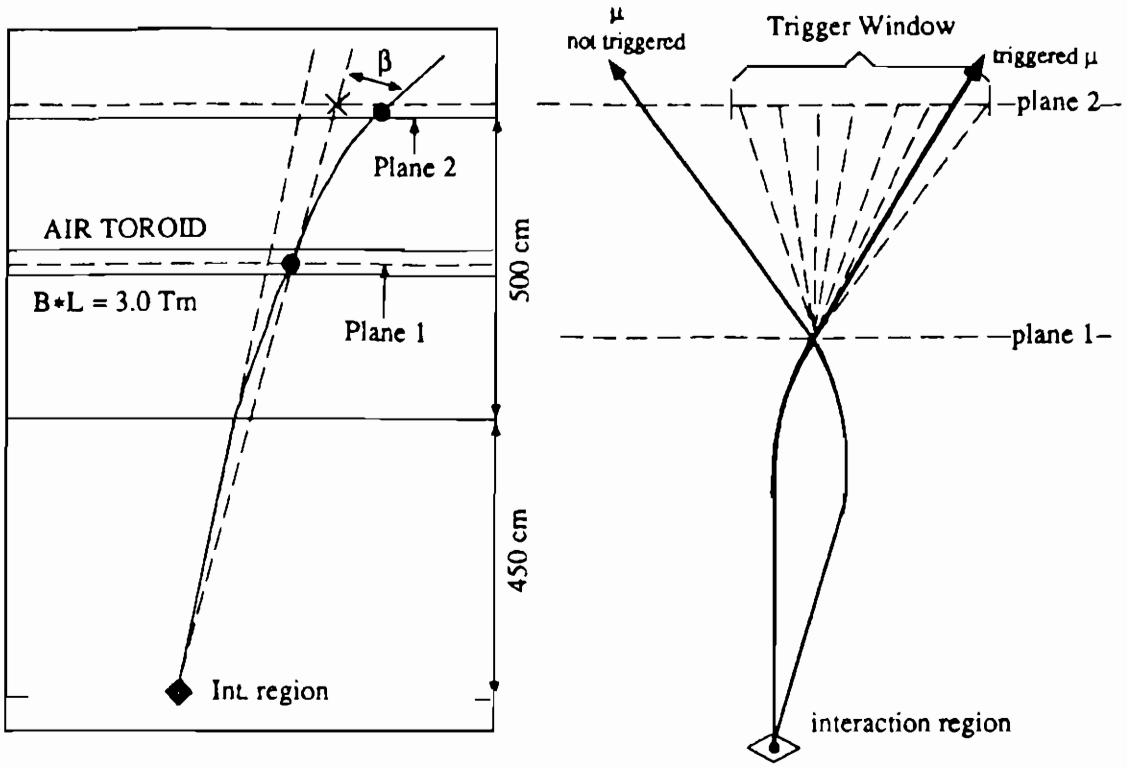
β
Plane 2
AIR TOROID
B*L = 3.0 Tm
Plane 1
500 cm
450 cm
Int. region
μ
not triggered
Trigger Window
triggered μ
plane 2
plane 1
interaction region

FIG. 4

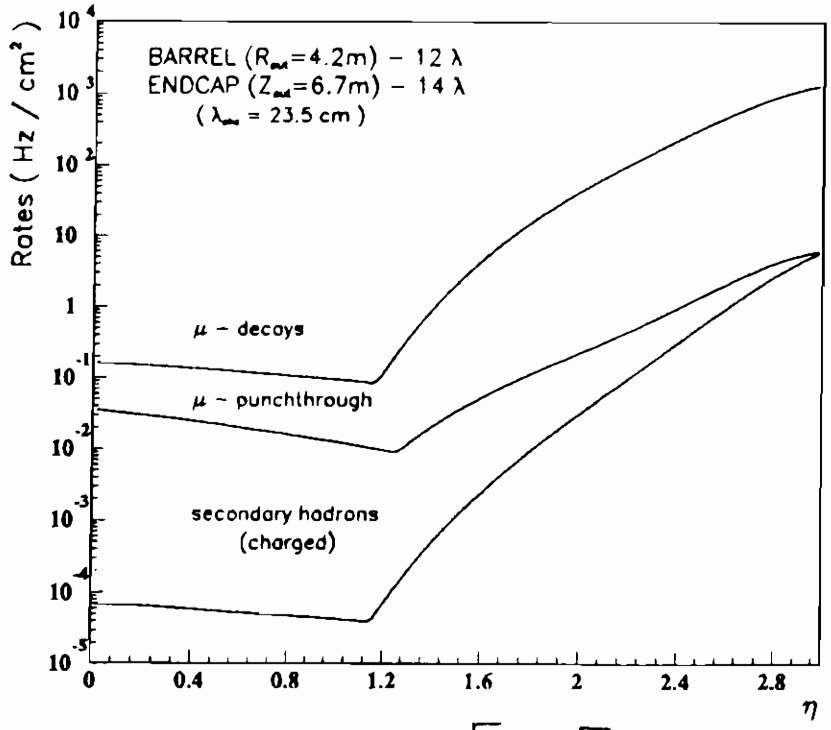
BARREL (R_{out}=4.2m) – 12 λ
ENDCAP (Z_{out}=6.7m) – 14 λ
(λ_{int} = 23.5 cm)
Rates (Hz / cm²)
μ – decays
μ – punchthrough
secondary hadrons
(charged)
η

FIG. 5

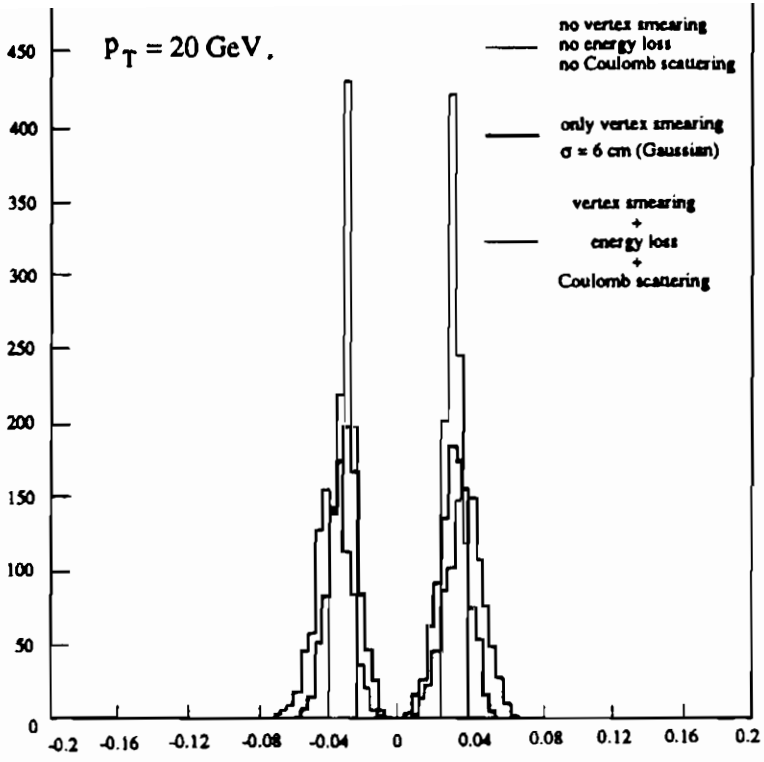
$p_T = 20$ GeV.
no vertex smearing
no energy loss
no Coulomb scattering
only vertex smearing
σ = 6 cm (Gaussian)
vertex smearing
+
energy loss
+
Coulomb scattering
450
400
350
300
250
200
150
100
50
0
-0.2
-0.16
-0.12
-0.08
-0.04
0
0.04
0.08
0.12
0.16
0.2
β, rad

FIG. 6

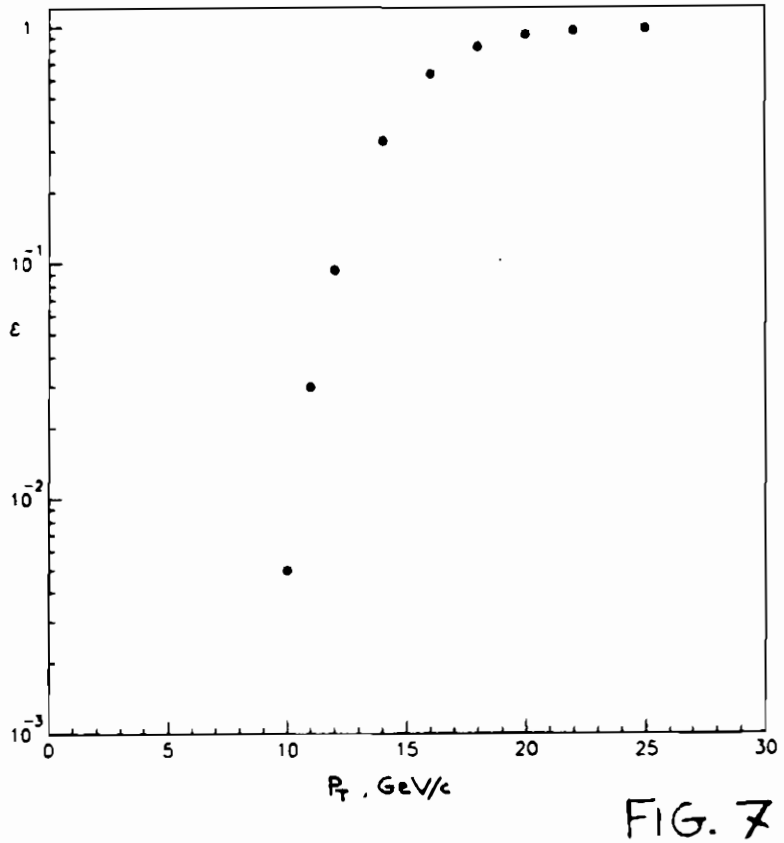
1
10^{-1}
ε
10^{-2}
10^{-3}
0
5
10
15
20
25
30
P_T, GeV/c

FIG. 7

RPC BASED MUON TRIGGER FOR THE CMS DETECTOR AT LHC

Grzegorz Wrochna [1]
CERN, CH-1211 Geneve 23, Switzerland
(for CMS Collaboration)

1 Introduction

The CMS detector [1] is one of the most challenging applications of RPC's nowadays. The total area covered by RPC's reaches 4000 m^2. The particle rate varies from 1 up to about 1000 Hz/cm^2 depending on the angle. In total of the order of 10^{16} pp collisions per year will be seen. On the average 25 pp collisions take place every 25 ns. The first level single muon trigger has to reduce this rate down to about 1 kHz, i.e. six orders of magnitude.

"CMS" stands for Compact Muon Selenoid, however the detector is capable to measure precisely electrons and photons as well as muons. The name reflects the way the detector has been designed. First a superconducting solenoid generating a magnetic field of 4T has been chosen to facilitate muon trigger and momentum measurement. The strong field leads to a compact design. Both calorimetry and high granularity inner tracker are accomodated inside a large diameter (≈6 m) coil. Overall outlook of the detector is shown in Fig. 1.

2 Physics potential

The CMS detector has been designed to study a wide range of physics phenomena accessible in pp collisions at LHC. Here let me mention only a few highlights:

- Standard Model Higgs search:
  $H \to \gamma\gamma$, $H \to ZZ^*$, Heavy Higgs ($m_H \approx 1$ TeV)
- Minimal Supersymmetric Standard Model Higgs search:
  $h^0, H^0 \to \gamma\gamma$, $A^0, H^0 \to \tau\tau$, $H^\pm \to \tau\nu$ cs
- Top physics
- CP violation (e.g. $B_d^0 \to J/\psi\, K_S^0$)
- Heavy ion physics (e.g. Υ', Υ'' suppression)

An example of a possible discovery for which the performance of the muon system is crucial is the $H \to ZZ^*$ channel. Simulated mass spectra are presented in Fig. 2. The signal is clearly visible over the background.

[1] On leave from *Institute of Experimental Physics, Warsaw University.*

3 Detector components

3.1 Inner tracker

A cylindrical volume of r<1.3m and |z|<3.5m around the interaction point is occupied by the inner tracker (Fig. 3). Barrel part is arranged in three superlayers, each having four detector planes. The innermost superlayer is a Silicon Microstrip Detector, others are MicroStrip Gaseous Counters (MSGC). Forward part consist of 5 discs with Silicon Detectors and 18 MSGC discs on each side. High granularity of the detectors has been chosen to allow an efficient pattern recognition in the high track density environment. In total there are $7 \cdot 10^6$ Si channels providing resolution σ=15μm and $12 \cdot 10^6$ MSGC channel giving σ=50μm.

3.2 Calorimetry

General layout of CMS calorimeters is shown in Fig. 4. Two possible solutions of Electromagnetic Calorimeter (ECAL) are investigated. One is made of 26 m^3 of CeF_3 crystals. Crystals are arranged in 110 000 towers, two crystals each. Front area of the tower is 1.6 x 2.4 cm^2. Length of the front and the back crystal is 15 and 27 cm respectively. This solution is expected to provide an energy resolution better than 1% at 50 GeV.

An alternative option is the so called Shashlik Calorimeter. It is a 2 mm lead / 4 mm scintillator sampling calorimeter. Light is collected by 1.2 mm diameter fibers arranged in a 1 cm grid (see Fig. 5). Energy resolution is about 1.5% at 50 GeV.

Hadron Calorimeter (HCAL) is a typical copper/scintillator sampling calorimeter with 4 scintillator plates per interaction length. It gives energy resolution of 10% at 100 GeV and 4% at 1 TeV. First 25 X_0 has finer granularity to be a tail catcher and trigger veto for the ECAL, and eventually to substitute the ECAL in the first phase of the experiment.

Very Forward Calorimeter (VFCAL) is an iron/gas sampling calorimeter. It ensures rapidity coverage up to $|\eta| < 5$.

3.3 Muon detector

The CMS muon system consist of 4 muon stations (see Fig. 1 and 6). Dead spaces are distributed in such a way that every track crosses the sensitive area of at least three stations. Each station is used for triggering as well as for momentum measurement. Momentum measurement requires precise position determination ($\approx 200\mu m$ per measuring plane). Since the expected occupancy is low, drift tubes are natural candidates for muon chambers. The only exception is a very forward region where Cathode Strip Chambers (CSC) are foreseen. Actually two types of chambers are considered: Drift Tubes with Bunch Crossing Capability (DTBX) and Wall-Less Drift Chambers (WLDC). Both will be presented in dedicated talks [2, 3]. Thus, here I describe only general features of the whole system. Total area of the muon stations exceeds 3000 m^2. Every station consists of several layers of chambers. In

case of DTBX 8 layers measure $r\varphi$ coordinate, 4 layers measure the orthogonal coordinate. In case of WLDC the corresponding numbers of layers are 6 and 4 respectively. Wires are spaced by 40 mm (DTBX) or 14 mm (WLDC). The total number of channels is of the order of half to one million. Momentum resolution of the muon system alone and combined with the inner tracker are presented in Fig. 8.

4 Muon trigger

4.1 Physics goals

In order to study the phenomena mentioned in Sec. 2 three types of the first level muon trigger are considered:

1. **Inclusive single muon trigger**, $|\eta| < 2$, $p_t^{cut} \approx 25 - 100$ GeV
   to study large p_t W physics and search for massive W'.

2. **Inclusive double muon trigger**, $|\eta| < 2$, $p_t^{cut} \approx 10$ GeV
   this is in fact a Z^0 trigger

3. **Triple muon trigger**, $|\eta| < 2$, $p_t^{cut} \approx 4$ GeV
   e.g. to study CP violation in b decays

4.2 Technical requirements

Rate

An original idea of CMS is to abandon classical three levels structure of the trigger system. Usually the second level trigger is made of fast, dedicated (and therefore expensive) processors providing simple arithmetic operations with high performance. Trends in the computer development suggests that in a few years this task can be taken over by cheap, commercial workstations. Thus after the first level trigger data goes to such an "event filter" which is a computer farm performing tasks usually done by the second and the third level triggers. In case of CMS this event filter is designed to operate with up to 50 kHz total first level trigger rate. In fact we estimate that this rate should not exceed 10 kHz, thus rather large safety margin is assumed. Such a scheme imposes quite high requirements for the first level trigger. For example the single muon trigger rate should be of the order of 1 kHz.

Flexibility

In order to access all the interesting physics channels and to tune the rate to the level acceptable for the event filter the p_t threshold must be adjustable. In the present design the full range 4–100 GeV is covered.

Time resolution

The trigger should be able to assign an event to the proper bunch crossing. Thus the time resolution should be much better than the bunch crossing interval, i.e. 25 ns.

Speed

An answer of the trigger must be available 1 μs after collision.

High acceptance

Searches for rare events require acceptance to be close to 100%. Therefore the muon stations are arranged in such a way that every track (with $p_t > 6$ GeV) crosses at least 3 stations.

Redundancy

Trigger system has to deal properly with all possible inefficiencies, noises, accidental pileup and products of muon radiation. Thus, it has to have substantial redundancy. In CMS this is ensured by the fact that the measurement is done in at least three stations.

4.3 Trigger detectors

In both cases of muon chambers, DTBX and WLDC, possibility of autotriggering is investigated. However, since it will be described in dedicated talks [2, 3] here I will concentrate on a third solution, i.e. muon trigger based on dedicated Resistive Plate Chambers.

The main properties of the RPC, which make them very good candidates for large surface muon trigger chambers, are

- Good time resolution (≤ 5 ns), limited by the signal propagation time along the strips.
- Large signals from m.i.p, allowing simple and cheap analog R/O electronics.
- Construction adapted to the mass production.

In the region above $|\eta| = 2$ particle rate can exceed 100 Hz/cm^2 which is a limit for standard RPC's. Therefore Parallel Plate Chambers (PPC) have been foreseen to cover this region. However recent encouraging results with pure Freon RPC's [4] give a hope that also that region can be accessible for this technique.

4.4 Principle of operation

The solenoidal magnetic field of the CMS detector causes track bending in a plane perpendicular to the beam direction (Fig. 6). In the central part of the detector the magnetic field is almost independent on z coordinate (along the beam direction). In the forward region, bending power of solenoidal magnetic field decreases with pseudorapidity η. However the bending is still big enough to distinguish transverse momenta in wide range of values.

In principle, knowing the vertex, two measuring planes after the coil giving a local track vector are enough to measure momentum and apply a p_t cut. However in order to deal with

fluctuations due to multiple scattering and energy losses we make use of 4 measuring planes (one per station). A four point pattern (Fig. 7) is more redundant than the simple vector and gives a sharper cut.

Above idea has to be modified for muons with $p_t < 6$ GeV in the barrel because they are not able to reach outer muon stations. Therefore we place two RPC planes in the first and the second muon station and again use four point pattern to make the p_t cut.

4.5 Practical realization

Since the track is bent in the plane perpendicular to the beam it is enough to know precisely only the φ coordinate. Thus measurement can be done with long strips positioned along the beam in the barrel and radially in the forward region. In the barrel the length of the strips is limited by the signal propagation time. To keep the time resolution below 10 ns the strip length should be of the order of 1 m. In the forward more fine segmentation is required because bending depends on η and different cuts have to be applied for different η regions.

Width of the strips is determined by the required momentum resolution. In order to have efficient p_t cut up to 100 GeV the strip width should be of the order of 5 mrad (3 cm at station 3). Cylindrical symmetry of the problem naturally leads to projective geometry.

4.6 Trigger processor algorithm

A particle passing the detector crosses muon stations, hitting the RPC strips on its way. In the absence of the energy loss and multiple scattering there will be one to one correspondence between the pattern of hits and the muon transverse momentum. In the real world with energy loss and multiple scattering there is a set of hit patterns (masks) for each value of the p_t. The sets of valid mask change with pseudorapidity η. They are practically η independent in the barrel region, but vary in the forward region. The mask sets for two different transverse momenta are ordered i.e. the set for the higher p_t is a subset for the lower p_t. This property allowed us to establish the mask set for a given value of the threshold p_t^{cut}. Such a set can be loaded into a trigger processor. Then every observed track pattern is compared with the predefined masks. A track gives a trigger if its pattern belongs to the set of valid masks.

4.7 Simulation results – efficiencies and rates.

Presented algorithm has been simulated in order to calculate efficiency curves and final trigger rates [5]. The GEANT package has been used to track muons with p_t between 3 and 100 GeV through the CMS detector. Multiple scattering, energy loss and production of secondaries has been taken into account.

The efficiency curves as a function of the muon p_t for different values of p_t^{cut} and η are shown in Fig. 9. The p_t spectra of muons from various processes were then convoluted with the efficiency curves. Starting from the inclusive hadron spectrum we have estimated the

rate due to punchthrough using GEISHA shower simulation. This has been checked against measurements made in RD5 experiment. The complete hit pattern in the muon stations was simulated on which the trigger algorithm was then applied.

The resulting integrated trigger rates for various p_t^{cut} values are shown in Fig. 10.

5 R&D

In order to turn ideas into reality an intensive R&D program has already taken off. Most of the work concentrates around the RD5 experiment [6] which will be described in a dedicated talk [7]. R&D on chamber construction is provided by Warsaw group. First prototype, 10x10 cm^2 (Fig. 11), has been built last year and tested with cosmic rays and radioactive sources. As an example, accuracy of the hit position reconstruction is shown in Fig. 12. Next prototype, 50x50 cm^2 is under assembling and it will be tested in April's RD5 run.

6 Conclusions

Resistive Plate Chambers offers a possibility to build powerful muon trigger systems. In the CMS detector the first level muon trigger based on 4000 m^2 of RPC's is able to select efficiently interesting events reducing primary rate by a few orders of magnitude. Adjustable p_t threshold covers the range 4–100 GeV. Robustness of the system is ensured making use of four triggering stations.

References

[1] *CMS Letter of Intent*, CERN/LHCC 92-3.

[2] F. Gasparini, *High Time Resolution from a System of Drift Tubes with a Meantiming Technique*, this conference.

[3] H. Tuchscherer, *WLDC: a Drift Chamber with a Pad RPC for Muon Detection at LHC*, this conference.

[4] R. Cardarelli, *Test of RPC Operating with Pure CF_3Br at RD5*, this conference.

[5] M. Konecki, Warsaw University M.Sc. thesis, 1992, unpublished,
M. Konecki, J. Królikowski, G. Wrochna, *Simulation study of the single muon, RPC based trigger for CMS*, CMS TN/92-39.

[6] *Status Report of the RD5 Experiment*, CERN/DRDC 91-53.

[7] A. Di Ciaccio, *RD5 Experiment: Physics Results*, this conference.

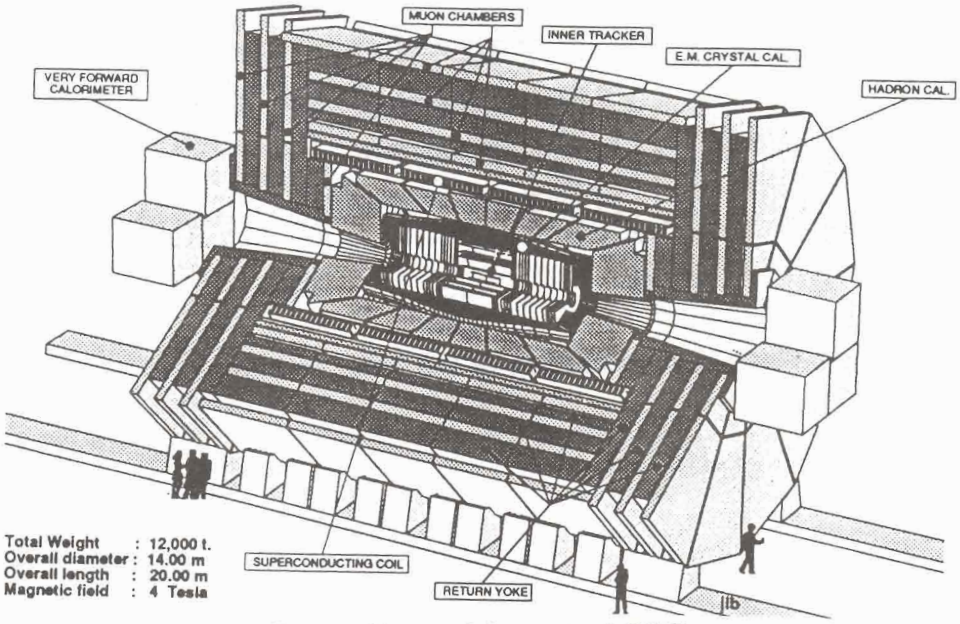

Fig.1. General layout of CMS

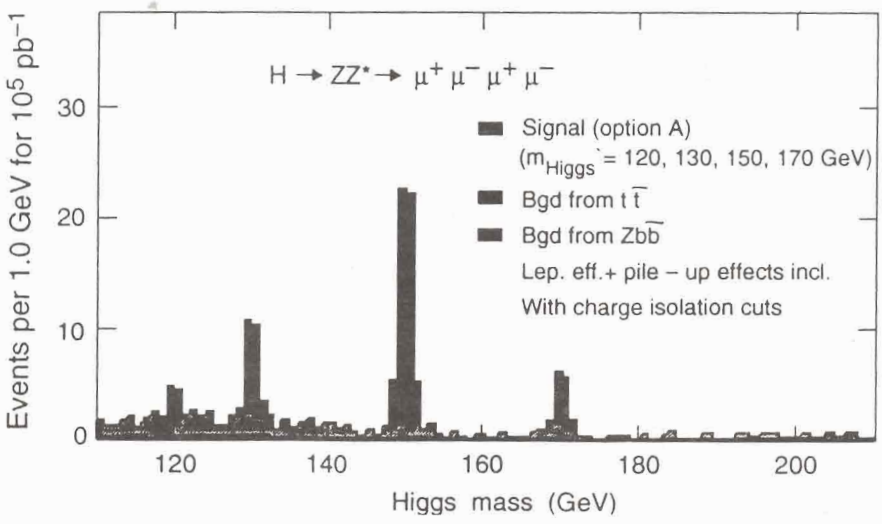

Fig.2. Simulated Higgs decays

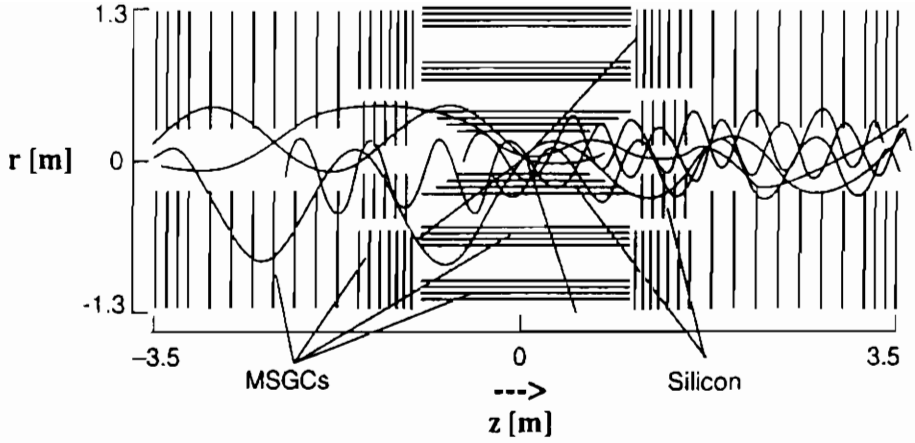

Fig.3. Cross section of the inner tracker

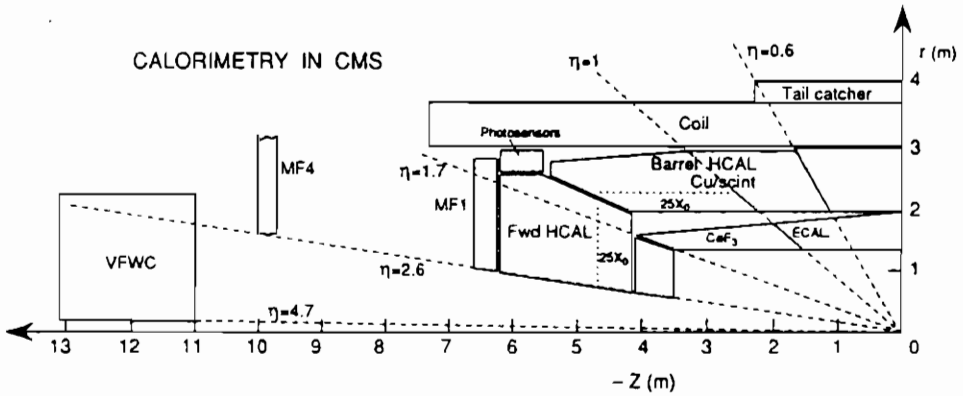

Fig.4. CMS calorimeters

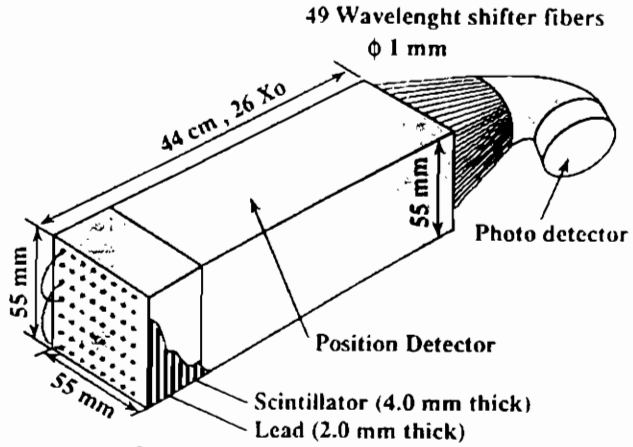

Fig.5. Shashlik calorimeter structure

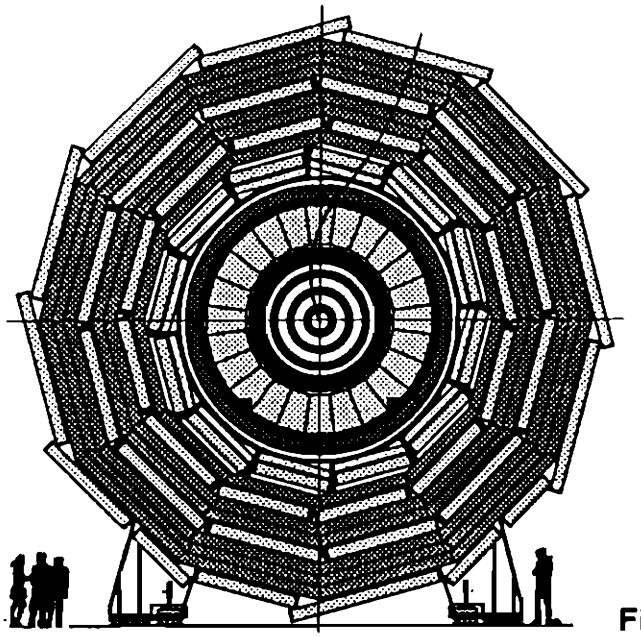

Fig.6. CMS cross section

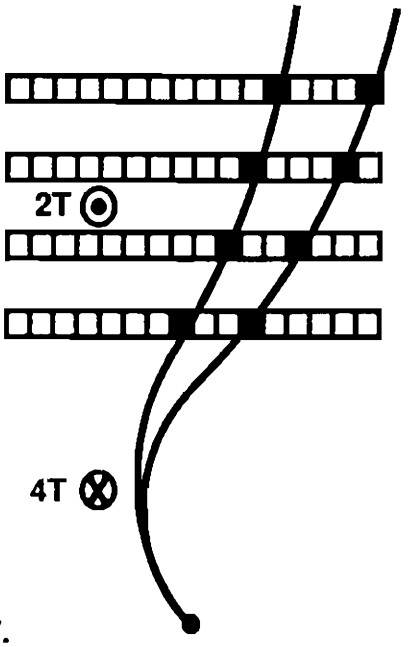

Fig.7.
Principle of trigger operation

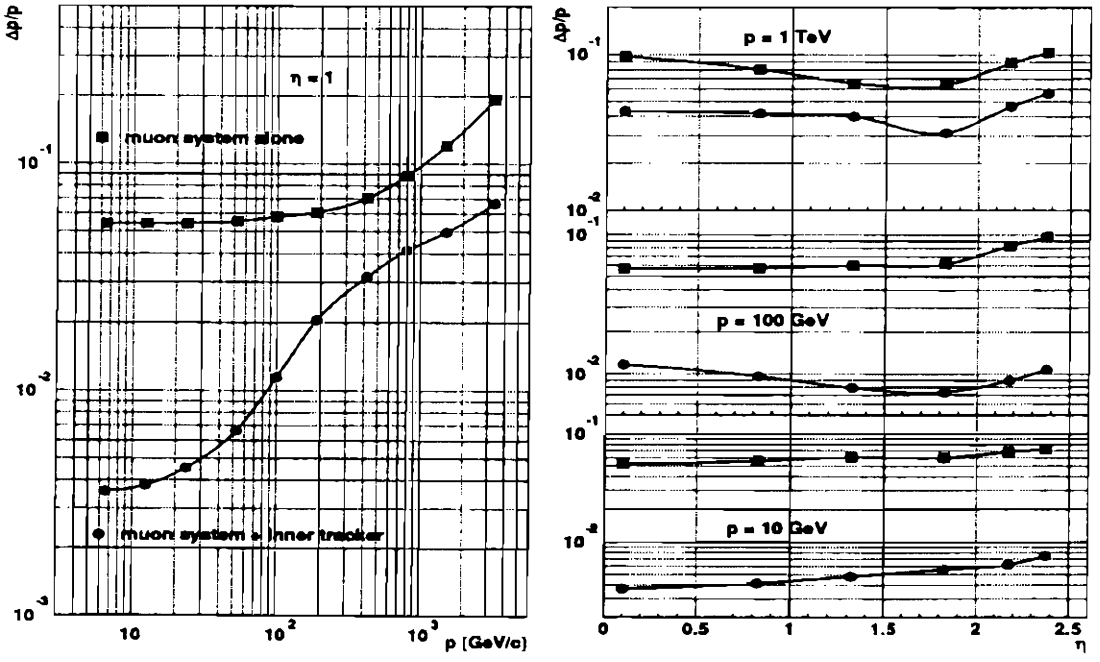

Fig.8. Momentum resolution

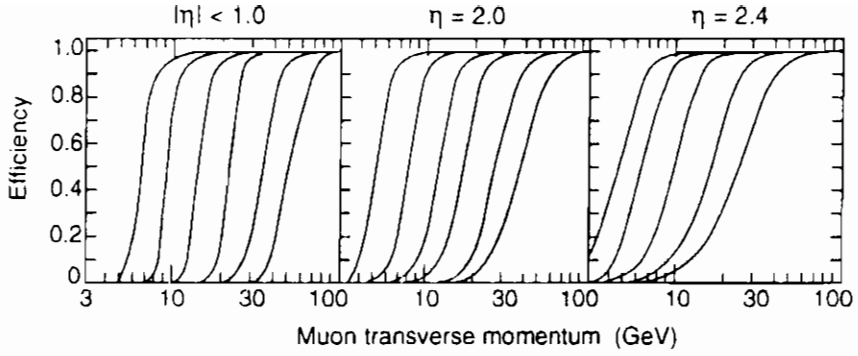

Fig.9. Trigger efficiency curves

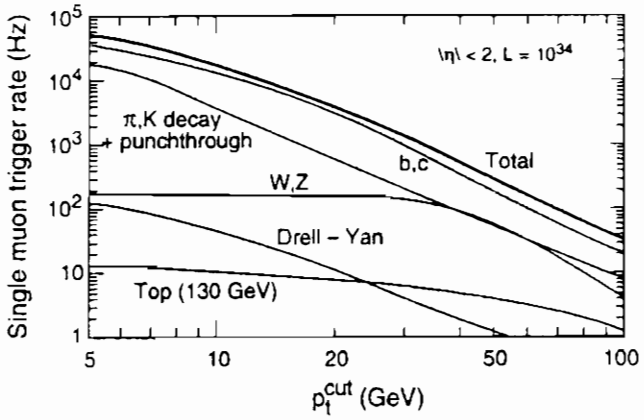

Fig.10. Simulated trigger rates

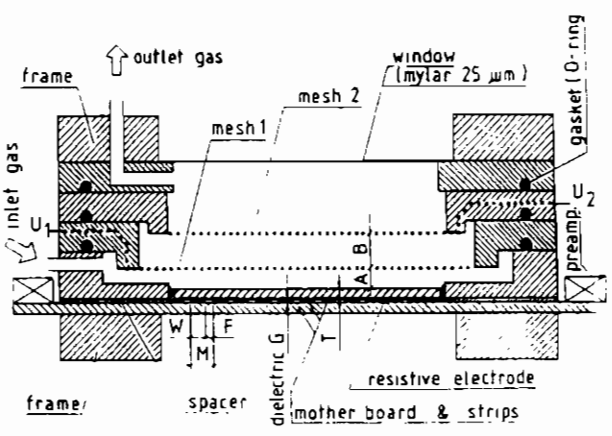

Fig.11. Warsaw RPC prototype

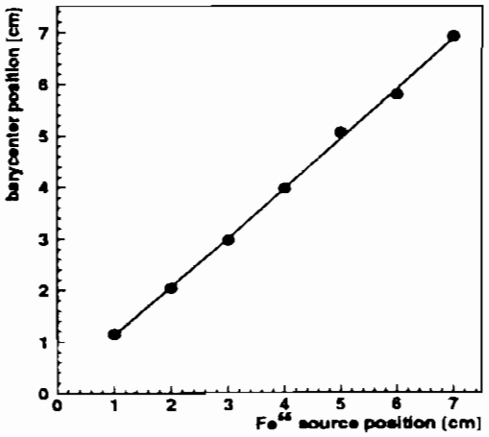

Fig.12. Position reconstruction

AN RPC MUON SYSTEM FOR SDC AT SSCL

Presented by Gianluca Introzzi for the Pavia SDC Group:

V. Arena, G. Boca, M. Cambiaghi, G. Gianini, G. Introzzi,
G. Liguori, S. Ratti, C. Riccardi, P. Torre, L. Viola, P. Vitulo.

INFN & Dipartimento di Fisica Nucleare e Teorica
Via A. Bassi, 6 - 27100 Pavia, Italy

1 SDC: the physics and the detector

The Solenoidal Detector Collaboration (SDC) has proposed [1] a general purpose collider detector to be used at one of the interaction regions of the Superconducting Super Collider (SSC), located near Dallas (Texas). The experiment is foreseen to be operational by the beginning of next century, at an initial luminosity of $10^{33}\ cm^{-2}s^{-1}$, that will be progressively increased up to $10^{34}\ cm^{-2}s^{-1}$. The energy available in the SSC proton-proton collisions (40 TeV c.m.), and the enhanced sensitivity of the SDC detector to high p_t physics, should provide an unique opportunity to look for deviations from the Standard Model.

The SSC physics program includes many topics, that can be summarized as :

- Hunting for the Higgs boson (Minimal Standard Model), or Higgs states (SUSY extensions as the Minimal Supersymmetric Standard Model);
- Investigating the top quark (provided it has already been discovered);
- Studying the Electroweak Symmetry Breaking;
- Looking for Supersimmetries (SUSY);
- Searching for heavy bosons (Z');
- Testing QCD and looking for new forces;
- Probing quark compositeness and lepton substructure.

The outlined physics program implies a detector that can identify and measure electrons, muons and jets with high efficiency and resolution over the whole solid angle down to $|\eta| < 2.5$ (corresponding to angles of about 10° with respect to the beam axis). Moreover, the spectrometer must be able to measure hadron jets up to $|\eta| < 6.0$ (equivalent to angles down to $< 1°$ from the beam axis), to have a precise measurement of the total and missing energy of each event. The capability to find the

vertex of primary interactions and secondary decays is also crucial, to exploit the heavy quark physics program [2].

In order to fulfill these requirements, the *SDC* spectrometer (Fig. 1) is a general purpose detector, with a central tracking system contained within a superconducting solenoid that provides a magnetic field of 2.0 T at the interaction point. The tracking system consists of an inner silicon tracker and an outer tracker composed by straw drift tubes ($|\eta| < 1.8$) together with an array of gas microstrip detectors ($1.8 < |\eta| < 2.8$). The tracking volume is 8.0 m long and 1.7 m in radius. The silicon tracker consists of 8 cylindrical layers of double sided silicon strip detectors, plus 26 double sided disk detector arrays, to cover a $|\eta| < 2.5$ rapidity range. The surface instrumented with silicon strips is $\sim 17\ m^2$, for a total of 6.5×10^6 channels.

The tracking system and the solenoid are surrounded by hermetic calorimetry. The central calorimeter is segmented into a barrel region ($|\eta| < 1.4$) and two endcaps ($1.4 < |\eta| < 3.0$). A shower maximum detector is included in the electromagnetic section of the central calorimeter, for a better electrons/photons disentanglement. Forward calorimeters, located about 12.5 m from the interaction point, cover the $3.0 < |\eta| < 6.0$ rapidity range at both ends of the detector, to insure hermeticity. Scintillating tiles and wavelength shifting fiber readout with lead (electromagnetic section) or iron (hadronic sections) will be used for the central calorimetry, while two options are still considered for the forward calorimeters: high pressure argon (100 atm) or liquid scintillator in glass tubes.

The muon system, surrounding the calorimetry region, provides the trigger and muon identification, as well as an independent measurement of muon momenta. The muon trajectories are measured, with a spatial resolution of $\sim 250\ \mu m$, by $\sim 90{,}000$ wire drift tubes approximately 8 cm wide and with a maximum length of 8.3 m. Momentum measurements are performed in the muon system through the bend of particles in magnetized iron toroids ($B \simeq 1.8\ T$), placed outside the calorimeter in the barrel and forward regions ($|\eta| < 2.5$). Measurements in the muon chambers are mainly devoted to the determination of the muon deflection in the bend (θ) plane. In addition, ϕ measurements are made in the barrel and intermediate regions for pattern recognition and, in association with the central tracker, to improve the momentum measurement precision at high p_t. Finally, stereo measurements are provided both in the barrel/intermediate and in the forward regions, to associate tracks in the non-bend direction. The detailed list of the detector planes of the muon system are reported in Table 1 and Table 2. In the baseline design, scintillation counters provide additional θ measurements and a precise timing signal to tag the bunch crossing associated to each detected muon. The required time resolution must allow an unambiguous tagging of the beam crossing, that has a period of 16 ns. A total of ~ 1850 (50×180) cm^2 scintillator counters is needed to cover the barrel region with a cylindrical layer (8.9 m radius) of scintillators (Fig. 2a). In the forward regions, due to the higher particle rates, two layers of scintillators are required for timing purposes. The width of the forward scintillator counters is scaled along the radial coordinate (Fig. 2b), to define

Table 1: Layout of muon system components in the barrel region

Label	Detector	Coordinate	Layers	Inner R (m)
BW1	wire chamber	θ	4	5.76
		ϕ	4	6.16
BT1	iron toroid			6.75
BW2	wire chamber	θ	4	8.48
BS2	scintillator	θ	1	8.91
BR2	*RPC**	θ	1	8.91
BW3	wire chamber	θ	4	9.96
		ϕ	4	10.36
		st	2	10.76

* Alternate detector; not part of the baseline design.

Table 2: Layout of muon system components in the forward regions

Label	Detector	Coordinate	Layers	Inner Z (m)
FW1	wire chamber	θ	4	7.54
FW2	wire chamber	θ, st_1	4	9.17
		θ, st_2	4	9.75
FT1	iron toroid			10.16
FT2	iron toroid			12.27
FW4	wire chamber	θ	4	13.86
FS4	scintillator	θ	1	15.52
FW5	wire chamber	θ, st_1	4	18.82
		θ, st_2	4	19.27
FS5	scintillator	θ	1	19.72

trigger roads in θ, and to obtain a roughly uniform p_t resolution. Their maximum length is 4 m. A total of $\sim$ 560 counters is needed for each forward scintillator layer, summing up to $\sim$ 2240 counters for the forward regions at the two ends of the detector.

Our group suggested the use of Resistive Plate Counters (RPCs) [3] instead of plastic scintillators, as an alternate muon detector for the barrel region.

2 RPCs: features and performances

The Resistive Plate Counters [4] [5] are gas particle detectors operated in a limited streamer mode, under a 4 kV/mm uniform electric field. The plateau region begins around $\sim$7.2 kV and is extended up to 10 kV. Their main characteristics are: low cost, the possibility to easily instrument large areas, excellent time resolution, good spatial resolution, short pulse risetime and large pulse signals.

The active region is usually filled with a mixture of argon (58%) and isobutane (38%) plus a small amount of freon (4%), at normal pressure. Free electrons generated inside the gas by ionizing particles induce an avalanche $\rightarrow$ streamer process. The high resistivity electrodes are transparent to the pulses originated in the active volume, and allow a capacitive readout of the signals by means of external pickup planes, segmented into strips or pads.

The discharge generated by ionizing particles is quenched by the following mechanisms :

- UV photons absorption by isobutane (preventing the propagation of the discharge);
- Capture of outer electrons by freon (reducing the size of the discharge);
- Switching off of the electric field around the discharge point (due to the high resistivity of the electrodes).

The characteristic time of the discharge process is $\tau_{dis} \simeq 10\ ns$ while the relaxation time of the resistive electrodes is $\tau_{rpc} \simeq 10\ ms$ [5]. Since $\tau_{rpc} \gg \tau_{dis}$ the plane electrodes behave like insulators during the discharge process. Consequently, only a small area ($S \simeq 5\ mm^2$) around the discharge point is deadened for a time of the order of τ_{rpc}. Since the surrounding area remains capable to detect charged particles crossing the volume of the chamber, RPCs are suitable as particle detectors operating under intense particle fluxes [6].

The schematic of a double gap RPC module is shown in Fig. 3. It consists of two chambers facing each other, mounted in the same mechanical structure, with independent HV and a common readout plane of strips placed in between. Each chamber is composed by two plates of bakelite, a phenolic polymer with high volume resistivity ($\sim 10^{11}\ \Omega cm$), separated by a 2 mm gap. The outer faces of the bakelite

Table 3: RPC's parameters and characteristics

Bakelite plates resistivity	$\sim 10^{11}\ \Omega cm$
Electric field	$\sim 4\ kV/mm$
Pulse amplitude	$\sim 500\ mV$
Pulse rise time	$\sim 2\ ns$
Generated charge	$100 \div 200\ pC$
Dark current	$8 \div 10\ \mu A$
Average stochastic noise	$600\ Hz/m^2$
Time resolution of an RPC module	$\sim 1\ ns$
Time of discharge	$10\ ns$
Recovery time of the dead area	$10\ ms$
Dead area	$\sim 5\ mm^2$

plates are coated with a conductive graphite paint, and covered by a 300 μm insulating PVC layer. Planarity of the two bakelite plates is assured by PVC spacers, located in between on a grid of 10 cm side. In order to avoid geometrical inefficiencies due to the spacers, one of the grids inside the two chambers belonging to the same double gap RPC module is shifted by 5 cm in one direction. Each chamber is sealed using a PVC frame. The metallic HV electrodes and ground are applied to the graphite surface of the bakelite plates. The two counters of each double gap RPC are lodged between two panels of expanded foam, previously preformed to guarantee the mechanical stiffness of the module. The electrical insulation is obtained adding to the outer faces of the foam layers a 0.5 mm aluminum foil, and laterally by a steel band that frames the entire module. The total thickness of a double gap RPC is 35 mm and the total weight is about 40 kg for a $(2 \times 1)\ m^2$ module. It is feasible to join together several $(2 \times 1)\ m^2$ modules to build RPC supermodules up to $(10 \times 1)\ m^2$.

A cosmic rays detection efficiency close to 100% has been obtained, with HV = 7.2 kV, using double gap RPCs [7].

The fast time response, the high spatial resolution and the low cost candidate the RPCs as an ideal detector for experiments of large dimensions in high energy physics. The RPCs were initially used as veto counters for cosmic radiation in non accelerator [8] and accelerator [9] experiments. Later on, they have been used as muon detectors in large area cosmic ray physics [10] and in fix target beauty hadroproduction experiments [11] [12]. At present, RPCs are part of the proposal of all major collider detectors for the next generation of high energy physics experiments [13] [14] [15] [16].

3 Resistive Plate Counters for SDC

The option of replacing the barrel scintillation counters of the *SDC* muon detector with *RPC*s [3] is interesting because of both technical and financial considerations.

3.1 Trigger considerations

The *SDC* Level 1 trigger operates at the beam crossing rate of 60 MHz (corresponding to a period of 16 ns) and the trigger latency, set by the pipeline length, is 4 μs [1]. Consequently, a simple and fast Level 1 trigger, able to reduce the accepted rate for each detector to a few kHz is required. In the present configuration of the detector, the Level 1 muon trigger is formed as a coincidence between wire chambers and scintillation counters which lies along a trigger road in the θ direction. Scintillation counters are mainly devoted to identify the beam crossing time associated to each detected muon. Wire chambers are not suitable for this function since their maximum drift time ($\sim$1.0 μs) corresponds to 60 beam crossings. Identification of the correct beam crossing is essential at all trigger levels as well as in the offline analysis since event's reconstruction combines data from many different devices that must be properly correlated in time. The required time resolution must allow an unambiguous tagging of the beam crossing, and is set to $8 \div 10$ ns by the beam crossing period of 16 ns [1].

In order to ensure the proper tagging of the beam crossing with almost unitary probability, mean-timing methods have to be used to remove the effect of the finite propagation speed of light in the scintillators. This imply the use of two photomultipliers for each counter in the barrel region, where only one layer of scintillators will be installed. Such a technique provides an instrumental time resolution of less than 1 ns, and a spatial segmentation of (Z, X) = (50×50) cm^2. As a side effect, the cost of the *SDC* barrel muon trigger for plastic scintillators and related electronics is estimated to be about 5 M$.

As shown in Table 3, the time resolution of an *RPC* supermodule[1] exposed to cosmic rays is about 1 ns, as good as the one of scintillators equipped with a mean-timer. Furthermore, using *RPC*s, a higher granularity of the detector can be achieved at a cost much lower[2] than using scintillators.

[1]Three modules have been assembled in a supermodule of (580×48) cm^2 useful area. Gas was flowing serially from a module to the next. The pickup strips where covering the full length of the supermodule [5].

[2]The cost of the *RPC* alternative could be as low as 2.5 M$. At present, it is hard to evaluate the total cost since the available prices for *RPC* modules are based on orders of a few counters. The unitary cost for orders of hundreds modules will decrease considerably, but the exact amount of the cost reduction is unknown. Moreover, the readout electronics for the *RPC* system has to be designed and built according to the specification requirements for devices used in the first level trigger. A realistic cost estimate for the electronics can only be done after completion of the technical design. Certainly a board built using VLSI technology will be much cheaper than the one presently used, based on discrete components.

Table 4: Segmentation of an *RPC* octant into sectors

Sector	ΔZ (m)	ΔX (m)	Number of *RPC*s
BR2.1	2.95	7.16	6 × 4
BR2.2	7.00	7.16	14 × 4
BR2.3	8.84	7.16	18 × 4
BR2.4	7.00	7.16	14 × 4
BR2.5	2.95	7.16	6 × 4

3.2 RPC and Muon System structure in SDC

The sketch of an *RPC* module for the SDC muon system is shown in Fig. 4. The external dimensions (Z, X) = (54 × 179) cm^2 are smaller than for usual *RPC* modules (100 × 200 cm^2) to preserve the possibility of removing a module from the system after the installation phase, since the BR2 (Barrel *RPC*) layer will be reachable only through small doors, once the detector will be completely assembled. The readout card is mounted on top of the module, as well as the HV connectors (Fig. 4). The gas mixture is fluxed inside the two chambers of each *RPC* module through gas connectors located laterally on opposite sides of the external frame. The same gas pipeline will serve four *RPC*s serially connected along X.

The *RPC* readout plane is segmented into aluminum strips. The maximum possible width of the single strip (in order to contain the total number of channels) will be determined by specific tests. To be conservative, let us assume (Z, X) = (50 × 3) cm^2 strips that certainly perform at least as well as standard (200 × 3) cm^2 strips. There would be ~60 strips for each *RPC* module, arranged into one row along X. A single board, able to handle up to 64 channels, is sufficient to read and to process all the signals coming from an *RPC* module. In order to reduce the total number of channels, the logic sum of 16 signals from adjacent strips (OR16) is performed by the front-end electronics [17]. Consequently only 4 signals from each *RPC*, corresponding to a detector granularity of approximately (Z, X) = (50 × 50) cm^2, are sent to the remote Level 1 trigger electronics.

The barrel region is segmented into octants (Fig. 5) and the inner radius of the BR2 layer, located externally to the BW2 layer, is 8.91 m. Each octant, (X, Z) = (7.16 × 28.74) m^2, is segmented into 5 sectors (Fig. 6). Four *RPC*s are aligned along X to form a row that covers a slice of an octant (Fig. 7). The *RPC* rows are shingled along Z to allow seamless coverage of the octant. The *RPC*'s overlap for the external (1, 5), internal (2, 4) and central (3) sectors are shown in Fig. 8 a, b, c. A total of 232 modules is needed to cover an octant (Table 4), corresponding to 1856 *RPC* modules and 7424 channels for the entire muon barrel region.

3.3 Open issues

Three major problems have to be solved in order to elaborate a feasible *RPC* muon system project for SDC: gas mixture flammability; use of freon; neutron and γ fluences.

• Gas mixture flammability

The gas mixture used so far for *RPC*s contains $\sim 1/3$ isobutane and is flammable. The use of such a gas mixture in a large area *RPC* detector exceeds the safety standards required by the *SSC* Lab, and would impose an exceedingly complex and expensive gas-leak monitoring system. It is also possible to operate the *RPC*s with isobutane at a concentration appreciably lower than $\sim 1/3$. The characteristics and performances of the *RPC*s are basically unaffected by this change of the gas.

Some preliminary results [18] indicate the possibility of using *RPC*s with a non flammable gas mixture. A 90% efficiency has been obtained testing a single chamber $(50 \times 50)\ cm^2$ *RPC* module, using the following gas mixture :

Argon	73 %
Carbon dioxide	16 %
Isobutane	8 %
Freon	3 %

The obvious extrapolation to a double chamber *RPC* with staggered spacers indicates an efficiency close to 99%. Such a gas mixture could result non flammable, due to the low isobutane percentage and to the presence of carbon dioxide that presents a high specific heat.

A set of careful laboratory tests using a low isobutane percentage gas mixture is in progress in Pavia to guarantee high performances of the *RPC*s using such a gas. After finding the best possible balance of the four gases, a flammability test will be performed on the optimized mixture, to guarantee the non flammability of the gas to be used for the *RPC*s in *SDC*.

• Use of Freon

Freon is well known to destroy the atmospheric ozone layer. For this reason his use is discouraged, and will be prohibited by law in the future. *SSCL* rules already requires to avoid the use of gases containing chlorine, the freon component that reacts with the ozone. For the *RPC*s, it could be possible to use some kind of freon that does not contain such element. Instead of usual freon (R12 or R22), some alternate candidates such as R14 (CF_4) or R13B1 (CF_3Br) have been considered. CF_4 seems to be an ideal candidate from an environmental point of view, since its ozone depletion potential is very low (Table 5). The *EPA* (Environment Protection Agency) requires

to prevent the escape of CF_4 into the atmosphere if the processed amount exceeds 10,000 *lbs/year*. The quantity of CF_4 to be used for *RPCs* in *SDc* is well below such a limit. In fact, the BR2 area is about 1650 m^2, corresponding to an *RPC* active volume of ~6.6 m^3. The CF_4 in the gas mixture is about 3%, and the gas flow is 0.1 *vol/hour*, corresponding to a CF_4 volume of ~170 $m^3/year$. For standard conditions (P = 1 *atm*, T = 293 °*K*), this is equivalent to ~620 *kg/year* i.e. ~1100 *lbs/year* of CF_4. At present, the industrial production of CF_4 in limited and consequently the gas is expensive. The situation should improve in the near future, as the CF_4 will progressively replace the standard freon. Some preliminary data obtained by the *GEM* collaboration using CF_4 instead of CF_3Br indicate that the *RPC* plateau is reached at a higher (100 to 200 *V*) value of high voltage [19].

Table 5: *ODP* for different kinds of Freon

Freon	Composition	*ODP**
R22	CHF_2Cl	0.05
R12	CF_2Cl_2	1.00
R13B1	CF_3Br	10.00
R14	CF_4	Very Low

* Ozone Depletion Potential

• Neutron and γ fluences

The neutron and γ (produced by neutron conversion) fluences experienced by the muon detectors have been calculated using Montecarlo simulation, and they result to be much higher than expected. The sources of the fluence and the detector specific responses to the neutrons are not currently known to sufficient accuracy. More detailed simulations on the fluences, the energy spectrum of neutrons and γ's and the possible shielding will be available in a few months. All these informations are important to estimate the long term effects of neutrons on the detector.

One of the main advantages of *RPCs* with respect to scintillators is their higher radiation hardness and transparency to intense neutron fluxes. Measurements with thermal neutrons, made by M. Terrani, show that the *RPC*'s detection probability per neutron is of the order of $10^{-4} \div 10^{-5}$ [20]. Data collected by I. Pless and collaborators using ~1 *MeV* neutrons give a result of 5×10^{-3} for single chamber *RPC* [16], equivalent to 10^{-2} for double chamber *RPCs*. The average *RPC* detection probability over the entire neutron energy spectrum is assumed to be 10^{-3} on the base of preliminary simulation data. An extensive study of *RPCs* behavior under intense

neutron fluxes at different energies will be conduct during 1993 at a $TRIGA$ reactor near Rome [21].

The SDC scintillators sensitivity to neutrons presents a threshold at a neutron energy of 1.1 MeV, reaches the peak (6%) at 2 MeV and drops slowly with the increasing of the neutron energy (4% at 10 MeV) [22].

Some data are available [23] for a first evaluation of the BR2 neutron background, before any attempt of shielding. Using Fig. 9 (from reference [23]) and the BR2 Z dimension (Z = 28.74 m i.e. $\mid Z \mid = 14.4\ m$), the neutron flux results to be:

$$1.4 \div 2.0 \times 10^4\ neutr/cm^2 s \quad \text{for} \quad 0.0\ m < \mid Z \mid < 12.0\ m$$
$$\text{up to } 1.2 \times 10^5\ neutr/cm^2 s \quad \text{for} \quad 12.0\ m < \mid Z \mid < 14.4\ m$$

These neutron fluxes, estimated before taking into account a careful shielding of the detector, are extremely intense. In such a noisy environment, the unambiguous bucket identification with a single timing detector layer becomes very challenging. A possible solution to this problem could be the use of a second layer of RPC's (BR3, external to the BW3 wire tubes) in coincidence with BR2, to drastically reduce the number of spurious counts due to neutron interactions. The accidental noise due to neutrons in the scintillation counters is certainly higher[3], and makes the use of a coincidence between two layers of scintillators almost unavoidable, unless the neutron rates will be drastically reduced by shielding.

Assuming the detection probability for neutrons in a double chamber RPC layer equal to 10^{-3}, the following rates are due to neutron background in the RPC counters:

$$14 \div 20\ Hz/cm^2 \quad \text{for} \quad 0.0\ m < \mid Z \mid < 12.0\ m$$
$$\text{up to } 120\ Hz/cm^2 \quad \text{for} \quad 12.0\ m < \mid Z \mid < 14.4\ m$$

The RPC efficiency dependence on the particle flux is still matter of debate. Different tests [6] [24] [25] [26] have been done in different experimental conditions. The results are considerably dependent on at least three parameters: the resistivity of the bakelite plates [26], the interacting beam dimensions [25] and the time structure of the beam [25] [26].

Final conclusions are premature but available data indicate that SDC neutron rates could be a hindrance for the use of standard RPCs in the external part (12.0 $m < \mid Z \mid < 14.4\ m$) of the barrel muon detector. Further investigations will be done as soon as more data on SDC neutron shielding[4] and RPC efficiency dependence on the counting rate[5] will be available.

The dependence of the RPC timing characteristics on the counting rate is shown in Fig. 10 (from reference [6]). For a rate below 20 Hz/cm^2 the delay is 3 ns, while for 120 Hz/cm^2 it corresponds to 13 ns. Such a difference is not bearable since the RPCs will be used in SDC for timing purposes. In the limited area of the barrel ($\sim$270 m^2

[3]The average neutron detection prob. for SDC scintillators is at least 20 times the one of RPCs.
[4]The SDC neutron task force will produce detailed data before mid 1993.
[5]The $RD5$ collaboration at $CERN$ will publish new systematic data before the end of 1993.

out of a total of 1856 m^2) that will experience a neutron flux $> 2 \times 10^4$ $neutr/cm^2s$ (i.e. a rate due to the neutron background > 20 Hz/cm^2), special techniques have to be employed, to reduce the time delay around 3 ns. The use of a dedicated readout electronics [27] can achieve such a result with a marginal additional cost (only 15% of the readout channels will require this sophisticate readout electronics).

3.4 Tests of RPCs for SDC

Some performances of the *RPC*s have to be investigated in detail before granting the possibility to use *RPC*s for *SDC*. Two tests, carried by the Pavia *SDC* group, are scheduled for this purpose. The first one, already in progress, is a bench test using cosmic rays that is investigating the following issues:

- *Gas mixture.*
  The gas mixture has to be optimized to the specific working conditions of *RPC*s in *SDC*. It has to meet the non-flammability requirements of *SSC* Lab and the kind of freon to be used should be classified as harmless for the environment;

- *RPC efficiency.*
  The overall efficiency of double chamber *RPC*s should be in excess of 98%;

- *Time resolution.*
  The instrumental time resolution of an *RPC* module has to be 2 ns at most. This will allow to have a precise bucket time association, with a 4 σ precision;

- *Stochastic noise.*
  The *RPC* system should exhibit an intrinsic noise of at most 2 kHz/m^2;

- *Strip size.*
  The bench test will reach a conclusive result on the maximum acceptable strip size, compatible with the noise and efficiency requirements reported above. *RPC*s equipped with readout strips of different pace (3, 4, 5, 6 cm respectively) will be used for this test.

The setup for the bench test of *RPC* modules consists of a muon telescope composed by 5 layers of scintillators, defining a (X, Y, Z) = (200 cm $\times$ 200 cm $\times$ 100 cm) sensitive volume. The muon trigger requires a 5-fold coincidence among the scintillator planes. The measured muon cosmic rate in the trigger telescope is 1.5 Hz, due to the strong requirements imposed to be certain that a signal identifies a muon. Two *RPC* modules, interleaved by scintillator planes, can be tested at the same time.

The second test is scheduled for Fall 1993 at *SSC* Lab. A muon tower equipped with wire tubes, *RPC*s and scintillators will be tested using cosmic rays. The prototype is a full scale model of sector 2 of an octant. The BR2.2 area is approximately 50 m^2 (Table 4) and $\sim$1/3 will be covered by 16 *RPC* modules. The mayor issue

to be investigated during the test is the system integration, to verify that the muon system operates as expected and it is able to identify muons with the required spatial and temporal accuracy. The aim of our group is also to test a new fast parallel *RPC* readout system [28] that represents a starting point for the project of the VLSI electronics to be used for the *RPC* readout in *SDC*.

4 Acknowledgements

We gratefully acknowledge F. Ceradini and L. Pontecorvo for discussions on the neutron flux problem. We also acknowledge J. Elias and E. Mach for providing useful informations on the *SSCL* gas policy. Finally, we acknowledge G. Gennaro for a careful drawing of most of the figures.

References

[1] Solenoidal Detector Collaboration; *Technical Design Report*; SDC-92-201, SSCL-SR-1215; April 1992.

[2] W. H. Smith; *The SDC detector*; in Proceedings of Particles and Fields 1991, Vancouver (Canada); August 1991.

[3] V. Arena et al.; *Resistive Plate Counters for the SDC Muon System*; SDC-92-380, INFN/TC-92/26; November 1992.

[4] R. Santonico, R. Cardarelli; Nucl. Instr. and Meth.; 187, 377 (1981).

[5] R. Cardarelli et al.; Nucl. Instr. and Meth.; A263, 20 (1988).

[6] M. Bertino et al.; Nucl. Instr. and Meth.; A283, 654 (1989).

[7] A. Aloisio et al.; *The RPC trigger system for the L3 Forward Backward Muon Detector*; L3 Note, January 1993.

[8] G. Bressi et al.; Nucl. Instr. and Meth.; A261, 449 (1987).

[9] FENICE collaboration; Preprint of Laboratori Nazionali di Frascati; LNF-87 (1987).

[10] F. D'Aquino et al.; Nucl. Instr. and Meth.; A324 330 (1993).

[11] L. Antoniazzi et al.; Nucl. Instr. and Meth.; A315 92 (1992).

[12] C. Bacci et al.; Nucl. Instr. and Meth.; A315 102 (1992).

[13] CMS collaboration; *Letter of Intent*; CERN/LHCC 92-3, LHCC/I 1; October 1992.

[14] ATLAS collaboration; *Letter of Intent*; CERN/LHCC 92-4, LHCC/I 2; October 1992.

[15] L3P collaboration; *Letter of Intent*; CERN/LHCC 92-5, LHCC/I 3; September 1992.

[16] M. Widgoff et al.; *Resistive Plate Chamber Technology Review*; GEM TN-92-206; October 1992.

[17] L. Antoniazzi et al.; Nucl. Instr. and Meth.; A307 312 (1991).

[18] P. Haridas; *Behavior of Large Resistive Plate Counters*; presented at DPF92; Fermi National Accelerator Laboratory, Batavia (Illinois); November 1992.

[19] P. Haridas, private communication.

[20] R. Santonico, private communication.

[21] L. Pontecorvo, private communication.

[22] R. Thun, private communication.

[23] L. Waters et al.; *Neutron currents is SDC*; SDC-92-361, November 1992.

[24] M. Iori, F. Massa; Nucl. Instr. and Meth.; A306, 159 (1991).

[25] I. Crotty et al.; *Investigation of Resistive Parallel Plate Chambers*; CERN/PPE 92-182, CERN/LAA-MC 92-018, October 1992.

[26] L. Pontecorvo for the RD5 collaboration; *RPC Tests at RD5*; These Proceedings, February 1993.

[27] R. Cardarelli for the RD5 collaboration; *Test of a RPC Operating with Pure CF_3Br at RD5*; These Proceedings, February 1993.

[28] A. Lanza et al.; *Fast Parallel RPC Readout System*; These Proceedings, February 1993.

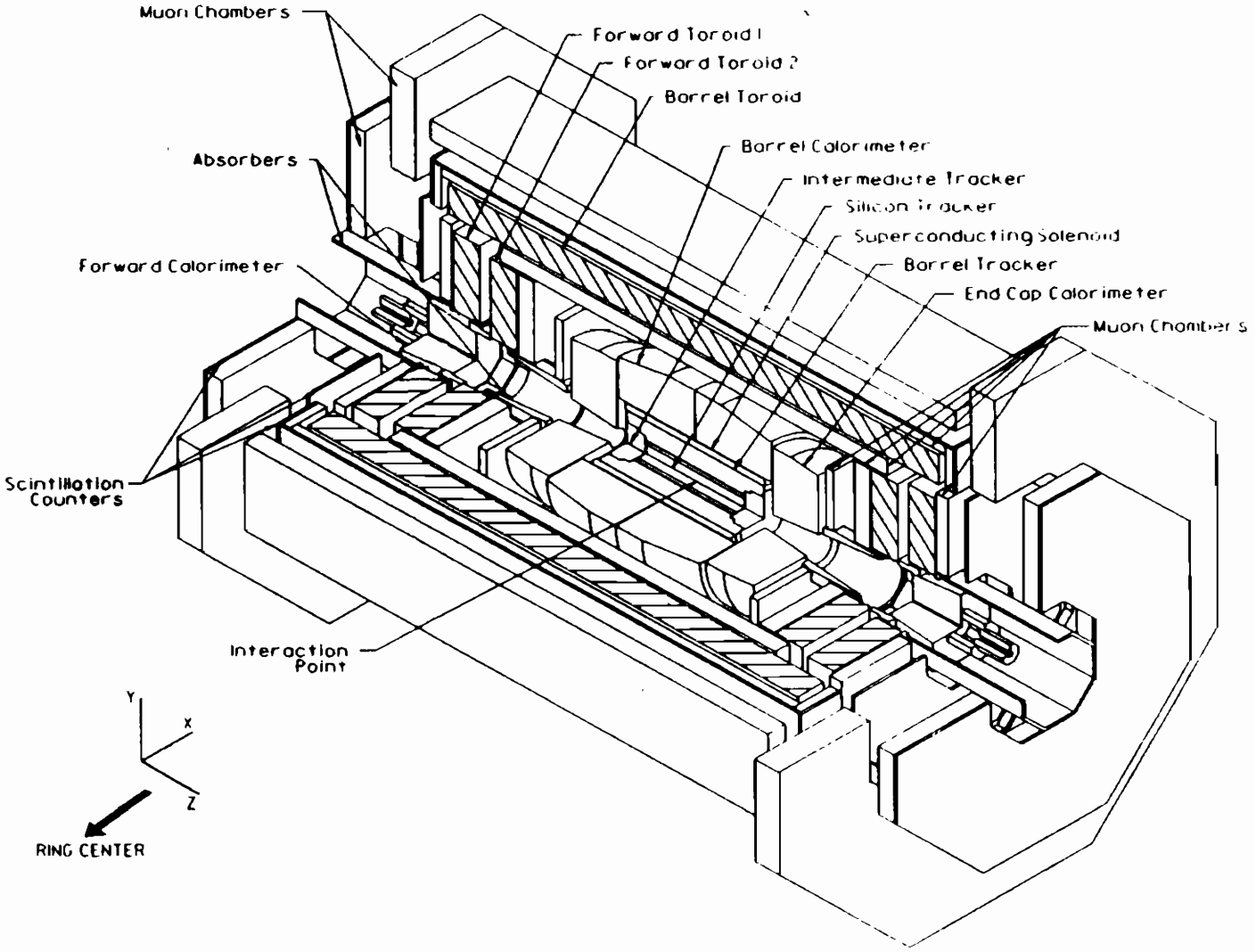

Fig. 1 - Isometric view of the preliminary SDC detector configuration.

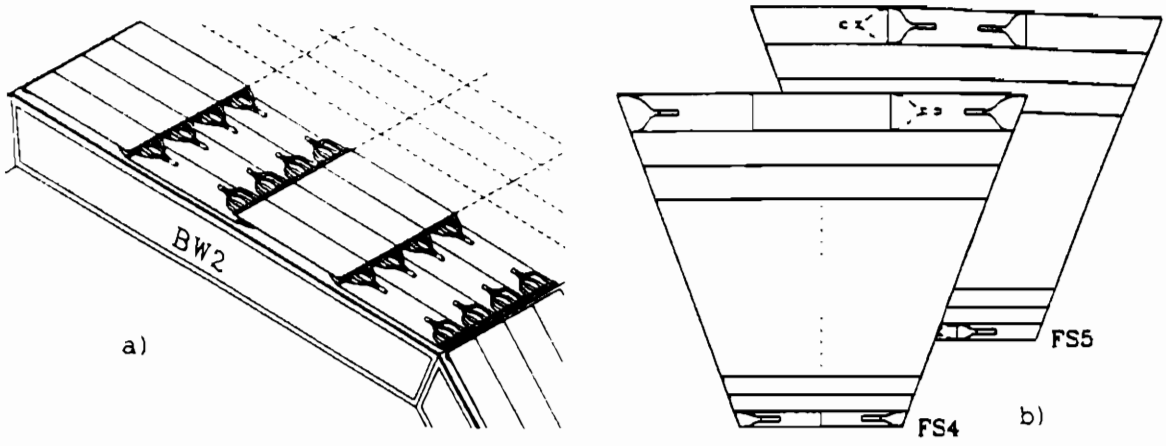

Fig. 2 - Configuration of muon scintillation counters.
a) In the barrel region; b) In the forward region.

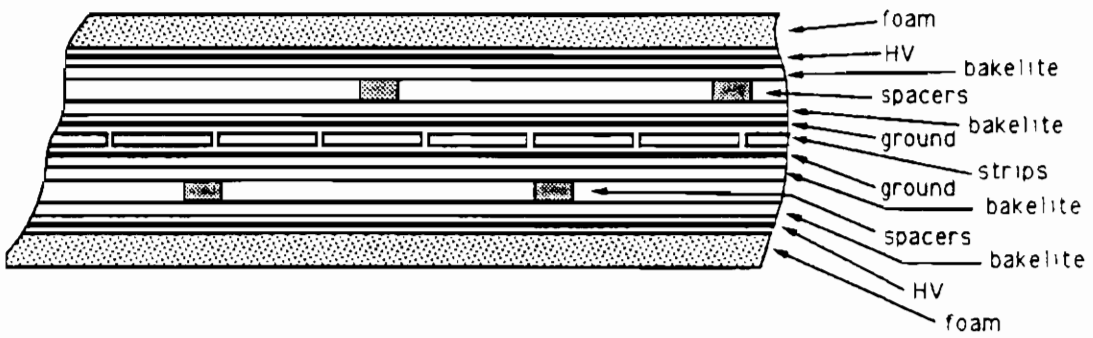

Fig. 3 - Stratigraphy of a double gap *RPC* module.

(the vertical axis in not in scale)

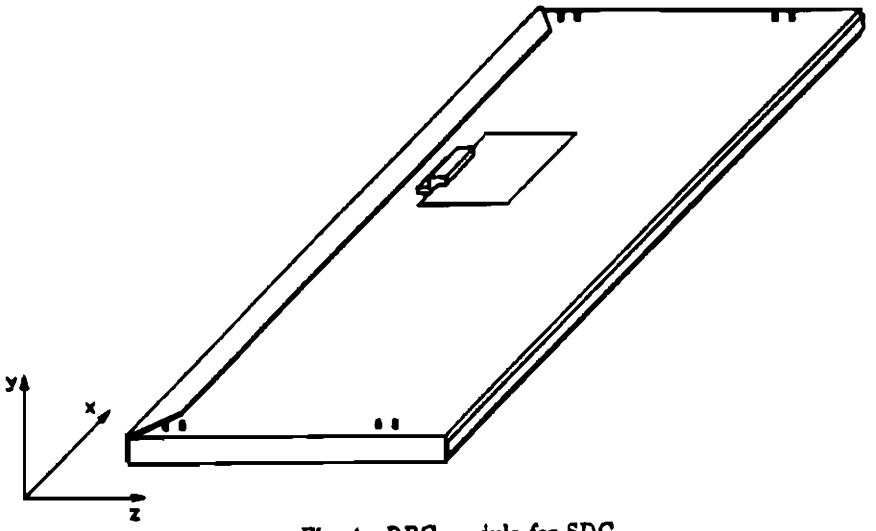

Fig. 4 - RPC module for SDC.

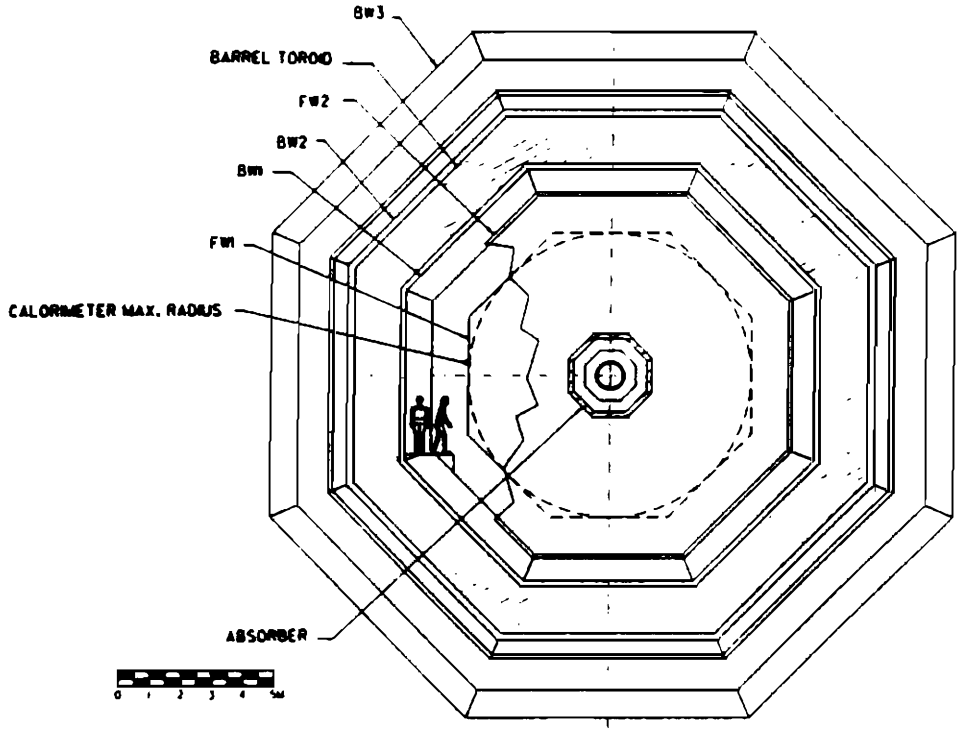

Fig. 5 - End view of the preliminary SDC detector configuration.

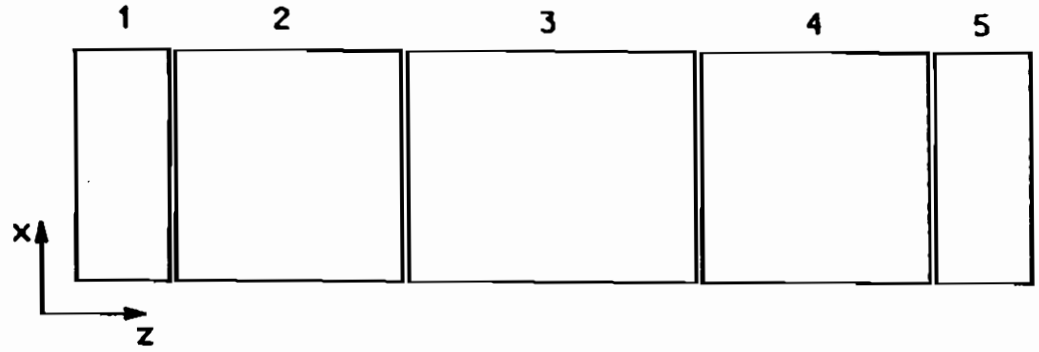

Fig. 6 - Segmentation of a BR2 octant into 5 sectors.

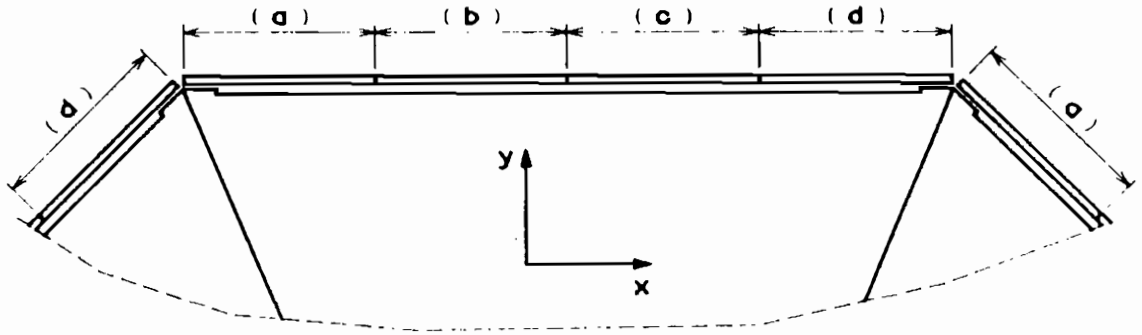

Fig. 7 - Alinement of the RPCs along X.

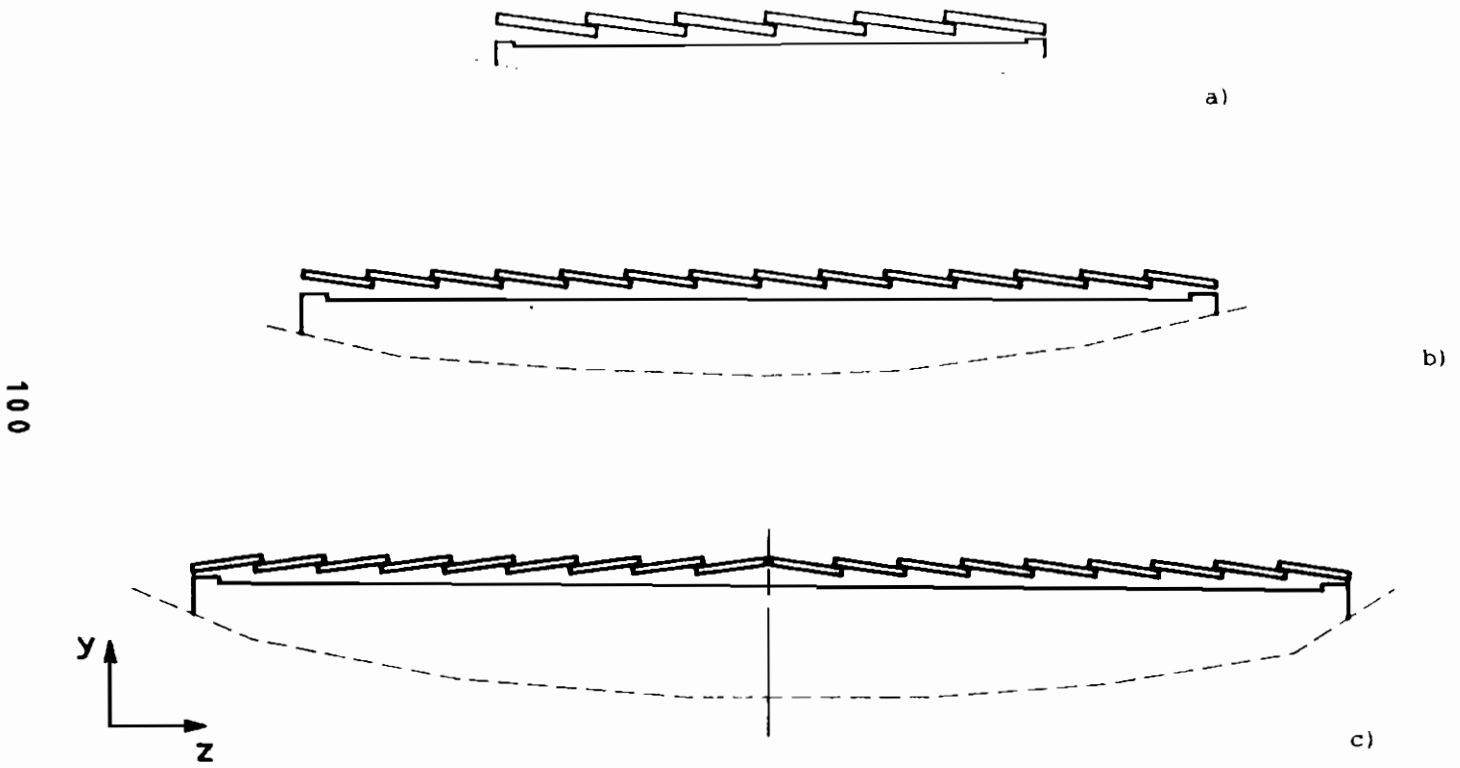

Fig. 8 - Overlapping of the RPCs along Z a) Sectors 1 and 5; b) Sectors 2 and 4; c) Sector 3.

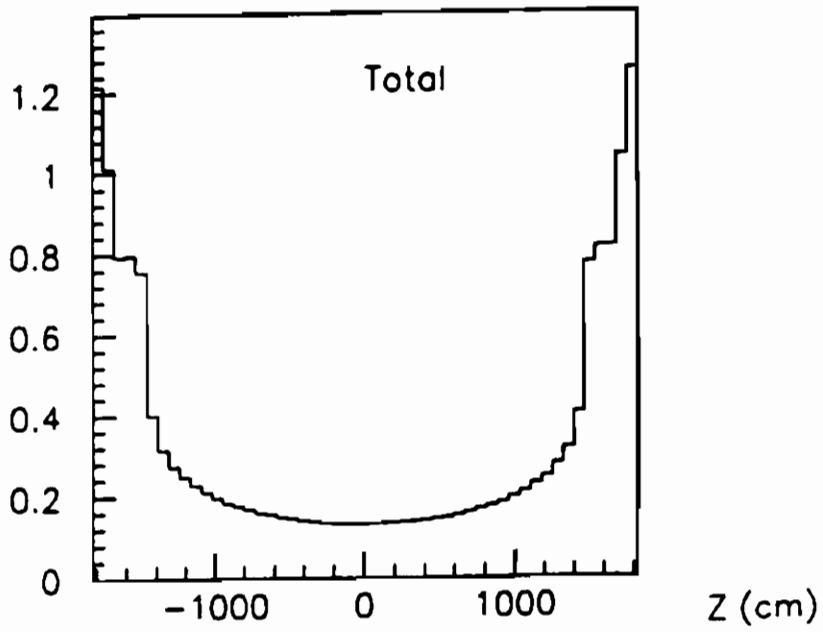

Fig. 9 - Neutron currents through BW2 (10^5 *neutr*/$cm^2 s$ full scale).

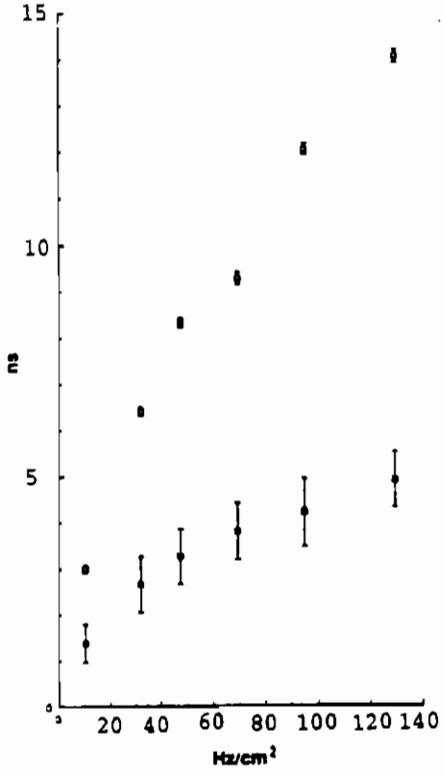

Fig. 10 - Mean value (o) and standard deviation (•) of the time of flight between an *RPC* and a beam counter vs beam flux.

A muon trigger for LHB

R. Santacesaria*
INFN - Sezione di Roma - Italy

1 Introduction.

The main features of the LHB (Large Hadron Beauty factory) project are briefly described. A scheme for a first level trigger based on high p_T muons is presented and some ideas on its realization using RPC counters are given.

2 The experiment.

LHB is a high energy fixed target experiment to be performed at the LHC and designed to study CP violation in B decays [1] . CP violation is expected to be large in the b system and it is particularly free of theoretical uncertainties when the transitions of neutral B mesons to final states of definite CP parity are considered.

The aim is to measure at least two of the angles of the triangle expressing the unitarity of the CKM mixing matrix (*unitarity triangle*) [2] namely, $sin(\beta)$ and $sin(\alpha)$, through the asymmetry :

$$\Lambda = \frac{\Gamma(B^0 \to f) - \Gamma(\overline{B^0} \to f)}{\Gamma(B^0 \to f) + \Gamma(\overline{B^0} \to f)}$$

where f are CP eigenstates corresponding, in our case, either to $J/\Psi K^0_s$ or to $\pi^+\pi^-$ respectively. To perform such a measurement, a tagging of the particle-antipaticle nature of the B meson is needed. A relatively easy and safe way to do it, is by looking at the charge of the lepton coming from the decay of the accompanying b hadron. This is one of the reasons why the identification of leptons is of primary importance in this experiment.

The beam. A 8 Tev proton beam can be extracted by the LHC accelerator with the technique of the *crystal channeling*. It is known that positively charged particles, impinging on a crystal nearly parallel to a planar direction, can be trapped between the crystal planes oscillating between very steep potential walls[3].

* Co-authors are : R. Cardarelli, F. Ferroni, S. Morganti, G. Piredda

Even in a bent crystal the particles are channeled and, following the planes curvature, they emerge from the crystal with a trajectory deflected with respect to the original one.

In order to avoid interference with the normal colliding mode of the LHC, the crystal should be placed sidewise to the beam in such a way to intercept the beam halo produced by beam-beam interactions which is expected to be of the order of $4 \cdot 10^9$ p/s and which will be anyway lost in the machine.

Assuming an extraction efficiency of the order of 10%, a proton beam of about $4 \cdot 10^8$p/s can be obtained.

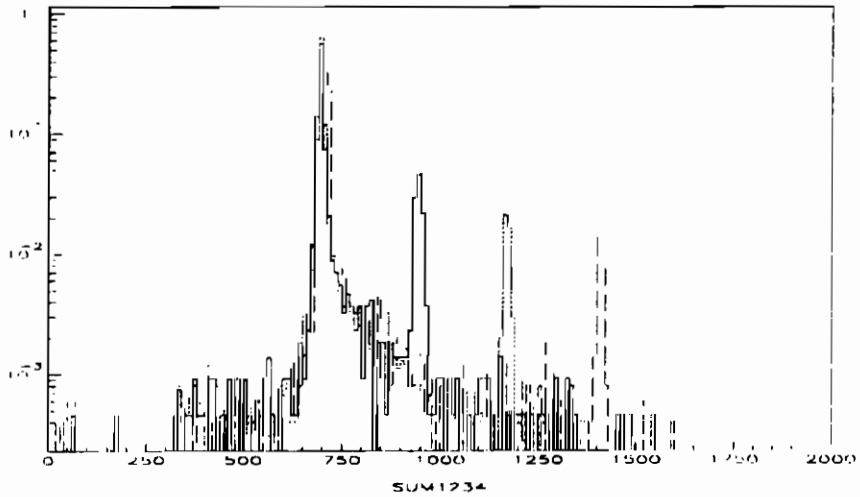

Fig.1) *The overlapped exit angular distributions after the crystal for the bending angle: 3.0 (solid line), 5.7 (dashed line), 8.0 (dotted line) mrad*

The RD22 [4] experiment has started, in 1992, a program to check the feasibility of this technique. The channeling efficiency of three crystals as a function of the bending angle has been measured on an extracted 400 Gev proton beam (H8) [fig.1] and found to be of the order of 10% in full agreement with the expectations once the beam angular divergence has been taken into account .

Two bent crystals have then been installed in the SPS beam pipe and the extraction has been studied by transversely exciting the beam to create halo conditions similar to what are expected for LHC.

The test has been successful and the extraction efficiency has been measured to be of the order of 4%.

The experiment has been approved to continue the research in 1993 to

improve the knowledge of the technique and to better understand its applicability at LHC.

The detector. The LHB fixed target approach (fig. 2) is characterized by the long average decay length of the B mesons due to the Lorentz boost and the almost full angular acceptance.

An accurate reconstruction of the secondary tracks, with direct observation of the B decay vertex, will be possible with a silicon vertex detector which follows a 5%Λ copper target. A π/K identification system is also needed to eliminate a large fraction of the background in the $B \rightarrow \pi^+\pi^-$ channel. An electromagnetic calorimeter and a muon detector are essential for lepton triggering and tagging.

A two dipoles magnetic scheme has been adopted for momentum reconstruction and trigger pourposes, as described later.

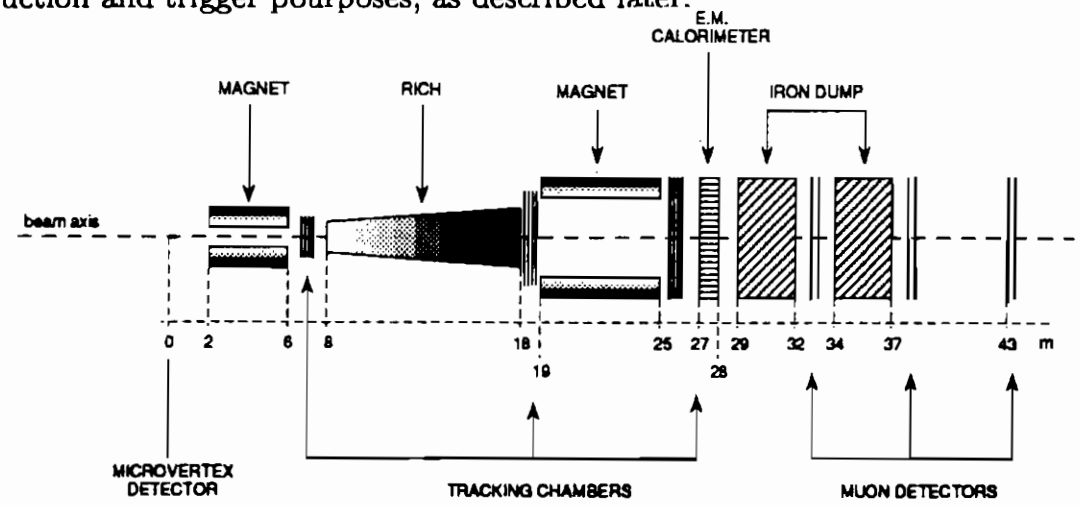

Fig. 2) *A schematic view of the LHB detector*

3 The muon trigger.

The cross section for $b\bar{b}$ production at $\sqrt{s} \sim 120$ Gev is estimated to be of the order of 1 μb [5]. This fact implies an experiment performed at high rate giving the additional problem of finding an efficient and selective trigger scheme. The identification of a high p_T lepton is a powerful tool to select B decays from so called minimum bias (MB) events.

We have designed a first level muon trigger based on the identification of at least one high p_T muon providing a reduction of rate larger than a factor 100 while keeping a very good efficiency for the signal.

In the following we recall the magnetic configuration, then we compare signal and background properties describing the possible criteria to separate them and their hardware implementation in terms of detector and trigger technology.

The magnetic scheme. The LHB magnetic design is determined by the following considerations:

a) the charged particle momenta should be measured in a forward solid angle of approximately 100 mrad with rather good precision ($\Delta p/p \simeq 10^{-4}p$). This ensures a very high acceptance and efficiency for B decays reconstruction.

b) K_s^0 decay products should also be measured with good efficiency; at this energy (8 TeV protons) quite a long decay path has to be foreseen ($\simeq$ 15 m).

Given that it is not easy to build a magnet with both a large aperture and providing the mentioned precision, we have envisaged a design incorporating two dipolar magnets (fig.3) as proposed also for other experiments [6]. A precise small aperture magnet is placed just after the vertex detector having the task of measuring most of the charged particle momenta while a second magnet with smaller acceptance is mainly used to measure the pions from K_s^0 decays. Its integral field is equal but opposite to that of the first magnet in such a way that all the charged particles conserve the production angle, being only shifted to a parallel trajectory. We believe that the existing Ω magnet [7] has sufficient acceptance and bending power to be used as the second dipole.

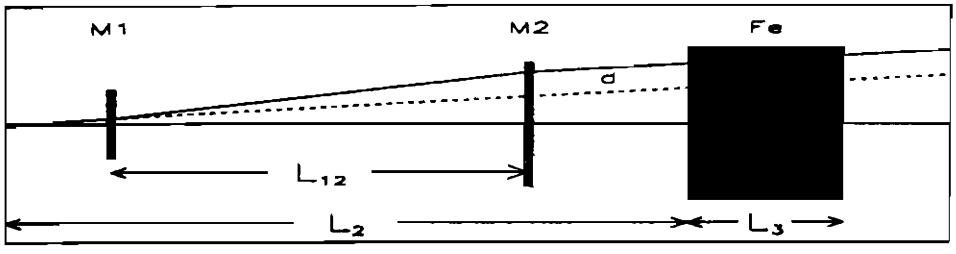

Fig. 3) *A schematic drawing of a double dipole magnetic setting. The parallel displacement d of the trajectory is inversely proportional to the particle momentum. The iron dump filters out hadron and low energy muons*

In the following we recall the magnetic configuration, then we compare signal and background properties describing the possible criteria to separate them and their hardware implementation in terms of detector and trigger technology.

The magnetic scheme. The LHB magnetic design is determined by the following considerations:

a) the charged particle momenta should be measured in a forward solid angle of approximately 100 mrad with rather good precision ($\Delta p/p \simeq 10^{-4}p$). This ensures a very high acceptance and efficiency for B decays reconstruction.

b) K_s^0 decay products should also be measured with good efficiency; at this energy (8 TeV protons) quite a long decay path has to be foreseen ($\simeq$ 15 m).

Given that it is not easy to build a magnet with both a large aperture and providing the mentioned precision, we have envisaged a design incorporating two dipolar magnets (fig.3) as proposed also for other experiments [6]. A precise small aperture magnet is placed just after the vertex detector having the task of measuring most of the charged particle momenta while a second magnet with smaller acceptance is mainly used to measure the pions from K_s^0 decays. Its integral field is equal but opposite to that of the first magnet in such a way that all the charged particles conserve the production angle, being only shifted to a parallel trajectory. We believe that the existing Ω magnet [7] has sufficient acceptance and bending power to be used as the second dipole.

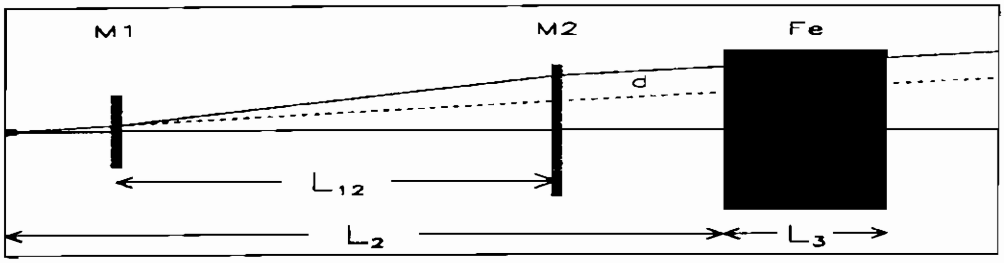

Fig. 3) *A schematic drawing of a double dipole magnetic setting. The parallel displacement d of the trajectory is inversely proportional to the particle momentum. The iron dump filters out hadron and low energy muons*

Muons from signal and background. Minimum bias and $b\bar{b}$ events have been generated with PYTHIA [8]. It appears that muons momentum from B decay is on average $< p_\mu^b >= 165$ GeV but only 7 GeV for pion and kaon decays. Fig. 4 shows that a cut at 10 GeV would reject a large amount of the background with a negligible loss of the signal. The conclusion is that an iron filter 6 meter long corresponding to 10 GeV muon range seems adequate in order to reduce considerably the muon rate.

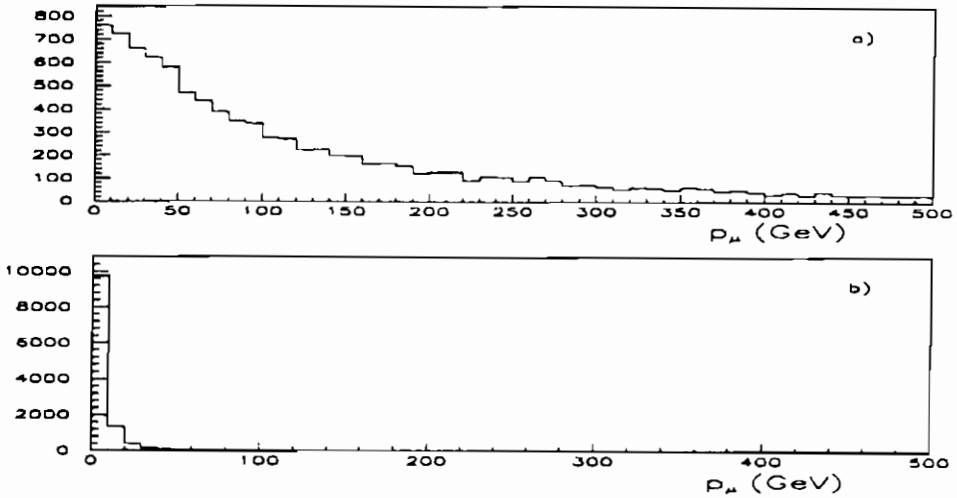

Fig. 4) *a) Momentum distribution of the muon from direct b semileptonic decays. b) Momentum distribution of the muon in minimum bias events.*

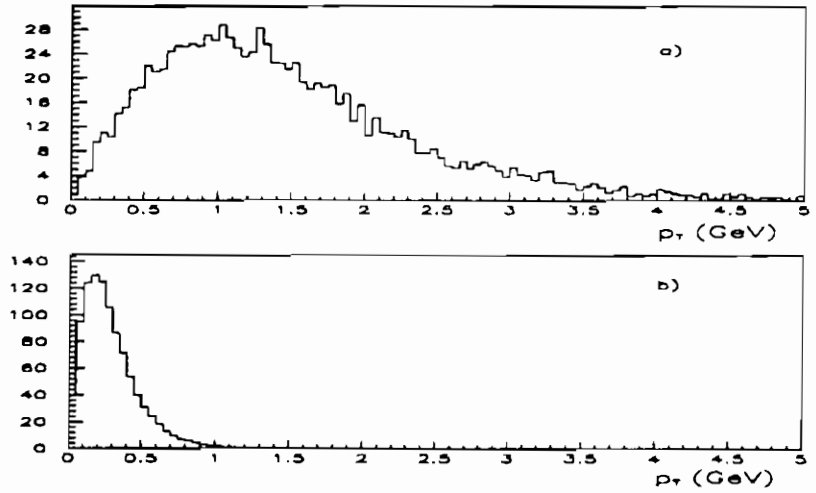

Fig. 5) *a) Muon transverse momentum distribution of* $B \rightarrow \mu X$.
b) Transverse momentum distribution of MB muons

GEANT montecarlo [9] has been then used to track decay muons in the detector and through the iron dump particularly to get a precise simulation of the track bending and of the multiple scattering. After the iron we have simulated the reconstruction of the projected angles, both in the bending and in the non-bending plane as ideally achieved by a set of counters of spatial resolution such to be negligible compared to the mean scattering angle induced by the traversed iron. In this simulation program we are then able to reconstruct the momentum of the muons $p = k/d$, determing the shift amount (see fig.3), the magnet constant $k = 0.3 \int Bdl$ being known. We can further reduce the background exploiting the large difference in p_T distributions. The average $< p_T^\mu >= 1.5$ GeV for B events (Fig.5a) is substantially different from that of the MB muon ($\simeq 0.3$ GeV (Fig.5b)).

Punch through probability has been extimated by RD5 data [see this conference] according to the parametrization given in [10]. It was found to be of the order of $5 \cdot 10^4$ Hz for 10^7 interaction rate.

The expected muon rates, as a function of the p_T cut, are shown in fig.6. Preliminary results from more realistic pCu interactions simulated using FRITIOF [11] show an rate increase of less than a factor 2. In tab. 1 the efficiency for muons from B decay is shown as a function of p_T cut.

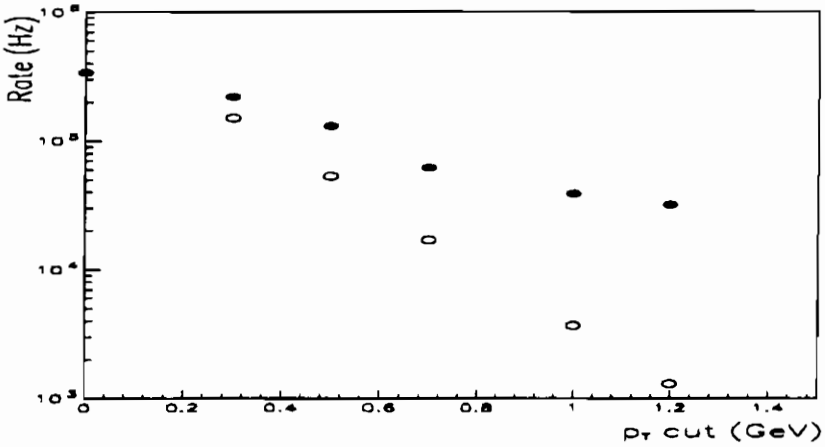

Fig 6) *Muon rates from MB events as a function of p_T^μ cut (dots) for 10^7 interacion rate. The rates corresponding to infinite p_T^μ resolution are also shown (open circles)*

Muon detectors. As any experiment operating at LHC, although with

p_T cut (Gev)	0.	0.3	0.5	0.7	1.0	1.2
Efficiency	.71	.69	.66	.61	.52	.45

Table 1: *Efficiency of prompt $B \rightarrow \mu$ as a function of the $p_T{}^{\mu}$ cut. Geometrical acceptance is accounted for*

an extracted beam, the dominant requirement for any detector partecipating in a trigger logic is the ability to provide the timing with the precision such to separate interactions coming from two consecutive bunches spaced by 25 nsec.

To cover our acceptance,we need an area of at least 4 x 2 m^2 instrumented with fast detectors capable to provide position (and therefore angular) measurements.

These detectors should permit fast track recognition also in multimuon events like those produced in $B \rightarrow J/\psi K_s^0 \rightarrow \mu^+\mu^-\pi^+\pi^- \otimes \overline{B}^0 \rightarrow \mu^- X$. This is one of the most compelling motivations for choosing a pad geometry which allows track reconstruction in space. All the above mentioned requirements lead to the choice of the Resistive Plate Chambers (RPC) [12], already in use in beauty fixed target experiments [13,14].

In order to ensure good tracking efficiency at trigger level at least 4 planes are foreseen distributed over 10 meter lever arm in total. Exact positions will be optimized after extensive MonteCarlo studies. For what concerns their capability of standing high rates of particles, present measurements indicate that fluxes above tens of Hz/cm^2 provoke a deterioration of the detector efficiency [15]. RPC technology is however improving quickly nowadays: recent results [see this conference] indicate that by operating the chambers with an high fraction of freon, the sustainable rate increases up to more than $1kHz/cm^2$ while our extimated maximum rate at the muon detectors level is of about 200 Hz/cm^2.

The pad size is dictated by the request to avoid further spoiling of the angular resolution of muons coming from b decays as measured after the iron filter. The resolution of such angle determination should be better of about a factor two with respect to σ_{MS}, the smearing induced by the Coulomb multiple scattering in the iron. Because of the $1/p$ dependance of σ_{MS} and the momentum-radius correlation the cell size of the muon detectors will

increase going from the center toward the edges.

Physical pad dimension in case of small charge collected cannot be large for capacity/noise reason. For a Freon operated RPC typical pad size will be 2x2 cm^2. Each chamber will be then read by 5000 pads. They will be ORed after signal discrimination in a way to match the angular resolution desired at a certain detector radius.

The total number of electronic pads is therefore about 2000/plane.

Trigger algorithm The muon trigger has the goal to find muon tracks and give an estimate of their four-momenta. A simple processor will accept or reject the event according to the desired (p, p_T) cuts. We stress that double track separation capability is particularly important given the fact that J/Ψ decay into a pair of muons not only is the easiest access to CP violation measurement but possibly is the simplest and unbiassed way to trigger the normal $b\bar{b}$ events. This requisite indicates that tracks have to be reconstructed in space rather than in their projections. We therefore decide to have the chambers read out by pads.

The trigger algorithm is based on the following considerations:

a) good muon tracks come in principle from a point, the event vertex, which is known.

b) the effect of the two magnets is to displace a track parallel to its original trajectory; it is absolutely equivalent to imagine the track coming from a virtual vertex along the x axis (magnetic field is along y).

c) the distance d of the virtual vertex from the real source is the measure of the momentum $(p = k/d)$.

The possible trajectories of a muon (*roads*) are identified a-priori drawing the set of rays which fan out from the vertex and span the entire area of the RPC chambers. These roads are quantized according to the pad segmentation of the chambers. In order to take into account the apparent vertex displacement due to the effect of magnets different vertices have to be taken as possible origin of the rays. The number of test vertices will be determined again by the multiple scattering in iron. It is, in fact, enough to scan the distributed source with steps which are smaller than the error on the backward extrapolation of the track from the iron dump.

An estimate of the number of roads needed is performed multiplying the number of electronics pads in a plane, which is of the order of 2000, times the number of test vertices (about 100), leading to a total of 200k roads. In fig.9 the trigger algorithm is schematically shown.

We believe that a way to realize such a trigger scheme is provided by a so-called Weighting Resistor Matrix system [16]. It is a conceptually very simple trigger processor based on a resistor network which is capable of a very fast pattern recognition.

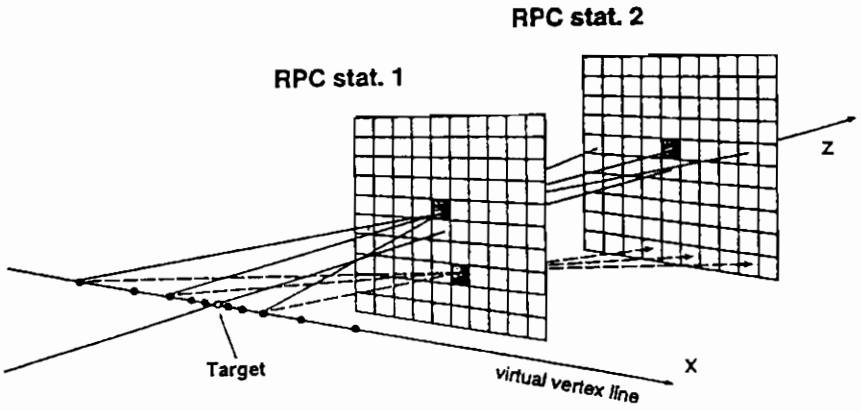

Fig. 7) *A simplified example of the trigger algorithm is sketched in this figure. Stations 1 and 2 are two planes of RPC pad chambers. Some predefined roads, traversing the pads hit in the first station are indicated. The continuous line is the result of the χ^2 algorithm used to determine the physical track.*

In our case every pad is interconnected with all the other pads of the same plane through resistors while a suitable set of *roads* is obtained by joining the pads on different planes as indicated in fig.8.

The resistors network on individual plane allows to weight the signal on each pad according to its distance from the physical trajectory. The weights depend on the value of the resistors. The maximization of the sum of the weights defines, in this scheme, the "best road". It identifies a set of values for the parameters θ,ϕ and d.

Recalling that $p_T = (k/d) \cdot \sin\theta$, it is then possible to define a region in the (d, θ) plane which corresponds to a condition on the p_T, that is our trigger requirement.

Both the roads and the trigger logic are implemented inside a processor

circuit. The response time of such a system is of the order of 30 nsec and does not increase with the complexity of the system. It is in fact determined only by the signal propagation delay i.e. on the dimension of the network and on the parasitic capacitance and inductance of the wiring.

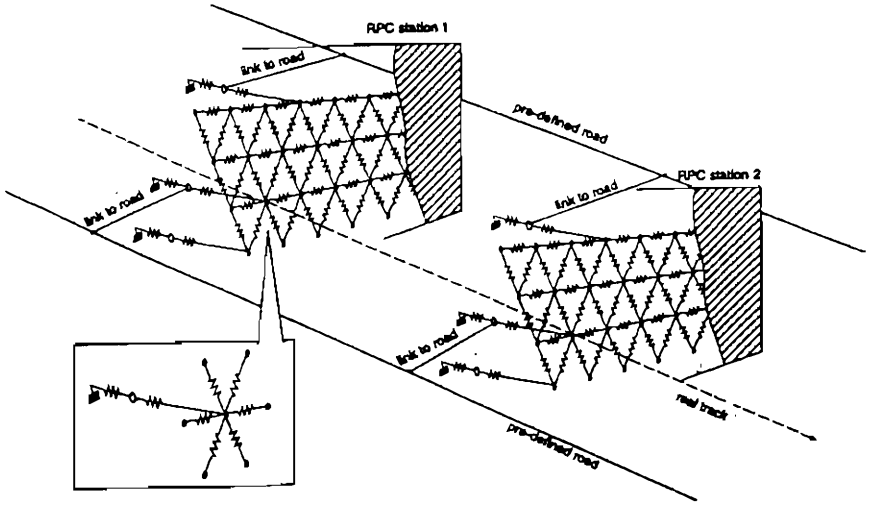

Fig. 8) *An example of the resistive network connecting pads is shown. Each pad is connected with the neighbouring pads in the same plane and with pads of the other planes to form the roads in space.*

4 Conclusion.

We have presented the muon trigger scheme of LHB proposal at LHC. We have shown that rejection factors exceeding 100 can be achieved tracking muons by RPC detector and measuring their momenta with a very fast and versatile processor based on completely passive network of resistors. Improvements to the scheme presented here are foreseen. The link of the muon track measured after the iron filter with its segment detected before should provide better precision in the reconstruction of the kinematics, allowing a sharper and more efficient cut. We believe that a trigger rate of tens of kHz at this level is well inside the demand. Once supplemented by the request of the presence of high p_T hadrons and tracks showing large impact parameters the rate should decrease at a level sustainable by a farm of RISC processors having the goal of filtering the events out to a recording medium.

References

1 G. Carboni, LHB Expression of interest, Proceedings of the General meeting on LHC Physics & Detectors, 409 (1992)

2 C.O. Dib et al.,Phys. Rew. D41 (1990) 1522.

3 "Relativistic Channeling" Nato ASI Series, Vol. 165 (R.A. Carrigan,Jr. and J.A. Ellison Editors, Plenum Press, New York 1986

4 CERN/DRCD 91-25 DRDC/P29 15 July 1991

5 D. Denegri in : proceedings of yhe LHC Workshop (G. Jarlskog and D. Rein Editors, Aachen 1990) Vol I, p. 56

6 B. Cox et al., SFT Expression of interest, SSC-EOI0014.

7 W. Beusch et al., CERN/SPSC 77-10 (1977).

8 T. Sjöstrand, PYTHIA Version 5.6, CERN-TH 6488/92 (1992).

9 GEANT Version 3.15, November 1992. See R. Brun et al., "GEANT 3", CERN-DD/EE/84-1 (Revised), Sept. 1987.

10 F. Lacava, Nota Interna 968, Dipartimento di Fisica dell' Università di Roma "La Sapienza", (1990).

11 Hong Pi, FRITIOF Version 7.0, LU-TP 91-28 (1992).

12 R. Santonico and R. Cardarelli, Nucl. Instr. & Meth., 187 (1981) 377, R. Cardarelli et al., Nucl. Instr. & Meth., A263 (1988) 20.

13 M. Adamovich et al., Nucl. Phys. B27 (1992) 251, C. Bacci et al., Nucl.Instr.& Meth., A234 (1993) 83.

14 T. Alexopoulos et al., Nucl. Phys. B27 (1992).

15 M. Bertino et al., Nucl. Instr. & Meth., A283 (1989) 654.

16 R. Cardarelli et al., Nucl. Instr. & Meth., A324 (1993),253.

MINI:A horizontal muon telescope implemented with Resistive Plate Chambers

G. Iaselli *
Dip. di Fisica e Sez. INFN -Bari

1. Introduction

In this paper it is described a horizontal cosmic rays telescope equipped with Resistive Plate Chambers (RPC). It is located at the Physics Department of the University of Bari, and it has already been used [Ref. 1] to investigate the possibility of building a large vertical telescope able to discriminate upward-going muons produced in high energy cosmic neutrino interactions in the earth from a 10^{11} background of downward-going cosmic rays muons.
Afterwards the apparatus has been upgraded with chambers of higher resistivity plates and their performances have been studied in a long run period. Due to the recent interest in these detectors for the design of a large gamma rays EAS detector [Ref. 2] , particular care has been put to the problem of the best time resolution achievable in experimental conditions. Possible dishomogeneities present in a small scale serial production are also monitored. The details of the apparatus and the results of these recent studies are given below.

2. Description of the telescope

"Mini" is a horizontal cosmic ray muon telescope instrumented with RPC modules [Ref.3]. It is 11.35 m long and it consists of fourteen $4m^2$ chambers interleaved with nine 1m thick concrete absorbers. The layout of the telescope is shown in figure 1, where the Z axis runs in the north-south direction.
Each chamber consists of two 2x1 m^2 RPC modules equipped with 2 m long and 3 cm wide pick-up strips (64 strips in total). In eight chambers the strips are oriented along the X axis direction('horizontal' chambers), while in the other six they are along the Y axis direction ('vertical' chambers). In this way particles crossing the telescope can be seen in two perpendicular projections (X-Z plane and Y-Z plane).
In each chamber the strips are read-out by eight front-end cards placed on both sides (four cards per side). Each card performs the serial read-out via shift- register of 16 strips and gives a FAST-OR signal with an input to output delay of about 10 nsec.
The 64 strips signals coming from only one side of each chamber are shifted along the read-out chain and sent to a CAMAC unit (STAS) which performs a 'zero suppression' and stores only the address of fired strips.

* co-authors: M. Abbrescia(1),M. Ambrosio(3),G.C. Barbarino(3),G. Bressi(4), D. Campana(3), R. Cardarelli(5), F. Guarino(3), M. Iacovacci(3),A. Lanza(4),S. Natali(1), S. Nuzzo(1), G. Osteria(3), P. Pistilli(2),A. Ranieri(1), F. Romano (1), R. Santonico(5)
(1) Dip. di Fisica e Sez. INFN -Bari (2) Dip. di Fisica e Sez INFN -Lecce (3) Dip. di Fisica e Sez. INFN Napoli
(4) Dip. di Fisica e Sez INFN -Pavia (5) Dip. di Fisica e Sez. INFN -Roma Tor Vergata

Moreover on both sides the four FAST-OR signals are OR-ed and sent to a Lecroy TDC operated at 250 ps/channel. Two time measurements per chamber are therefore available , which allow to reconstruct the hit position along the strip.The chamber layout is also shown in figure 1.

The RPC detectors have a resistivity of the phenolic polymers plates of about 10^{12} Ω/cm. The gas mixture usedas been slightly modified , mainly reducing the amount of freon from 4% to 2% , in order to have larger signals then before.The RPC are now operated with a 58% argon , 40% butane and 2% freon mixture.

3. The data sample

Data have been collected over a period of 6 months operation (April 92- September 92) at various high voltages.

A 'penetrating muon' trigger has been set by requiring the coincidence of two extreme chambers and some internal chambers (chambers 4 ,5 ,6 ,7) according to

(Plane 1 **OR** Plane 2) **AND** (Plane 9 **OR** Plane 10) **AND** (Central Chambers)

where 'Central Chambers' indicates a majority 3/4 of the chambers 4,5,6,7.

The trigger circuit is only based on the west side signal of the 'horizontal' chambers. The trigger imposes a minimum energy of 3 Gev to a muon crossing the apparatus; moreover it corresponds to a maximum elevation angle of about 13° on the horizon. About 200.000 events have been taken with the described trigger.

A simple reconstruction program has been implemented to separate muons from showers.On the selected muons a linear three dimensional fit is performed and the direction cosines are computed.

The counting rate of each chamber has been monitored during the data taking to spot possible deterioration at the level of the detector's feateures. The rates have been found costant along the all period of operation.

Figure 2 shows,superimposed on the plot, the counting rates vs the applied high voltage for several chambers. The curves are appreciably clustered to indicate reliability and stability on the medium scale production.

The rate increases slowly with the voltage.A flattening up of the curves is however evident in the range 7-7.5 KV , where the average rate is of about 250 Hertz/m^2.

4. Computation of efficiencies

Since all the chambers with vertical strips are not involved in the trigger logic, a simple counting of the number of times a chamber is fired , normalized to the number of events collected allows the computation of the efficiencies.

For the 'horizontal' chambers a series of dedicated monitoring runs with each chamber in succession out of the trigger would be needed. Since this operation is extremely time consuming , we have therefore developed a method to monitor the efficiency of the chambers, during the normal data taking runs , no matter whether they are consider in the trigger or not.

When a muon goes through the apparatus a definite sequence of chambers is fired. In the following we will assume as "fired" a chamber with TOF (i.e. FAST-OR) information from the west side electronics associated to the particle. The computed efficiency will be therefore related to such hardware configuration.

Moreover , in order to be able to compute the efficiency of the extreme 'horizontal' chambers n°1 and n° 10 , only tracks completely contained in the apparatus are considered.

The probability of a definite sequence of "firing" and not "firing" chambers is $P = \Pi p_i$, where the index i runs over the eight chambers in the trigger and p_i is equal to the efficiency ε_i or to $(1- \varepsilon_i)$ for "firing" and not "firing" chambers respectively.

The probability to enable the trigger can be therefore computed by summing P over all the possible relevant combinations ($P_{Trig} = \Sigma P_i$). We find $P_{Trig} = \alpha \beta \gamma$, where

$$\alpha = (\varepsilon_1 + \varepsilon_2 - \varepsilon_1 \varepsilon_2)$$

$$\beta = (\varepsilon_4\varepsilon_5\varepsilon_6 + \varepsilon_4\varepsilon_5\varepsilon_7 + \varepsilon_4\varepsilon_6\varepsilon_7 + \varepsilon_5\varepsilon_6\varepsilon_7 - 3\varepsilon_4\varepsilon_5\varepsilon_6\varepsilon_7)$$

$$\gamma = (\varepsilon_9 + \varepsilon_{10} - \varepsilon_9\varepsilon_{10})$$

Similarly one can compute the probability P(i) to have the i-th chamber fired by summing P over all the corresponding relevant combinations compatible with the trigger logic and the chosen geometry. For example we find

$$P(1) = \varepsilon_1 \beta \gamma \quad ; \quad P(2) = \varepsilon_2 \beta \gamma$$

Therefore out of N particles crossing the apparatus , only $N_{Trig} = N * P_{Trig}$ will be selected by the trigger . Moreover

$$N(1) = N * P(1) \quad ; \quad N(2) = N * P(2)$$

are the numbers of cases in which respectively chamber 1 and chamber 2 respectively have TOF information associated to the particle. The ratio $N(i)/N_{Trig}$ does not depend on the total (and unknown) number of crossing particles:

$$N(1)/N_{Trig} = \varepsilon_1/\alpha \quad ; \quad N(2)/N_{Trig} = \varepsilon_2/\alpha$$

and the efficiencies can be easily computed as

$$\varepsilon_1 = [\, N(1) + N(2) - N_{Trig} \,]/ N(2) \quad ; \quad \varepsilon_2 = [\, N(1) + N(2) - N_{Trig} \,]/ N(1)$$

The same procedure can be extended to the other chambers. Of course the computation of the efficiency in the central region of the telescope (chamber 4 to 7) will be somehow more elaborate due to the higher number of possible combinations which enter in the algorithm. For example

$$\varepsilon_4 = [N(4)+N(5)+N(6)+N(7)-N_{Trig}]/ [N(5)+N(6)+N(7)-2N_{Trig}]$$

The efficiencies of the remaining central region chambers can be obtained by permuting the indexes in the previous formula.

The above method allows the simultaneous computation of the efficiency of all the chambers , irrelevant of the fact that their signals are used or not for trigger purposes.

Figure 3a shows the efficiencies computed with the described method as function of high voltage , for some chambers. All curves have the same behaviour and reach the

plateau at about 7000 volts. This is reassuring on the reproducibility of stable working conditions on different detectors.
Figure 3b shows the average values of efficiency for all the chambers in the apparatus. The quoted value of 95% includes however some geometrical inefficiency due to both the spacers between the two RPC's plates and the 4 cm dead space in the central region of the chambers , where two RPC modules are connected together.
The corrected average plateau efficiency is of about 98.5%.

5. Calibration and time resolution

In order to achieve the best possible results in the Time Of Flight (TOF) measurement ,a major effort is needed in the calibration of the different read-out channels involved. Although great care has been put in the cabling of the apparatus in order to equalize the time delay of all the channels, additional calibration constants must be taken into account to include read-out electronic delay time and other systematic unknown effects.
For each chamber the absolute average time measurement from east-side end west-side TDC information is taken (T_{Ai}). This allows to develop a calibration procedure independent on the muon impact point on the chamber.
Moreover since we have no external reference time and being our trigger time not fixed , only relative delays between pairs of chambers are meaningful for TOF measurements. In the following we select the chamber 2 as that giving the reference time and we scale consequently each T_{Ai} as $T'_{Ai} = (T_{Ai} - T_{A2})$. The sequence of T'_{Ai} times will then be used in the analysis.
Although only one time measurement is available per chamber , it is however the result of the OR-ing from four different read-out cards. Such cards may have different intrinsic time delays and are connected with separate cables to the OR circuit.
A plane by plane calibration procedure is therefore not sufficient ; we will then try to implement a card by card procedure by computing four calibration constants per plane (one per card pair).
For each chamber 16 different topologies of tracks can be selected according to the read-out cards involved on the chamber itself and on the reference chamber n° 2 .
Event by event the time measurement is corrected to account for the different total length of the tracks in the apparatus. This is done by multiplying the TDC value by the direction cosines of the track , as obtained in the geometrical reconstruction.
For example the distribution of TOF measurements T'_{A5} on the 'horizontal' chamber 5 is given in figure 4a for muons travelling in the south direction. Only the contributions from the two more statistically relevant subsamples of event topologies are considered. The partial distributions are also superimposed on the plot
It is clear that the resolution may be improved by introducing some calibration constants which have the effect of overlapping the sub-sample distributions. In the following we define

- $\langle T'_{Ai} \rangle (i_c, j_r)$ as the average value of TOF measurements for the $N_{Ai}(i_c, j_r)$ muons giving signal on card i_c of chamber i and on card j_r of the reference chamber ($i_c = 1,....,4$, $j_r = 1,....,4$)

- $\langle T'_{Ai} \rangle (j_r)$ as the average value of TOF measurements for the $N(j_r)$ muons crossing any card of chamber i and card j_r of the reference chamber ($j_r = 1,....,4$)
- $\langle T'_{Ai} \rangle$ as the average value of TOF measurements for the muons crossing any card of chamber i and any card of the reference chamber

We first compute the four correction coefficients $C_2(j_r)$ for the reference chamber n° 2 with the formula:

$$C_2(j_r) = \frac{\sum_{i=1,14;\ i\neq 2} \langle T'_{Ai} \rangle (j_r) - \langle T'_{Ai} \rangle) N_{Ai}(j_r)}{\sum_{i=1,14;i\neq 2} N_{Ai}(j_r)} \qquad j_r = 1,4$$

The time measurements of the chamber 2 are therefore calibrated by means of the above coefficients and used to compute the calibration constants $C_i(i_c)$ for all the other chambers , through the formula:

$$C_i(i_c) = \frac{\sum_{j_r=1,4} \langle T'_{Ai} \rangle (i_c, j_r) - \langle T'_{Ai} \rangle) N_{Ai}(i_c, j_r)}{\sum_{j_r=1,4} N_{Ai}(j_r)} \qquad \begin{matrix} i = 1,14;\ i \neq 2 \\ i_c = 1,4 \end{matrix}$$

Since this is only an approximated procedure , it should be used as a iterative algorithm.We find however that one iteration gives already satisfactory results.
The TDC values are finally corrected with the computed coefficients. Figure 8b shows the same TOF distribution as in figure 4a , after the calibration procedure has been implemented. The improvement on the over all resolution is evident; again various contributions due to different event topologies are superimposed.The resulting calibrated TOF distribution is fitted with a gaussian function. The resolution is computed as $\sigma/\sqrt{2}$ of the fitted curve , which is also superimposed in figure.
The average resolution for all the chambers is plotted in figure 5a versus the high voltage. Also the less conservative value computed by means of the FWHM of the distribution is given (FWHM/2.36*$\sqrt{2}$) .
It can be seen that with an operating voltage of 8.1 KV , the resolution is below 1,3 nanosecond. In figure 5b the resolution (computed as $\sigma/\sqrt{2}$) for few chambers is superimposed on the same plot. At 8.1 KV the fluctuation around the average value is indeed very small.

References

[1] F. D'Aquino at all , N.I.M. A324(1993) 330
[2] P. Pistilli , Nuclear Physics B (Proc. Suppl.) 14B(1990)69
ARGO Collaboration , Letter of Intent to INFN
[3] R. Santonico , R. Cardarelli , N.I.M. A187(1981) 377
R. Cardarelli et al. , N.I.M. A263(1988)20-25

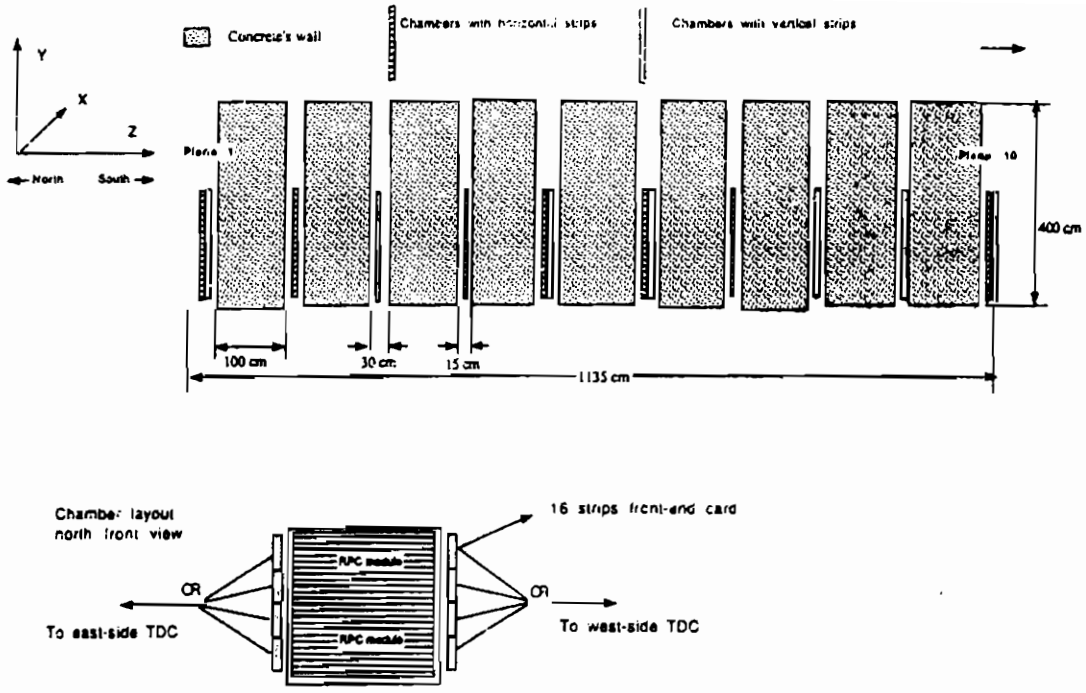

Figure 1 Layout of the apparatus MINI. The layout of a single chamber is also shown.

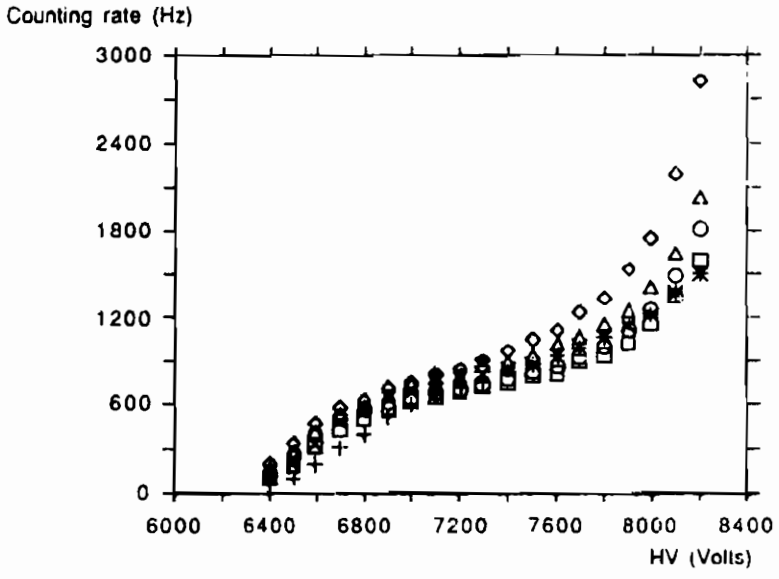

Figure 2 *Fig. 2* : counting rates versus high voltage for different $4m^2$ chambers.

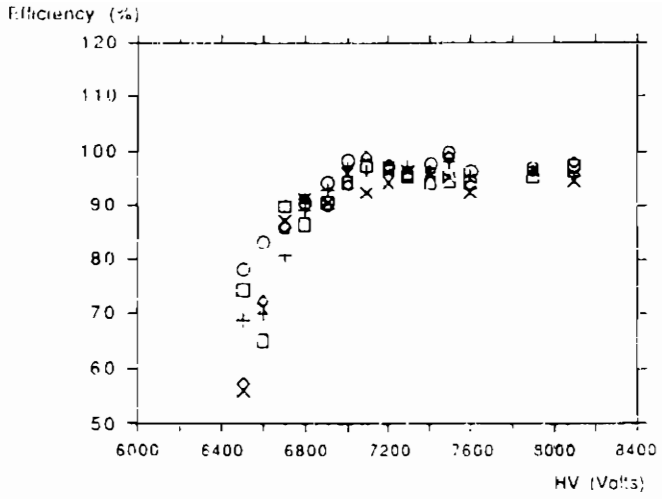

Fig 3a : efficiency versus high voltage for different chambers.

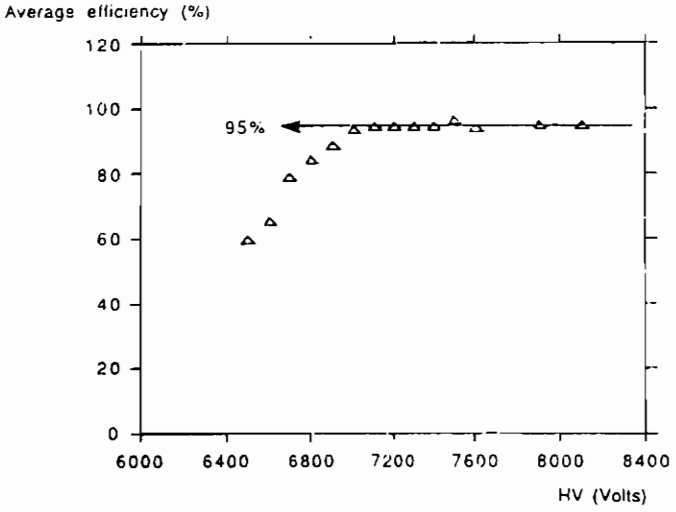

Fig. 3b : average efficiency of all the chambers in the apparatus, versus the high voltage.

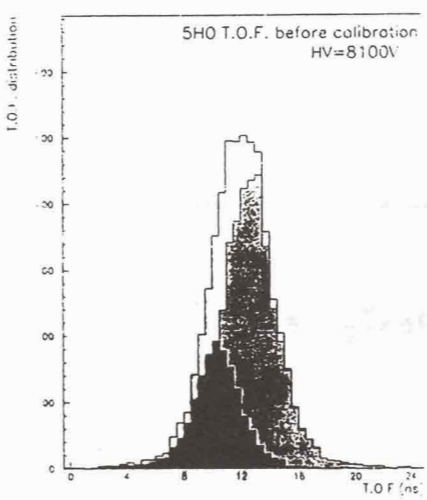

Fig. 4a : time of flight distribution , as defined in the text , for the 'horizontal' chamber n° 5 at 8.1 KV , before the calibration procedure has been applied. The partial distributions for the two considered subsamples are also plotted.

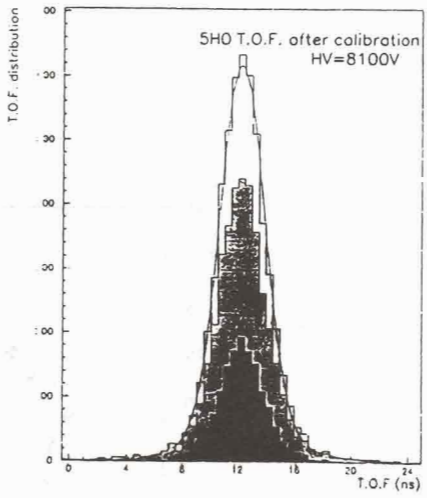

Fig. 4b : same as before , after the calibration procedure.

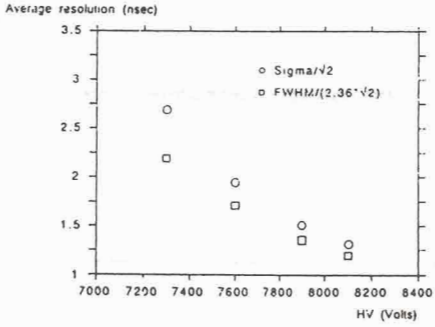

Fig. 5a : average time resolution of the chambers in the apparatus versus the high voltage. The resolution is computed both as $\sigma/\sqrt{2}$ of the fitted gaussian and as FWHM/2.36•$\sqrt{2}$ of the distribution itself.

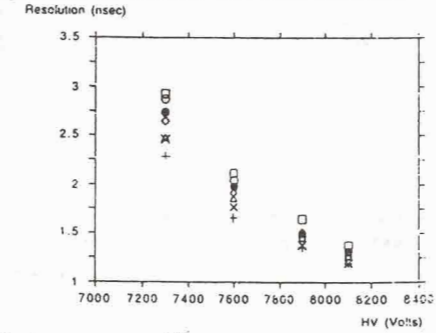

Fig. 5b : time resolution ($\sigma/\sqrt{2}$) versus the high voltage for some of the chambers.

T&T: A New Design For A Front-End Time Digitizer Electronics

T&T Collaboration:
M. Ambrosio, G.C. Barbarino, A. Lauro, G. Osteria
INFN and Dipartimento di Fisica dell'Universita' di Napoli.
G. Agnetta, O. Catalano, L. Scarsi
IFCAI - Istituto di Fisica Cosmica e Applicazioni all'Informatica, CNR, Palermo and INFN, Sezione di Napoli.
A. Lanza, G. Liguori, P. Torre
INFN and Dipartimento di Fisica dell'Universita' di Pavia.

Abstract

A front-end readout electronics of new design is described. This electronics can operate in Cosmic Ray and E.A.S as well as in accelerator experiments. The T&T (Tracking and Timing) electronics has been planned to cover large area detectors avoiding the necessity of tedious and time consuming cable calibrations. It is characterized by a 2 *ns* time resolution, multihits recording capability, no ambiguity in event-pulse reconstruction, daisy-chain interconnection, low power consumption and low cost.

Introduction

E.A.S. arrays for high energy cosmic ray physics are usually builded with scintillator units, few square meters each, distributed over a large area to sample the front of the showers. The scintillators measure the time profile and the front particle density distribution. By time measurements it is possible to deduce the direction of the shower axis, while by density measurements it is possible to individuate the core position. This *standard* method works well, but gives an information integrated over the area of the scintillator unit, measuring only the time of the first particle arriving in each detector: it is not practicable therefore to measure the front time spread which depends from the core distance, the nature and the energy of the incoming particles. Measurements of the arrival time of the individual particles belonging to the shower front allow a better reconstruction of the shower axis direction and give useful information

on the shower structure. The T&T front-end electronics [1] has been designed to read signals from RPCs (Resistive Plate Counters) detectors [2], equipped with pads or strips, allowing their use in high energy cosmic ray physics. Using RPCs equipped with 12x12 cm^2 pads, the shower front can be sampled with a great granularity [3]. The T&T electronics recognize the fired pads and give precise measurements on the arrival time of all the detected particles. The RPCs, arranged with tracking devices, allow time correlations between the various families of particles [4], providing a definite improvement in accelerator as well as in non accelerator physics experiments.

General description

The T&T electronics is able to measure the arrival time at the detector for each particle of the shower front with a resolution time of 2 *ns*. Two consecutive signals in the same channel can be recognized if their relative delay is > 2 *ns*. A wide memory stores information up to 64 μs, allowing to detect particles delayed respect to the first arriving one. Within the memory depth the time values are measured in comparison with the trigger time . The electronics allow the automatic calibration of each channel and the zero suppression of not fired channels. The memory readout is performed via a parallel BUS connected to a computer interface or to a VME readout system, selecting by computer the number of words to be read. Up to 256 channels can be connected to the bus. The threshold of the input discriminators, as well as the duration of the fast OR of the input channels, can be selected by the computer. Finally, a digital pattern of all channels is available for acquisition.

Logical scheme

Fig. 1 shows the arrangement of the readout system including processor and Data Recording Boards (DRBs). The front-end logic unit, located in the motherboard shown in fig. 2, consists of 16 input boards, a trigger board, a fast OR board and a control electronics board. A parallel bus, managed by a processor or by a computer to allow the readout of the stored information, connects in cascade several motherboards to build a chain up to 16 DRBs.

Input board

As shown in fig. 3, each signal is discriminated and shaped by a fast and retriggerable discriminator. The threshold of the discriminators and

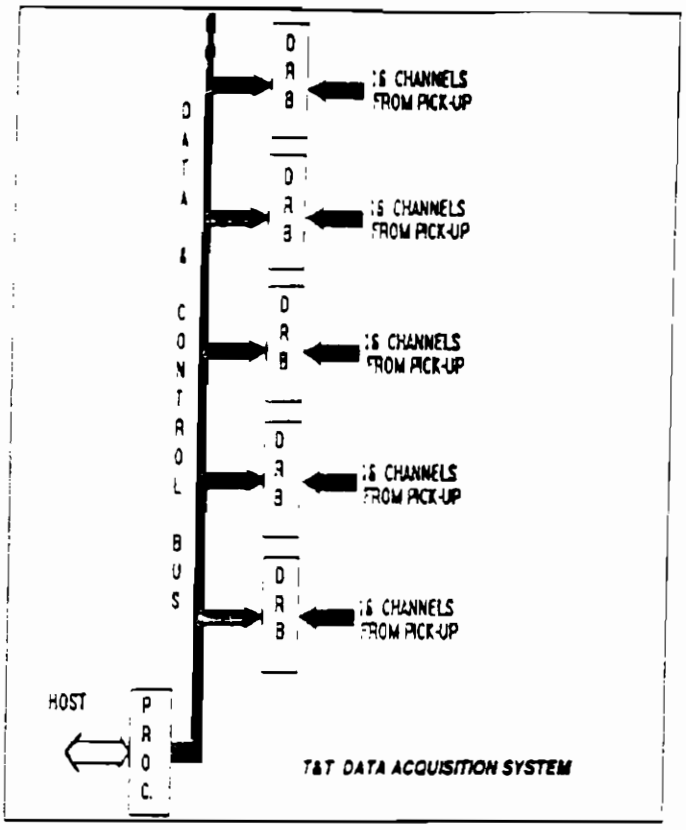

Fig. 1 - Arrangement of the T&T readout system

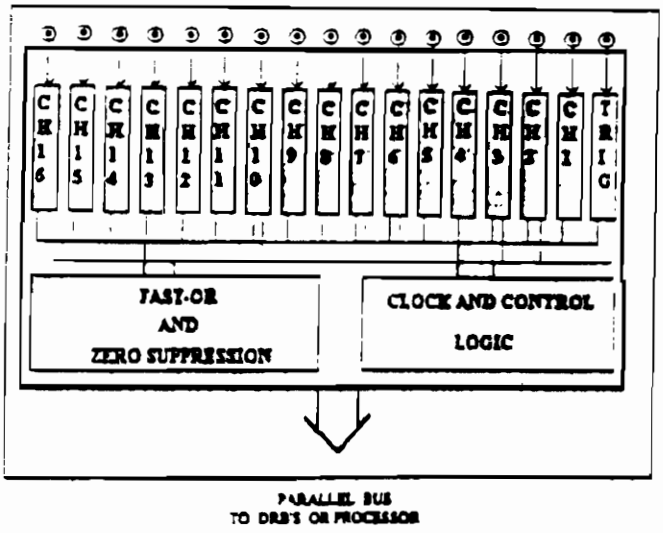

Fig. 2 - Mother board configuration.

the width of the shaped signals are programmed by the processor. The input board is based on the property of the integrated passive delay lines to transmit a signal with a fixed delay. Three delay lines connected in cascade, 2 *ns* per tap, 10 taps per delay line, allow a total delay of 60 *ns* from the time of the input signal.

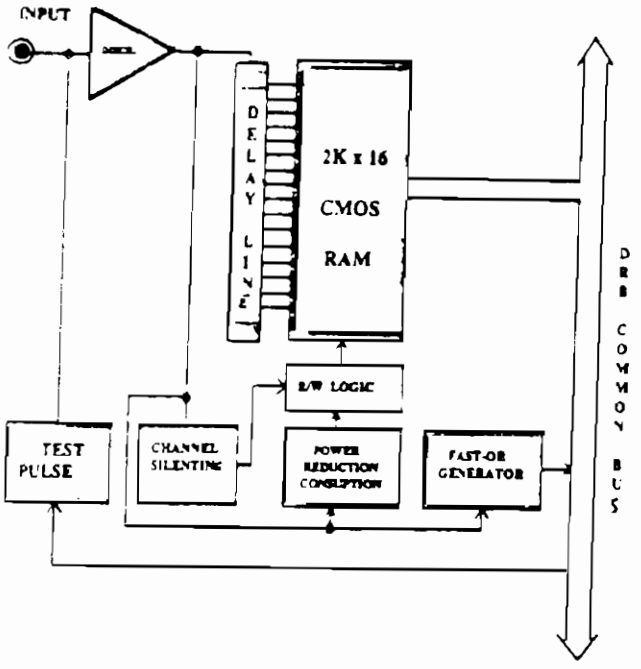

Fig. 3 - Logical layout of the input board

An incoming signal crossing the lines is seen as a cluster of fired taps wide as the signal duration. Fig. 4 shows the sequences of input signal through the delay lines. Every 32 *ns* a fast latch fixes the image of the last 16 taps of the lines and writes this image into a cyclic memory. The latching of the taps occurs in free running mode, and a word is written into the memory every 32 *ns* although no signal is in input, in the same way as a stroboscope fixes an image on a film. To minimize power requirements the memories stand by: the arrival of a signal determines the power up to the corresponding memory channel. In this way the power requirement of each card is less then 800 μA for a rate of 100 *Hz* per channel. To avoid a continuous writing of a noised channel, a silencing device is present on

each channel. This is formed by an integrator loading a capacitor that inhibits the writing into the memory if signals arrive on the same channel with very high frequency. As the integrator unloads, the writing is again enabled.

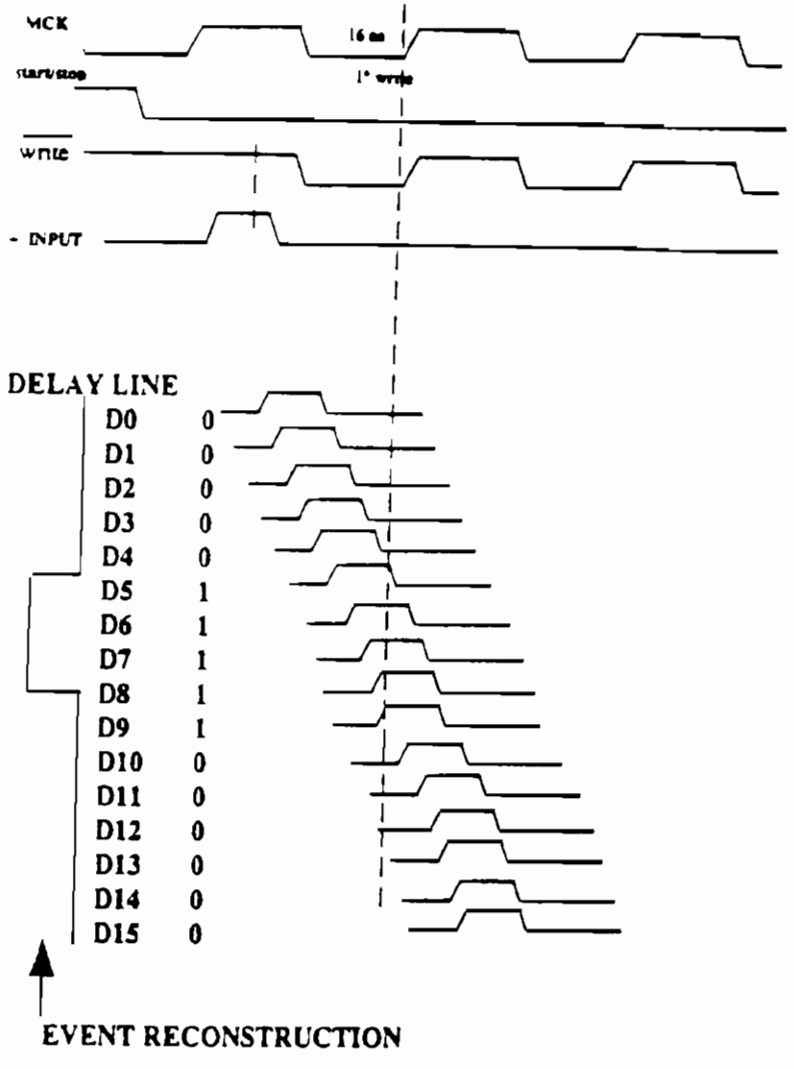

Fig. 4 - Sequences of input signal trough the delay lines

Reading the memory, it is possible to reconstruct the history of the input signals, measuring their duration and their relative arrival time, with the resolution of the delay lines. If the trigger signal is also written into the memory in the same way, it is possible to measure the arrival time of each signal generating the trigger respect to the trigger itself. When

a trigger arrives, the process is stopped waiting for the memory readout. The relative time between the trigger and any arrived and registered signal is easily measured considering that a memory word corresponds to 32 *ns*, and each bit of a word corresponds to 2 *ns*.

A test pulse device allows to the processor to automatically test each board. The test command delivers a signal of a given shape to the selected input boards: the memories must record this signal at the correct time and with the correct shape.

Trigger board

The trigger board is like an input board. The only difference is that it is used to register the trigger signal. The comparison between the memory location of the trigger and the memory location of the input signals on the same motherboard permits to reconstruct the time differences between input and trigger signals. The trigger arrives to each DRB at different times due to the different length of connecting cables and to the electronic spread. In order to automatically calibrate the system, the processor sends the trigger signal to one of the DRB connected in daisy-chain, and simultaneously to a Time to Digital Converter (TDC), an input board used as a usual TDC. Each motherboard echoes the trigger signal to the processor which registers the echo and measures the time needed to the trigger signal to reach the motherboard and go back to the processor. The results are stored for the use during data acquisition and off-line analysis.

Fast OR and Zero suppression board

The fast OR board collects the signals from all the input boards of a DRB, reshapes and sends them to a 16 bit pattern register generating a fast OR of 16 channels. The width of the output signals is defined by the processor and it ranges from 480 *ns* to 20 μs. By the pattern, the processor can immediately recognize the fired channels and can limit the readout only to them, operating the zero suppression. It is also allowed the spatial reconstruction of the event.

Clock and control logic board

The control logic board manages all the cards of a DRB. A 31.2 *MHz* clock synchronizes the memories in writing as well as in the reading process. Only the memories interested by the event are read, distinguished by a fired pattern in the fast OR board. The trigger can arrive a long time

after the event, and with a not fixed delay, but only the memory words around the event are read. The time between the event and the trigger is measured via the fast OR delay time. This permits to reconstruct the event position in the memories of a DRB and to read only few words around this position. The number of words to be read is programmable by the processor. The memories are read in a *bustrophedes* way as shown in Fig. 5. In this way automatic zero suppression, data compression and speedy reading is allowed.

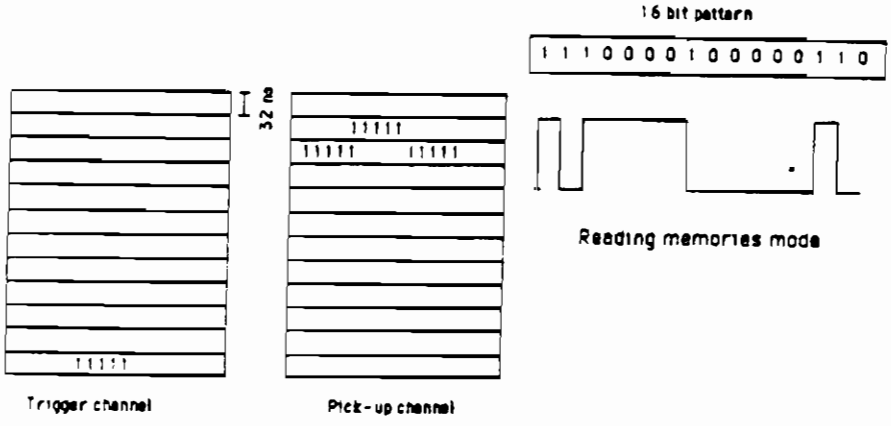

Fig. 5 - Readout scheme of the T&T memories

Present hardware

So far the system under test is composed by a Personal Computer (PC) used as processor, a DRB equipped with only one trigger channel as TDC and 3 DRBs, each one arranged with 16 input channels, 1 trigger channel, 1 fast OR and 1 control logic. The PC controls the DRB's chain, sets the input threshold of all channels, sets the duration of the shaped signals and of the fast OR signals, calibrates the trigger channels and performs the data acquisition.

Test and results

The tests have been focused to measure the linearity of the system and its capability to register the signal duration. Fig. 6 shows the response to delayed signals by using a pulse generator. The linearity of the entire system including discriminators, passive delay lines and memory is promising. The standard deviation for delayed signals shows a good agreement with the expectation, finding a resolution time better than 1.4 *ns*. The same for the response to the increasing signal width, as shown in Fig. 7.

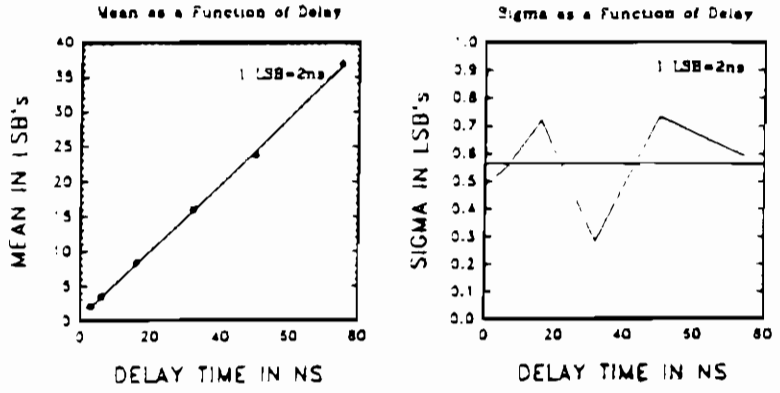

Fig. 6 - Response to delayed signals

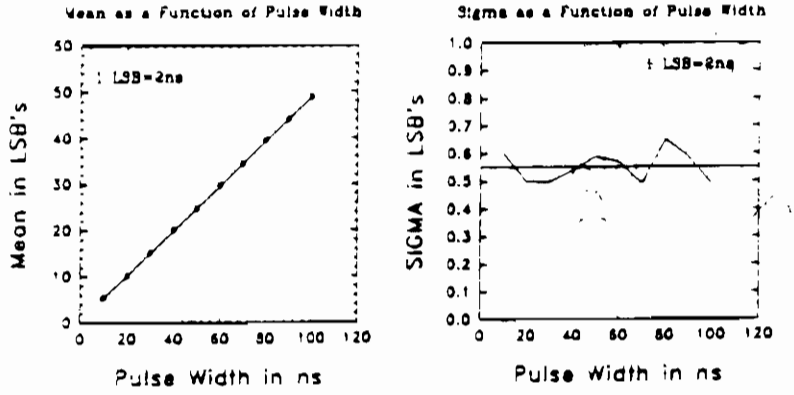

Fig. 7 - Response to increasing signal width

Conclusions

The described system allows to measure the arrival time of signals directly on the front-end, with a precision of 2 *ns*. Autocalibration, autotest, zero suppression, power reducing and noise silencing devices are also allowed. The tests enhance a good linearity on the time response of the system, and a good linearity for measuring the shape of incoming signals. We stress that this system avoids the use of long cables to park the signals, waiting for trigger building, and also the necessity of accurate calibrations of cables and electronics. For our purposes we developed a 2 *ns* time resolution system using 2 *ns/tap* passive delay lines. It is possible to reach 1 *ns* time resolution simply by using 1 *ns/tap* passive delay lines and latching every 16 *ns* by changing the clock frequency. The engineered system is now produced by the CAEN company, and it is ready for mass production.

Acknowledgment

We are grateful to Prof. M. Bonori of the University of Rome who first suggested the possibility to measure time by continuously writing a cyclic memory. We also are grateful to the CAEN Company for its effort to realize a engineered system and for its participation to discussions and to development of the described electronics.

References

[1] M. Ambrosio et al., Nucl. Instr. and Meth. A315, 415 (1992).

[2] R. Santonico and R. Cardarelli, Nucl. Instr. and Meth. A187, 337 (1981).

[3] ARGO proposal to INFN 1992.

[4] COVER_PLASTEX proposal to INFN 1993.

Atmospheric and Accelerator Neutrino Physics with RPC's in the Soudan 2 Cavern.

D. J. A. Cockerill
Rutherford Appleton Laboratory,
Chilton, Didcot,
Oxon, OX11 0QX, UK

1 Introduction

Resistive plate chambers have certain properties which could make them useful as detectors for atmospheric and accelerator neutrino physics. In this paper we outline how RPC's might be used in the Soudan 2 cavern to upgrade the present 980 ton Soudan 2 detector [1] and how they might be used to provide the detecting medium for an 8 kton detector, in the same cavern, for neutrinos produced from the Main Injector under construction at Fermilab, 750 km away. The Soudan 2 cavern is located 2090 mwe (713 m) beneath Soudan, Minnesota, USA.

2 Physics - neutrino oscillations or proton decay ?

Atmospheric neutrinos are produced as a result of cosmic ray particles interacting with nuclei in the upper atmosphere, ~10 km from the earth's surface. These interactions produce pions which subsequently decay as follows :

$$\pi \longrightarrow \mu\overline{\nu_\mu} \tag{1}$$

$$\mu \longrightarrow e\overline{\nu_e}\nu_\mu \tag{2}$$

Thus two muon neutrinos are produced for every electron neutrino. The neutrino energy spectrum peaks at 300 - 400 MeV and tails of by ~1500 MeV.

About 100 - 150 atmospheric neutrino interactions are detected per kiloton year in the large underground water Cerenkov detectors and in the large ionisation detectors built initially to search for proton decay. The type of neutrino which interacts in the detector can be asertained by examining the Cerenkov ring profile in the water Cerenkov detectors or by looking at the event topology in the ionisation detectors. Fig. 1 shows a characteristic electron shower produced from a ν_e interaction in the Soudan 2 detector. In contrast a ν_μ interaction would have

produced a muon track which is easily distinquished from an electron shower in the Soudan 2 detector for momenta above 300 MeV/c.

The 2:1 ratio for the number of ν_μ and ν_e produced by pion decay implies that twice as many contained muon tracks should be seen in the underground detectors as electron showers, after correcting for detector acceptance. In fact the observed ratio of contained μ and e events is about 0.6 of the value expected as measured by two water Cerenkov detectors [2] [3]. The results from two ionisation detectors [4] [5] and from Soudan 2 [6] are consistent with this finding, although these results have larger statistical errors (see Table 1) [7]. One possible explanation for the discrepancy is in terms of neutrino oscillations, $\nu_\mu \rightarrow \nu_\tau$. Thus the ν_μ interaction rate in the detectors will be diminished. This provides a possible explanation for the observed shortage of muons.

Fig 2 shows the momentum distribution for electrons and muons seen in the Kamiokande detector [2]. The heavy line shows the Monte Carlo expectation of Barr, Gaisser and Stanev (BGS) [8] for electrons and muons for the case of no oscillations. The muon data are clearly well below the Monte Carlo expectations. The narrow line shows the best fit using the BGS Monte Carlo with neutrino oscillations.

The probabilty of oscillation between two neutrinos of different mass is given by

$$P_{\nu_1 \rightarrow \nu_2} = sin^2(2\theta) sin^2(1.27 \cdot \Delta m^2 \frac{L}{E_\nu}) \qquad (3)$$

where θ is a mixing angle, Δm^2 (in eV^2) is the difference of the squared masses of the two neutrinos, L (in km) is the distance travelled from production and E_ν (in GeV) is the energy of the neutrino.

This probability can be tested by examing the rates for neutrino interactions in underground detectors where L is the same but E_ν is different. Such a test has been carried out by the IMB collaboration [9]. The group studied upward going muon tracks produced by ν_μ interactions in the rock surrounding their detector. Some of these muon tracks stopped in their detector, others passed through. The stopping muons come from ν_μ with an median energy of $\sim$6 GeV whereas the through going muons come from ν_μ with a median energy of $\sim$100 GeV. Each neutrino set is produced over the same region of the upper atmosphere and therefore has the same average distance, from production, to the rock surrounding the detector (in some cases the distance from production can be up to 13,000 km, i.e. for neutrinos traversing the diameter of the earth).

The IMB group found that the stopping fraction of upward going muons in their detector was 0.16$\pm$0.019. Various Monte Carlo models predicted this fraction to be between 0.154 and 0.163 for the case of no oscillations. Thus the IMB group find no evidence for oscillations with this analysis.

The conflicting evidence for neutrino oscillations has led part of the Soudan 2 group to question whether the contained event data comes entirely from atmospheric neutrino interactions or whether there is evidence for proton decay [10]. They argue that if they use the Monte Carlo flux generated by Bugaev and Naumov (BN) [11], instead of the BGS flux, then the flux for muon tracks seen in the Kamiokande detector, from ν_μ interactions, is described quite well. This is shown in fig. 3 in the top box, where the dashed line shows the Monte Carlo expectation (the dotted line indicates the detector efficiency) [12].

If the atmospheric neutrino flux rates are normalised to the contained muon data in Kamiokande, as the BN Monte Carlo suggests they should be, then the expected electron flux in their detector is given by the open triangles in the middle box of fig. 3. The filled circles indicate the data for the observed electron showers in Kamiokande. The observed electron flux is clearly in excess of the expected rate. The Tufts group [10] interpret this excess as evidence for proton decay. The bottom box in fig 3 shows the residual data after the expected electron spectrum has been subtracted from the observed electron spectrum. Shown on the plot is a dotted line for the expected shape of the spectrum for positrons from proton$\rightarrow e^+\nu\nu$. The lifetime over branching ratio thus implied for proton decay is $(\tau/B) = 3.7^{+1.7}_{-1.0} \cdot 10^{31}$ years.

3 Proposed Experiments

In order to investigate the neutrino oscillation question proposals have been made to Fermilab [13] to provide a neutrino beam from the Main Injector which is currently under construction. One of these proposals [14] requests that a neutrino beam be aimed at the Soudan 2 cavern 750 km away. Neutrino physics on a long baseline could then be carried out by the existing Soudan 2 detector. In order to extend the physics reach a new 8 kton detector could be built in the same cavern, adjacent to Soudan 2. This detector would provide higher statistics and thus greater physics coverage than Soudan 2 could provide alone. The average neutrino energy from this beam would be ~10 GeV. About 430 neutral current and charged current events would be expected per year per kiloton, for a detector in the Soudan 2 cavern, for 2.10^{20} 120 GeV protons on target at Fermilab per year.

In the near term a measurement could be made on upward going stopping and throughgoing muons in the Soudan 2 detector in order to check the IMB result discussed above. This would require detectors with fast timing to ascertain the muon direction for the through going muons. Unfortunately the long drift times in the Soudan 2 detector (of up to 80 μsec) preclude it from determining the muon direction for through going muons.

4 The possible roles for Resistive Plate Chambers

In order to construct an 8 kiloton detector in the Soudan 2 cavern the space occupied by chambers must be kept to a minimum. One proposal is for the detector to be made up of consecutive walls of 2 cm thick steel each followed by a plane of chambers occupying a space of about 1 cm as shown in fig. 4. This is the optimum granularity, obtained from Monte Carlo simulations, for studying neutrino oscillations with the Fermilab beam. Resistive plate chambers fit conveniently into this scheme. The basic structure of the chamber is only 6 mm thick. Monte Carlo simulations suggest a read-out strip width of 2 cm from these chambers would be sufficient in order to distinquish tracks from neutral current and charged current interactions. The strips might be ganged together to provide 8 m and 6 m long X and Y strips read out from each plane.

Each 2 cm thick steel wall would be 6 m high and 8 m across and would weigh 8 tons. Thus 1000 walls of steel and 1000 planes of chambers would be required to achieve an instrumented detector mass of 8 kilotons. Each plane of chambers would be made up from 24 2 m^2 resistive plate chambers. Thus 24,000 RPC's would be needed in total. About 400,000 X and Y strips would be read out. Although the good timing resolution of the RPC's has not been required it may be useful for the trigger. The trigger will be required to work locally over 3 or 4 successive walls anywhere within the 1000 wall detector. The timing resolution of the chambers could be used to reduce the accidental trigger rate.

Such a project, involving so many RPC's, would be a major undertaking. However, in the near term, RPC's could be used in order to measure the upward going muon rates discussed in the two previous sections. It has been proposed that two arrays, each consisting of 60 RPC's, be built initially [15]. These arrays would be placed above and below the existing Soudan 2 detector as shown in fig. 5. The direction of muons passing through the two arrays would be determined by time of flight, using the fast timing resolution of the RPC's. The arrays would be 6 m or more apart, vertically.

Downgoing muons would trigger the top array first. Upward going muons would trigger the bottom array first. By using only one of the arrays for a start time, then at least 40 nsec will exist between the recorded stop times for the two muon sets. The 2 nsec timing resolution of an RPC is easily adequate to correctly assign the through going muon direction with this arrangement. Stopping muons are seen directly by the Soudan 2 detector. The acceptance for upward going muons could be increased eventually by covering all sides of the Soudan 2 detector with RPC's, as is also illustrated in fig. 5.

5 Research needed on RPC's

The prime area of research needed for RPC's is that of finding a non flammable gas mixture with which to operate the chambers in the Soudan 2 cavern. The results presented at this RPC workshop, obtained from chambers operating with a pure freon gas, may be of considerable importance for employing RPC's in the Soudan 2 cavern.

We require that the singles counting rates from the RPC's be as low as possible in order to reduce background hits and accidental triggers. We would like to investigate the sources of background counting rates such as the dischage problems around the RPC spacers. Other sources of background counting rates are known and have been measured in the Soudan 2 cavern. One of these is due to gamma rays emitted from the rock in the Soudan 2 cavern. These gammas can create Compton electrons in the detectors which have enough energy to enter the chamber gas gap. In the Soudan 2 cavern these electrons contribute a counting rate of 80 Hz per m^2 of exposed detector area to the gas gap.

6 Conclusions

Resistive plate chambers have properties which make them attractive as possible detectors for atmospheric and accelerator neutrino physics. The need for a new generation of neutrino detectors is amply demonstrated by the controversy over whether neutrinos oscillate or whether protons decay or whether both or neither of these phenomena occur. We would like to thank Professor Santonico for providing an RPC for the Rutherford Appleton Laboratory in the UK, in order to enable research and developement to be carried out in preparation for possible future applications in the Soudan 2 cavern.

References

[1] J. Thron et al., Nucl. Instr. and Meth. 283 (1989) 642.
D. Cockerill, The Soudan 2 Detector, 4th Topical Seminar on Experimental Apparatus for High Energy Physics and Astrophysics, San Miniato, Italy, May 28 - June 1, 1990.

[2] K.S. Hirata et al Phys. Lett. B280, 146 (1992).

[3] D. Casper et al. Phys. Rev. Lett. 66, 2561 (1991);
S.T. Dye, Proc. Workshop on Long Baseline Neutrino Oscillations, Fermilab (Nov. 91)

[4] O. Perdereau et al Proc. of Tests of Fundamental Conservation Laws in Physics, Moriond (1991).

[5] M. Aglietta et al Europhys. Lett. 8, 611 (1989).

[6] D.M. Roback, Thesis "Measurement of the Atmospheric Neutrino Flavor Ratio with the Soudan 2 Detector", University of Minnesota (1992)
M. Goodman et al, Interactions of Atmospheric ν_μ and ν_e observed in Soudan 2, submitted to the Proceedings of the Division of Particles and Fields, American Physical Society Conference, Nov 1992, Fermilab.

[7] Taken from D.H. Perkins, The Atmospheric Neutrino Problem: A Critique, OUNP-93-03.

[8] G.D. Barr, T.K. Gaisser and T. Stanev, Phys. Rev. D 39 (1989) 3532.

[9] R. Becker-Szendy et al., Phys. Rev. Lett. 69, 1010 (1992).

[10] W.A. Mann, T. Kafka, W. Leeson, The atmospheric flux ν_μ/ν_e anomaly as manifestation of proton decay $\rightarrow e^+\nu\nu$, Phys. Lett. B291 (1992) 200.

[11] E.V. Bugaev and V.A. Naumov, Phys. Lett. B232 (1989) 391.

[12] Authors and title as for [10], Meeting of Particles and Fields of the American Physical Society, Fermilab, 10 - 14 Nov 1992.

[13] Proc. of the Workshop on Long-Baseline Neutrino Osillations, Fermilab, 17-20 Nov, 1991.

[14] Proposal for a Long-Baseline Neutrino Oscillation Experiment using the Soudan 2 Neutrino Detector, Fermilab P822.

[15] D.J.A. Cockerill and P.J.Litchfield, A Soudan 2 upgrade with resistive plate chambers, Internal Soudan 2 note, PDK-543.

Table 1: Contained event μ to e ratios

Experiment	Kton yr	$(\mu/e)_{obs}/(\mu/e)_{calc}$
Kamioka[2]	6.1	$0.60 \pm .07$
IMB[3]	7.7	$0.54 \pm .07$
Frejus[4]	1.56	0.87 ± 0.21
Nusex[5]	0.40	0.99 ± 0.40
Soudan 2[6]	0.50	0.55 ± 0.27

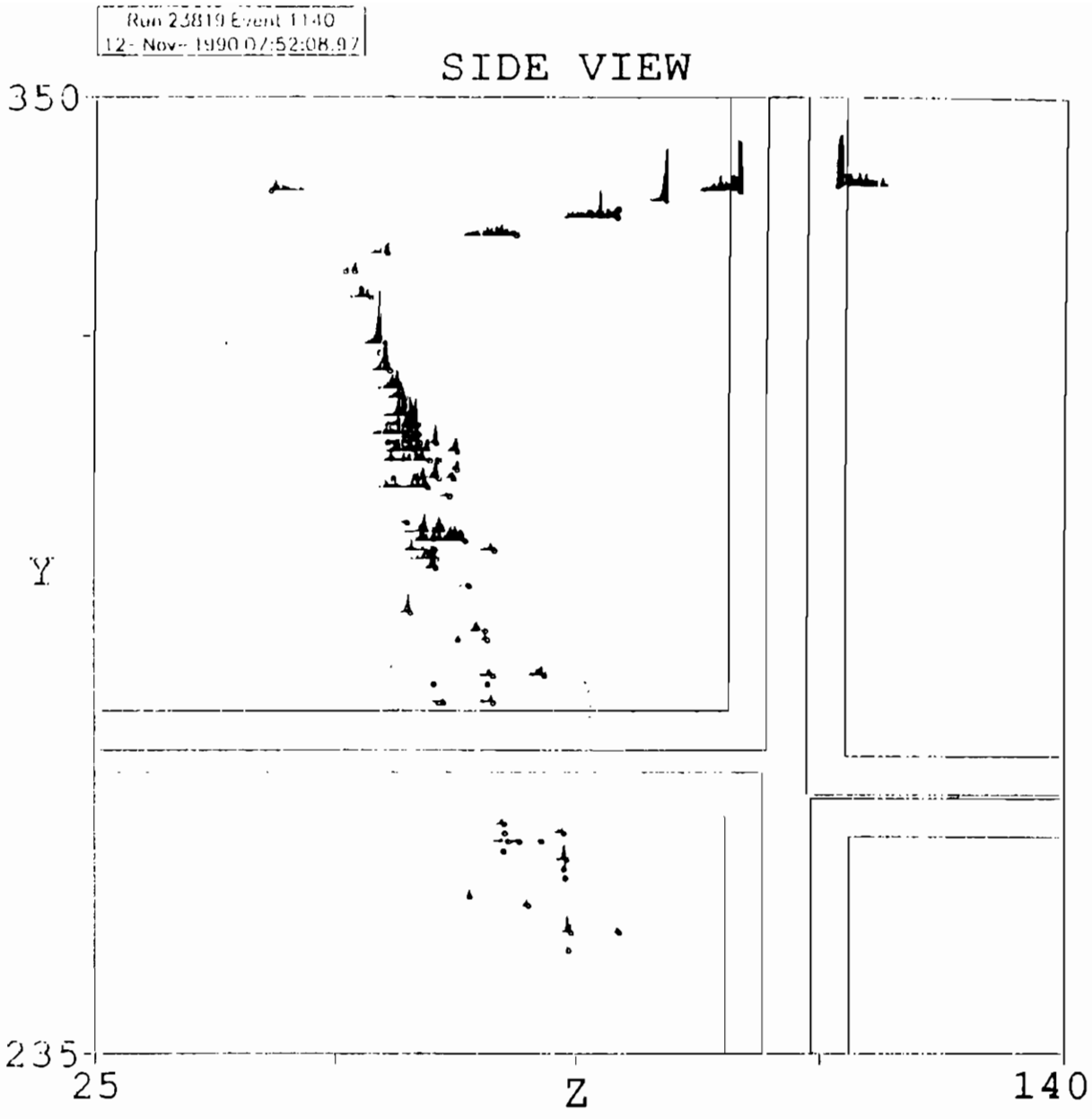

Fig. 1. A characteristic electron shower from a contained event in the Soudan 2 detector. The shower (coming from the top down) has an energy of 1635 MeV. A recoil track can also be seen going from top left to right.

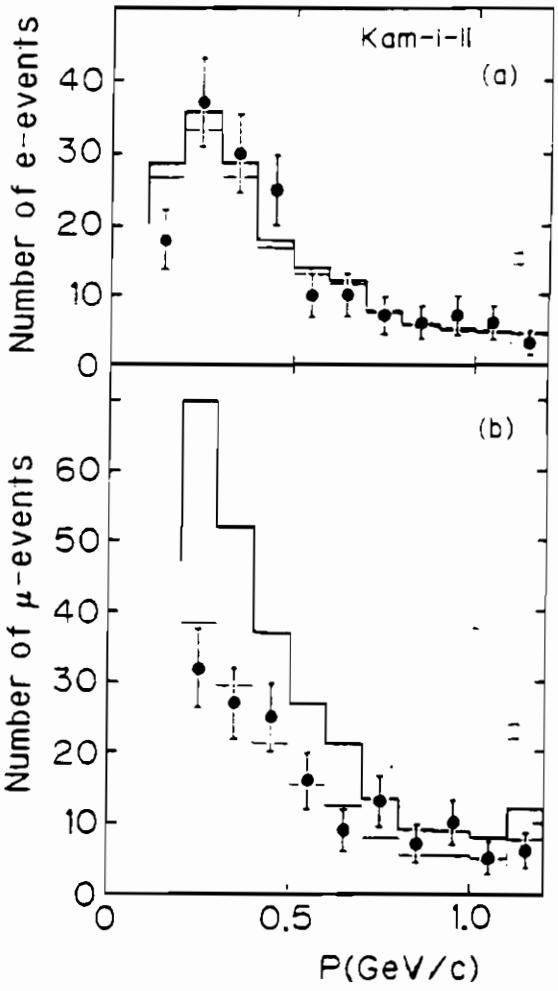

Fig. 2. The momentum spectra of e- and μ-events in the Kamiokande water Cerenkov detector together with the BGS Monte Carlo predictions.

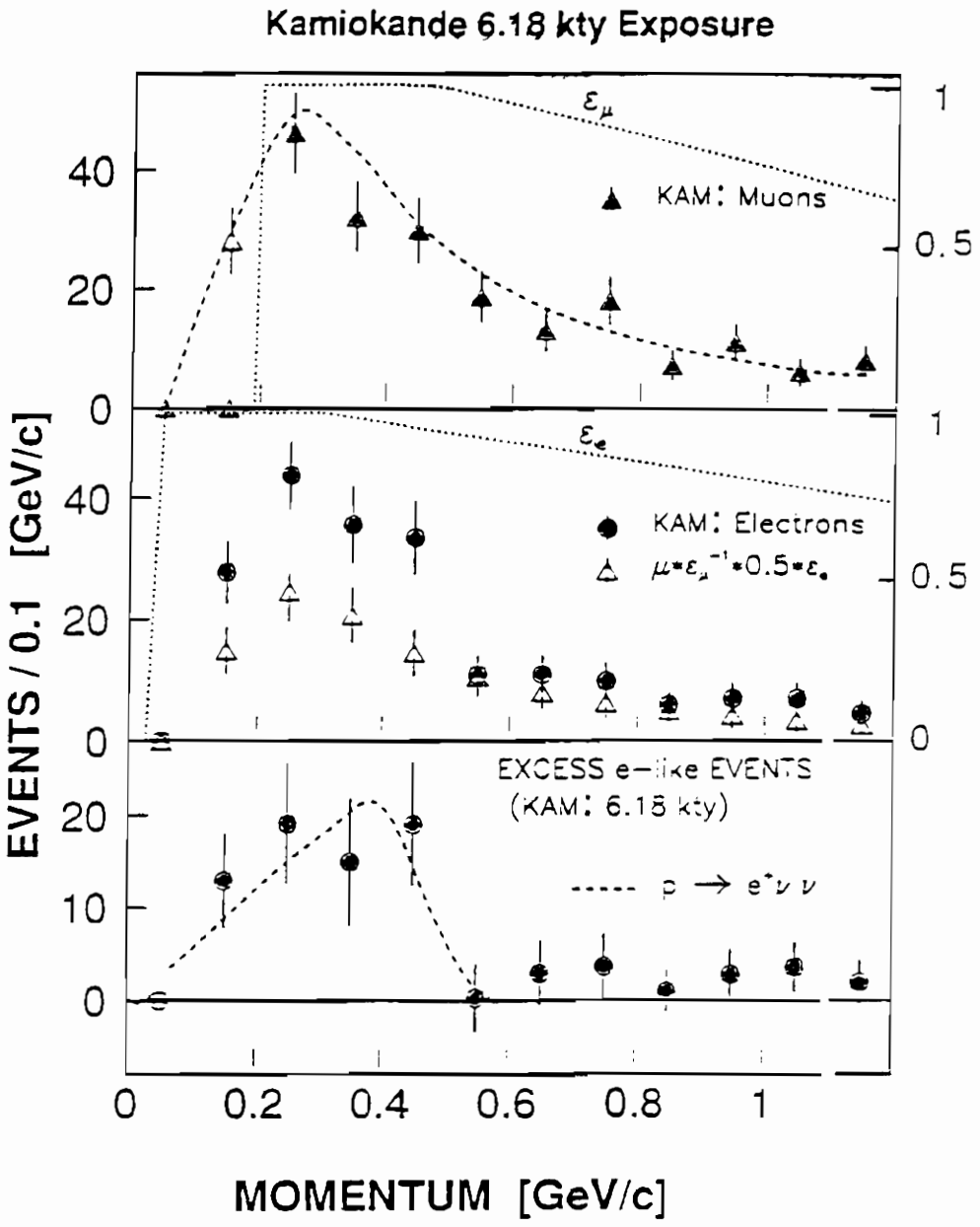

Fig. 3. Momentum distributions for muons and electrons in the Kamiokande detector together with the prediction of the BN Monte Carlo (top dashed curve) for the muon flux. The excess of electron events, which could be interpreted as coming from proton decay, is shown in the bottom box.

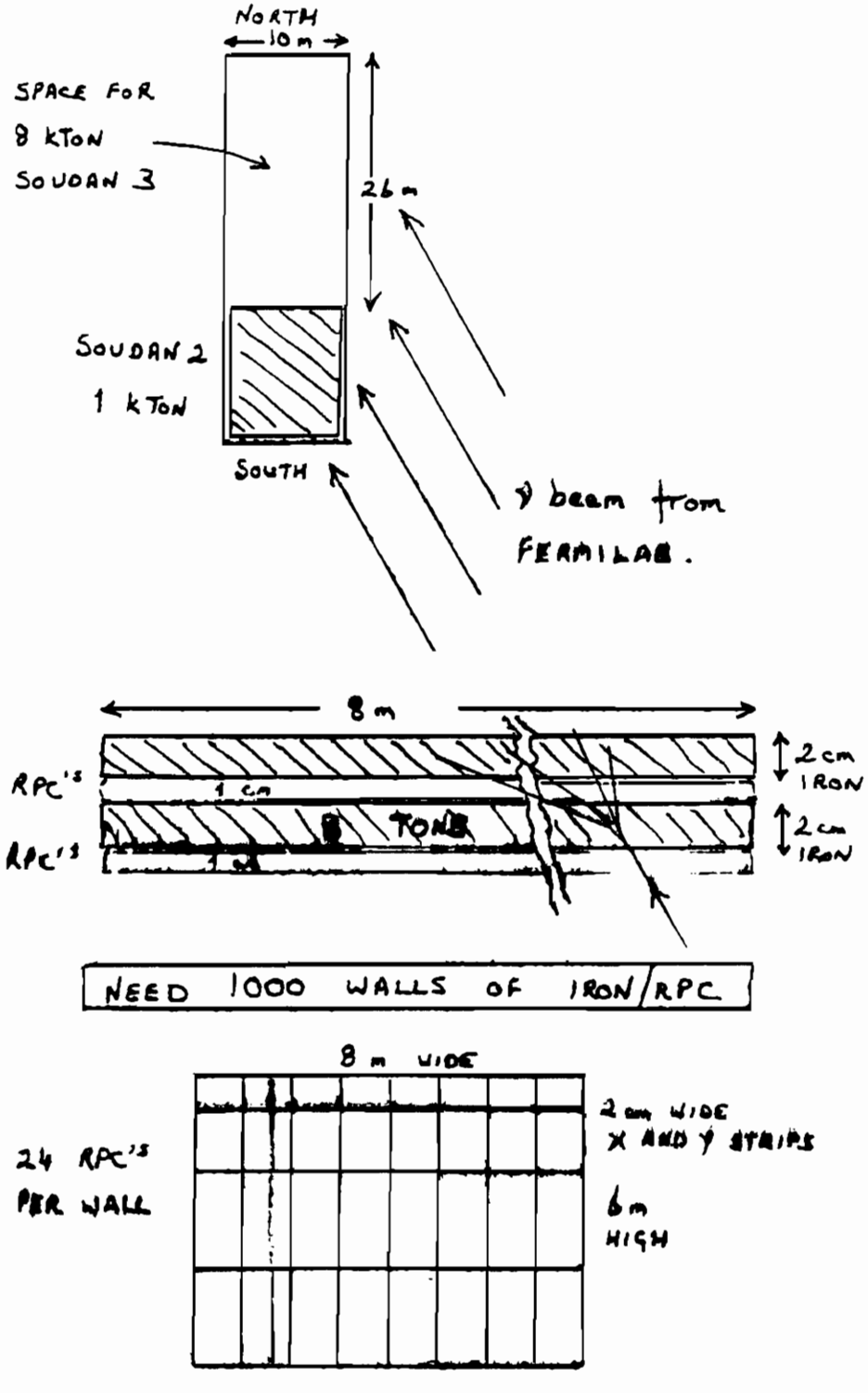

Fig. 4. The arrangement for an 8 kiloton neutrino detector in the Soudan 2 cavern using RPC's.

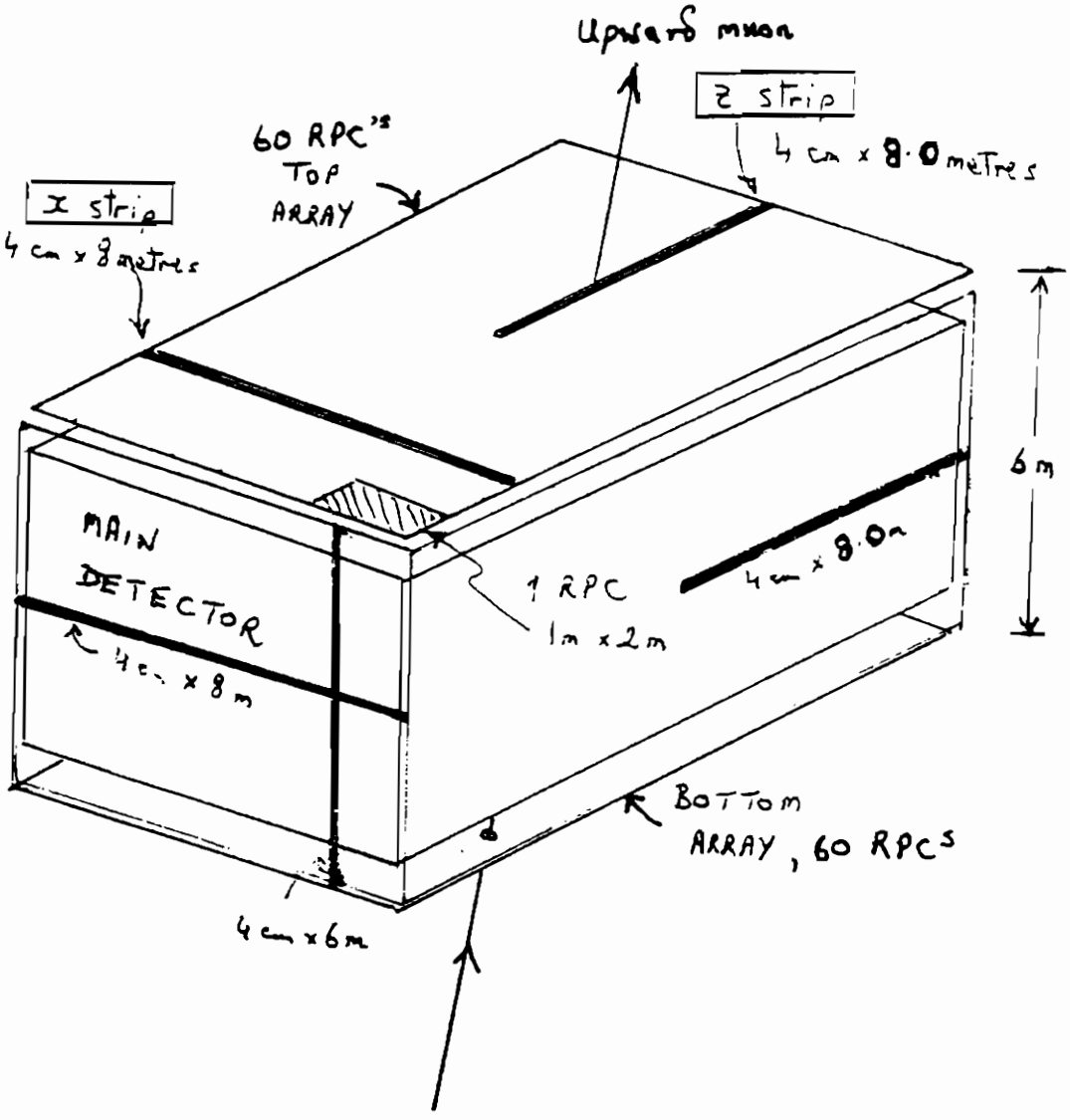

Fig. 5. The arrangment for two arrays of RPC's above and below the Soudan 2 detector in order to detect upward through going muons.

Study of the characteristics of Resistive Plate Chambers in the RD5 experiment

Ludovico Pontecorvo
INFN, Sezione di Roma, Rome, Italy

The RD5 Collaboration *

Abstract.

We present the results of measurements on the Resistive Plate Chambers (RPC) installed in the RD5 experiment. We studied the working parameters of RPC, the relation between the incident particle flux and the detection efficiency for single and double gap RPC, the time resolution for different incident particle fluxes, and we present a preliminary determination of the space accuracy.

The RD5 experiment.

The purpose of the RD5 experiment at CERN [1] is to study the problems related to muon detection for future experiments at hadron colliders. The layout of the RD5 experiment is shown in Fig.1. It consists of two magnets: the superconducting magnet of the EHS experiment, producing a 3 T field, followed by an iron torus producing 1.5 T field. In front of the EHS magnet there is a beam defining scintillator hodoscope, a tracker of silicon microstrips and multiwire proportional chambers and, four RPC of 50x50 cm^2 equipped with 0.78 cm pitch strips, read out with an analogic chain. A tracking calorimeter, TRACAL, of 10 interaction lengths made of stainless steel plates alternated with proportional gas tubes, honeycomb chambers, is installed inside the EHS magnet.

In front, in the middle and behind the iron magnet there are three muon measurement stations with large area drift chambers [2] and RPC. The first two stations are equipped with single gap RPC while Station 3 is equipped with double gap RPC. Single gap RPC are also inserted in two thin gaps in the first half of the torus. Fig.1 shows a perspective view of the drift chambers and RPC installed in Station 1.

The Resistive Plate Chamber hodoscope.

The RPC hodoscope consists of 16 planes of single gap and 4 planes of double gap chambers. Each plane has dimensions 2x2 m^2 and is equipped with 64 read out strips of 31 mm pitch. The planes are coupled in pairs providing one measurement in the

---

* Physicalishes Institute RWTH, Aachen, FRG - CERN, Geneva, Switzerland - SEFT, Helsinki, Finland - CIEMAT, Madrid, Spain - NIKHEF and University of Nijmegen, The Netherlands - Università di Padova and INFN, Padua, Italy - Università di Roma La Sapienza and INFN, Rome, Italy - Università di Roma Tor Vergata and INFN, Rome, Italy - University of California Los Angeles, USA - University of California Riverside, USA - HEPHY, Vienna, Austria - Institute of Experimental Physics, Warsaw, Poland.

horizontal projection, z, and one in the vertical projection, y. Station 1 has four pairs with two y-z measurements before and after the drift chambers. There is one y-z pair in each of the two slots in the iron toroid. Station 2 has two y-z pairs single gap RPC with one measurement on either side of the drift chambers, in addition there is one double gap RPC plane reading the y coordinate on each side of the drift chambers. Also in Station 3 we have one plane of double gap RPC reading the y coordinate on each side of the drift chamber. Each plane provides a fast-OR signal of the 64 readout strips used for timing and trigger. For a description of the RPC construction and parameters see [3].

Performance of the Resistive Plate Chambers.

Chambers with two different resistivity of the electrode plates have been tested. The resistivity of the electrodes is an important parameter that defines the recovery time of the electric field after a local discharge and thus influence the efficiency of the chamber as function of the particle flux. Low resistivity chambers, $\rho \approx 4\ 10^{10}\ \Omega$xcm, were placed in Station 1, where a larger flux of particles is expected from the leakage of hadron showers in the tracking calorimeter, and in Station 2 and 3 (double gap RPC). The chambers in the slots of the iron magnet and single gap RPC in Station 2 have resistivity a factor of about 5 higher.

Most of the data were taken with the chambers filled with a gas mixture of 58% argon, 38% n-butane and 3.8% of freon. The supply voltage was 7.0 kV and 7.2 kV for the low and high resistivity chambers respectively. The efficiency, averaged over the whole surface of the chambers, was measured using the fast-OR signals with muons of the beam halo and was, on average, 96%. The rate of the fast-OR signal was, on average, 5 kHz/m^2 (0.5 kHz/m^2) for the low (high) resistivity chambers. The probability of accidental hits in coincidence with a trigger was between 10^{-3} and 10^{-4} per plane. Fig.2 shows the behavior of the power supply current and of the fast-OR rate, as a function of the high voltage, for two extreme cases of chambers that differ in resistivity of the electrode planes.

The performance of the chambers was studied by tracking high momentum muons, 100-300 GeV/c, through the different planes. Signals from adjacent strips were grouped in clusters, then tracks were defined with a least square fit to a straight line. Fig.3 shows the distribution of the residuals from the track fitted in the non-bending projection: the average r.m.s space resolution is 8 mm.

The efficiency of each plane was measured requiring that a hit is found in three strips centered on the line fitted requiring the presence of at least three other planes. At low beam intensity, for muon fluxes smaller than 10 Hz/cm^2, the efficiency for the different chambers varies between 94% and 99%. Fig.4 shows the efficiency as a function of the muon flux in different chambers. For this measurement the beam was defined by two scintillators of dimensions 10x15 cm^2 and 15x15 cm^2 respectively and the particle flux was measured by the rate of the 10x15 cm^2 scintillator and of a smaller scintillator of dimensions 4x4 cm^2 centered on the beam line. The particle flux was conservatively estimated as that measured on a 10x15 cm^2 surface with a 4x4 cm^2 hole in the center. The scintillators rate was uniform over the 2.6 s of the extraction cycle of the beam: thus the

data shown in Fig.4 represent the average efficiency over this time interval. A significant degradation in efficiency is observed in the RPC with high resistivity electrodes for particle fluxes larger than 20 Hz/cm^2. The efficiency of low resistivity RPC degrades at fluxes larger than 50 Hz/cm^2. The behavior of the efficiency as a function of time during the beam extraction cycle is shown in Fig.5, for fluxes of 6, 64, 210 Hz/cm^2. We have divided the spill time in bins of ≈ 80 ms and we measured the efficiency for each bin. For high resistivity chambers the efficiency drops during the time of the spill for fluxes greater than 15 Hz/cm^2 while the low resistivity chambers begin to loose efficiency only for fluxes higher than 50 Hz/cm^2. We fitted the results with a simple exponential form, $A+Be^{-t/\tau}$, where A represents the efficiency of the chamber as if exposed to a continuous flux of the same intensity of the one used for the measurement. The result of the fit is relevant only for high fluxes, and is presented in Table 1 for the average of five representative low resistivity and five high resistivity chambers for the run with the highest flux. The efficiency for continuous operation is much lower than the average efficiency measured during the beam spill.

High resistivity	Low resistivity
A = 0.246±0.007	A = 0.59±.02
B = 0.487±0.009	B = 0.37±0.02
τ = 0.68±0.04 s	τ = 1.7±0.2 s

Table 1

From this study we observe that the behavior of the RPC efficiency versus incident flux is dependent on the time interval during which we perform the efficiency measurement. To compare our results with previous measurements we have plotted in Fig 6 the efficiency of one low resistivity RPC and one high resistivity RPC, measured in the first 300 ms and in the whole spill (2.6 s), against the incident flux. Our 300 ms measurement for high resistivity RPC is compatible with the published data by Bertino et al [4], while it is not possible to compare these results with what has been published in [5] and [6] because the condition of the measurements is different, namely the illuminated area for our measurement is a small fraction of the total area while in [5] and [6] the whole surface of the RPC was irradiated.

Double gap RPC.

A double gap RPC consists of two single gap RPC assembled together as shown in Fig 7. The spacers used to keep the bakelite plates of each gap at a fixed distance of 2 mm represent a dead area for each RPC of the order of 1% of the full area. We have staggered the position of these spacers in the two gaps in such a way to eliminate the dead area. The read out is done by a strip plane inserted between the two RPCs, in this way we expect to have an efficiency close to 100% and also a better time resolution. The measured efficiency for double gap RPC is (99.9 ± 0.1)%. We studied the dependence of the efficiency from the incident flux for double gap RPC. The behavior is very similar to

that measured with single gap low resistivity RPC, this is due to the spatial correlation of the discharge point in the two gaps, so that in this respect we cannot consider the two gaps as independent.

RPC Time and Space Resolution.

We measured the time and space resolution of single gap RPC using four small 50x50 cm^2 RPC, read out by 0.78 cm pitch strips. These chambers were positioned in front of the EHS magnet at a distance of 57 cm from the last plane of the silicon tracker, which measures the impact position of the incoming particle on the RPC planes with an error of ≈ 30 μm. We equipped 12 strips per plane and we read them out with a LeCroy 2249A, 11-bit resolution, integrating ADC. The gain of the electronic channels were equalized injecting a fixed charge at the input of the read out chain. The gate signal to each ADC, 50 ns long, was given by the coincidence of the RD5 trigger signal with the fast-OR signal generated by each chamber. Each chamber forms the fast-OR signal discriminating the analog sum of the four strips illuminated by the beam. This signal, delayed, has been also used to send the stop to a LeCroy 2228A TDC used for the timing measurement, the start being given by the RD5 trigger signal. Each bin in Fig.8 corresponds to 50 ps.

Time Resolution measurement.

In Fig 8 it is shown the distribution of the difference between the arrival time of the RD5 trigger signal and the fast-OR signal generated by each RPC. We fitted this distribution with a gaussian function, whose width gives the time resolution of the system (RD5 trigger + RPC). After unfolding the jitter due to the trigger we find that the time resolution of the RPC is (1.8 ± 0.1) ns. We have to remark that there is a significative non gaussian tail towards long delays in the distribution, for example with a 3 σ cut one looses 7% of the events. This problem could be solved using double gap RPC, the expected time distribution for the double gap RPC has been calculated folding two measured time distributions for a single gap RPC in an uncorrelated way. With this device we expect to reduce to 1.3% the number of events that would fail a 3 σ cut. The time formation of the signal is also very sensitive to the applied voltage and to the incident particle flux. In Fig 9 we show the measured time resolution for different incident fluxes and the time resolution for different values of the applied voltage.

Space resolution measurement.

The reconstruction of the impact position of a charged particle has been done using the center of gravity method. From the study of the charge profile on the strips we deduce that there are five strips with a signal greater than the noise. In Fig.10 we show the correlation between the impact position as extrapolated from the silicon telescope on the RPC planes and the center of gravity calculated using five strips. From these plots we can conclude that the intrinsic resolution of the chambers is rather good, but there are some systematic effects, that are only in part due to the position reconstruction method, that we still have to take into account.

To measure the position resolution we studied the distribution of the difference between the impact position given by the center of gravity method and the position given by the extrapolation of the track from the silicon telescope, Fig.11. We fitted this distribution with a Gaussian function and we obtained a position resolution of 280 μm. We have to remark that at this stage of the analysis no cut and no systematic correction has been applied. To take into account the effect of the systematic error due to the position reconstruction method it is necessary to know the distribution of the charge induced on the strips. To fit this distribution we have chosen the following function [7]:

$$Q_i=\int_{S_i} [A/\cosh((x-x_0)/\delta)]dx \qquad \{1\}$$

where Q_i is the charge induced on strip s_i, x_0 is the particle position and δ is the width of the charge distribution. In figure 12 we show the fit to an event and the distribution of the width of the charge function on a sample of 425 events centered on one strip *. The average value of the δ parameter is 4.1 mm, in reasonable agreement with what expected from the dimensions of the chamber, and also with what has already been measured in [7] using a different method.

Knowing the value of the δ parameter we can evaluate the systematic error in the reconstructed position due to the center of gravity method and compare it with the measured systematic error. In Fig 13 it is shown the behavior of the systematic error, defined as the difference between the center of gravity position and the particle position extrapolated from the silicon tracker, as a function of the center of gravity position. The dashed line superimposed represents the systematic error as derived from the charge distribution {1}. Subtracting on event basis the systematic error given by the previous calculation we obtain the distribution shown in fig 14. The width of this distribution is 250 μm and there are no big non Gaussian tails, the number of events that fail a 3 σ cut is 2 %.

Conclusions.

We have studied the behavior of the RPC installed in the RD5 experiment. We noticed that during the 2.6 s of the beam spill, there is a decrease of the efficiency when the particle flux is bigger than few Hz/cm^2, and for this reason it will be very important to measure the efficiency of those chambers when illuminated by a continuous particle flux. A comparison of the behavior of RPC built with plates of different resistivity shows that low resistivity chambers have significant better efficiency at fluxes larger than 10 Hz/cm^2. We have shown that double gap RPC of low resistivity have full efficiency and the flux capabilities are similar to those of single gap low resistivity RPC. The measurements that we presented confirm the good timing resolution already measured for these chambers (σ_t = 1.8 ns). We measured for the first time the spatial accuracy for RPC using the center of gravity method. We found that, with 0.78 cm pitch read out strip, the spatial resolution is σ_S = 250μm.

---

* The fit procedure introduces a correlation between the particle position and the width δ, which tends to increase the value of δ on the edge of the strips.

References

[1] M.Della Negra et al.: "Study of muon triggers and momentum reconstruction in a strong magnetic field for a muon detector at LHC", CERN/DRDC/90-36, DRDC/P7, September 1990.

[2] K.Eggert et al.: Nuclear Instruments and Methods, 176 (1980) 217.

[3] R.Santonico and R.Cardarelli: Nuclear Instruments and Methods in Physics Research, A187 (1981) 377; R.Cardarelli et al.: Nuclear Instruments and Methods in Physics Research, A263 (1988) 20.

[4] M.Bertino et al.: Nuclear Instruments and Methods in Physics Research, A283 (1989) 654-657.

[5] I.Crotty et al.: "Investigation of resistive parallel plate chambers" CERN/PPE 92-182.

[6] M.Iori and F.Massa: Nuclear Instruments and Methods in Physics Research, A306 (1991) 159-168.

[7] F.Ceradini et al.: "Measurement of the hit distribution in Resistive Plate Chambers equipped with a digital read out of the charge induced on strips", preprint n.990, Dipartimento di Fisica, Università di Roma La Sapienza, December 1991

Figures

1. RD5 Experiment Layout and muon measurement station.
2. RPC working parameters.
3. Tracking accuracy for digital RPC.
4. Efficiency vs particle flux, high and low resistivity RPC.
5. Efficiency vs time in the spill (6, 64, 220 Hz/cm^2).
6. Efficiency vs particle flux averaged in the first .300 sec and in 2.6 s.
7. Schematics of a Double Gap RPC.
8. RPC time resolution.
9. Time resolution vs particle flux and time resolution vs applied voltage.
10. Measured impact position vs extrapolated position.
11. Residual distribution not corrected.
12 Fit to the charge distribution on the strips and distribution of the δ parameter.
13. Measured and calculated systematic error.
14. Residual distribution corrected.

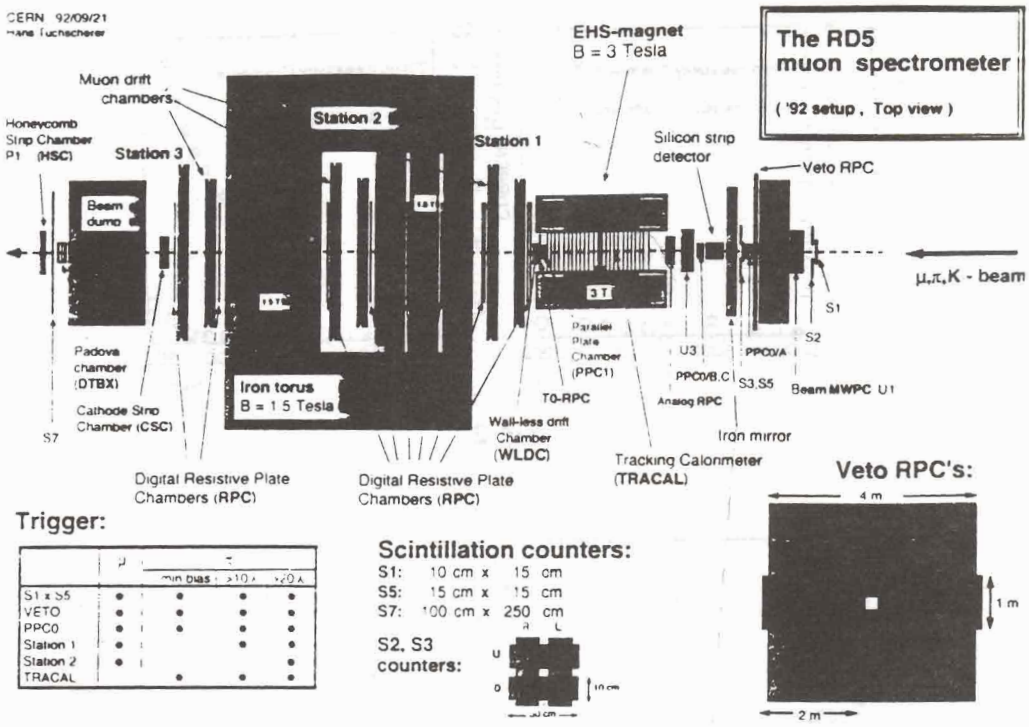

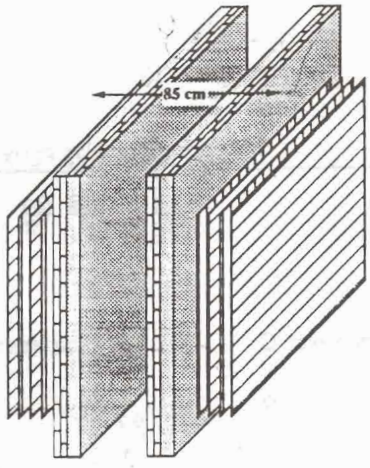

Muon Station 1

Fig 1

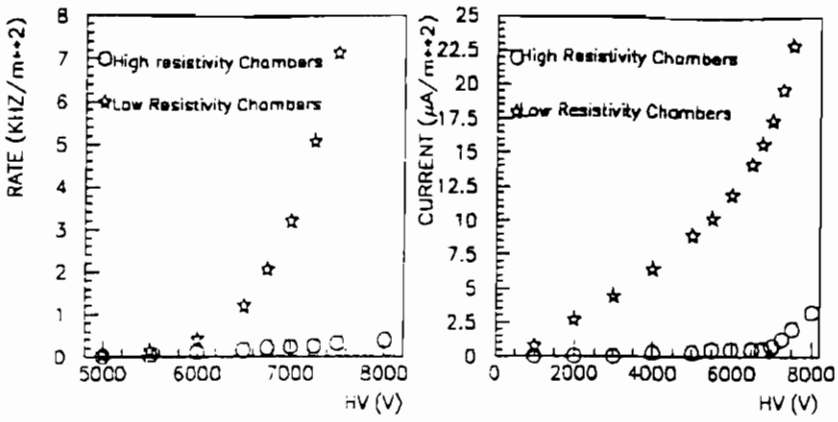

Fig 2

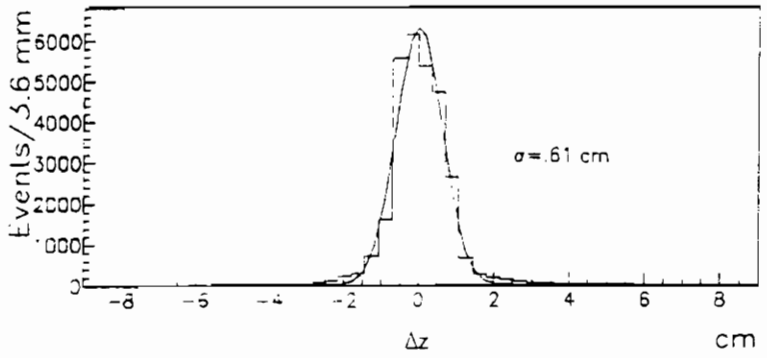

Fig 3

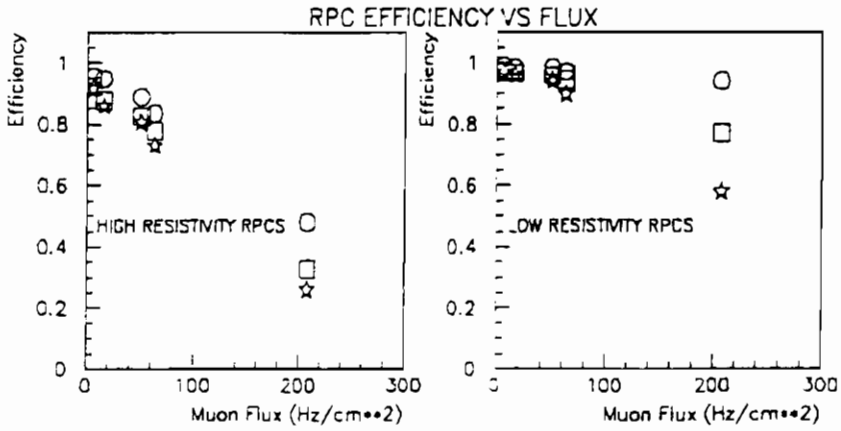

Fig 4

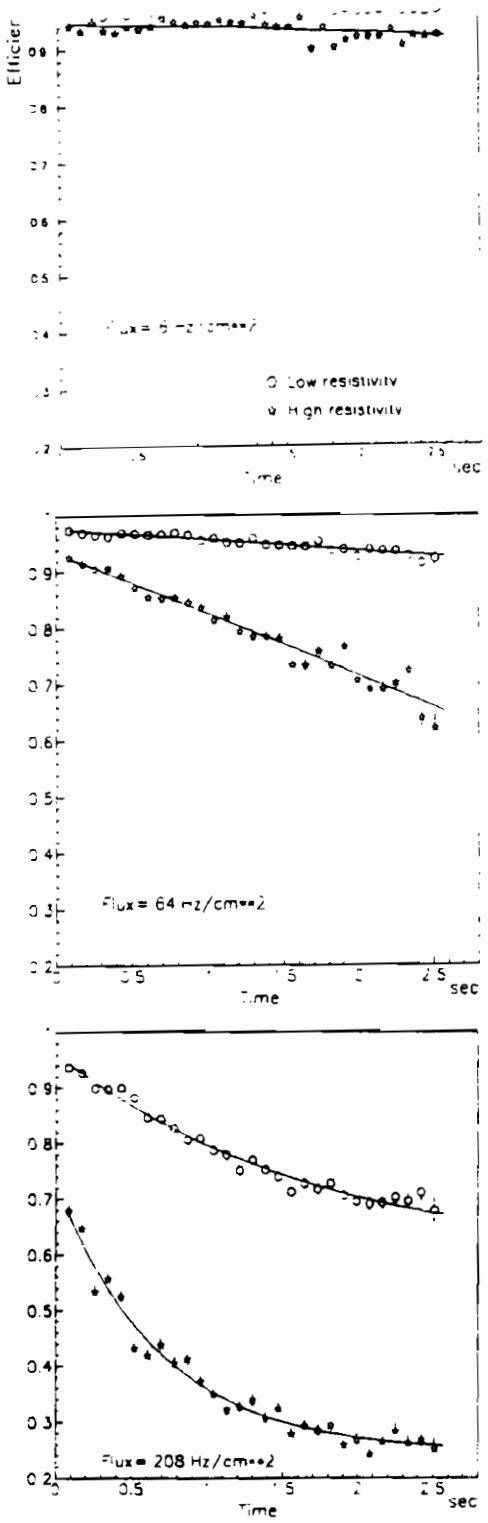
Efficier
Low resistivity
High resistivity
Time
sec
Flux = 64 Hz/cm**2
Flux = 208 Hz/cm**2

Fig 5

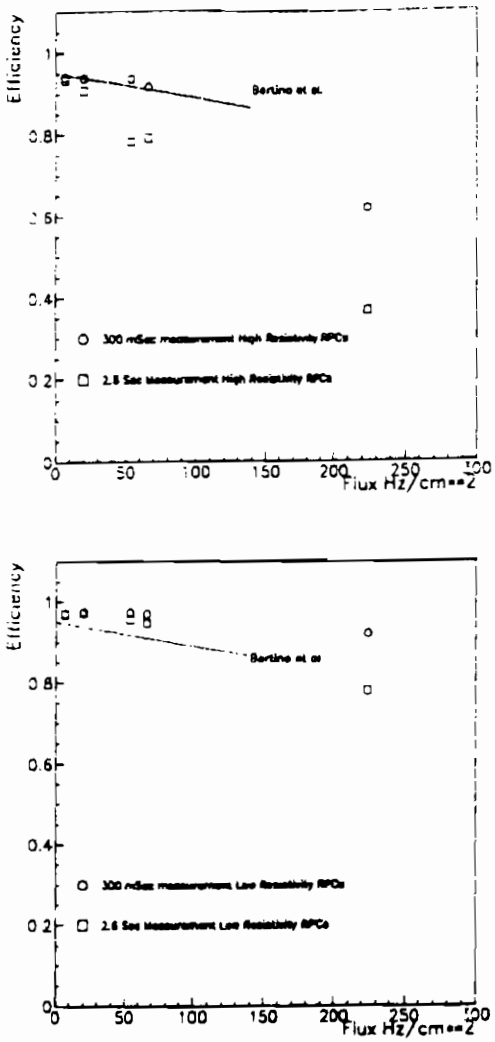
Efficiency
Flux Hz/cm**2

Fig 6

DOUBLE RPC LAYER

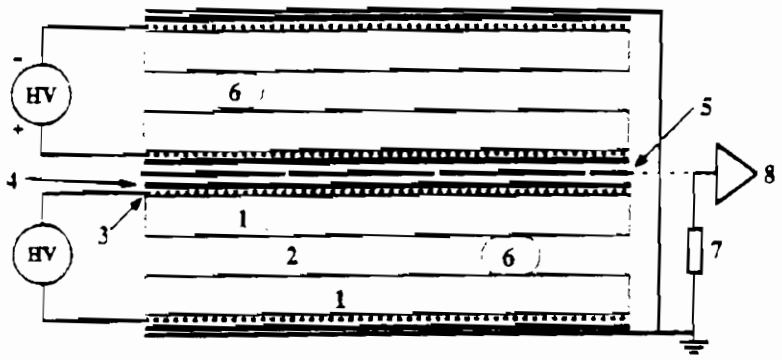

1 bakelite plate
2 gas
3 graphite coating
4 pvc insulating foil
5 aluminum strips
6 pvc spacer
7 line termination
8 front end electronics

Fig 7

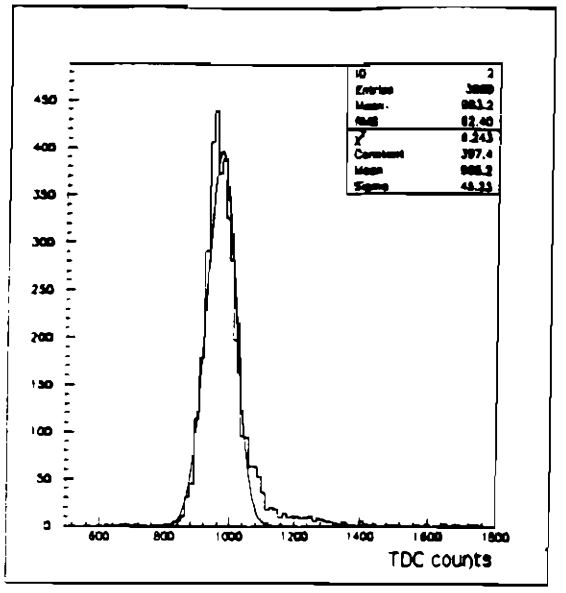
TDC counts

Fig 8

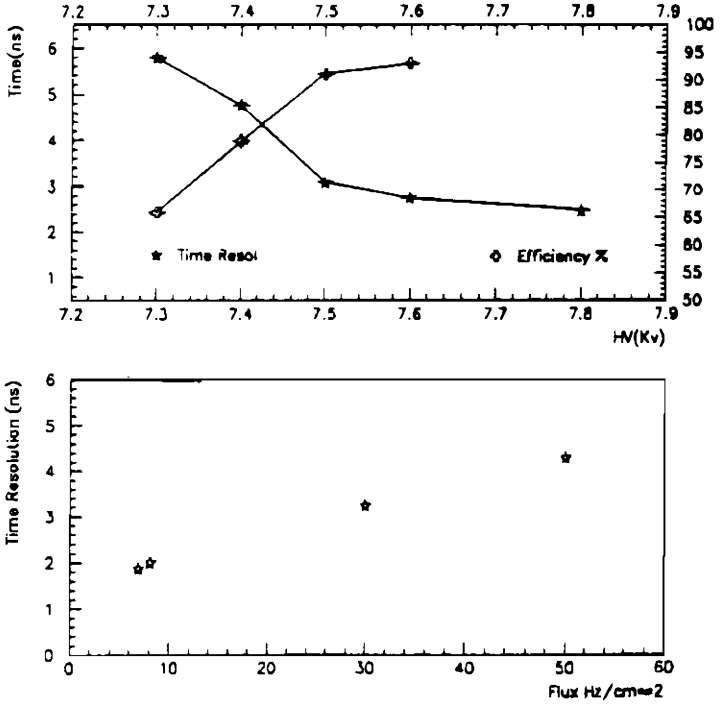
Time(ns)
HV(Kv)
Time Resol
Efficiency %
Time Resolution (ns)
Flux Hz/cm**2

Fig 9

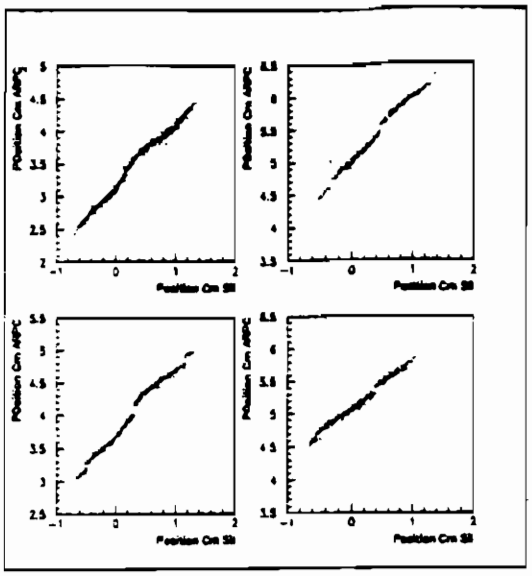

Fig 10

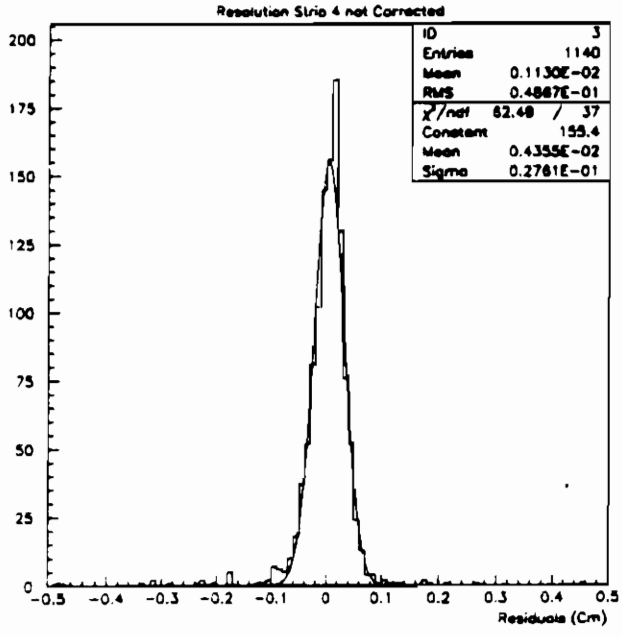
Resolution Strip 4 not Corrected
ID 3
Entries 1140
Mean 0.1130E-02
RMS 0.4887E-01
χ²/ndf 82.49 / 37
Constant 155.4
Mean 0.4355E-02
Sigma 0.2761E-01
200
175
150
125
100
75
50
25
0
-0.5 -0.4 -0.3 -0.2 -0.1 0 0.1 0.2 0.3 0.4 0.5
Residuals (Cm)

Fig 11

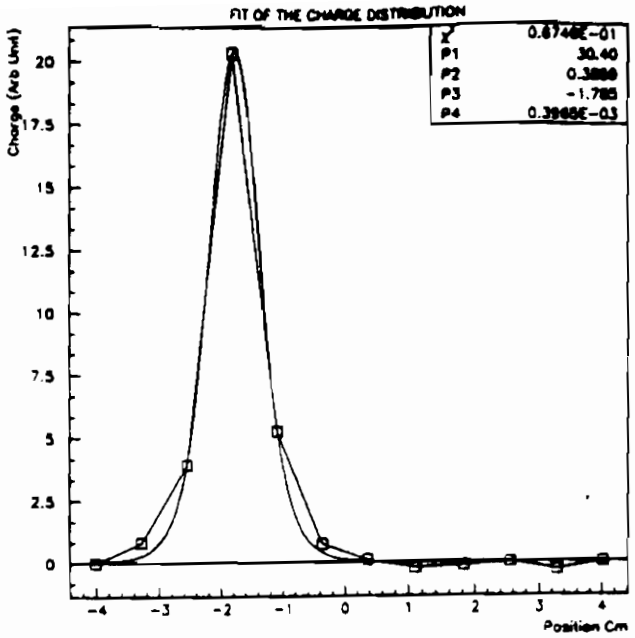
FIT OF THE CHARGE DISTRIBUTION
Charge (Arb Unit)
Position Cm
P1 30.40
P3 -1.785

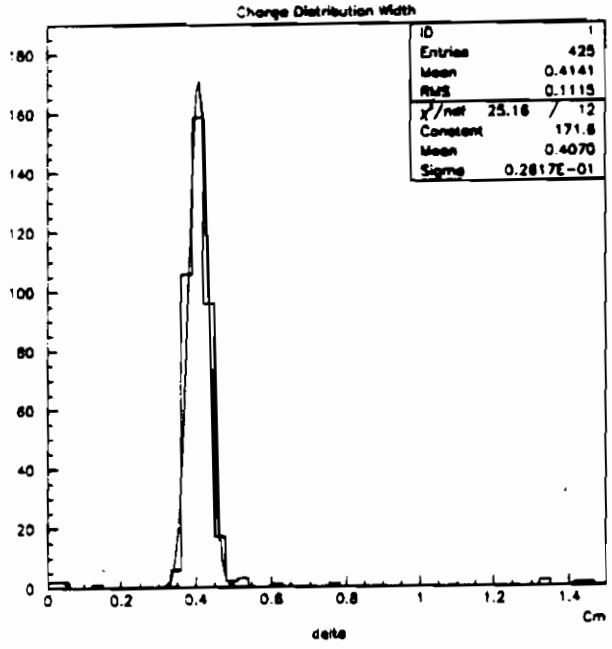
Charge Distribution Width
ID 1
Entries 425
Mean 0.4141
RMS 0.1115
Constant 171.6
Mean 0.4070
Cm
delta

Fig 12

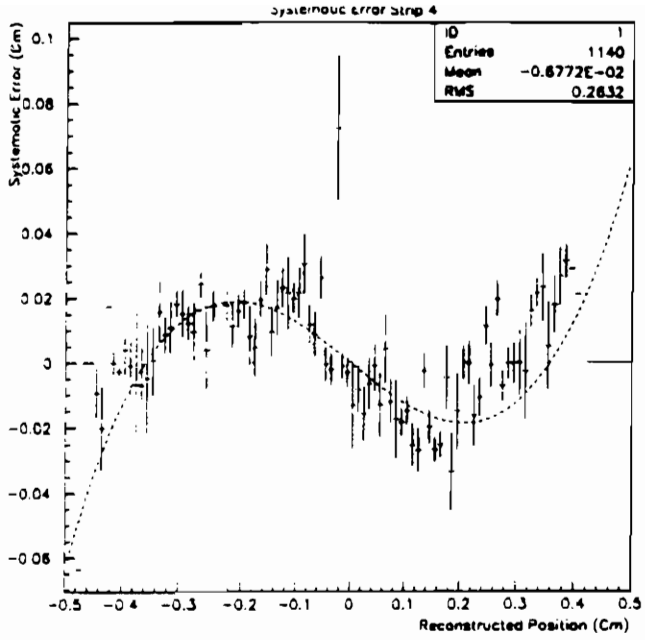
Systematic Error Strip 4
ID 1
Entries 1140
Mean -0.6772E-02
RMS 0.2632
Systematic Error (Cm)
Reconstructed Position (Cm)

Fig 13

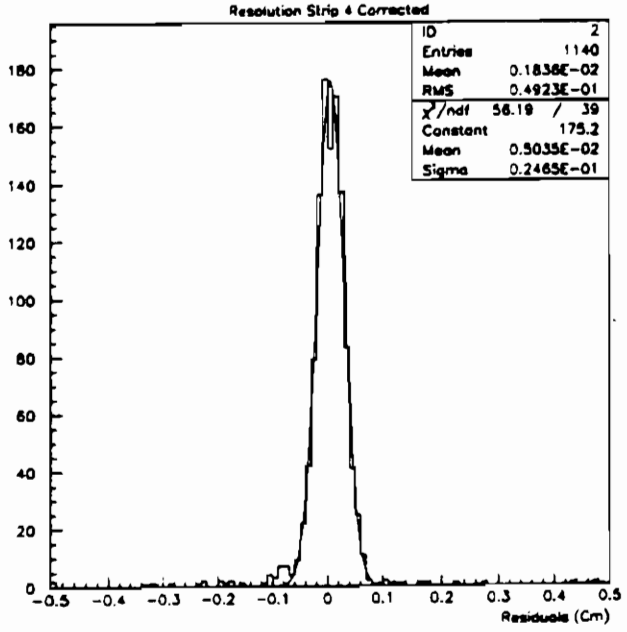
Resolution Strip 4 Corrected
ID 2
Entries 1140
Mean 0.1838E-02
RMS 0.4923E-01
χ²/ndf 56.19 / 39
Constant 175.2
Mean 0.5035E-02
Sigma 0.2465E-01
Residuals (Cm)

Fig 14

Operation of RESISTIVE PLATE CHAMBERS with pure CF_3Br

R. Cardarelli

Universita' di Roma "Tor Vergata" and INFN Sezione di Roma2

Via della Ricerca Scientifica - 00133 Roma, Italy

The use of the resistive plate chambers [1] in accelerator physics [2] was limited up to now by the maximum rate [3], presently of about 100 Hz/cm^2, at which this detector can be efficiently operated. This limit is due to the fact that the discharges occurring in the gas can only be fed by a limited current that can flow across a pair of electrode plates whose resistivity ranges around values as high as $10^{11}\ \Omega/\square$.

A natural way to improve the RPC rate capability is therefore to reduce the current needed to feed the discharge originated by a ionizing particle crossing the gas. This requires a higher amplification frontend electronics to compensate the lower gas amplification.

A low amplification gas can be obtained with the addition of electronegative compounds, like freons, to the ordinary Argon/Butane mixture.

Fig. 1 shows the charge distribution of signals generated by cosmic rays in a 50×50 cm^2 RPC operating with a gas mixture of Argon/Butane in the ratio of 60/40 in volume and an amount of freon CF_3Br ranging from zero to 8%. The three distributions of fig. 1, corresponding to 0%, 4% and 8% of freon respectively show a sharp peak corresponding to the single discharges, followed by a quite long tail due to multiple discharges that tends to increase with the operating voltage. The size of the discharge drastically decreases for increasing freon content in the gas: as shown in fig. 1, an increase of Freon from 0% to 8% reduces the average charge of the single discharge peak of about one order of magnitude.

This paper presents the results of two tests carried out on a chamber operating in pure freon. This operating condition is characterized by signals of extremely small charge and short duration which required the development of new high amplification, wide band frontend electronics.

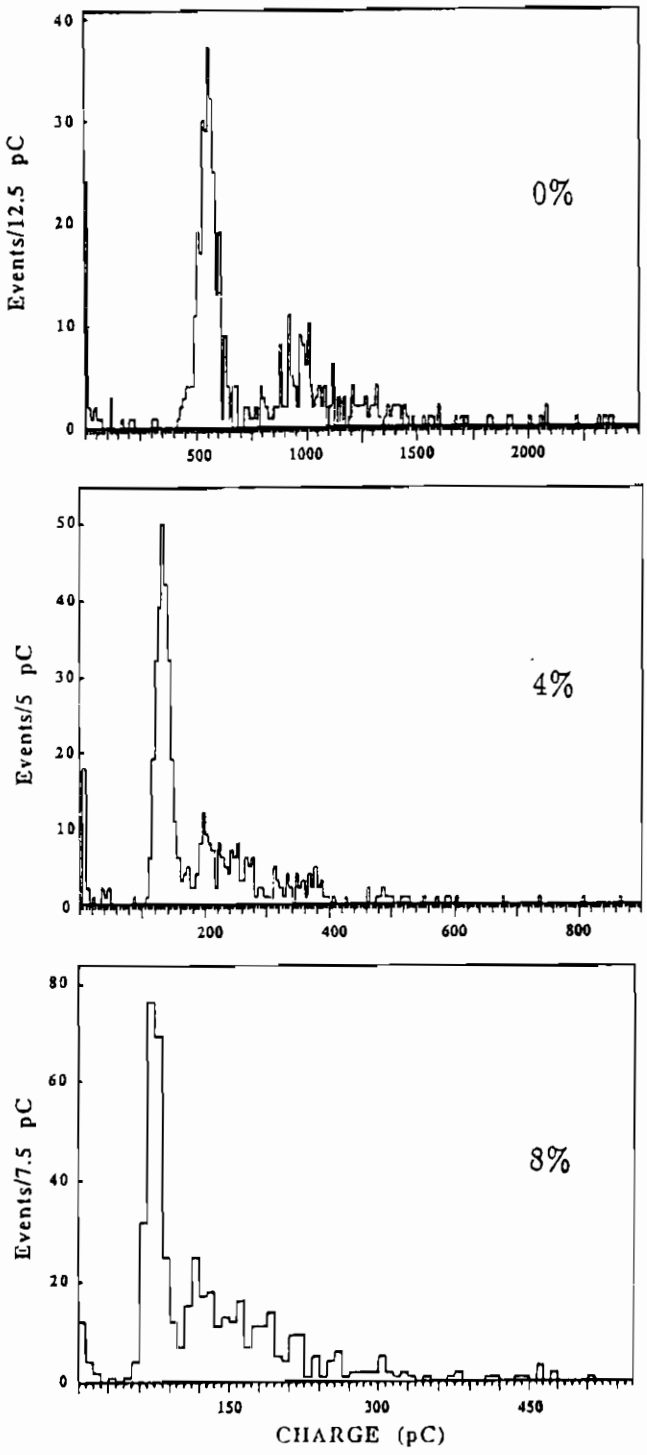

Figure 1: Charge distribution of signals generated by cosmic rays in a RPC for different amounts of freon, CF_3Br, in the gas mixture: 0%, 4% and 8%. The Argon/Butane ratio is 60/40 in volume

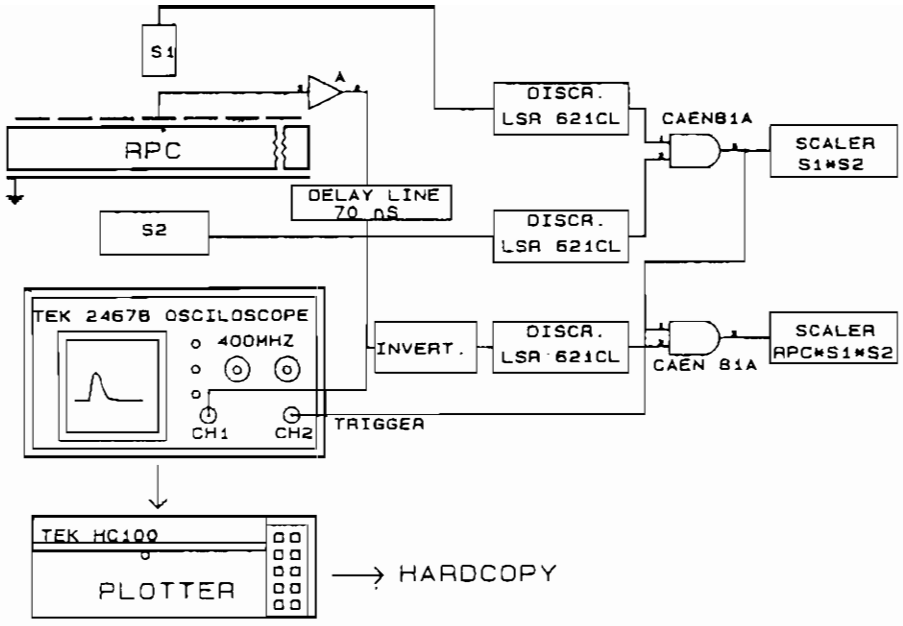

Figure 2: Set-up of the cosmic ray test

Both tests were done utilizing a completely standard 50×50 cm^2 RPC equipped with copper pick-up strips 8 mm wide and 2 mm spaced from one another which were printed on a standard G10 board 1.6 mm thick pressed against the chamber on the non coppered side. The detector is electrically shielded by a 100 m thick Aluminium foil. A polyurethane rigid foam layer 1 cm thick is inserted between the aluminium foil and the pick-up strips in order to keep the strip-line impedance high. Each strip has one end terminated by a 50 Ω resistor and the other end connected to the frontend electronics.

The first test was carried out with cosmic rays and the corresponding set-up is shown in fig. 2. The signal of the pick-up strip is fed into a fast amplifier of 50 Ω input impedance, 150 MHz bandwidth, 50 μV integrated noise and amplification factor of about 50. The amplified signal is delayed and split between two coaxial cables: half of the signal current is feed into a Tek 2467B 400 MHz digital oscilloscope and the remaining current into a LSR 621CL discriminator. The oscilloscope operation is supervised by a processor which allows to store all the sampled data and to print the recorded waveform on a color hardcopy where the relevant working conditions of the scope like the trigger level and the time of the triggering signal are also recorded.

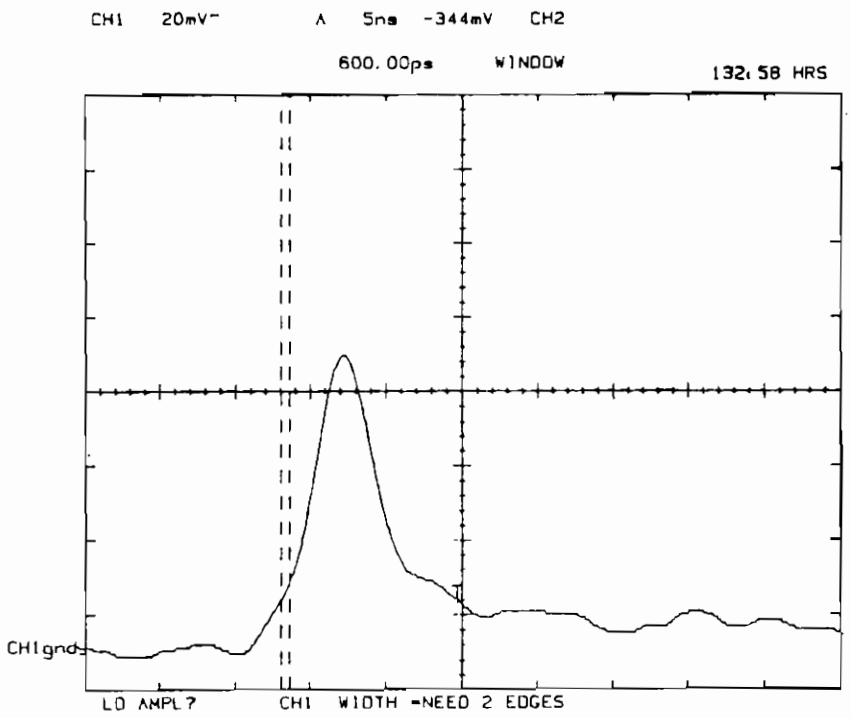

Figure 3: Typical amplified output signal of the RPC operated with pure freon. The amplifier has 50 Ω input impedance, 150 MHz bandwidth, 50 μV integrated noise and amplification factor 50

Two scintillators of sections 0.5 × 2 cm^2 and 3 × 10 cm^2 respectively, placed at the opposite sides of the chamber as shown in fig. 2 and oriented in the direction of the pick-up strips are used to select cosmic rays crossing a fixed detector strip. The scintillators are coupled to Philips XP2020 photomultipliers whose signals are discriminated and sent to a coincidence circuit which is used to trigger the scope. At any trigger occurrence the waveform of the signal produced by the RPC was registered and recorded on hard-copy.

About 200 waveforms were collected in this way. A typical one is shown in fig. 3.

It exhibits 80 mV amplitude over 50 Ω impedance, 4-5 ns FWHM and 2-3 ns risetime from 10% to 90% of the full amplitude. It must be stressed here that these features are those expected by the 150 MHz bandwidth of the frontend amplifier, indicating that the risetime and width of the input signals are shorter than those of the recorded waveform. Assuming that the time integral of the signal is not seriously affected by the limited amplifier bandwidth, the charge of the amplified signal shown in fig. 3 turns out to

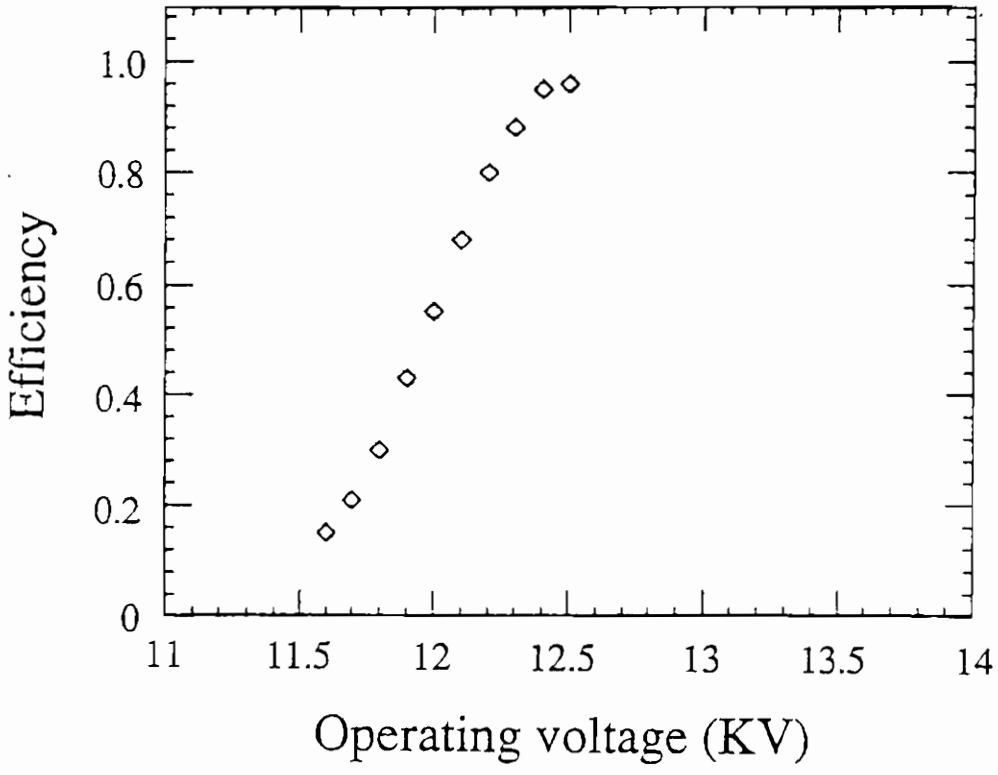

Figure 4: RPC efficiency vs. operating voltage in the cosmic ray test

be about 5 pC, the input impedance of the scope being 50 Ω. Taking into account the splitting of the current and the amplification factor of 50, the charge of the input signal at the end of the pick-up strip can be estimated to be about 0.2 pC, i.e. 500 times smaller than in the case of the usual operation with a gas mixture containing 3-4 % of freon.

The detection efficiency is measured by counting the number of times the chamber fired normalized to the number of cosmic rays detected by the coincidence S1 S2 of the two scintillators. It is plotted in fig. 4 as a function of the operating voltage. A plateau value of .95 is reached for voltages in excess of 12.5 KV. However it should be remarked that the detection efficiency could be higher than 0.95 due to the difficulty to exclude from the trigger cosmic rays crossing the the chamber outside of the region covered by the only detected strip.

The 200 events collected at the oscilloscope were also used to measure the time jitter of the chamber. As shown in fig. 5 indeed in any waveform recorded on hardcopy it is marked the trigger time which is always given by the scintillator S1 whose signal was delayed in such a way to define the time of the coincidence S1 S2 triggering the scope. The distribution of the

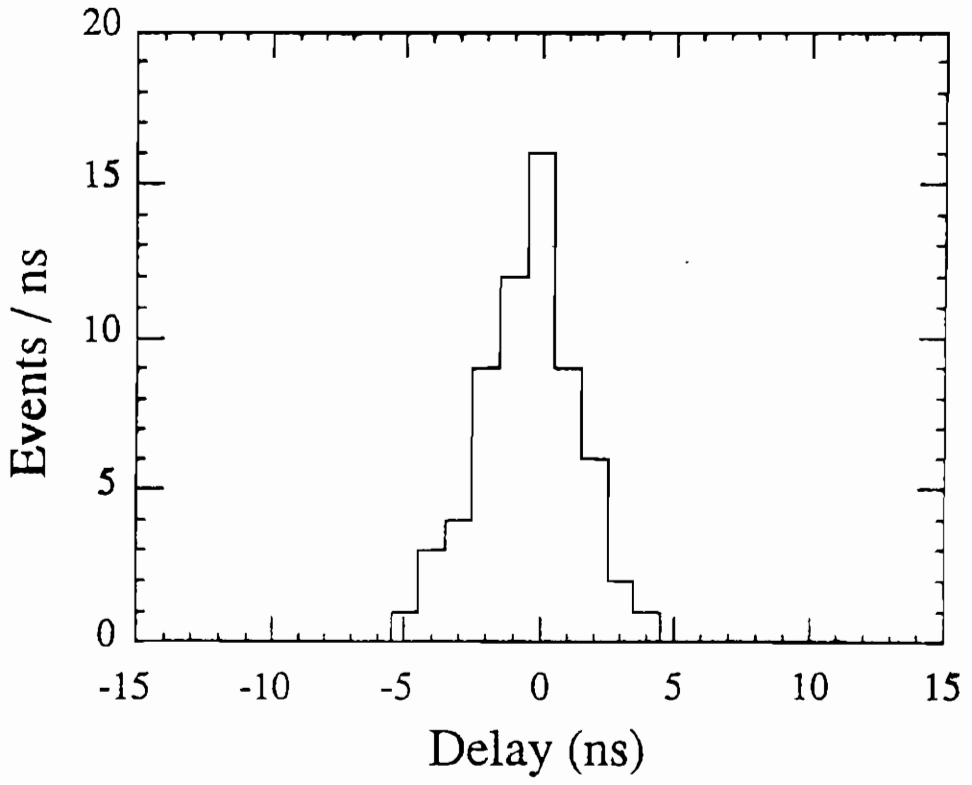

Figure 5: Distribution of the relative delay between the signals of scintillator and of the RPC operated at 13.1 KV

delay between the trigger and the time corresponding to the maximum of the signal is plotted in fig. 5 and shows a peak of 4 ns FWHM corresponding to a standard deviation of 1.7 ns which is essentially due to the RPC time jitter, the effect of the scintillator being expected to be considerably smaller.

The second test was carried out at the CERN laboratory on the RD5 test beam. The chamber configuration was identical to that of the cosmic rays test already described except for the frontend electronics which had a much wider band, 2 GHz, with the purpose of more easily detecting very short signals. The chamber was irradiated with a 200 GeV/c pion beam of sections about 2 cm^2. Only two strips, approximately centered on the beam, were read out in the test.

The detection efficiency, for different values of the beam intensity, was measured from the coincidence of the RPC signal with two small beam scintillators. Fig. 6 shows the chamber detection efficiency vs the operating voltage for three values of the beam intensity corresponding to a particle flux of 3.5, 7 and 10 KHz/cm^2. The measured efficiency approaches unity even at the highest value of the flux. The absolute value of the efficiency

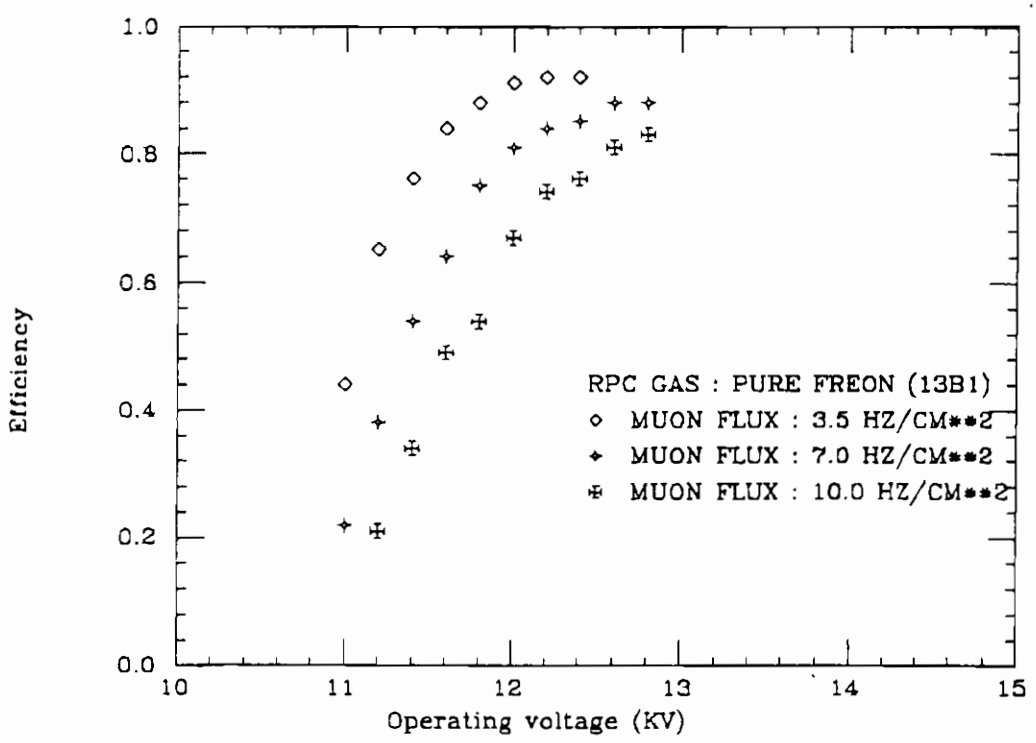

Figure 6: Detection efficiency vs. operating voltage for a RPC exposed to a muon flux of 3.5, 7 and 10 KHz/cm^2 in the RD5 test beam

could be affected by the coarse positioning of the beam with respect to the chamber.

References

[1] . Santonico and R. Cardarelli, Nucl. Instr. and Meth. 187 (1981) 377; R. Cardarelli et al., Nucl. Instr. and Meth. A263 (1988) 20.

[2] . Ceradini et al., Proc. ECFA LHC Workshop, ECFA 90-133, vol III, eds. G. Jarlskog and D. Rein, (CERN, 1990) p.99;
R. Santonico, Proc. ECFA LHC Workshop, ECFA 90-133, vol III, eds. G. Jarlskog and D. Rein, (CERN 1990) p. 838;
C. Bacci et al. Nucl. Intr. and Meth. A315 (1992) 102-108.

[3] . Bertino et al., Nucl. Instr. and Meth. A283 (1989) 654.

WLDC: a Drift Chamber with a Pad RPC for Muon Detection at LHC

H. Faissner, Th. Moers, R. Priem, B. Razen, D. Rein, H. Reithler, D. Samm, R. Schleichert, H. Schwarthoff, H. Tuchscherer, H. Wagner

Phys. Inst. IIIA, RWTH Aachen

Presented by Hans Tuchscherer

Abstract

A concept of a detector well suited for muon detection at the LHC is presented. It consists of a Wall-Less Drift Chamber (WLDC) [1] with 10 layers of drift tubes measuring the track segments in two projections, and of two layers of a resistive plate chamber (RPC) with square pad electrodes, providing locally the time of arrival of the particle and resolving at the same time spatial ambiguities. For the muon momentum determination, each track segment is measured with an accuracy of 100 μm. Measurements with a small prototype of a WLDC have been performed in the laboratory. The same prototype combined with a single gap pad RPC (10 x 10 cm^2 pad size) by the Rome group was submitted in '92 to extensive tests in the high energy test beam of the RD5 experiment at CERN. First results from these data confirm the good performance of this drift chamber.

1 Introduction

Experiments at the planned Large Hadron Collider (LHC) [2] will largely rely on muon based signatures in their search for rare decays [3,4,5]. The detectors will need good *muon identification, momentum measurement, trigger with momentum threshold*, as well as *association to one beam crossing*. This will be achieved with large area muon chambers [6] placed behind an absorber of some 10 interaction lengths. For a detector like CMS [3] the total area amounts to about 3000 m^2. For cost reasons, gaseous detectors are a good choice. Their spatial and temporal resolution seems to be well adapted to the needs of the muon detection. Taking multiple scattering of the muon in the absorber layers into account, a space resolution of 100 μm for a *muon track segment*

is commonly judged sufficient [2]-[5]. When the track segment is measured in a few layers and over a length of 20–30 cm, the associated angular resolution is also adequate for the momentum measurement.
Most signals searched for in LHC experiments will be characterized by multiparticle signatures. It is therefore essential to make sure that the individual track segments belong to the same track, and that the reconstructed tracks, energy deposits etc. do indeed belong to the *same* event. A temporal resolution below 7 ns, necessary to allow an association of each event piece with a unique beam crossing, should be achieved directly by hardware to be available at the 1^{st} level trigger. Resistive plate chambers are well suited to meet these requirements. Finally, the acceptance for the rare signal events should be kept high which requires to have a minimum of dead spaces and to cover a large angular range.

2 Drift Chamber with local t_0 Measurement

It would be ideal for the event reconstruction to have all measurements finished before the next beam crossing, hence within 15 ns. For a drift chamber, on the other side, it is more economical to have large drift space, i.e. less cells and longer drift time. As a compromise, we plan a drift space of about 7 mm corresponding to a max. drift time of 150 ns for an Ar/CO_2 80%/20% gas mixture, and of up to 300 ns when there is a 2.5 T magnetic field orthogonal to the chamber plane. The number of layers foreseen for each module of the muon detector is relatively modest: 6 layers to measure the coordinate along the track bending (measures muon momentum) and 4 layers to measure the coordinate orthogonal to it. To resolve spatial ambiguities and to measure the time of arrival (t_0) of the particle, a double plane of *Resistive Plate Chambers* (RPC) [7] with small quadratic pads will be used. The arrangement of the drift chamber and the RPC is sketched in fig. 1.
Since 10 to 20 beam crossings take place within the max. drift time a correct and fast assignment of each drift chamber hit to its associated beam crossing is needed. This will be directly measured by the t_0 chamber.
The sensing electrodes of the t_0-RPC must be limited in size, otherwise the travelling time of the signals within one electrode would spoil the intrinsic time resolution of the chamber. Square pads are thus better suited than very long strips. A further compelling reason for the choice of square pads is their ability to resolve spatial ambiguities in the space reconstruction of a track from its two projections in multitrack events.In

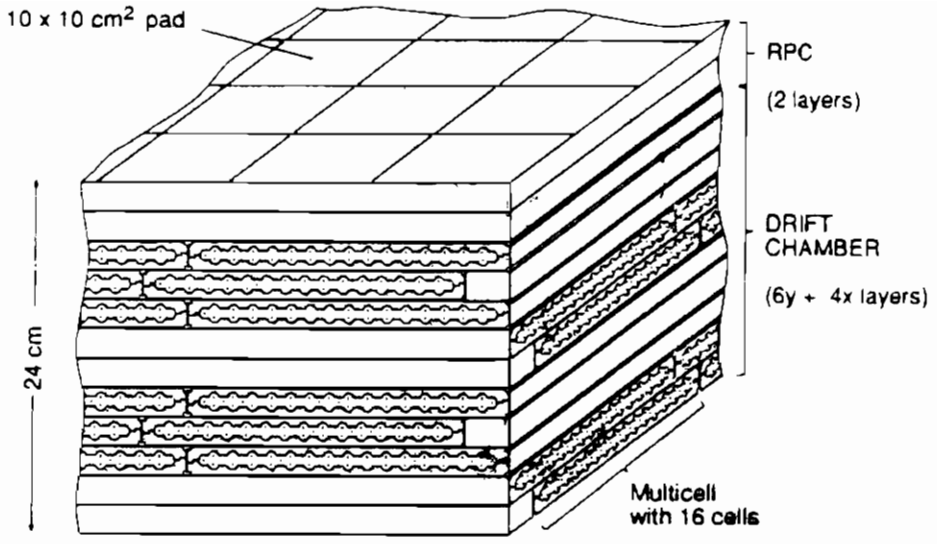

Figure 1: *A small section of the proposed WLDC detector with 10 drift cell layers and two layers of resistive plate chambers (RPC) with square pad electrodes.*

our design, the spatial ambiguities are resolved simultaneously with the temporal ones, which is illustrated in fig. 2. The RPC design foresees square pads of about $10 \times 10\,\mathrm{cm}^2$. On its read out board the signals from several pads can be combined as a logical OR to provide an output corresponding to a logical pad of suited larger size and shape. A double layer of RPCs with staggered spacers will avoid losses within the chamber.

2.1 Wall-less Multicell Design

To minimize the dead spaces between the $2 \times 7 = 14\,\mathrm{mm}$ wide drift cells, there is no wall between them. They are separated by a pair of cathode wires (fig. 4,3). The drift cells form a wall-less plane. The planes are separated by specially shaped conducting plates. To guarantee a good space resolution and to avoid high voltage problems, their grounded surfaces are cylindrical segments centered on the anode and on the cathode wires. Since the two covers do not touch each other within the drift cells, for reasons of stability we limited the number of wall-less neighbour cells to 16, corresponding to a 23 cm wide multicell unit. A cross section of such a multicell is shown in fig. 3.
The wire diameter is 50 μm for the anodes and 125 μm for the cathodes. The wire length

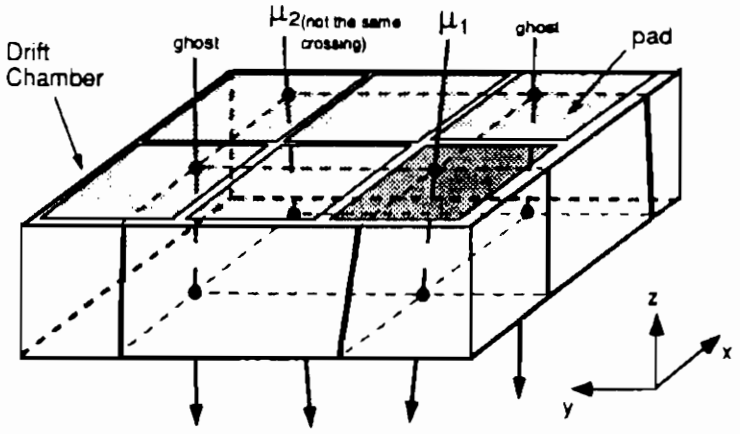

Figure 2: *Strip or wire devices like WLDC reconstruct both projections xz and yz separately. The case above shows an example for two tracks μ_1, μ_2 hitting the chamber and coming from different bunch crossings. From the four reconstructed track projections four track candidates can be combined in space, however only track μ_1 is tagged by the local pad, whereas μ_2 is associated with a different bunch crossing and the 'ghosts' are rejected.*

needed is expected to range from 1 to 5 m. In view of the small distance between wires and walls, the very long wires might require some support. They are operated at +1900 V and -1000 V. Since for operation at LHC only non flammable gases will be allowed, we started our laboratory tests with Ar/CO_2 mixtures; an 80%/20% mixture with a drift velocity of about 60 μm/ns is currently favoured and used throughout this report.

The drift cell is sketched in fig. 4; only the electric field lines reaching the anode are shown, hence indicating the sensitive area of the cell. A quantitative description of the

Figure 3: *Cross section of a 23 cm wide multicell unit with 16 wall-less drift cells. The single wires are anodes, the pairs of wires shown are cathodes and serve as separation between two cells.*

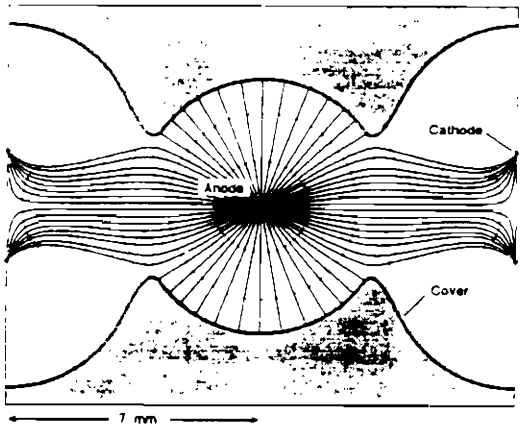

Figure 4: *Computed electric field lines [8] displayed. The lines perpendicular to the field lines correspond to drift times of 20, 40... ns.*

measuring capability of this cell can be judged from the isochrones shown in fig. 4. Since they show only small distortions, a good resolution is expected. At larger angles more isochrones are passed by one track and the resolution is therefore probably dominated by fluctuations in primary ionization.

3 Measurements with prototypes

Laboratory tests were performed with a small prototype 50 cm long with 8 horizontal drift layers all in one projection and a total of 44 drift cells as shown in fig. 5 a.
Vertical cosmic ray muons were used for these first measurements. The drift times were digitized with a binning of 8 ns. In addition, for some wires the analog output of the preamplifier with a gain of 100 was digitized by an FADC with a sampling rate of 100 MHz and an amplitude resolution of 16 mV. The chamber used in the laboratory was submitted in '92 to extensive tests at the high energy test beam of the RD5 experiment [9] at CERN, where also first tests together with a 80 × 100 cm^2 large single gap t_0-RPC (pad size 10 × 10 cm^2) took place.
The chamber is operated in the proportional mode as indicated by the exponential dependance of the average amplitude on the anode voltage in fig. 6. The average number of pulses per trigger is a simple measure of the single hit efficiency. There is a relatively flat plateau between 1750 V and 1950 V. As a good compromise between

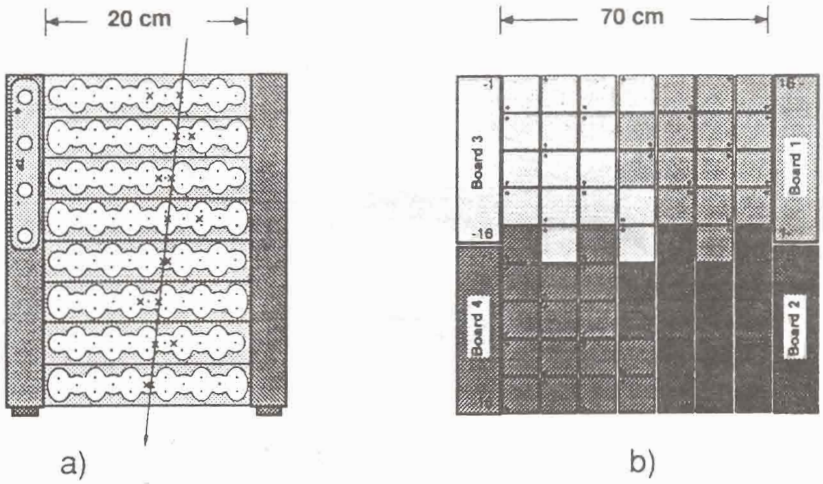

Figure 5: *Prototypes for a) a 8-layer wall-less drift chamber and b) a single layer t_0-RPC used together with the drift chamber at RD5.*

desired high amplitude and a narrow rise time distribution of the pulses 1900 V was chosen as working point. The third curve shows the number of additional hits in neighbour cells which stay at a negligible level over the whole H.V. plateau. For the working point at 1900 V, the average length of the pulses is 250 ± 40 ns. The average rise time of the pulses is 26 ± 7 ns.

3.1 Efficiency and Resolution of the Drift Chamber

The calibration of the chamber was obtained from the measurements in its 8 layers, without any external position measurement. This is the situation one will also face when running the final detector. Muon tracks were reconstructed as straight lines assuming a constant drift velocity. The spatial resolution of the chamber was assumed to be independent of the drift time and of the muon incidence angle. The fit to the hits in the 8 layers used to reconstruct the muon track was also used for calibration of the reference time t_0 and of the drift velocity v_d.

To measure the detection efficiency of a single hit, tracks were reconstructed excluding one of the detector layers. It was then checked whether there was a hit in this layer and whether it was associated to the track. To avoid possible bias arising from uncertainties in the calibration parameters or from a delta ray pulse making the muon pulse, hits

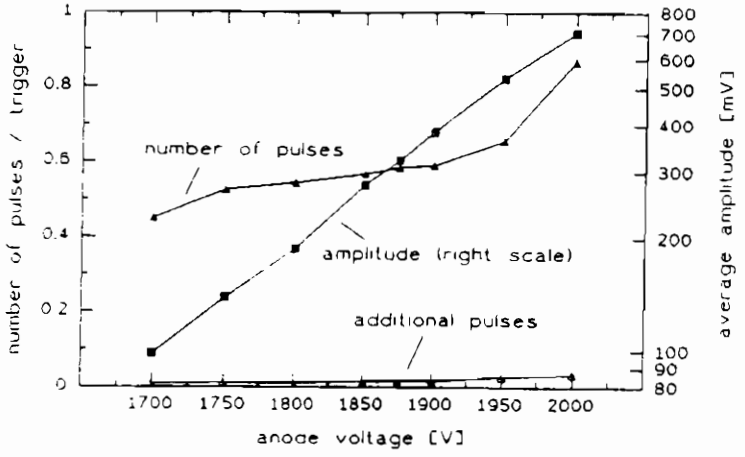

Figure 6: *Amplitude, number of pulses and number of additional hits per trigger as function of the anode voltage. Note the logarithmic scale of the amplitude curve.*

within 7 mm from the extrapolated track position were accepted. About 2% of the hits are more than 2 mm away from the track and there is none beyond 7 mm. The resulting detection efficiency as a function of the track position in the drift cell is shown in fig. 7. The average single hit efficiency is 99.9%.

The width of the residue distribution is a measure for the spatial resolution of one drift cell. With our simple reconstruction this width is approximately 250 μm. This includes all systematic uncertainties from the calibration constants, from possible delta rays and from reconstruction ambiguities. From this value one derives a track segment resolution of 118 μm for a six layer projection.

In order to acount for these uncertainties in a first approximation we have used the approach of removing the hit with the largest residue and repeating the track fit with the remaining 7 hits. The resulting residues are shown in fig. 8 as a function of the track position in the drift cell. The average residue is 180 μm. This corresponds to a single hit resolution of $\sqrt{\frac{7}{7-2}} \times 180\,\mu\text{m} = 212\,\mu\text{m}$, which translates to a resolution for the track of $212/\sqrt{N}$ μm for a projection with N layers. Thus if we apply the same method of rejecting one hit, a 6-layer projection will feature a resolution of $212\,\mu\text{m}/\sqrt{6-1} = 95\,\mu\text{m}$ and therefore be able to achieve the desired resolution of about 100 μm. For small angles, the resolution is independent from the incidence angle of the muon. This residue distribution is also flat in x, the distance of the hit from the anode (signal) wire (fig. 8). Deviations from a linear $x(t)$ relation or from the expected drift velocity are determined by plotting 'signed' residues, where the sign tells whether the observed hit

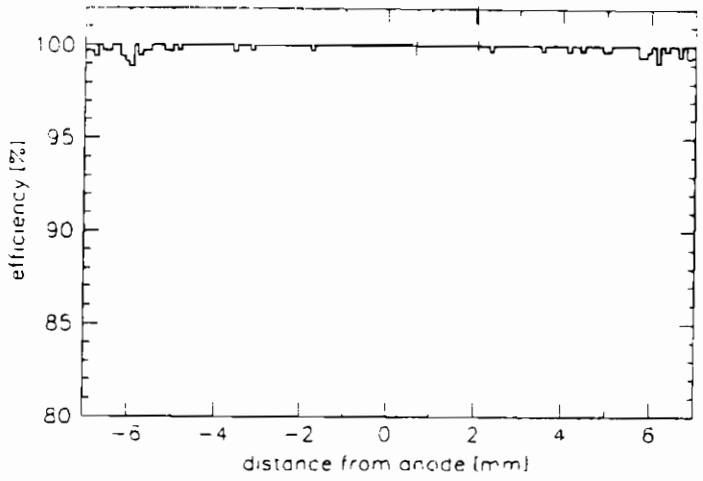

Figure 7: *The single hit detection efficiency as a function of the position in the 14 mm wide drift cell, for a preamplifier threshold of 0.5 V. The anode is at the center of the figure. The average single hit efficiency is 99.9%.*

is too near or too far away from the anode. In the 7 mm wide drift space the deviations from linearity are below 100 μm and were not yet corrected for.

For a distance of 2 cm between anode layers in the arrangement of fig. 1, the single hit resolution of 250 μm translates into an angular resolution for the track segment of better than 2 (2.5) mr for the projection with 6 (4) hits.

An alternative method based on a straight forward calculation of x(t) from the dN/dt distribution from data taken with 0.15 ns binning leads to a still better resolution. For this method a clean event sample is needed: a) tracks have to be distributed uniformly, b) the efficiency has to be flat over the drift volume, c) no additional hits should be present.

In fig. 9 a) a typical time distribution is presented reflecting the change of the drift velocity along the cell. Its integral is the x(t) vs t relation shown in fig. 9 b). In a wide range of the cell the curves behave quite linearly which means a constant drift velocity. Larger deviations are visible only in the first 1.4 mm and the last 0.5 mm of the drift cell.

The advantage of this method is that x(t) is determined directly for each cell without using any track fitting. Hence calibration is not affected by local distortions happening elsewhere. Residuals calculated by this method are considerably smaller than those resulting from track fitting with constant drift velocity. This is demonstrated in fig. 9 c).

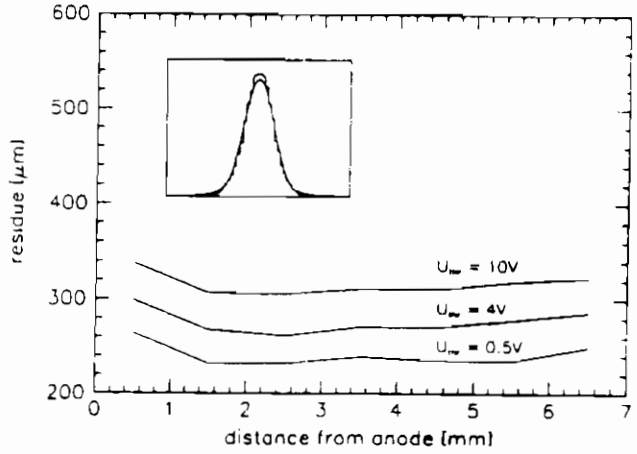

Figure 8: *Residues vs. distance from the anode for three different preamplifier thresholds U_{thr}. The spatial resolution is nearly independent of the distance of the hit to the anode wire. The small picture shows a typical residual distribution, to evidence its Gaussian shape.*

In the central part of the cell the residuals are near to 100 μm, evidencing further potential of this cell. The relative merits of both methods and of the time binnings are still under study.

3.2 The t_0 – RPC at RD5

The RPC (fig. 5 b) mounted together with the 8-layer drift chamber in the test baem at RD5 is a single layer chamber with 70×90 cm^2 sensitive area. The 'slow signals' of the 63 pads , each 10×10 cm^2 large, are read individually for pattern studies with a 8 ns resolution. In addition four groups are formed by ORing 16 pads, as indicated in different grey scales in fig. 5 b. Each group outputs a 'fast signal' for trigger purposes and is measured with a 0.15 ns resolution. A typical distribution of the 'fast' times for 100 GeV muons is shown in fig. 10. Since the distribution is asymmetric a σ is not well defined. The following values are derived: $\sigma_{rms} = 6.5$ ns, $\sigma_{fwhm} = 1.9$ ns and $\sigma_{68\%} = 3.7 = {}^{+4.9}_{-2.4}$ ns. The distribution shown in fig. 10 was not expected to be an improvement over earlier data [7]; it should simply confirm that the first t_0-RPC plane installed behaves properly. Installation of the second plane should follow soon, once tests for a considerable increase in rate capability [10] are finished.
It is clear that a resolution of $\sigma \approx$ 3-4 ns will not identify all bunch crossings (15 ns assumed) and a twin chamber foreseen for the final detector is expected to give better

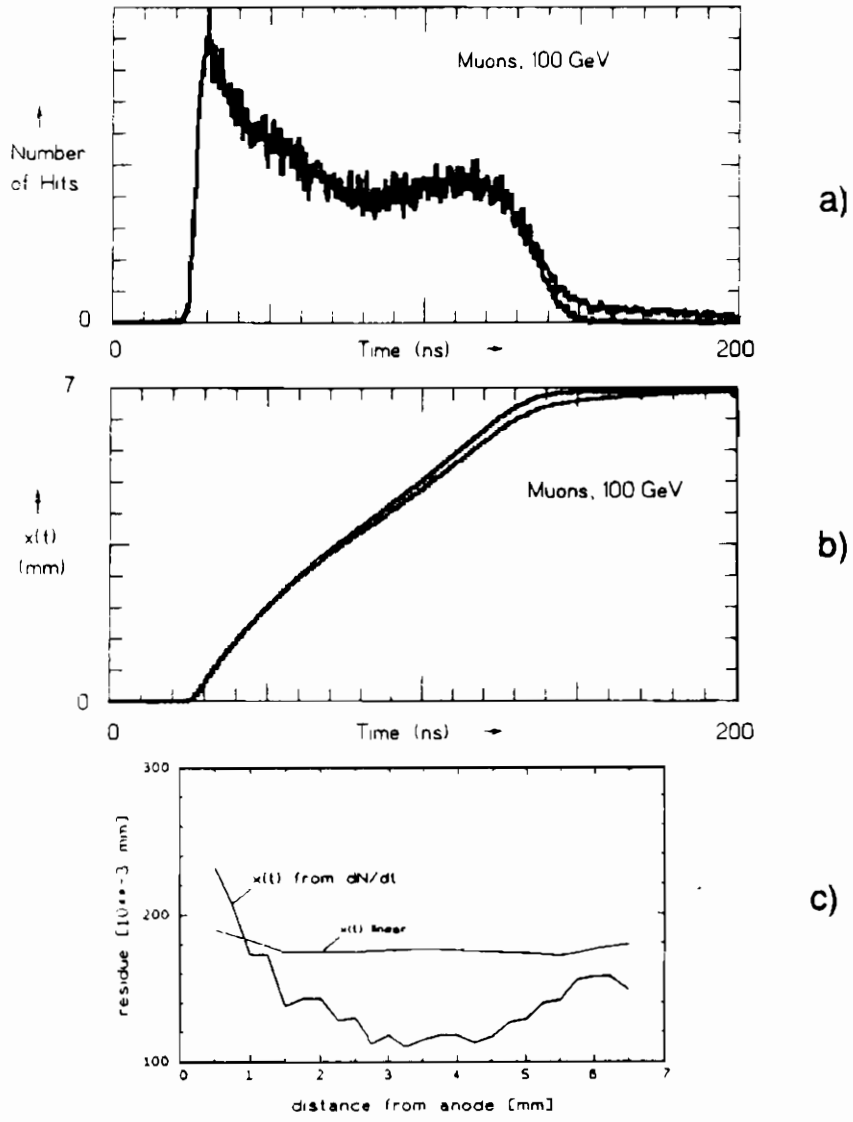

Figure 9: *Direct calculation of x(t) from dN/dt: a) A typical dN/dtdistribution for only one hit per layer (black) and for all hits (gray). They are nearly identical. Data were taken with a Ar/CO_2 gas mixture at 80%/20%. The time resolution is 0.15 ns. b) The x(t) vs t relation derived from the time distribution. c) Comparison of residuals using the 'x(t) from dN/dt' method and using track fitting with the assumption of constant drift velocity.*

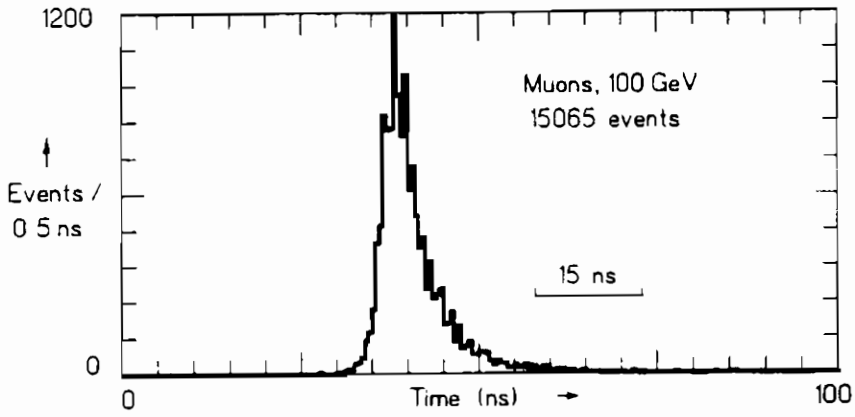

Figure 10: *Time distribution from the RPC.*

time resolution.

4 Triggering with WLDC

A basic idea in the concept of WLDC is the capability to trigger autonomously, without help of external trigger signals, on track segments compatible with particles coming from the interaction point. The trigger process, including the 1^{th} level can be subdivided into three steps which are sketched in fig. 11. The first one is to assign at a very early stage the correct beam crossing number as an event number to each track locally. For this so called 0^{th} level trigger pad shaped fast devices like i.e. a pad RPC are well suited . Furthermore one should be free to adjust the logical shape of the pads, depending on the rates. The degree of granularity (no. of channels) will be a compromise between physics requirement and cost. After this 'level 0 trigger' all subsequent processing of the event data may be done asynchronously.
The 1^{th} level trigger checks whether a group of ≥ 4 (≥ 3) hits lies within a narrow road pointing to the vertex in the projection with 6 (4) layers. Depending on how restrictive this selection has to be done, use of the knowledge on the position of the firing pad may be necessary. Also a multithreshold selection will be provided for each track segment. Data from bunch crossings with a 0^{th} level but no valid 1^{st} level trigger will be discarded. This procedure implies that a muon chamber delivers either data for a good muon candidate or no data at all. It must nevertheless be possible to keep data from no-trigger events, at least for test purposes.

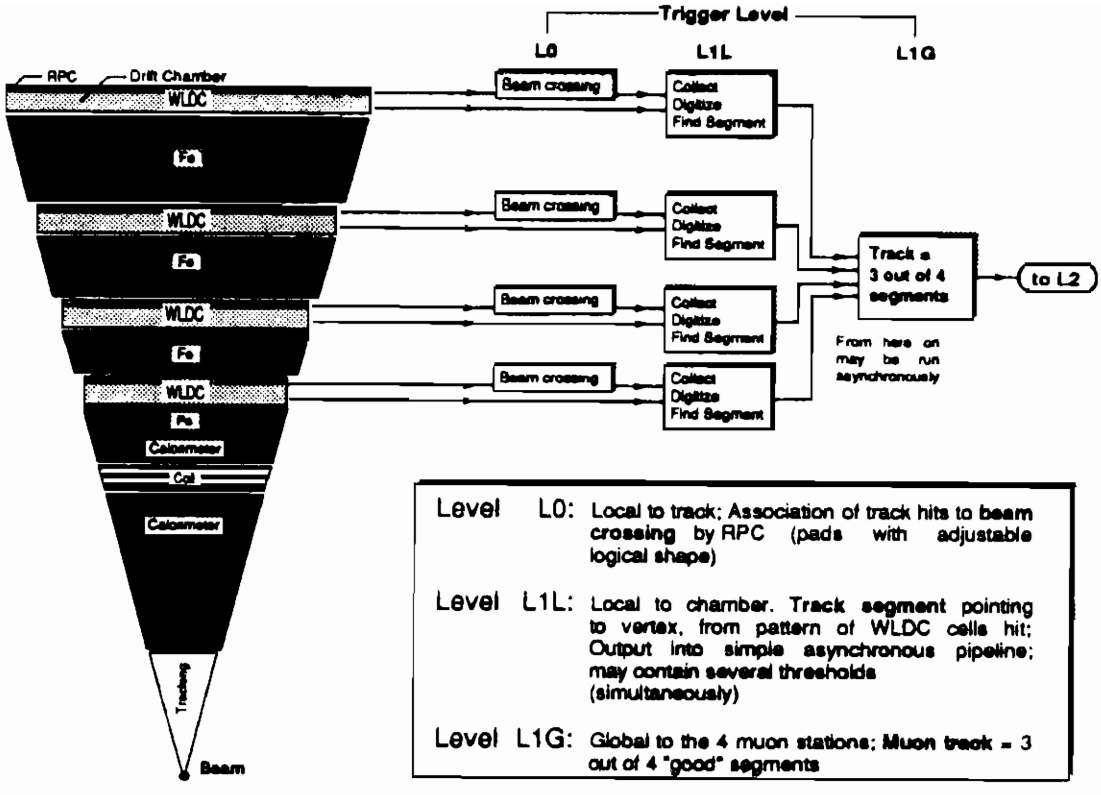

Figure 11: *Trigger scheeme of WLDC.*

5 Conclusion

The proposed drift chamber with a local measurement of the reference time t_0 is a modular, versatile, and robust instrument well suited to all requirements for operation as muon detector at the LHC.

The spatial accuracy for track segments meets the requirements for muon momentum measurement. The local t_0 measurement allows an unambiguous assignment of each track segment to a certain beam crossing and helps to resolve spatial reconstruction ambiguities. This is achieved in a very short time and can therefore also be used for an early reduction of the amount of data. The modular design keeps costs and dead space at a tolerable level.

Prototypes of a wall-less drift chamber and a t_0-chamber were tested extensively with cosmics and in the test beam. Compared to the results with cosmics the data taken at the high energy muon beam of the RD5 experiment at CERN seem to indicate that

a better space resolution of the drift chamber can be achieved. Studies are going on. Further improvement in the performance of the RPC is also planned [10]. Eventually, a measurement of the drift chamber behaviour when operated in a 3 T magnetic field is planned.

Acknowledgements

This work was supported by the Bundesministerium für Forschung und Technologie, Germany.

References

[1] H.Faissner et al., NIM(1993) in press

[2] Proceedings of ECFA Large Hadron Collider Workshop, Aachen 1990, CERN 90-10, ECFA 90-133, vol. I–III
The LHC Study Group, Design Study of the Large Hadron Collider (LHC), CERN 91-03 (1991)
Towards the LHC Experimental Programme, Proceedings of the General Meeting on LHC Physics & Detectors, Evian-les-Bains 1992, CERN, ECFA

[3] Letter of Intent, CMS-Collaboration, CERN/LHCC 92-3 (1992)

[4] Letter of Intent, ATLAS-Collaboration, CERN/LHCC 92-4 (1992)

[5] Letter of Intent, L3P-Collaboration, CERN/LHCC 92-5 (1992)

[6] For a recent review of large aerea drift chambers see: U. Becker, in Instrumentation in High Energy Physics, ed. F. Sauli (World Scientific, Singapore 1992) p. 513

[7] M. Bertino et. al., NIM A283 (1989) 654
R. Cardarelli et al., Nucl.Instr. and Meth. in Physics Research**A310** (1991) 607
R. Cardarelli et al., Nucl.Instr. and Meth.**A263** (1988) 20

[8] We used the programs WIRCHA by J. Fehlmann, J. Paradiso and G. Viertel (ETH Zürich/IHP, 1983), and GARFIELD by R. Veenhof, CERN program library.

[9] A. Böhrer et al., Satus Report of the RD5 Experiment, CERN/DRDC 91-53.

[10] R. Santonico, private communication and contribution to this conference.

Glass Electrode Spark Counter

G.Bencivenni, G.Felici, E.Iacuessa
Laboratori Nazionali di Frascati - INFN, Frascati, Italy

C.Gustavino, M.D'Incecco
Laboratori Nazionali del Gran Sasso - INFN, L'Aquila, Italy

Introduction.

The development of the Spark Counters started from the idea to use a highly resistive material for at least one electrode in a spark gap [1]. In such a way one spark discharges only a limited area around the spark location. The time to recover the electric field, depending on the electrode resistivity, avoids self sustaining sparking. The maximum tolerable particle flux depends on the electrode volume resistivity, that must be stable with the device operation. The electrode surface must be smooth and the material homogeneous, to prevent discharges due to the high electric field applied, of the order of a few kV/mm.

Our investigation shows that the use of glass electrodes, together with a proper detector design, allows both the realization of noiseless Spark Counters, stable in time, and non-critical operation. The modular detector design allows the realization of large sensitive planes at low cost, due to the choice of materials and the low manpower needed. The high gap uniformity achievable by using glass electrodes allows a time resolution less than 1 ns.

In the following we describe the design and the performance of the Glass Spark Counter (GSC) for cosmic ray applications. The performance of a GSC prototype for higher rate applications, realized with low resistivity glass, is also described.

1. GSC for low rate environments.

1.a) Float glass electrical properties.

Low rate applications, as extensive air shower experiments, allows the use of commercially available float glass ($\rho \approx 10^{12}\ \Omega$cm). In fig.1 is shown the volume resistivity at room temperature of a sample of commercial float glass produced by the "Società Italiana Vetro". We tested the float glass stability in time by applying a 2kV voltage to a glass sheet for several tens of days. In fig.2 is shown the glass volume resistivity as a function of the time. We note that, apart from temperature fluctuations, the resistivity does not change with the time. After 52 days, the total integrated charge flowed through the glass sheet is about 10 mC/cm^2. The same charge flows through the device in a time greater than 10 years, at an incident particle rate of 600 Hz/m^2.

1.b) GSC design.

A sketch of the GSC design is shown in fig.3. It consists of a couple of glass electrodes 2 m long, 8 cm wide and 2 mm thick. The 2 mm distance between the electrodes is ensured by PVC spacers inserted without gluing

at the edges of the plates. The spacers are 1 cm long, 5 mm large and are placed 20 cm apart. The high voltage is applied to the electrodes by means a coating of graphite water-based, with a surface resistivity of about 100 kΩ/square. The detector is inserted in an extruded PVC envelop, which acts as a gas container. The H.V. connections to the graphite are located in one of the two end caps which close the GSC module. The gas flows along the module through inlets on the end caps. External pick-up electrodes (not shown in fig.3) are used to detect the induced pulses, transmitted through the resistive graphite coating applied to the electrodes.

The advantages of this design respect to the one of standard RPC are manifold:

- The gas containment is ensured by the external PVC envelop and not by the electrodes themselves. This solution allows uncritical gas pressure operation, avoiding any change of the distance between the electrodes due to variations of the differential gas pressure.
- The use of a discrete number of spacers instead of a continuous frame minimizes the geometrical dead zone and the possibility of spurious discharges due to the high voltage between the electrodes.
- The "E" shaped spacers sustain both the electrodes such that the curvature of the glass is the same for both plates, thus maintaining the gap uniformity. Fig.4 shows that the maximum glass sagitta for spacers 20 cm apart is less than 100 μm. However, as shown in Fig.5, the measured gap uniformity is about 20 μm.
- The long structure of the modules optimizes the gas flowing.
- The simple assembling minimizes the manpower: a preliminary estimate of the costs for a large production is about 100 $/m^2$ [2].

In fig.6 is shown the high voltage connection side of a module, before the insertion in the PVC envelope. In fig.7 shows a 0.5x2 m^2 plane obtained placing 6 GSC modules one next to the other.

The GSC design is open to further developments. One possibility is the use of larger electrodes, say 20 cm wide, in order to minimize the geometrical dead zone of a plane. A production of about 300 modules (8 cm wide, 1 m long), is now in progress, to realize a sampling calorimeter prototype.

1.c) Float GSC performances.

In fig.8 is shown the single counting rate as a function of the high voltage for a GSC plane of 1 m^2. The gas mixture is Ar+Iso-C_4H_{10}+Freon 13B1 = 60%+35%+5%. A wide plateau is visible, the counting level is essentially due to the cosmic rays and ambient radioactivity. The noiseless operation exhibited by GSCs is very important in a large area apparatus, as it allows easy monitoring and calibration.

The efficiency of a module as a function of the high voltage is shown in fig.9. Note that the efficiency knee corresponds to the single counting rate one.

Fig.10 shows the time resolution (rms) as a function of the high voltage. A safe region with a time resolution less than 1 ns is obtained.

1.d) Long term measurements.

Fig.11 shows the counting level of a 0.5x2 m^2 plane as a function of the time. The applied voltage is 8 kV. We note that the counting level is stable during the 3 months of operation. Fig.12 shows the current drawn by the plane as a function of the time. After about 20 days the current level stabilizes, at the level of about 0.4μA/m^2. This value is compatible with the one estimated from charge and counting measurements.

A lifetime test performed by irradiating an area of about 20 cm^2 with a ^{137}Cs source is in progress. In this measurement, the radiation level is about 40 times greater than the level due to the cosmic rays and the ambient radioactivity. After 2 months of irradiation, no changes on the detector performance (i.e. efficiency and time resolution) have been observed. This time corresponds to several years of operation at normal conditions.

2. GSC for high rate environments.

2.a) Semiconductive glass properties.

A big advantage of glass as electrode material is the possibility to adjust the volume resistivity in order to improve the rate capability of the detector. In general, the electrode conductivity can be due to the ion drift inside the electrode (ionic conductivity) or to the electron mobility (electronic conductivity). In the case of the ionic conductivity the device operation can cause an increase of the resistivity due to a reduction of the carriers inside the electrodes, with a worsening of the rate capability.

The semiconductive glass developed and used to build the GSC prototype is characterized by the presence of an appropriate fraction of iron-oxides (Fe_2O_3 + FeO) and a small amount of vanadium-oxides (V_2O_5 + VO_2). Under particular melting conditions, Fe^{2+}+ Fe^{3+} (V^{4+} + V^{5+}) sites, responsible for the electronic conductivity [3], are generated. The resistivity depends on the percentage of iron and vanadium oxides and on the value of the R=FeO/(Fe_2O_3+FeO) ratio.

The electronic conductivity glass has a good stability in time. Fig.13 shows the glass resistivity as a function of time of a glass sheet sample. The applied voltage is 2 kV. After 25 days, the integrated charge per square centimeter flowed through the glass sheet is about 240 mC/cm^2. In the detector the same value is reached after about 10^9 sparks/cm^2.

In conclusion, the electrical characteristics of the developed glass seems adequate to realize a device that can be used in relatively high rate environments. Reproducibility tests indicate the possibility of tuning the resistivity at the 30% level.

2.b) Test beam measurement.

A prototype using 10x10 cm^2 glass with a volume resistivity of about 10^{10} Ωcm has been realized. Also in this case, the device is essentially noiseless even though the glass resistivity is two order of magnitude less than the float glass one.

The GSC performance in a high rate environment was studied at the T7-PS beam facility at CERN [4]. The beam has a spill duration of 220 ms and a spill time separation of about 10 seconds. The beam particles are mainly 10 GeV charged pions.

In the experimental set-up the coincidence of six plastic scintillators select a 1x1 cm^2 beam area on the GSC prototype. The beam spot is about 3 cm in diameter.

Fig.14 shows the efficiency as a function of the incident particle flux. The supplied voltage is 400 V above the knee. From this plot the 90% efficiency level infers a maximum operating rate of ~150 Hz/cm^2. The counting level during the spill time is constant, even at the maximum particle flux achievable. Taking into account that the dead zone is of the order of few millimeters, we estimate a local dead time of about 20 ms, compatible with the calculated value.

Conclusions.

Float GSC for cosmic ray experiments is ready for a large industrial production at low cost. Glass electrodes does not need extra surface treatments and allows the realization of noiseless detectors. The modular design proposed ensures simple assembling and a good gap uniformity.

For the use of GSC in relatively high rate environment, we developed a low resistivity glass. The measurements performed with a small prototype are encouraging. However, further work is needed to realize long semiconductive glass at low cost.

We would like to thank M.C.Spitalieri who helped us in the measurements, and L.Iannotti who built the GSC modules.

REFERENCES

[1] M.V.Babykin et al.,Sov. Journ. of Atomic Energy VI,487,(1956).

[2] M.Meoni (Pol.Hi.Tech), private comunication.

[3] N.F.Mott, Jour. of Non-Crystalline Solids I (1968) 1-17.

[4] G.Bencivenni et al., LNGS Int. Note 92/38, Accepted by Nucl.Intr.&Meth.

FIGURE CAPTIONS

1) Distribution of the volume resistivity of a float glass sample.
2) Float glass volume resistivity as a function of the time. The supplied voltage is 2 kV.
3) Sketch of a GSC module.
4) Glass sagitta as a function of the distance for spacers 20 cm apart.
5) Distribution of the distance between the electrodes.
6) H.V. connection side of a GSC module.
7) A 0.5 x 2 m GSC plane.
8) Single counting rate as a function of the high voltage for a GSC plane of 1 m^2.
9) Detection efficiency as a function of the high voltage.
10) Time resolution as a function of the high voltage.
11) Single counting rate as a function of the time for a GSC plane of 1 m^2.
12) Current drawn by a GSC plane of 1 m^2 as a function of the time.
13) Semiconductive glass volume resistivity as a function of the time. The supplied voltage is 2 kV.
14) GSC efficiency as a function of the incident particle flux.

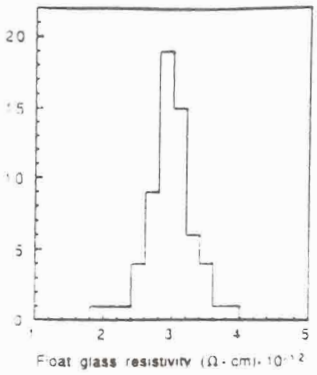

Fig. 1

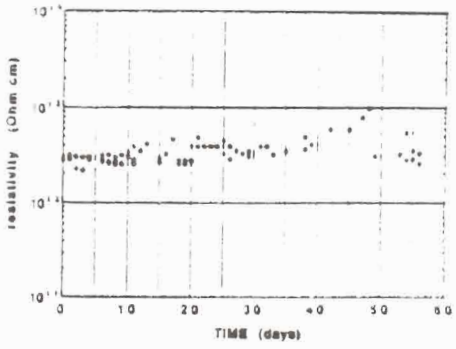

Fig. 2

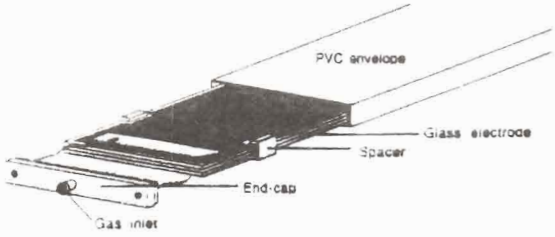

Fig. 3

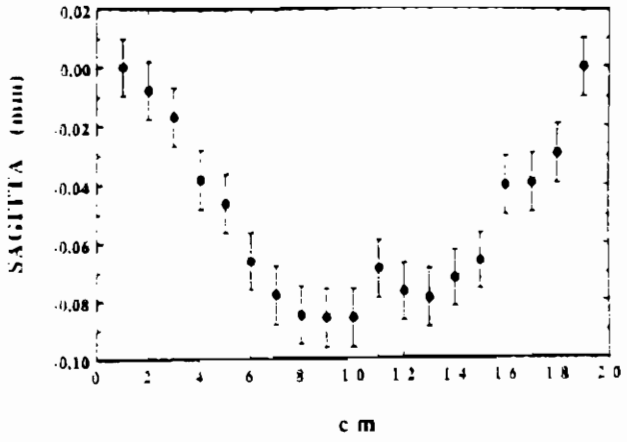
SAGITTA (mm)
0.02
0.00
-0.02
-0.04
-0.06
-0.08
-0.10
0
2
4
6
8
10
12
14
16
18
20
c m

Fig. 4

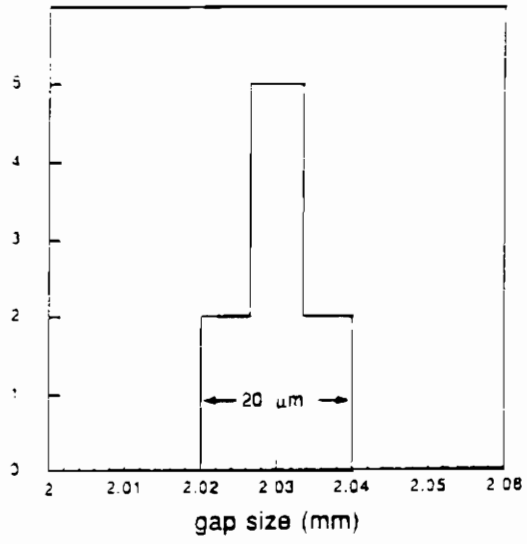
5
4
3
2
1
0
20 µm
2
2.01
2.02
2.03
2.04
2.05
2.06
gap size (mm)

Fig. 5

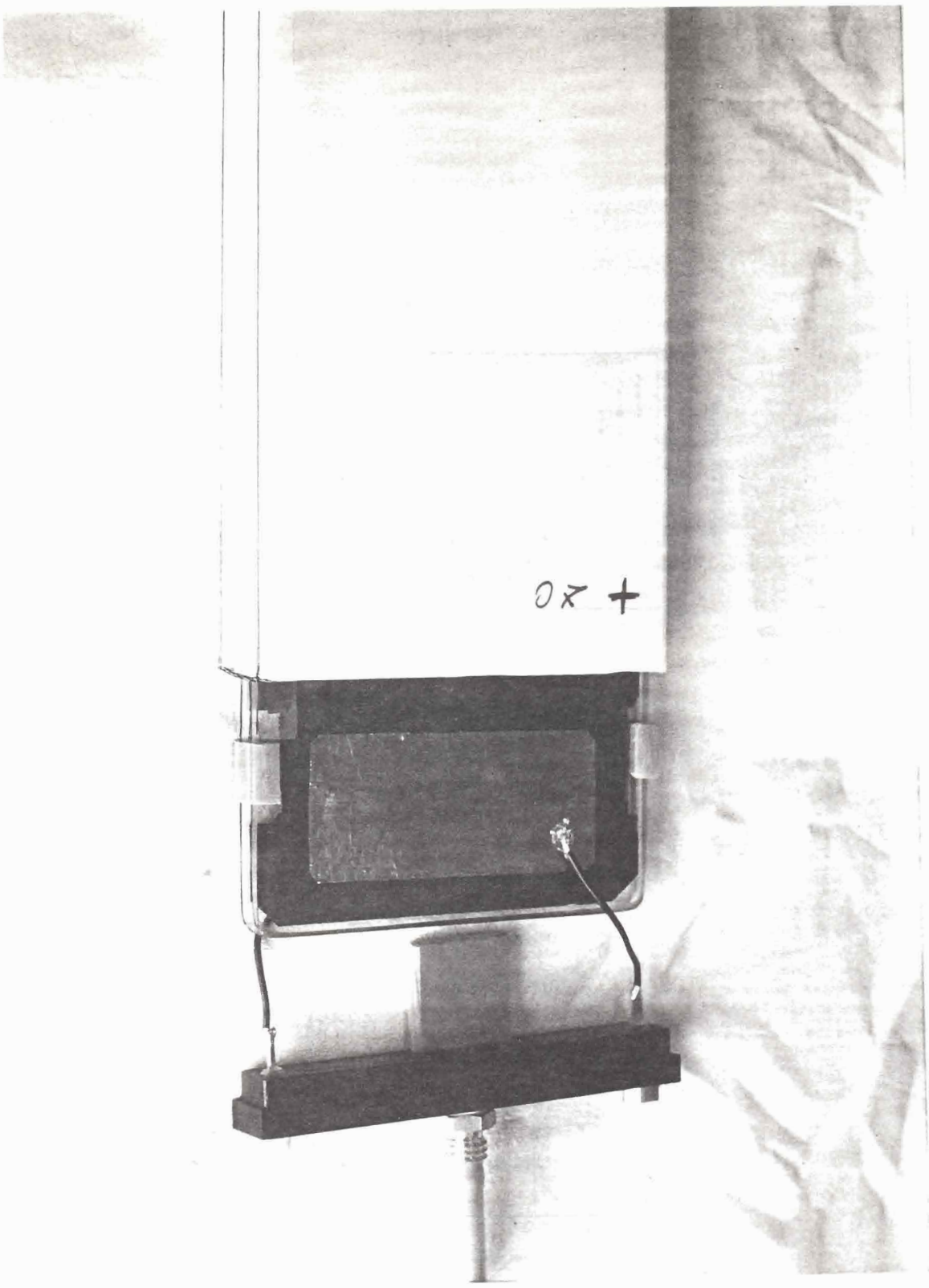

Fig. 6

189

Fig. 7

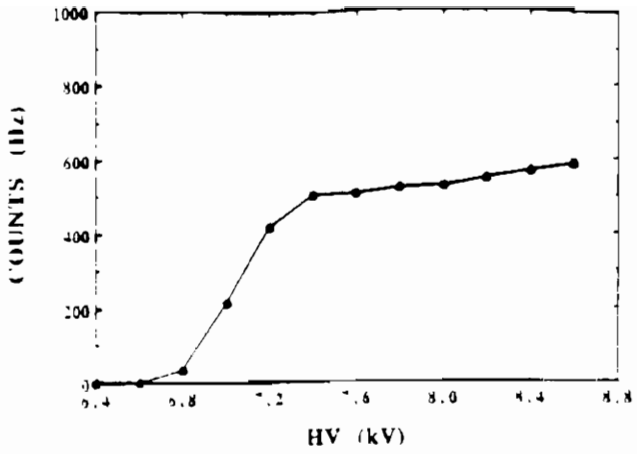

Fig. 8

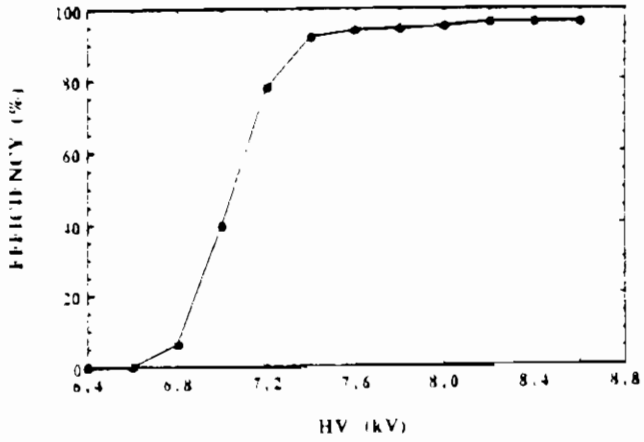

Fig. 9

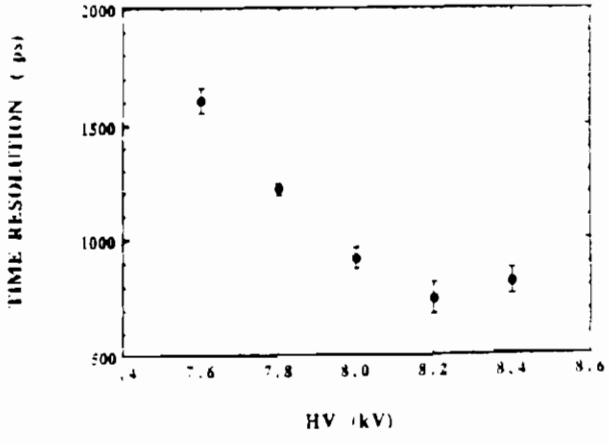

Fig. 10

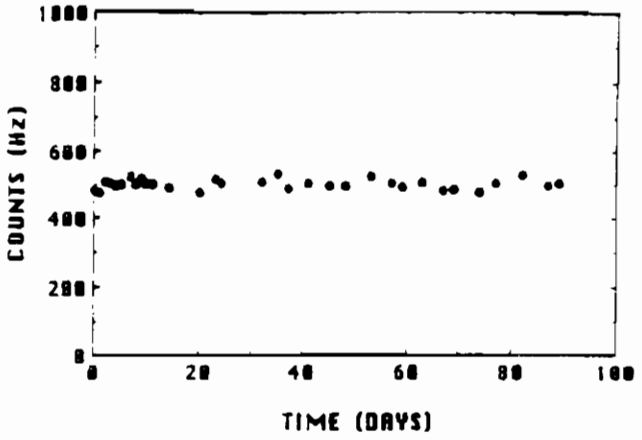
1000
800
600
400
200
0
COUNTS (Hz)
0
20
40
60
80
100
TIME (DAYS)

Fig. 11

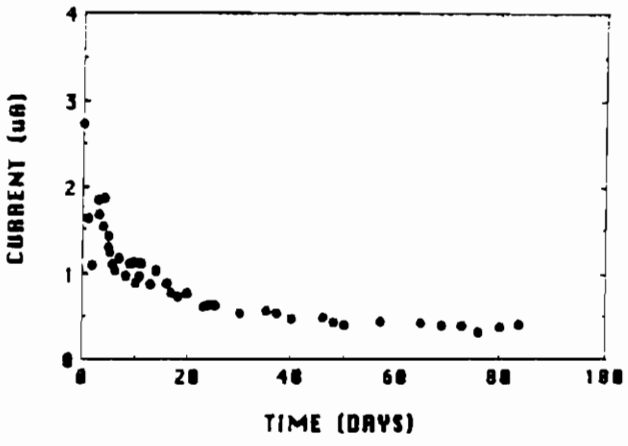
4
3
2
1
0
CURRENT (uA)
0
20
40
60
80
100
TIME (DAYS)

Fig. 12

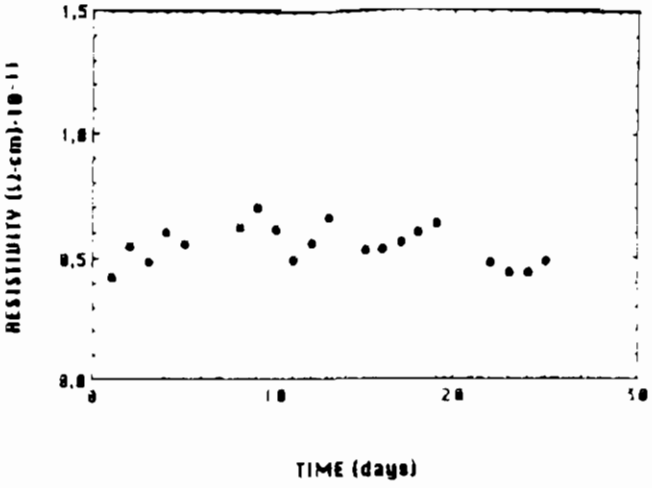

Fig. 13

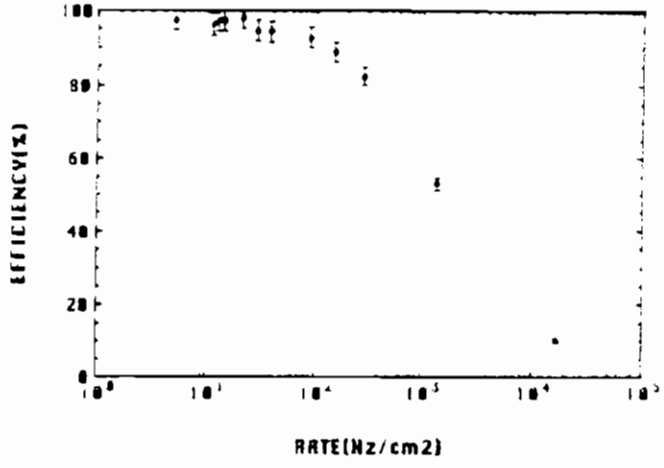

Fig. 14

RPC READOUT FOR PARTICLE ASTROPHYSICS

M.Bonori, U. Contino, F.Massa
Dept. of Physics University "La Sapienza" and INFN Rome
P.le A. Moro, 2 - 00185 Rome, Italy
(presented by U. Contino)

1. Introduction

In this paper we want to illustrate the electronic readout system developed for Resistive Plate Chambers (RPC) [1], [2]

Typical signals from these detectors are characterized by amplitudes of hundreds of millivolts and length of tens of nanoseconds, with rise time of 1-2 ns. This feature characterizes RPC as a good detector for time measurements and makes it a very promising candidate for future experiments in particle physics and astrophysics.

The need of capturing signals with such a small length and rise time, without the typical problem of the ECL technology (power and heat dissipation) leads us to the CMOS technolgy at very large scale integration. Both in passive physics experiments and in those of next generation colliders, typical numbers of readout channels are $>10^4$, each one asking for a time resolution of at least one nanosecond. A solution based on more power expensive electronics, such as ECL technology, could be inacceptable if compared with those numbers. In our research, which was done with the technological support of CAEN firm, we decided to use a monolithic 4-channels TDC [3]: it is produced in a 0.8 μm CMOS technology, which guarantees a very low power dissipation (only 7 mW/channel) with a single pulse time resolution of 1 ns (2 ns for double pulse). Using this chip we have designed a sixteen-channels electronic readout board for our RPC, in which we have reduced the use of the ECL family to the front-end only, gaining a big save in power dissipation without losing timing performances of the integrated TDCs. An on board very fast CPU manages the data to/from the TDCs and the board via a full custom fiber optics interface.

In the next paragraphs we will briefly describe the hardware characteristics of the board, the structure of the integrated TDC and the performances of the prototype.

2. Hardware characteristics of the prototype

The block diagram of the board is shown in fig.1. The TDC board can be splitted in two main blocks: a mother board which contains a very fast CPU (DSP56001 by Motorola), a 96KB RAM (Random Access Memory, 35 ns access time), a 32KB EPROM (Erasable Programmable Read Only Memory), bus drivers and receivers for DSP interfaces and some programmable logic; four smaller printed circuits ($7x15$ cm^2) each one with an integrated TDC and the front-end electronics for four channels. In this way we granted a minimum of modularity to the board, reducing the penalty in case of electronics damages of the front-end electronics of one or more channels, of the integrated TDCs or, finally, of the mother board logic. It is also possible to configure the board to accept 4, 8, 12 or 16 channels.

An on board low power supply circuits (+5V for TTL logic, +3V for TDC CMOS logic, -2V and -5V for ECL front-end electronics), based on switching power supply, completes the hardware of the board and makes it fully independent form read-out electronics and power supply electronics, with direct advantages for the data read-out system logistic.

The *ECL Front-End* (see fig.2 for one channel only) has been developed in order to shape both the signal and the trigger in different ways. Moreover as the TDC measures time differences beetween signals and a common trigger signal, both of them come in the TDC on the same physical line.

We report now a short description of the working principle of the front-end electronics: as a negative pulse (Sx) comes to the negative input of the comparator F1, if it goes over the threshold Vth, the outputs (O1, /O1) of the comparators change their logic status (O1: 0 =>1 and viceversa). As a consequence a short pulse, whose length depends on the transition time (td) of the OR gate (F2), appears at the output of the AND gate (F3). In this way, being td of 2-3 ns (F2 is an ECL gate), it is possible to shape signals coming from the detector with very short time length. A small capacitor could be eventually introduced to increase the shaping time td. On the other side a trigger signal arriving at the positive input of the comparator will not be shaped with the same time because of the presence of the trigger signal itself at one of the two inputs of the OR gate. The shaping time will depend therefore only on the time during which the trigger signal is over the threshold. An ECL-CMOS translator has been added to the front-end logic to be compatible with TDC input signal logic.

As we said, the front-end electronics has a quadruple modularity; a logic FAST-OR is generated for every block and, subsequentially, or-ed on the mother board to produce the 16-channel trigger output signal.

Finally, same *facilities* have been introduced to increase the flexibility of our board:

a) a remote controllable variable threshold (from 0 to -250 mV);

b) a mask register (software programmable) which acts directly on the discriminators (inputs LE and /LE).

In fig.3 typical shapes for a signal and a trigger, as they appear at the input of the integrated TDC, are shown.

The *Integrated TDC* that we chose in our project, was developed for the read-out of wire chambers operating in high rate environments. It is based on the mechanism of Time Memory Cells (TMC), schematically shown in fig.4: the logic status of the input signal (TIN, TIN*) is *frozen* in contiguous memory cells in coincidence with a write signal (WL) delayed of 1 ns from cell to cell. To keep the write delay constant a special signal (Vg) is supplied to the delay gates. This correction voltage is generated using an external reference clock and a feed-back circuit inside the TMC. The logic block diagram of this TDC is shown in fig.5: as it can be seen, it is internally organized in four matrixes (32 rows x 32 columns per matrix), in which are stored the four input signals. Each cell represents a 1 ns storage unit and so the time interval that can be memorized inside the TMC is $\geq$ 1 μs/channel. By using special configuration bits of an on-chip control register, it is possible to associate two (four) matrixes to two (one) channels, thus creating 2 μs/ 2 channels or 4 μs/ 1 channel configurations. A 7 bit decoder register (WRITE POINTER) transfers sequentially the write pulse to the rows of the TMC. Data are read-out through four 32 bit registers (COLUMN I/O) using a second 7 bit decoder register (READ POINTER). The four matrixes have, infact, a double port structure, which allows to work in real time. However due to the general task of the board we

discarded this feature of the TMC, although it could be possible to modify our circuits if future developments asked for it.

To reduce data outputs from 32x4 bits to 6x4 bits a special encoding logic was used inside the TMC. The encoding gives information only about the first transition (if there is one) from 0=>1 in a row: then signals whose time distance inside the TMC in the same matrix is less then 32 ns (the length of a row) will be not distinguishable when they appear in the same row. This problem can be solved using a different way of data read-out, called Serial I/O Mode: in this mode matrixes are read-out bit by bit through a special four bit register (CSR0, see fig.5). However it needs more read cycles of the encoded data mode to be completed. The best solution is a compromise between these two modes and that is why we decided to implement both of them on our board.

The Data Control and Tranfer System is represented by a DSP based hardware architecture, with an on board RAM (96KB deep) and a read only memory U-V erasable (EPROM, 32KB deep). We do not want to describe this particular processor technically, for which we refer to bibliographic notes [4], but to illustrate the motivations which are at the bases of our choice.

First of all DSP56001 has two on board interfaces, which can be configured either as general I/O ports or as dedicated interfaces (a 1-byte parallel port, which is called Port B, and two serial ports, Port C, respectively). We configured Port B as a general purpose I/O port (15 bits wide) and using an asynchronuos programmable logic we realized the control system which generates all the data taking signals and synchronizes the four TMCs. This block (referred as Asynchronuos Control Logic in the block diagram of fig.1) generates also some particular signals used for the calibration of the TMCs. The possibility offered by the Port C has been exploited to implement:

- an RS232 interface which allows to work in a stand alone mode and an easy hardware debug of the board ;
- a serial synchronous interface with a rate of 5 Mbit/sec for data transmission via a full custom fiber optic interface.

Another feature of the DSP56001 is its data bus parallelism (24 bits), which matches with the one of the encoded data TMC register.

This DSP is also a very fast CPU, with an instruction cycle of 100 ns (at a 20 MHz clock frequency) or 50 ns (with the new 40 MHz version), which allows TMC data buffers read-out to be completed in a very short time. For example, when using the serial I/O mode DSP at 40-20 MHz clock frequency it takes about 150-300 μs to download completely up to a maximum of 6 TMCs (our board contains four TMCs), while the encoded data read-out DSP needs 3.2-6.4 μs/TMC.

Finally DSP56001 has two hardware interrupt lines, that we have used to implement a particular algorythm suited to reduce TMC dead time (i.e. the time interval during which TMC can not receive signals) to its data buffers read-out time only (see below). Fig. 6 summarizes the interfaces capability of DSP56001, and the way we used them for our TDC board.

In conclusion we want to stress the fact that having adopted hardware architecture based on a local processor unit (DSP), it is possible to build automatic procedures for remote calibration of the several functional blocks of our TDC, in particular the front-end electronics, the trigger machine and the TMCs. We think that this feature is of outstanding importance in all TDC system read-out distributed on very large surfaces (such as in passive physics experiments) or with a very high number of channels (such as in colliders for high energy physics experiments). This is also true if you wanted to process the TMC data to extract further information (such as a mean time for example) in a short time and locally on the detector.

3. Test of the prototype

The prototype of the TDC board we used in our preliminary test consisted of the mother board onto which we plugged one TMC board. Only the first test concerned DSP-TMC interface: in particular, by using the set-up showed in fig.7 we verified the encoded data interface and the serial I/O interface. In a further test we substituted the pulse generator with the outputs of four phototubes (PM) according to the experimental set-up shown in fig.8. The histogram of fig.9 of the time difference beetween the start of the PM#4 and the stop given by the quadruple OR of the four PMs shows clearly that the electronic front-end does not degrade the TMC performance concerning its time resolution (about 1 ns), the intrinsic time resolution of the PM being smaller.

With the tests we have verified the proper functionality of the electronics and have controlled the time performances of the TMCs. All of them gave good results.

4. Conclusion

We have presented a 16-channel TDC with a time resolution of about 1 ns, a time pipe-line of 1 μs/channel, a very low power dissipation (7 mW/channel for the integrated TDC), with good flexibility (thanks to a local processor unit) and with the possibility to be interfaced to fiber optics trasmission lines via a full custom fiber optic interface and a serial sinchronous interface with data transfer rate of 5 Mbits/s. The tests we have done are preliminary, but are very promising for the future possibilities offered by this board in the field of RPC read-out for particle physics and astrophysics.

Acknowledgments

We want to thank CAEN firm for all the technological help which supported our work.

References

[1] M.Bonori, U.Contino and F.Massa: "Glass Electrodes RPC: Performances and Working Model"; proceedings of the Internat. Conf. on RPC technology; Feb. the 18th-19th 1993, Tor Vergata University, Rome (Italy).

[2] R.Santonico et al.: "Progress in Resistive Plate Counters"; NIM, A263 (1988), p.20.

[3] Y.Aray et al.: "A CMOS 4 channel x 1K Time Memory LSI with 1 ns resolution; KEK preprint 91-49.

[4] Motorola Corp.: "DSP56000/DSP56001 Digital Signal Processor; User's Manual", DSP56000 UMD/AD Rev 1.

Figure Captions

Fig.1 - Schematic block diagram of the TDC board
Fig.2 - Functional block diagram of the ECL front-end (for one channel)
Fig.3 - Signal and trigger as shaped by the front-end shaper
Fig.4 - Schematic diagram for one time memory cell
Fig.5 - Logic block diagram of the integrated TDC
Fig.6 - DSP56001 interface layout for the TDC board
Fig.7 - Experimental set-up for the preliminary test on the TDC board
Fig.8 - Experimental set-up for the front-end electronics and TMC performance test
Fig.9 - Histograms of the time difference beetween the PM#4 and the quadruple of the four PMs (see fig.8).

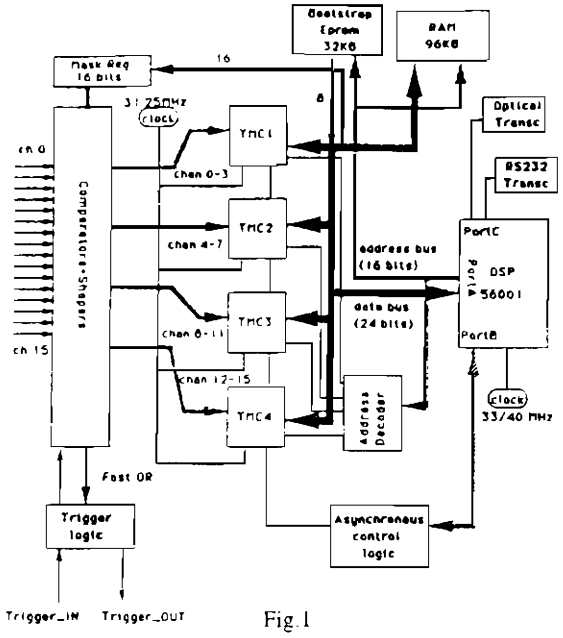

Fig.1

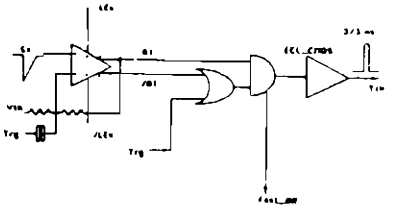

Fig.2

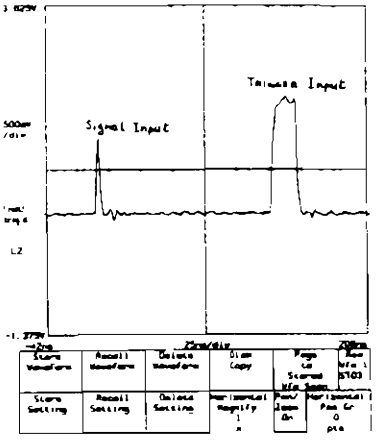

Fig.3

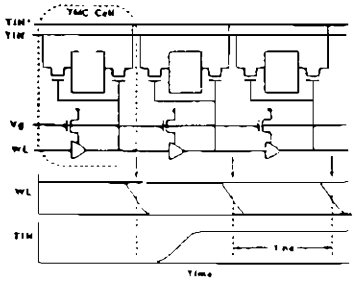

Fig.4

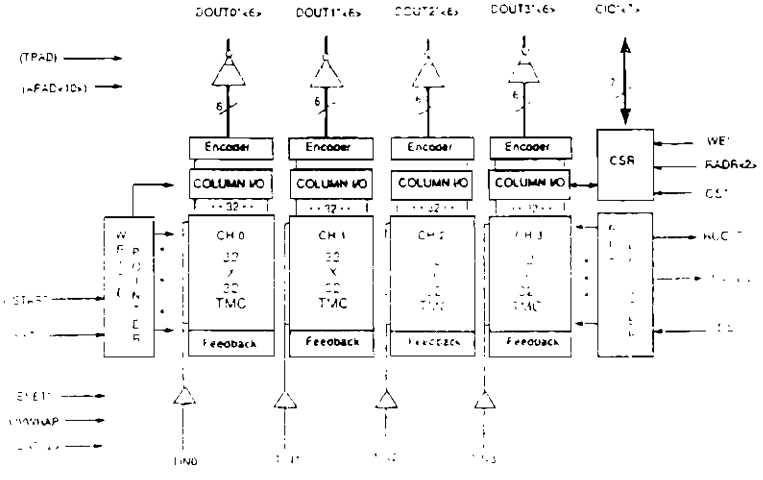

TMC1004 Block Diagram

Fig.5

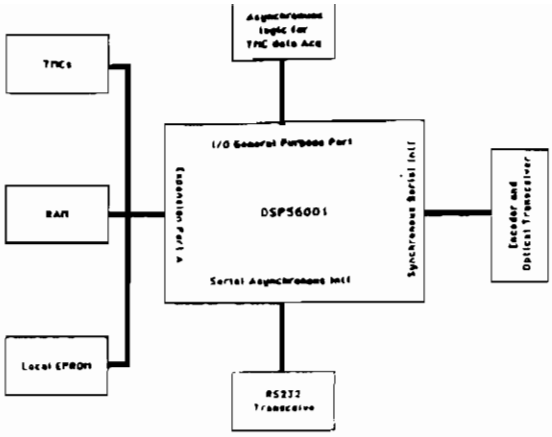

Fig.6

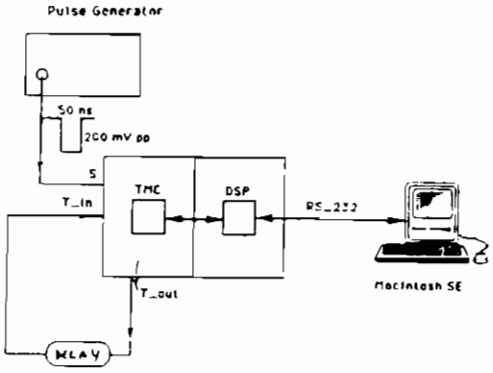

Fig. 7

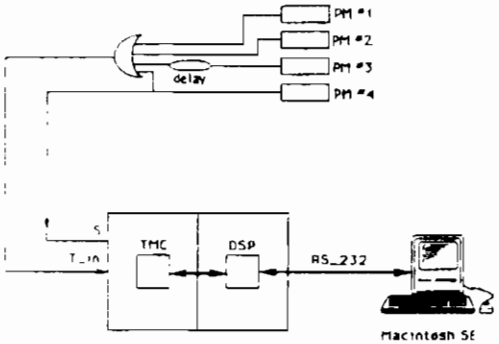

Fig.8

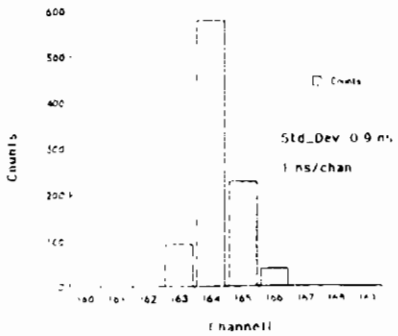

Fig.9

RESULTS OF TESTS OF PROTOTYPE RESISTIVE PLATE CHAMBERS

I. Crotty, J. Lamas Valverde, G. Laurenti, M.C.S. Williams and A. Zichichi

L.A.A. Project, PPE Division, CERN, Geneva, Switzerland.

1. Introduction

In this paper we discuss the results of our tests performed on two prototype RPC chambers. Most of these results have already been reported[1] and here we will extract our principle findings and discuss them in the context of understanding some of the parameters that control the operation of the RPC.

2. The Construction of the Test Chambers

We tested two types of chambers, the cross sections are shown in figures 1 and 2. The chamber with phenolic plates was an attempt to reproduce the chambers described in references 2 and 3. The phenolic plates are 2 mm thick paper based phenolic available in the CERN stores. We measure the resistivity to be 3×10^{11} Ω cm over the full test range of 0 to 8000 volts across the plate. The plates are 30 x 35 cm^2 in size. On one side we cover an area of 25 x 30 cm^2 with carbon paint that has a resistivity of 5 k$\Omega/\square$. We cover this with a thin sheet of glass-epoxy board (0.2 mm thick) also painted with carbon paint on one side; the carbon paint is connected to a copper electrode on the glass-epoxy foil. The layers of carbon paint are in contact, thus a voltage can be applied to phenolic plate by applying the voltage to the copper electrode on the glass epoxy foil. This is covered with a 200 μm thick foil of mylar, and finally we place the signal pickup board. This is a printed circuit board, 1 mm thick, on which we have etched just one pickup pad of 22 x 26 cm^2. The same procedure is used for both phenolic plates making the chamber. The two plates are held apart by a PVC spacer 2 mm thick. This

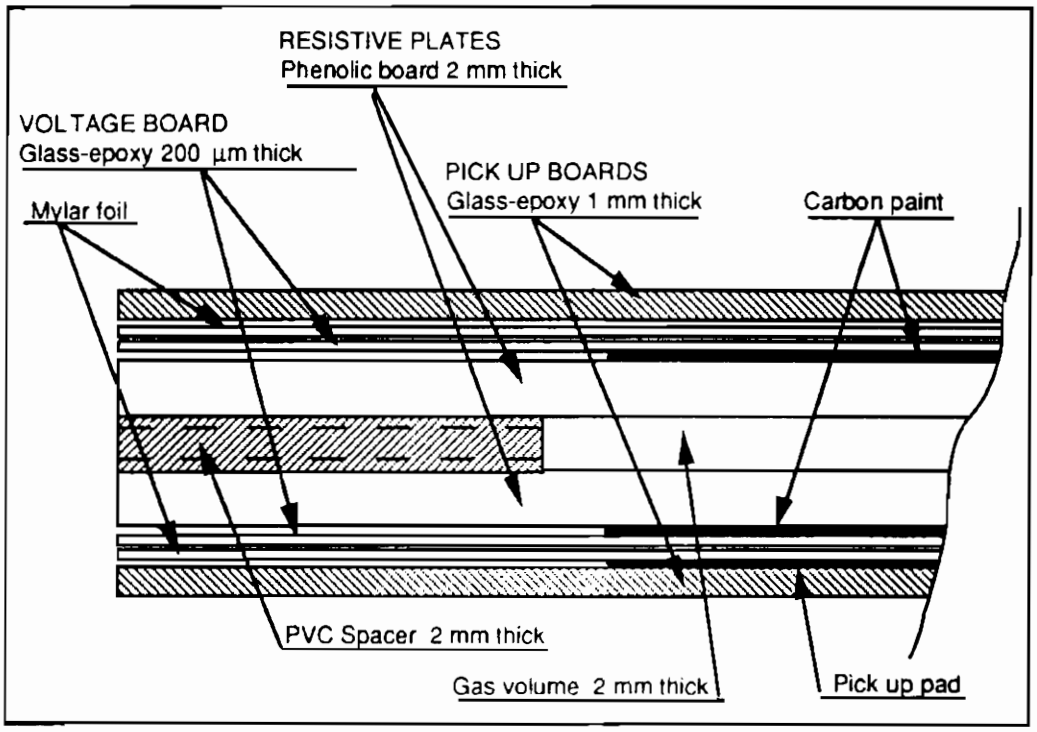

Figure 1: Cross section of Phenolic type Chamber.

spacer is glued to the edges of the phenolic plates making a gas tight envelope. Gas is fed into this gap with small pipes through this 2 mm spacer. Finally this test chamber is held together and rigid by clamping it between two sheets of 1 cm thick Plexiglas. One difference between our test chamber and those built by Santonico et al. is that they apply a layer of oil to the surface of the phenolic. This is required to remove finger prints and fill scratches created in the construction of the chamber. Since our test chamber is small we could ensure that the surface was not scratched. We cleaned the phenolic plates just before sealing the chamber.

The chamber shown in figure 2 has been constructed by Pol.hi.tech# . This chamber has an active area of 26 x 26 cm^2. The cellulose foil is painted with carbon paint in a similar way as the phenolic boards. The cellulose is then glued to a polycarbonate support board 6 mm thick with tubular cross section. The pickup strips are glued to this support board, followed by another support board with the tubes running orthogonal to the first. Finally a ground plane forms the outer surface. We measure the resistivity to be 0.9 x 10^{12} Ω cm at

Pol.hi.tech, S.P. Turanense Km. 44,400. 67061 Carsoli (AQ), Italy

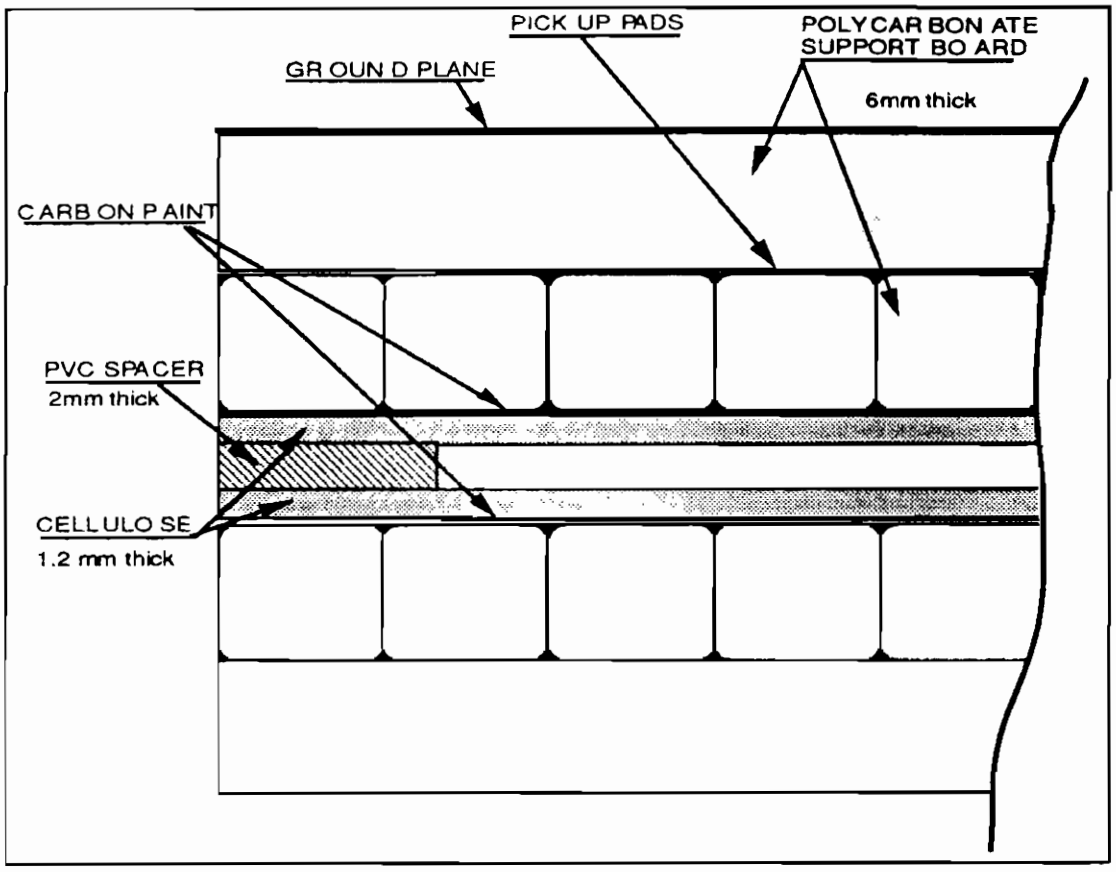

Figure 2: Cross section of 'Cellulose' type Resistive Plate Chamber

22°C and 3.6 x 10^{12} Ω cm at 11°C. For our tests we have connected all strips to form one pad.

3. Test with Cosmics

We mounted the chambers horizontally and tested with cosmic rays. In figure 3 we show the detection efficiency versus high voltage for various gas mixtures. The curves are to guide the eye. The cellulose chamber appears to have a higher value for the efficiency, but the efficiency drops with increasing high voltage; however with 6% freon the plateau appears flat. For these tests the signal from the chamber was amplified by a x10 amplifier and then discriminated by a standard discriminator. The threshold was set to be just above the noise and was typically between 50 and 100 mV (i.e. between 5 and 10 mV of the chamber signal).

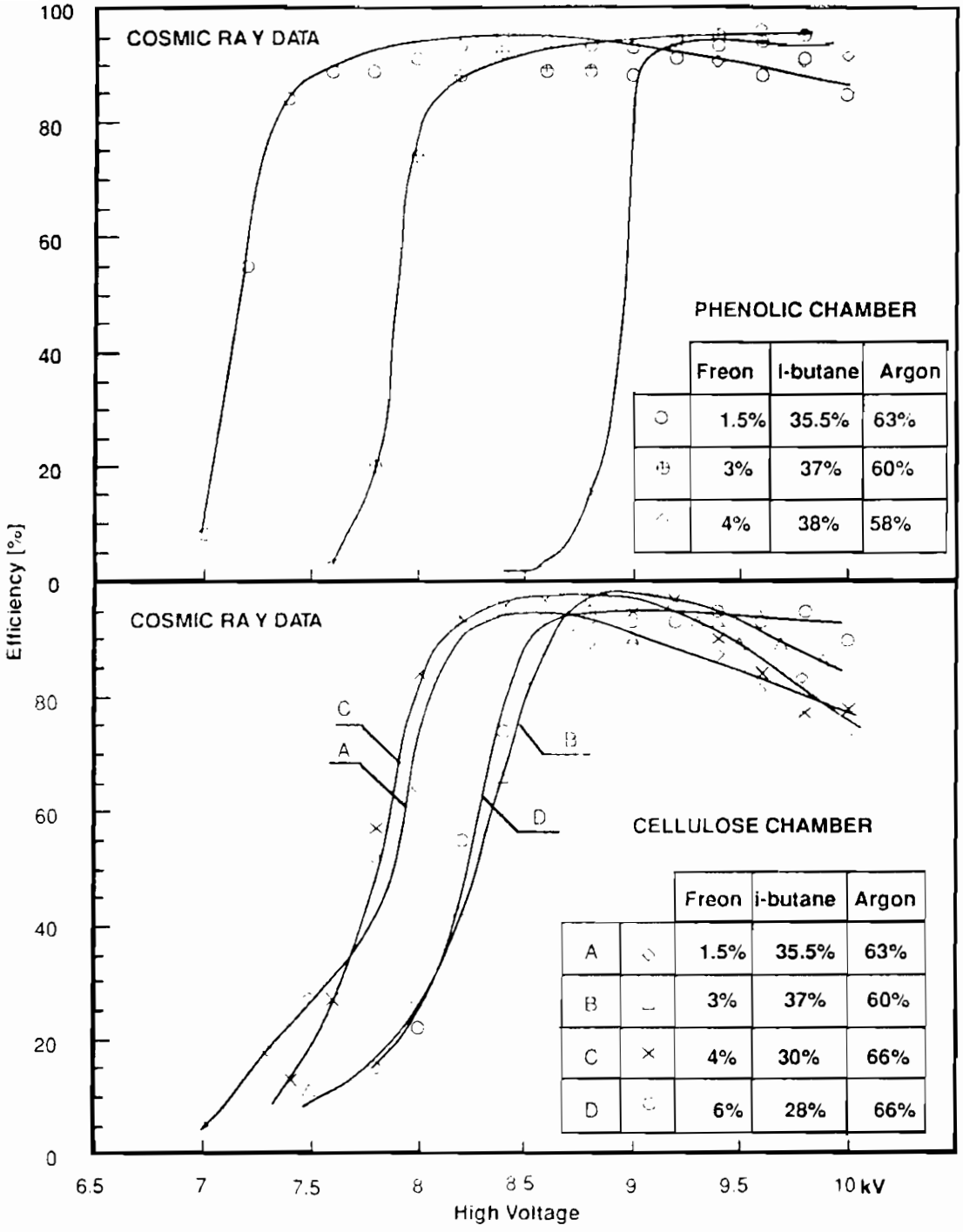

Figure 3: Efficiency versus voltage for cosmic rays using different gas mixtures

4. Test with Test Beam

We have mounted the chambers in a test beam in the East Hall at CERN. The beam was defocused (by turning off the last two quadruple magnets) so that the particle flux was largely contained in a 10 cm diameter spot. We selected the central 10 x 10 cm^2 of the chambers with a scintillator. We measure the efficiency by counting the number of particles in our scintillator telescope and also the number in coincidence with a signal from the chamber under test. The telescope signal width was 150 ns and the chamber signal width was 50 ns. The timing was set so that a coincidence would be registered if the chamber produced a signal within 100 ns of the average time of the signal from the chamber. With this arrangement we feel confident that our results have not been affected by (a) changes in the timing of the chamber signal at high rates and (b) effects due to two particles not being resolved at high rates. The particles arrived in a spill of 350 ms every 15 seconds. The efficiency was calculated by integrating over several spills, and the flux is the average flux during a spill. We observed a large drop of 45% in the efficiency with an increase in flux from 0 to 100 Hz/cm^2. This is in disagreement with the rate dependence measured by Bertino et al.[4] who measured a drop from 97% to 86% for the same increase in flux (0 to 100 Hz/cm^2).

A possible explanation of this discrepancy is as follows. These chambers operate in a quenched spark mode. Through-going ionising particles initiate a discharge. This discharge deposits charge on the surface of the resistive plates. This charge reduces the electric field making this particular region less efficient. This charge on the surface is removed by conduction through the resistive plates. However, on a shorter time scale the charge can diffuse laterally, thus reducing the voltage by a small amount over the whole plate. Bertino et al. tested a chamber with an active surface of 2m x 1m; the test beam was concentrated in a spot (3 x 3 cm^2 or maybe a bit bigger). In comparison our chamber is much smaller and we used a beam that covers a large part of the chamber. Thus for the test performed by Bertino et al. lateral diffusion can play a role.

To check this hypothesis we tested the chambers with a beam spot of (a) 4 x 5 cm^2 and (b) totally defocused, thus completely covering the chamber. The efficiencies as a function of the beam intensity for these two conditions are shown in figure 4. One can see that when the beam is confined to a small area of the chamber (the beam spot of 4 x 5 cm^2 is 3.5% of the phenolic chamber area of 22 x 26 cm) a rate of 1 kHz/cm^2 (in this spot) will reduce the efficiency to

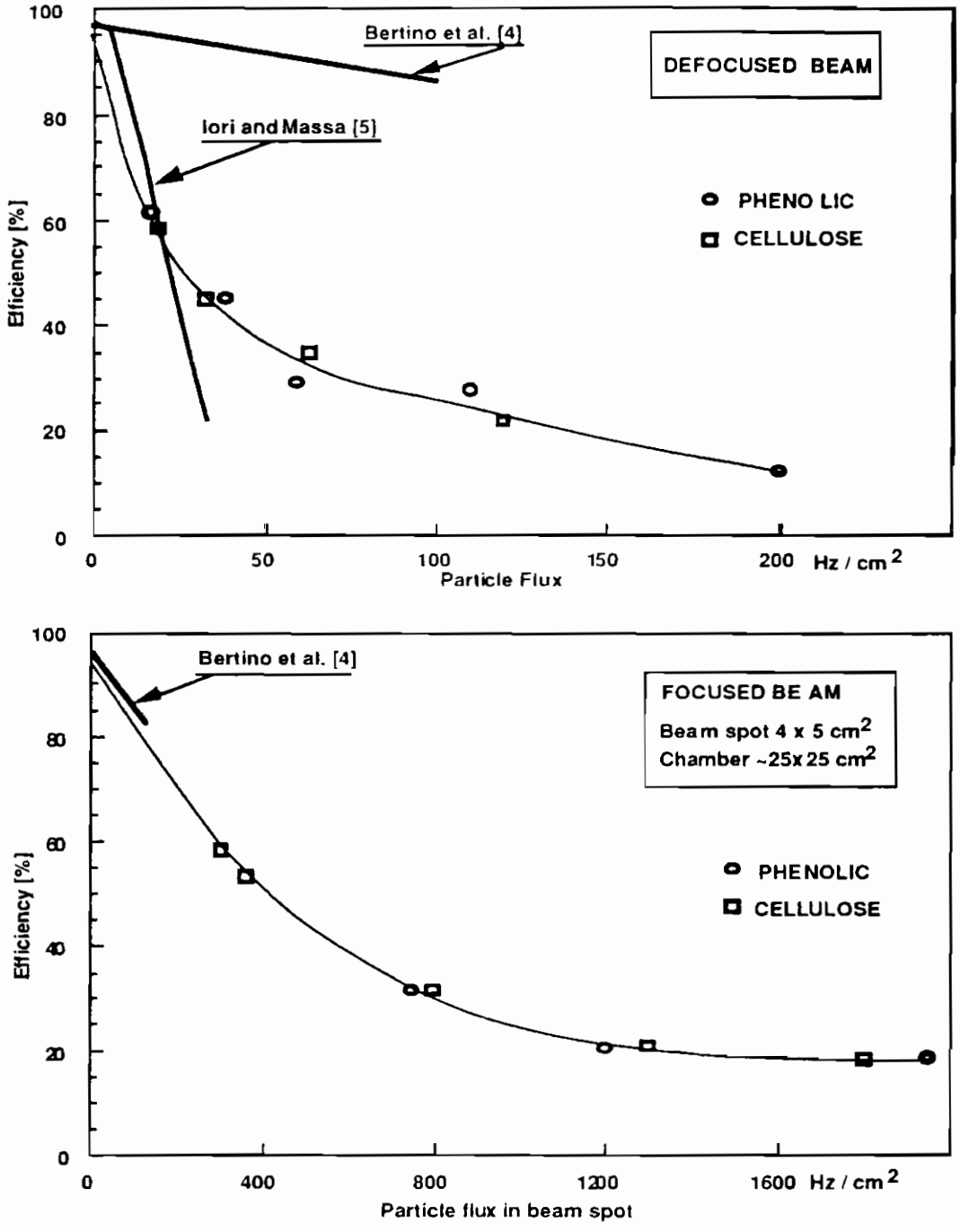

Figure 4: Efficiency versus particle flux for two conditions; focused refers to a beam spot of 4x5 cm^2. Defocused refers to a uniform beam illuminating the whole chamber.

25%. A similar drop in efficiency can be obtained by having a rate of 100 Hz/cm^2 over the whole chamber area. One should also note that if we extrapolate the focused beam results to 95% at 0 Hz (the smooth curve), the slope of this curve for the focused beam data is very similar to the result published by Bertino et al. We also show in figure 4 the results from a rate dependence measured by Massa and Iori[5]. For this test they exposed a large chamber to a continuous flux of photons from the Triga reactor and measured the efficiency at various places of the chamber with cosmic rays. Our result is in good agreement with theirs.

5. Discussion

It appears to us that the drop in the efficiency is dominated by the charging of the plates. We have measured the capacitance of the 2 mm thick phenolic plates by charging a plate and then discharging through a known resistance. We did this by coating two surfaces of a phenolic plate with a conductor (copper and carbon both gave similar results) and then charging this plate to 100 volts with a power supply. An oscilloscope, with a 100 MΩ impedance probe, monitored the voltage across the plate. We then opened the switch connecting the power supply to the plate and observed the voltage drop. The drop in voltage shown in figure 5 on a log scale. The surface coated with a conductor is 20 x 20 cm. Thus using a resistivity of 3 10^{11} Ω cm, the internal resistance of the plate is 150 MΩ. If one calculates the capacitance using the standard formula for a plate capacitor, and using a dielectric constant of 5, one calculates a capacitance of 2.5 pF/cm^2 and thus has a capacitance of 1 nF for the 20 x 20 cm^2 plate. Using this information one calculates a time constant τ of 60 ms. Obviously figure 5 shows disagreement with this simplistic calculation. First one sees that the drop in voltage is not a simple exponetial and secondly, in the most part the time constant is 10 times larger and there is a long tail. The charge in actually fact does not sit on the surface of the plate, as in a classical parallel plate capacitor, but migrates through the plate. The rate dependence of a RPC must depend on this time constant, this measurement shows that one should take a larger time constant than one obtains from the classical calculation.

The average charge in a discharge has been estimated by Cardarelli et al.[3] to be 0.1 nC. However this is only a measure of the fast component. The charging of the resistive surface will be dominated by the residual positive ions and electrons left after the discharge. This quite easily can be 100 time larger than the fast component. However even if we use this average charge of 0.1 nC and consider 50 discharges per cm^2 together with a capacitance of 2.5 pF (since the charge is initially deposited on the surface this may be the

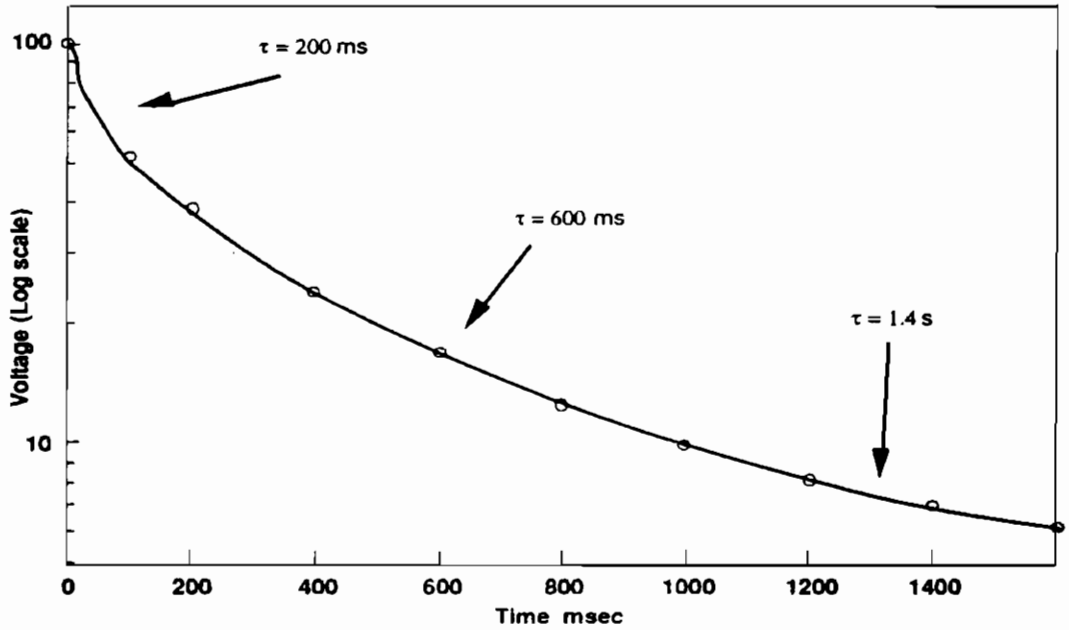

Figure 5: Voltage across phenolic plate being discharge through an external 100MΩ resistor.

correct figure to take), we obtain a voltage of 2000 volts. This is balanced by the conductivity through the plate with $\tau > 1$ sec. Obviously the time between spills (15 sec) is enough to discharge the phenolic plate and the also the cellulose plate, which has a resistivity 5 times higher. Given these figures our measured drop in efficiency is not so extraordinary.

6. Conclusion

RPC's with plates of 3 10^{11} Ω cm have severe rate problems. The good timing resolution is also destroyed with increasing rate. We have tried using plates of materials with lower resistivity (10^9 Ω cm); however chambers with these plates would enter a mode of continuous discharge. It appears that several groups have operated chambers with plates of ρ = 4. 10^{10} Ω cm. One assumes that the rate dependence of these chambers should be better, but we suspect that the operation of these RPC's will still be limited to below 50 Hz/cm^2.

References

1. I. Crotty et al., CERN/PPE 92-182, CERN/LAA-MC 92-018, accepted for publication in Nucl. Instr. and Meth.
2. R. Santonico and R. Cardarelli, Nucl. Instr. and Meth. 187 (1981) 377;
3. R. Cardarelli et al. Nucl. Instr. and Meth. A263 (1988) 20.
4. M. Bertino et al., Nucl. Instr. and Meth. A283 (1989) 654.
5. M. Iori and F. Massa, Nucl. Instr. and Meth A306 (1991) 159.

GLASS ELECTRODES RPC : PERFORMANCES AND WORKING MODEL.

M. BONORI, U. CONTINO, F. MASSA
Dipartimento di Fisica, Universita' di Roma "La Sapienza" and INFN, Sezione di Roma, Rome, Italy
(presented by F. Massa)

1. Introduction

We present the results of a test of the performances of three resistive plate counters (RPC) with glass electrodes of volume resistivity $\rho \approx 2 \times 10^{12}$ Ωcm and of relative dielectric constant $\varepsilon \approx 5$. All the counters have a sensitive area A = 27x125 cm^2.

For each counter negative signals are induced on nine strips (3cm wide and 125 cm long) placed on one of the two surfaces of the counter (signal surface) and a negative high voltage Vo is distributed over the opposite surface (high voltage surface).

For two of the counters a graphite film is used on the respective RPC surfaces for the high voltage distribution and for the capacitive coupling of the strips. One of these two counters (counter A) has the gas gap dg = 1.6 mm and a glass thickness dv = 2.0 mm. The other one (counter B) has dg = 2.0 mm and dv = 3.0 mm.

A third counter (C) has been built in all similar to the counter B, but instead of the graphite it has a silver film deposited on the glass[1] (**fig. 1**). On the signal surface the direct coupling of the silver strips to the glass electrode eliminates the expected inevitable signal losses due to the graphite film. The silver read out strips directly deposited on the glass electrodes provide an undistorted pick up signal, which is a fundamental requirement for a study of the spark formation and development. On the high voltage surface the silver film has been used first with a rectangular shape covering the sensitive area, then the high voltage electrode has been cut in strips of the same dimension of the read out strips (see par. 2).

A cosmic ray telescope has been used to measure the RPC performances. The telescope consists of four scintillation counters selecting an area of 10x10 cm^2, assembled in two couples with a 5 cm thick lead plate inserted between them. The signals from one end of the strips are sent to an ADC (LeCroy 2249 A, .25 pc/chan) to measure the signal charge. The signals from the other end of the strips are first discriminated and shaped (20 mV threshold, 50 ns width), then sent to a logical OR.

The time of the OR signal is measured with a TDC (LeCroy 2228 A, 100 ps/chan) started by the scintillator telescope signal. This last signal, shaped at 200 ns, is also used as gate of the ADC.

The RPC efficiency is then measured not only from the coincidences with the scintillator telescope, but also from the number of events in the 100 ns time window of the TDC spectrum and from the number of events separated from the pedestal peak in the ADC charge spectrum. The data show an excellent agreement between the different efficiency measurements.

2. RPCs performances

The gas mixture normally used is, if not otherwise specified, 71% of argon, 24 % of isobutane and 5% of freon at a flow rate of 5.6 volume per hour.

---

[1] the glass framework with the associated silver deposition has been produced by the Saint Gobin s.p.a. of Pisa (Italy)

The ADC spectrum of the strip signals shows a large amount of charge distributed at values less than the ADC pedestal. The charge q_+ of these signals has polarity opposite to the charge q- expected for ionizing particle induced signal. A voltage independent value $q_+/q_- \approx .5$ is observed.

This effect is interpreted as the capacitive coupling of the strips to the high voltage plane (graphite or silver plane). In fact a spark generated by an ionizing particle crossing a strip induces signals of opposite polarity on the same strip and on the high voltage plane. Cutting the high voltage plane in strips of the same dimension of the read out ones, the effect is heavily reduced to $q_+/q_- \approx .1$.

Fig.2a shows an example of the charge distribution obtained summing the charge of the nine strips for the cosmic ray telescope triggers for HV = 5.6 KV (8 db of attenuation). One sees pedestal events at channel 50 and a peaked charge distribution (average value equal to 123. pc) due to single sparks, well separated at this voltage from the flat distribution due to the events with after pulses.

A different spectrum is obtained gating the ADC with the logical OR of the strip signals , that is for all the RPC signals greater than the 20 mV threshold discriminators (self trigger). This spectrum is shown in **fig.2b** for HV=5.6 KV (8 db of attenuation). One recognizes the same charge distribution induced by ionizing particles as in **fig.2a**. Moreover a charge spectrum of the noise events, not correlated with the ionization due to the cosmic rays, extends itself up to the pedestal.

Fig.3 shows the efficiency (close points) and the charge of the single sparks (open points) at different high voltages for counter C. In **fig.4** the same charge distribution is compared with that of counters A and B at different high voltages. Zero voltage is assumed at the knee of the respective efficiency plateau, in order to compare the charge released at the same counter efficiency. It is evident a gain of about a factor two in the charge collection with the use of the silver electrodes (counter C), compared to the graphite electrodes (counters A and B).

3a. Working model : charge characterization

We now examine a possible electrical model defining the charge and time characteristics of an RPC pulse. As in the model no charge dispersion over the graphite film is supposed, we assume the pulse characteristics of counter C as a guide for the model.

The present study deals with the signals induced on the read out load by the electrons released during a local breakdown of the counter. In **fig.3** the slope of the linear variation of the charge respect to the high voltage defines an equivalent capacitance (Ceq) equal at 79.5×10^{-3} pF and the extrapolation at zero charge a voltage Vs equal to about 4.2 KV.

These parameters are expected to be related with the intimate mechanisms of the RPC spark formation. In particular, supposing that the spark current crossing the RPC gas gap acts like a current generator, then the equivalent capacitance is expected to be related to the intensity of such generator, because Ceq settles the charge collected in the read out strips at a defined voltage. Moreover Vs is interpreted as the residual voltage across the gas gap in the region crossed by the discharge when the spark opens.

As a direct consequence of the previous interpretation we expect that if we change the intensity of the current generator the equivalent capacitance will change, but not Vs. **Fig.5** shows the charge of the single spark as function of the high voltages for counter C at three values of the freon flow rate : .2 l/h, .35 l/h and .5 l/h for fixed flow rates of argon (3. l/h) and isobutane (1. l/h). The presence of the freon gas reduces the detected pulse charge because of electron capture. In correspondence with the increase of the freon flow rate the values of the equivalent capacitance Ceq= 79.5×10^{-3} pF, 56.0×10^{-3} pF and 38.8×10^{-3} pF are observed. Whereas Ceq changes of about a factor two, Vs changes of about 14%.

We assume (**Ref. 1**) that, because of the volume resistance of the glass, in a time of $\rho\varepsilon\varepsilon_0 \approx 1$ sec a voltage equal to the high voltage power supply Vo is stabilized across the gas gap. So on the sensitive

surface A of the glass in contact with the gas a charge $q_A = \varepsilon_o A Vo/d_G$ is distributed, where $d_G = 2$ mm is the gas gap. This charge results 5 orders of magnitude greater than the detected pulse charge q (e.g. for Vo= 6. KV, $q_A = 8.95\ \mu c$ and q = 144 pc). As the charge q is expected to be a not negligible fraction of the spark charge (see later), this shows as the spark charge deposits itself over an area S equal to about Aq/q_A, that is of some mm^2. We assume that the spark process brings the voltage of this area from the initial voltage V_O to the final one Vs, when the spark opens leaving undisturbed the rest of the surface A in contact with the gas.

Following these assumptions, the circuit of **fig. 6** is used to describe the development of the detected pulse in times $<< \rho\varepsilon\varepsilon_o$. In this figure

$$i_g(t) = i_{go} e^{-t/\tau s} \qquad (1)$$

is the spark current generator and

$$C_G = \varepsilon_o S/d_G \text{ and } C_V = \varepsilon\varepsilon_o S/d_V \qquad (2)$$

($d_V = 3.$ mm) are the capacitances that the surface S[2] locates respectively across the gas gap (gas capacitance) and across each of the two glass electrodes (glass capacitance), Co is the capacitance due to the external read out, Vo is the high voltage and R the load resistance. This resistance is crossed by the current i(t) during the spark process, so that V(t) = -i(t)R is the voltage of the detected pulse.

We assume the signal capacitive pick up shaped in pads of surface so small that the transit time of the pulse over this surface can be neglected. Then Co can be considered as a local capacitance, characterizedby the full pad area. The glass resistance $R_V = \rho d_V/S$ in parallel to Cv of **fig. 6** can be neglected in our model, because the time length of the detected pulses is many orders of magnitude smaller than the recovery time of the original voltages.

In the appendix the differential equation of the circuit of **fig. 6** is solved on the base of the initial conditions. In particular **A(4')** gives the charge of the detected pulse. This result can be easily obtained from **fig. 6** considering the expected final voltages, when the output pulse is finished and the output current is zero. In fact at this time it results Vg=Vs and one has

$$2V_V + V_S = V_O \qquad (3)$$

where Vv is the voltage across each glass capacitance.

If q_V is the final charge contained in the glass capacitance, one has $q_V = C_V V_V$. Becouse of the resistance Rv, the glass capacitances are initially discharged. Then q_V is actually the total charge transported by the current i_V crossing the glass capacitances during the complete development of the spark. As the capacitance Co is charged at the same voltage Vo at the start and at the end of the spark process, all the charge q_V crosses the load resistance during the complete spark development. Then $q = -q_V = -C_V V_V$. Once substituted the value of Vv from (3), one obtains $q = -C_V/2(V_O - V_S)$ in agreement with **A(4')**.

This result compared with the measurements of **fig. 5** interprets the value of Ceq as

$$C_{eq} = C_V/2 \qquad (4)$$

From **fig. 4** the ratio between the equivalent capacitances of counters A and B can be estimated to be $C_{eq}(A)/C_{eq}(B) = (54.1 \times 10^{-3}\ pF)/(41.8 \times 10^{-3}\ pF) = 1.29$. Taking into account the unknown contribution of the graphite, this value can be compared with the one expected from (4), equal to the inverse of the ratio of the glass thickness of counters A and B : (3mm)/(2mm)=1.5

From (4) and from the definition (2) of Cv one can calculate the area

---

(2) becouse of the large boundary effect expected, in the application of the (2) S must be considered as an effective area

$$S=2d_v C_{eq}/\varepsilon\varepsilon_0 \qquad (5)$$

For example, for the case of the freon flow rate equal to .2 l/h one obtains S=11 mm^2.

A(6) gives the total charge of the spark q_g. This result is also easely obtained from **fig.6**. In fact the current generator of **fig.6** supplies not only the charge q_v before calculated, but also the charge $q_G=C_g(V_o-V_s)$ crossing the gas capacitance. Then one obtains $q_g=q_v+q_G=(C_g+C_v/2)(V_o-V_s)$.

The value of the total charge released from the current generator (1) has been until now characterized. In fact (see **A(6)**)

$$q_g=i_{g0}\tau_g=(C_g+C_v/2)(V_o-V_s)$$

is known being V_o a given parameter, V_s measured from **fig.5**, S calculated from (5), where C_{eq} is measured from **fig.5**, C_g and C_v calculated from (2). In the next paragraph we describe the measurement of the characteristic time τ_g.

3b. Time characterization

The current on the read out resistive load is calculated in the appendix (see **A(1')**)

$$i(t)=C_v/2(V_o-V_s)(e^{-t/\tau_s}-e^{-t/\tau_L})/(\tau_g-\tau_L)$$

where $\tau_L=R(C_o+C_gC_v/2/(C_g+C_v/2))$. τ_L is a time characteristic of the load. In fact for any realistic apparatus it results $C_o>>C_g$, C_v and then $\tau_L\approx RC_o$.

The current presents a maximum at the time

$$t^*=\tau_g\tau_L/(\tau_L-\tau_g)\ln(\tau_L/\tau_g) \qquad (6)$$

A(2') gives the voltage $V_g(t)$ across the gas gap. Following the previous approximation one has

$$V_g(t)\approx V_s+(V_o-V_s)e^{-t/\tau_s} \qquad (7)$$

It is interesting to analyse the detected signal in the two extreme situations :

(a) $\tau_g<<\tau_L$. In this case for $\tau_g<t<\tau_L$ we obtain from **A(1')** the voltage of the detected pulse:

$$V(t)=i(t)R\approx(C_v/2C_o)(V_o-V_s)e^{-t/\tau_L}.$$

This result can be easily interpreted following (7) and **fig.6**. In fact the output voltage has a maximum value at the time (see (6)) $t^*\approx\tau_g\ln(\tau_L/\tau_g)$. At that time the voltage across the gas gap results from (7): $V_g(t^*)\approx V_s$ and its variation $-(V_o-V_s)$ appears on the output as attenuated by the capacitive partition between the two serial glass capacitances C_v and C_o. So it is expected

$$V(t^*)\approx-C_v/2(V_o-V_s)/(C_v/2+C_o)\approx-(C_v/2C_o)(V_o-V_s)$$

and at the time considered : $V(t)\approx V(t^*)e^{-t/\tau_L}$.

Considering the expected shape of the detected signal, because it results $t^*\approx\tau_g\ln(\tau_L/\tau_g)$, this signal presents a first front ($t<t^*$) whose time development practically coincides with τ_g and a tail ($t>t^*$) of decay time τ_L, that is the first front of the signal follows in time the voltage signal across the gas gap independently from the load impedance. The load impedance only attenuates the gas voltage signal of a factor $C_v/2C_o$.

(b) $\tau_g>>\tau_L$. From **A(1')** for $\tau_L<t<\tau_g$ one has

$$V(t)\approx-(RC_v/2\tau_g)(V_o-V_s)e^{-t/\tau_s}$$

These results can be interpreted as follows : at the time considered the spark is still active and the voltage across the gas gap is changing toward the value Vs. Because from (6) we have $t^* \approx \tau_L \ln(\tau_g/\tau_L) << \tau_g$, we expect from (7):

$$Vg(t^*) \approx Vs + (Vo-Vs)e^{-t^*/\tau_s} \approx Vs + (Vo-Vs)(1-\tau_L/\tau_g) = Vo - (Vo-Vs)\tau_L/\tau_g$$

so that the variation $-(Vo-Vs)\tau_L/\tau_g$ of the voltage across the gas gap appears on the output as attenuated by the capacitive divider. Then one expects

$$V(t^*) \approx -(Vo-Vs)(\tau_L/\tau_g)(Cv/2Co) \approx -(Vo-Vs)(RCo/\tau_g)(Cv/2Co) = -(RCv/2\tau_g)(Vo-Vs)$$

and at the time considered $V(t) \approx V(t^*)e^{-t/\tau_s}$ This case describes the shape of the RPC signals picked up on pads of small area and at low(≤5%) flow rate of freon as usually observed on a oscilloscope terminated on 50 Ω. For example, at freon flow rate of .2 l/h the value τ_g=6.4 ns is observed at Vo=6.0 KV(see later) and with the used pad of capacitance Co=13 pF one has τ_L=.7 ns for R= 50Ω. In this case we have from (6) t^*=1.7 ns. Hence we can deduce that the usually observed (on a 50Ω terminated oscilloscope) rise time of the order of 1 ns is not related to the spark time development, but mostly to the effect of the load impedance. The characteristic spark time τ_g is instead observed as the slope of the detected signal tail.

Once this time τ_g is known, **A(1')**, the data of **fig.5** and the knowledge of the load impedances R and Co allow us to calculate the average shape of the expected output pulses at a given value of the high voltage and of the freon flow rate. However it can be useful to know the expected amplitude and the time length of the first front of these pulses at fixed condition of high voltage and gas mixture. This can directly be obtained from **fig.7**, where $x=\tau_L/\tau_g$, $g(x)=x/(x-1)\ln x$, $f(x)=e^{-g(x)}$ are reported, being $g(x)=t^*(x)/\tau_g$ and $f(x)=i(t^*)/(q/\tau_g)$, as it is easily calculated from **A(1)** and **(6)**. So for example if the read out pad capacitance is Co= 30 pF, it results τ_L=1.5 ns for R= 50 Ω. From **fig.7** one has g(.23)= 44 and f(.23)=.64 Moreover at Vo= 6.0 KV and freon flow rate .2l/h one has from **fig.5** q/τ_g=(144. pc)/(6.4 ns)=22.5 mA. Then an average output pulse of amplitude .64x22.5mAx50Ω≈.7V and with a first front of time length .44x6.4 ns=2.8 ns is expected (we suppose the transit time of the signal over the surface of the read out pad to be negligible).

A fundamental assumption of the proposed model is that the development time of the spark τ_g is independent from the load impedance, being this the characteristic time of a current generator. In order to verify this assumption and to measure the time we have cut a strip in the center of the counter, obtaining a 3x3 cm^2 pad. We have also grounded all the strips surrounding this pad in order to eliminate possible induced signals from those strips. The pad current crossing a probe is read on the 50 Ω input impedance of a LeCroy 9450 oscilloscope (350 MHz,see **fig.8**). The probe consists of a resistance Ro directly mounted on the pad and a LEMO cable (50Ω characteristic impedance, 3 ns time length). The digitized signal are sent via a serial port RS232 to a Macintosh SE. Tests with the LEMO cable directly connected to the pad (Ro=0,R=50Ω), with Ro=1 KΩ and 10 KΩ have been done.

In the case of Ro=10 KΩ a parasitic capacitance of the resistor has to be compensated in order to eliminate overshoot signals. An integration time of 1 ns introduced by the probe and the oscilloscope is measured pulsing the probe with a signal of < 1 ns rise time and reading the output signal on the same oscilloscope.

In **fig. 9a** and **9b** a detected pulse of 181.7 pc taken at Vo=6.4 KV and .2 l/h of freon flow and with Ro=10 KΩ (full points) is shown as an example. In the same figures the calculated voltage values using τ_g=4.97 ns and τ_L=130. ns are reported as a line. This τ_L value points out a Co pad capacitance of 13. pF.

In **fig. 10** for the same conditions of high voltage and gas of **fig. 9**, but with R=50 Ω, a detected pulse of charge 139.2 pc and the calculated pulse using the values τ_g=5.61 ns and τ_L=.65 ns are reported. Moreover in the calculation the current function given from **A(1')** is integrated with a time constant of 1 ns to take into account for the probe and the oscilloscope action. The τ_L value again points out Co=13. pF.

In **fig. 11** the measurements of τ_g at different high voltages, for .2 l/h of freon flow andrespectively R=50 Ω (open dots) and Ro=10 K Ω (full dots) are reported.

In **fig. 12** measurements of τ_g for R=50 Ω and.5 l/h of freon flow are reported.

4. Conclusions

The good agreement between the two sets of measurements of τ_g done at very different values of the load resistance (R=10 KΩ+50Ω and R=50 Ω of **fig. 9** and **fig. 10** respectively) and between the measured and calculated pulse shapes confirms the validity of the model.

We want to stress that only one characteristic time of the spark development is assumed to describe the detected pulses. This would indicate that only one physical mechanism of the spark development is pointed out. An additional charge released at a time smaller than the one observed would produce a variation of the first front slope of the signal in **fig. 9b**. Our detection capability is limited at time signals slower than 1 ns . However we can limit the contribution of a possible presence of a faster mechanism of charge production at no more than about one third of the observed charge.

Acknowledgments

We wish to thank Ing. S. Natali. and Mr. M. Zet of the Saint Gobin s.p.a. for the suggestions and the help in designing and prototyping the RPC glass framework with associated silver deposition. We are also indebted with Mr S. Guerra and Mr. A. De Simoni for the technical work and support to realize the experimental apparatus.

Appendix

From **fig. 6**, being at the initial time $Vg(0)=Vc_0(0)=Vo$ one has

$$Vg(t)=Vo-\int_0^t i_G(t)dt/Cg \text{ and } Vc_0(t)=Vo-\int_0^t i_O(t)dt/Co$$

The following equations can be written

$$i_g=i_G+i_V,\ i_V=i_O+i,\ Rdi/dt=i_O/Co,\ i_O/Co+i_V2/Cv+i_G/Cg=0$$

We suppose $i_g(t)=i_{g0}e^{-t/\tau_s}$, where the parameters i_{g0} and τ_g are expected the be Vo dependent. One obtains

$$R(CgCv/2/(Cg+Cv/2)+Co)di/dt+i=i_g/(1+Cg/Cv/2)$$

Integrating this equation with the initial condition : i(0)=0 one has

$$i(t)=i_{g0}\tau_g(e^{-t/\tau_s}-e^{-t/\tau_L})/((\tau_g-\tau_L)(1+2Cg/Cv)) \qquad A(1)$$

where $\tau_L=R(Co+CgCv/2/(Cg+Cv/2))$. Moreover one has

$$i_G(t)=i_g(t)-i_Q(t)-i(t)=i_g(t)-RCodi/dt-i(t)$$

and from **A(1)**

$$i_G(t)=i_{g0}e^{-t/\tau_s}(1+Cv/2Cg)-R(CgCv/2/(Cg+Cv/2))(i_{g0}/\tau_L)$$

$$(\tau_L e^{-t/\tau_s}-\tau_g e^{-t/\tau_L})/(\tau_g-\tau_L)$$

and then from the integration of $i_G(t)$

$$Vg(t)=Vo-i_{g0}\tau_g(1-e^{-t/\tau_s})/(Cg+Cv/2)-(RCv/2/(Cg+Cv/2))(i_{g0}\tau_g)$$

$$(e^{-t/\tau_s}-e^{-t/\tau_L})/(\tau_s-\tau_L) \qquad A(2)$$

From **A(2)** for $t\to\infty$ one has

$$Vg(\infty)=Vo-i_{g0}\tau_g/(Cg+Cv/2) \qquad A(3)$$

The charge detected on the read out is obtained integrating **A(1)**

$$q=-i_{g0}\tau_g Cv/2/(Cg+Cv/2) \qquad A(4)$$

Following the results of **fig. 5**, we can put

$$q=-Ceq(Vo-Vs) \qquad A(5)$$

Because from **fig. 11** one sees that τ_g gets bigger at low values of Vo, from **A(4)** and **A(5)** we conclude that $i_{SO}=0$ for $Vo=Vs$. Then from **A(3)** for $Vo=Vs$ we have $Vg(\infty)=Vs$. Moreover after the substitution of **A(4)** in **A(3)** we have

$$q=-Cv/2(Vo-Vg(\infty))=-Ceq(Vo-Vs)$$

We conclude that $Ceq=Cv/2$ and $Vg(\infty)=Vs$ for any Vo value. From **A(3)** we obtain the total spark charge

$$q_g=\int_0^\infty i_g(t)dt=i_{g0}\tau_g=\frac{Cg+Cv/2}{Vo-Vs} \qquad A(6)$$

Substituting the $i_{g0}\tau_g$ expression in **A(1)**, **A(2)** and **A(4)** one has

$$i(t)=Cv/2(Vo-Vs)(e^{-t/\tau_s}-e^{-t/\tau_L})/(\tau_g-\tau_L) \qquad A(1')$$

$$Vg(t)=Vs+(Vo-Vs)e^{-t/\tau_s}-RCv/2(Vo-Vs)(e^{-t/\tau_s}-e^{-t/\tau_L})/(\tau_g-\tau_L) \qquad A(2')$$

$$q=-Cv/2(Vo-Vs) \qquad A(4')$$

References

(1) R. Cardarelli et al. Nucl. Ins. and Meth. in Ph. Res. A263 (1988) 20-25

Figure captions

(1) Graphite RPC cross section

(2a) Silver RPC charge spectrum for telescope trigger events (HV= 5.8 KV, attenuation=8 db, .25 pc/chan). The average charge of the peaked distribution is 123 pc

(2b) Silver RPC charge spectrum in the same conditions of fig(4a), but for self trigger events

(3) Efficiency and single spark charge of the silver RPC as a function of high voltage

(4) Silver and graphite RPC charge as a function of the voltage corresponding to the same counter efficiency. For each counter the voltage of the efficiency plateau knee is assumed equal to zero. (C : silver RPC; B : graphite RPC, d_G= 2. mm; A : graphite RPC, d_G= 1.6 mm)

(5) Silver RPC single spark charge as a function of high voltage at different freon flow rate

(6) Electrical model describing the spark. development. Cg and Cv are respectively the gas and glass capacitances located by the discharge, Co the pad capacitance. ig the spark current generator and Vo the high voltage power supply

(7) Relative time of the maximum of the current pulse $g(x)=t^*(x)/\tau_g$ and relative maximum amplitude of the current pulse $f(x)=i(t^*)/(q/\tau_g)$ as a function of $x=\tau_L/\tau_g$

(8) Experimental layout for the spark time measurements

(9a) RPC pulse read (dot) with the 10 KΩ probe on the 50 Ω input of a 3450 LeCroy oscilloscope (HV= 6.4 KV, freon flow. = .2 lt/h) and calculated one (line). The values q=181.7 pc, τ_L=130.0 ns and τ_g=4.97 ns are used in the calculation

(9b) Exploded view of **fig. 9a**

(10) RPC pulse read with a 50 Ω LEMO cable (dot) and calculated(line). The values q=139.2 pc, τ_L=.65 ns, τ_g= 5.61 ns and an integration time of 1 ns are used in the calculation

(11) τ_g values measured with a 50 Ω LEMO cable (open dot) and with the 10 KΩ probe (full dot) as a function of the high voltage at .2 l/h of freon flow. τ_g values measured with a 50 Ω LEMO cable at .5 lt/h of freon flow (cross)

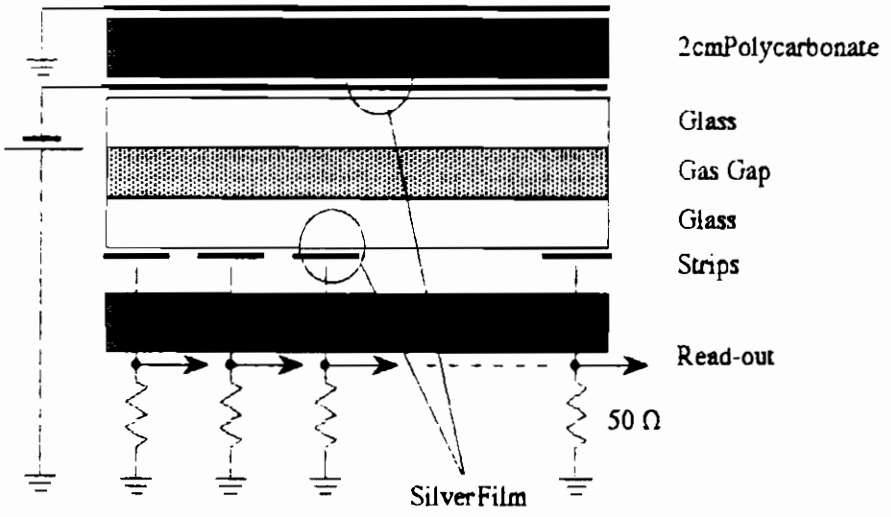

Fig. 1

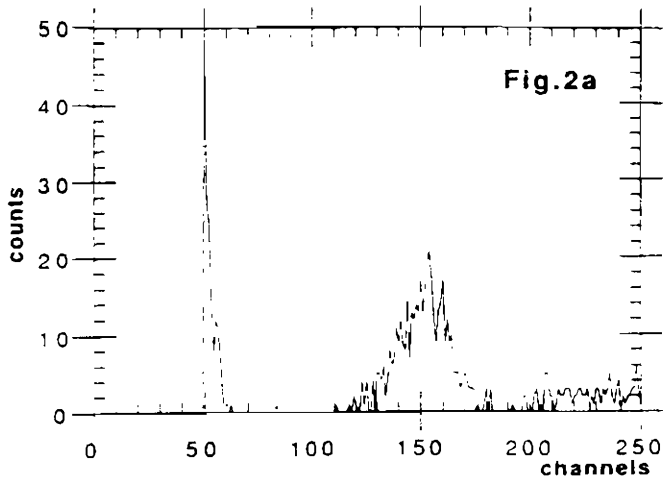
Fig.2a
counts
channels
0
10
20
30
40
50
0
50
100
150
200
250

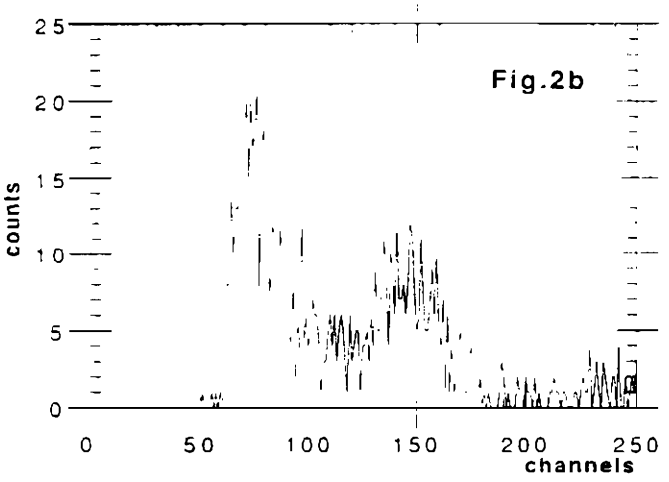
Fig.2b
counts
channels
0
5
10
15
20
25
0
50
100
150
200
250

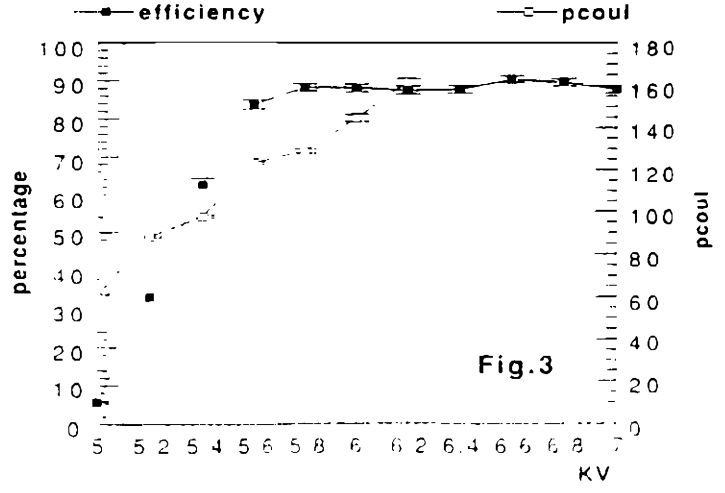
efficiency
pcoul
percentage
pcoul
KV
Fig.3

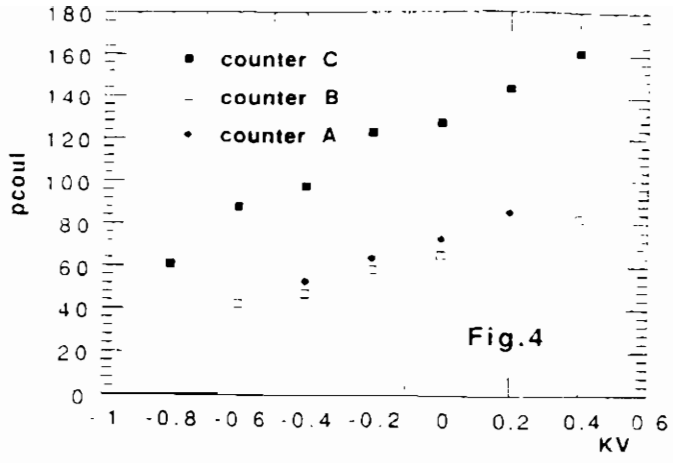

Fig.4

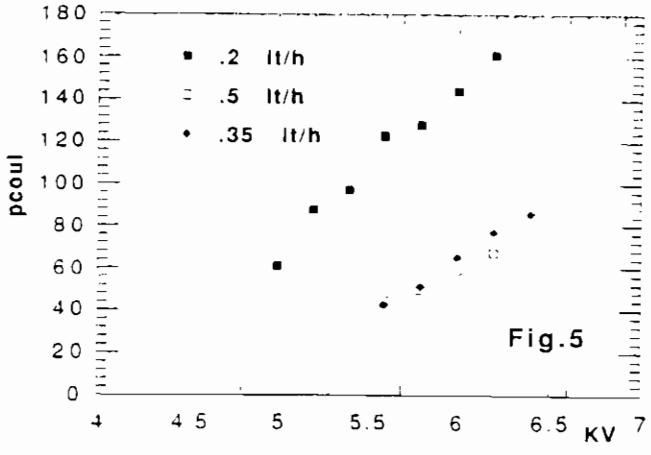

Fig.5

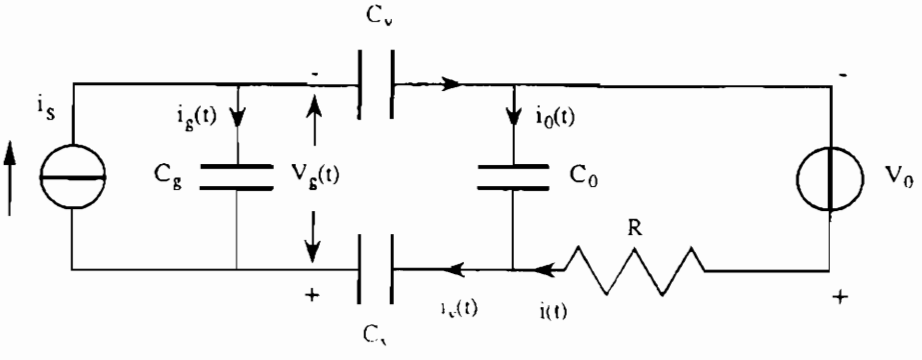

Fig.6

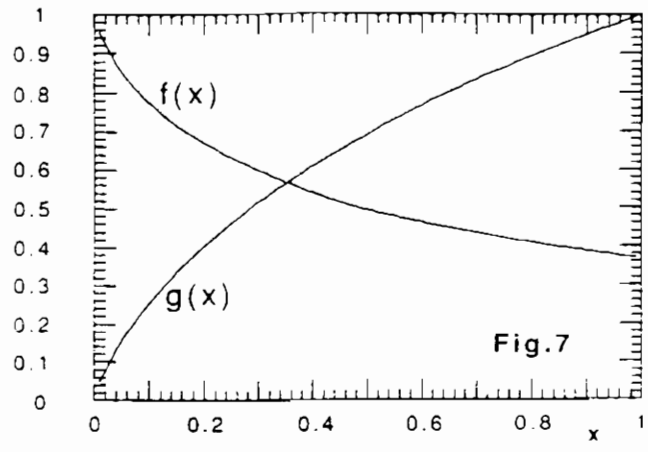

Fig.7

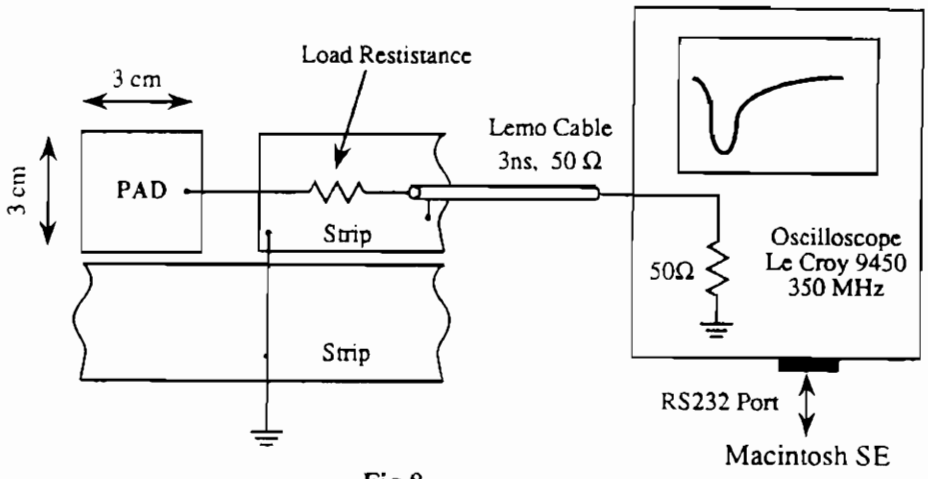

Fig.8

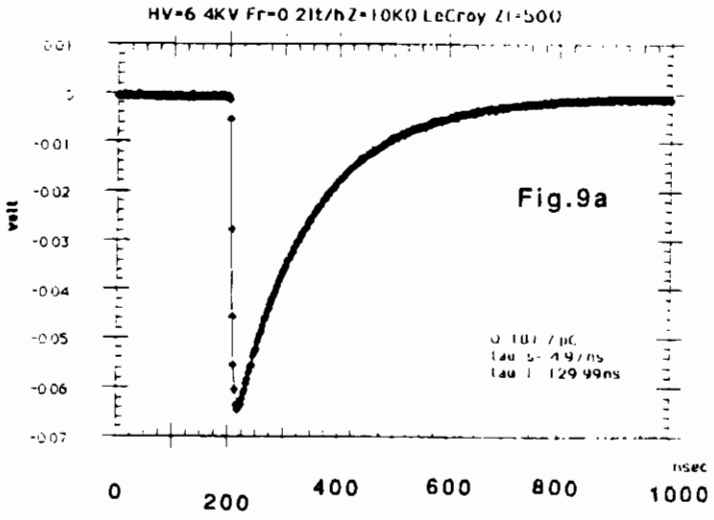

Fig.9a

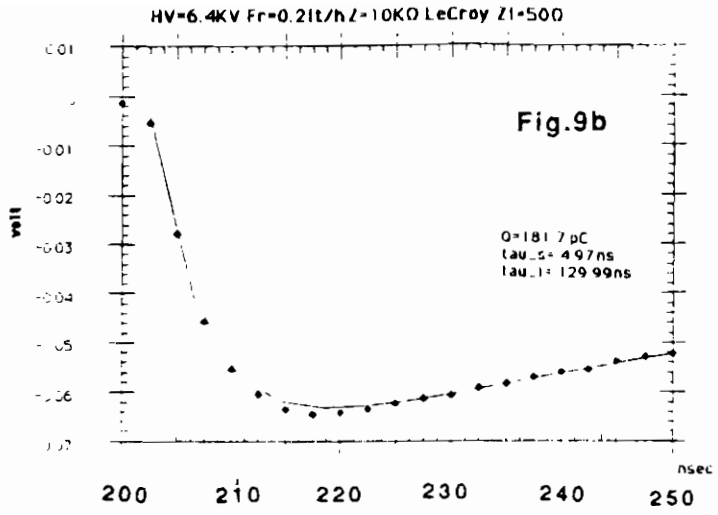
HV=6.4KV Fr=0.2It/h Z=10KΩ LeCroy Z1=50Ω
Fig.9b
Q=181.7pC
tau_s=4.97ns
tau_l=129.99ns
volt
nsec
200
210
220
230
240
250

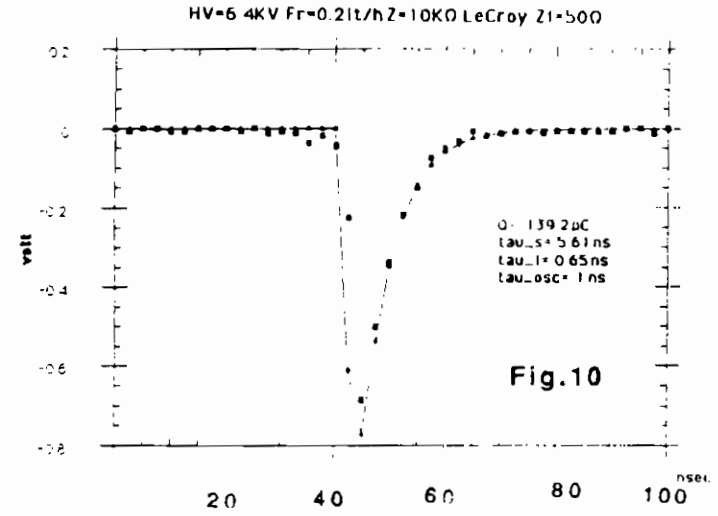
HV=6.4KV Fr=0.2It/h Z=10KΩ LeCroy Z1=50Ω
Q=139.2pC
tau_s=5.61ns
tau_l=0.65ns
tau_osc=1ns
Fig.10
volt
nsec
20
40
60
80
100

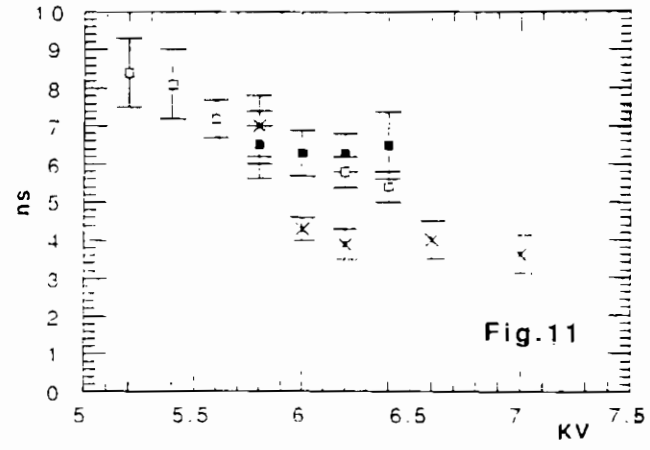
Fig.11
ns
KV
0
1
2
3
4
5
6
7
8
9
10
5
5.5
6
6.5
7
7.5

FAST PARALLEL RPC READOUT SYSTEM

A. Lanza, G. Liguori, P. Torre
Dip. Fisica Nucleare. e Teorica dell' Universita' di Pavia e INFN, Sezione di Pavia.
M. Ambrosio, G.C. Barbarino, M. Iacovacci, A. Lauro, G. Osteria
Dipartimento di Fisica dell' Universita' di Napoli e INFN, Sezione di Napoli.
G. Agnetta, O. Catalano, L. Scarsi
IFCAI - Ist. di Fisica Cosmica e Applicazioni all'Informatica, CNR, Palermo e INFN, Sezione di Napoli.

Introduction

Since the first years of the eighty the Resistive Plate Counters (RPC) [1] was used as veto counters for cosmic radiation in accelerator and non accelerator physics [2]. Because of the low cost, the high spatial resolution and the good time resolution, in comparison with the scintillator counters, in the past few years the RPCs started a new life as muon detectors in large area cosmic radiation [3] and high energy physics experiments [4].

Using the RPCs as a detector in accelerator experiments, it was evident the need of a new kind of electronics to readout and handle the RPC's signals in a fast and reliable way. In this report we describe the parallel VME readout system developped by the T&T collaboration with the full support of the CAEN S.p.A. in design and engineering the electronics.

Trigger detector electronics requirements

The main difference between the use of a detector in experiments with beams coming from accelerators, or in cosmic rays experiments, is that the particles reach the detector in a timed sequence instead of random in the time. The beam is bunch structured and the particles going against the target leave the accelerator only during the spill. Within the spill the particles are synchronized in buckets by the accelerator radio frequency (RF). In order to recognize the exact beam crossing particle, the system have to resolve two particles in two different buckets. This time can be very short, due to the RF of the accelerator.

In addition, if the apparatus have to be used as trigger detector, the information coming out from it need to be handled in two different ways:

- in order to generate the trigger;
- in order to be read for monitoring and data acquisition purposes.

Really the requirements for the two previous items are quite different. The most evident differences in handling signals for trigger and for data acquisition purposes are described below.

Triggering requirements	Data acquisition requirements
The signals have to be handled as fast as possible in order to minimize the time required to generate the trigger.	In principle, it is not necessary to go at maximum speed of the electronics because of the defined quickness due to the data acquisition computer.
It is not required a high spatial resolution to avoid a too much selective trigger.	The higher spatial resolution is required to reconstruct the tracks.
Each data coming from the detector must be processed. The trigger system have to handle signals coming at a frequency equal to the RF of the accelerator.	Only the data selected from the trigger have to be processed.
No memory need: the signals are processed in real time one by one.	It is necessary to use some memory to temporary store the incoming data, waiting for the trigger.
	It is fancy to have a simple interconnection with the data acquisition system.

We attempted to answer to these requirements designing a new RPC's readout system.

Schematic of the system

Fig. 1 is a sketch of the system. The RPC's signals, coming from pads or strips, are discriminated and amplified; then they are sent by twisted flat cables to the readout modules located in a VME crate. A computer reads the data by mean of a standard VME interface while the signals useful for the trigger go to the electronics to generate the trigger.

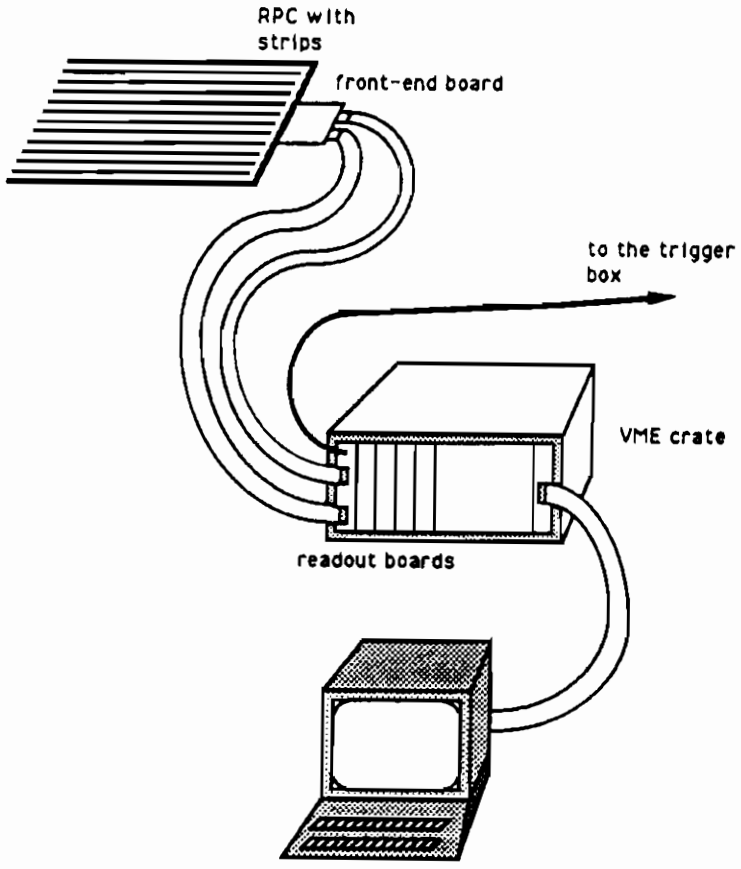

fig. 1: RPC readout system

The system is two board based: the front-end board and the readout board.

The front-end board (A544) outlined in fig.2 and connected to the strips or pads, must be located closest to the RPC to avoid the degradation of the signals. Thirtytwo channels are received, discriminated and amplified by each board. Sending different voltage bias to the comparators, it is possible to preset the threshold values in a range from -500 mV up to 500 mV. The width of the shaped signals can also be remote arranged from 15/20 ns up to microseconds. Differential TTL line drivers send the information to the readout board via twisted flat cables. A fast logic OR of the 32 channels is also available in TTL logic, appropriate to be used for measurements of time.

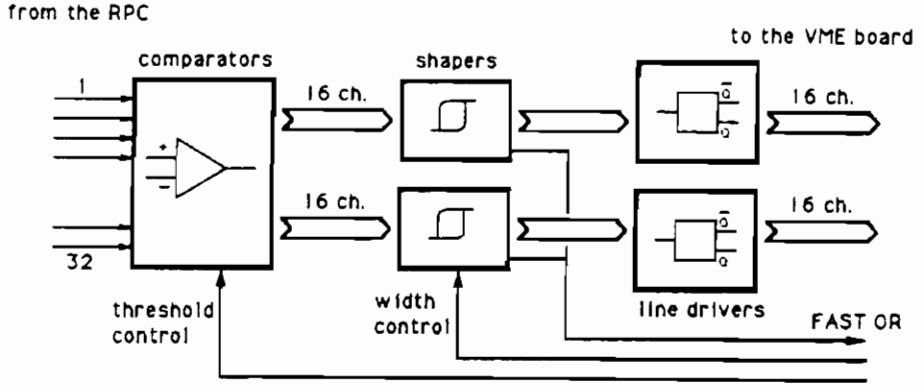

fig.2 : front-end board

The readout board (V533), which can be located far from the RPCs, mainly performs three functions: executes some logic operations for the trigger, stores the information for the data acquisition and accesses to the VME BUS. The fig.3 is a sketch of the board. After have been received, by mean of the front panel connectors, from the TTL line receivers, the signals are splitted in two BUSES: one goes to the logic block and one goes to the memory block.

Logic block

The logic block is based on an Erasable Programmable Logic Device (EPLD) which performs:

- 16 logic ORs of 2 adjacent strips

- 8 logic ORs of 4 adjacent strips
- 4 logic ORs of 8 adjacent strips
- 2 logic ORs of 16 adjacent strips

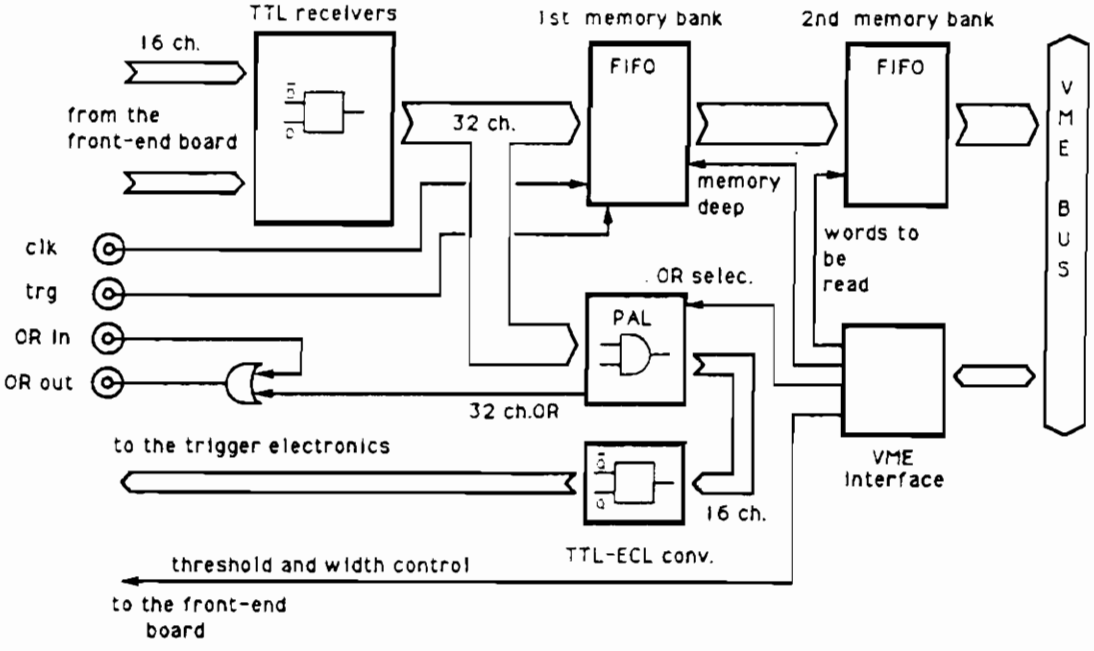

fig.3 : readout board

By a command, it is possible to select one of the above choice and to send the selected signals to the front panel connector, for triggering purposes. The information is available at ECL logic. The logic OR of the all 32 channels (OR32) is also available in the front panel, at NIM level, and can be daisy-chained with the OR32 of the other boards in the crate.

Memory block

The RPCs signals are written into a first FIFO memory bank when a clock signal reach the board. The store of the information lasts since a trigger signal occurs. In this instance, a number of words, previously preset by computer, is transferred into a second bank of memory. In order to be sure that the word correlated with the trigger will be read, the deep of the first bank of memory have to be programmed taking into account the trigger generation time:

memory deep (words) = trigger generation time (ns)/ clock freq.(ns)

The data stored in the second memory bank is available for reading by the data acquisition computer.

VME interface

All the commands, functions and the readout are carried out by means of the VME interface provided on the board. A standard VME controller can connect the system to a data acquisition computer.

Conclusions

The table below shows the main performances of the system:

- new front-end electronics
- remote preset of threshold and width
- remote test of the board
- maximum clock frequency of 62 MHz
- 32 channels per board
- VME interface
- readout and data handling for triggering purposes.

The system was bench tested and it seems to well work. A test with the electronics connected to the RPCs, will be the next step.

References

[1] - R. Santonico e R. Cardarelli, Nucl. Instr. and Meth. A187, 337 (1981).

[2] - G. Bressi et al, Nucl. Instr. and Meth. A261, 449 (1987).
- FENICE Collaboration, Preprint of the Laboratori Nazionali di Frascati, LNF-87 (1987).

[3] - ARGO, Proposal to INFN, 1992.
- F. D'Aquino et al, MINI Collaboration, Nucl. Instr. and Meth. A324, 330 (1993).
- COVER-PLASTEX, Proposal to INFN, 1993.

[4] - L. Antoniazzi et al, Nucl. Instr. and Meth. A315, 92 (1992).
- C. Bacci et al, Nucl. Instr. and Meth. A315, 102 (1992).

DATA ACQUISITION SYSTEMS DEVELOPED AT CAEN

F. Catarsi, C. Landi, G. Franchi, M. Lippi

C.A.E.N. S.p.A.
Via della Vetraia 11, 55049 VIAREGGIO, Italy

1. INTRODUCTION

The latest developments made in CAEN will be presented in this paper to inform researchers on the general purpose units which have been designed following the requirements of the various groups we have collaborated with over the last two years.
The description will be completed by a general overview of the general purpose High Voltage modules necessary to supply the RPCs.

2. READ OUT CONTROLLER MODULES

2.1 V 533, 50 MHz 32 bit PIPELINE UNIT

Figure 1 reports the block diagram of the unit. The 32 inputs are connected to the front end module A 544 placed near the detector. The VME controller can set both threshold and output pulse widths via two analog levels. The unit receives the RFCLOCK pulse and the trigger input. At each rising edge of the RFCLOCK the status of the 32 inputs is stored inside the circular buffer; the programmed slice of the circular buffer is then transferred to the event memory buffer at the time of the trigger. The exact time reference is achieved via a buffer which stores the trigger counter number.

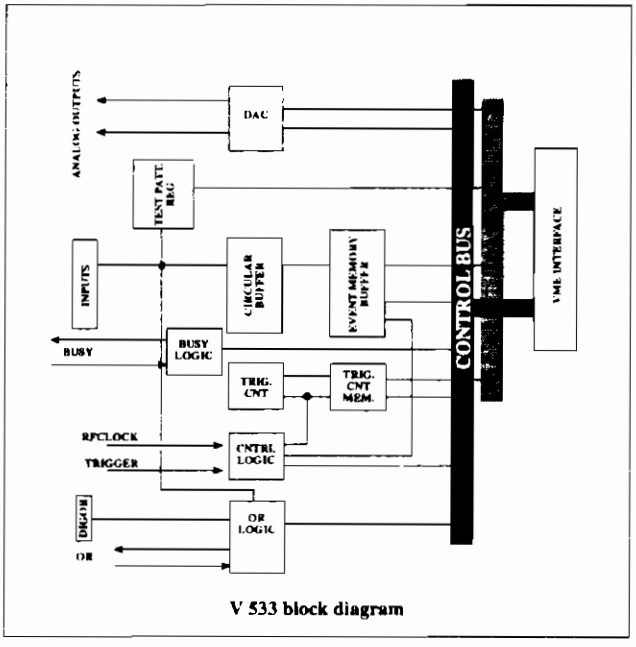

V 533 block diagram

2.2 V 528 SERIAL RPC READ-OUT CONTROLLER

This is a prototype VME module which houses a single acquisition channel. It can control up to 32 read-out modules, A 544. All the channels are read in serial way at a maximum speed of 4 MHz.
The module is particularly suitable when a large number of channels have to be controlled and the speed of the acquisition is not the critical parameter.
We foresee for the series production a sufficient number of acquisition channels on the same VME unit in order to reduce the total set-up cost.

2.3 C 267 SYNCHRONOUS FAST STAS

This unit is a standard CAMAC module designed to be used in DAQ based on STREAMER TUBES, but it can be used in conjunction with the RPCs via the A 544 front end module in the serial version.
Each module can control up to 8 chains of front end modules, with 1024 bits each one.
It supports the multi event operations and can read data from the read-out modules at the maximum speed of 4 MHz.
The C 267 has a companion module: the SY 480 SPLITTER BOARD which interfaces the front-end modules and also supply them. A special version of the system can be used.

2.4 A 514 DIGITAL FRONT END TDC

This unit is an open frame board which includes both front-end and digitizing hardware in order to make a complete tracking system.
The module houses 16 independent channels multi-hit TDC with a time resolution of 1 ns.
It is interfaced to the host controller via an on board DSP.

3. FRONT END MODULES

3.1 A 544 32 CHANNEL RPC FRONT END

The unit is an open frame board that can be placed near the detector. It allows the reading of the 32 channels either in parallel or in serial mode (the minimum power consumption is achieved in serial mode read-out); the desired read-out mode has to be specified.

The main features of the unit are:
32 input channels;
32 differential TTL outputs;
1 OR of 32 channels;
1 input OR;
minimum input width ~8 ns;
double pulse resolution 10 ns;

from the controller (V 533 or V 528) , via two analog signals, can be programmed
threshold in the range -500 mV to 500 mV
output width in the range from 25 nS to 2 µS

independent connectors to link the unit with the parallel read-out controller V 533
serial read-out controllers V528 or C 267
(max clock speed 4 MHz)

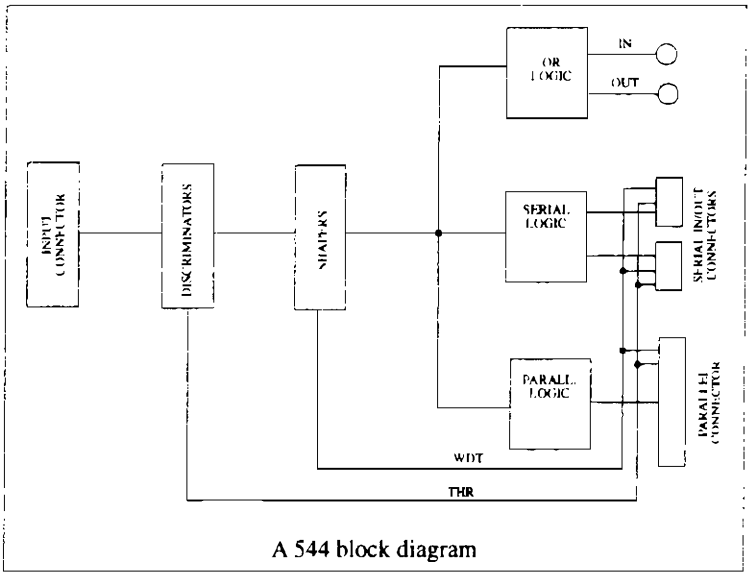

A 544 block diagram

3.2 A 532 8 CHANNEL RPC FRONT END BOARD

It is a replica, realized in SMD technology of the front-end hardware developed at the INFN of Rome for the FENICE experiment.We have made only a few modifications increasing the input sensitivity.

The main features of the unit are:
- 8 channels per board
- 1 TEST input
- 8 outputs
- 1 OR of 8 channels

The unit can be assembled over a mother board to fulfill the requirements of the single collaboration and to interface the remote controller.

4. HIGH VOLTAGE POWER SUPPLY FOR RPCS

To complete the set of equipments necessary to use this detector CAEN also developed the necessary H.V. channels.

4.1 N 570 2 CH PROGRAMMABLE HV POWER SUPPLY

The model N 570 is a double NIM unit which houses 2 independent High Voltage channels. The output voltage of each channel has two different ranges:

from 0 to ±8 KV / 1 mA and from ±8 KV to ±15 KV / 500 μA;

Output polarity: independently selectable.
It is possible to control several working parameters for each channel: two levels of presettable high voltage, two levels of current limit, Ramp-up, Ramp-down.
All these parameters can be programmed in remote mode via H.S. CAENET link or in local mode, via front panel alphanumeric keypad and two 8-character displays. In addition some LEDs show the status of each channel.
All the functional parameters are stored in a non-volatile memory.
2 front panel trimmers allow the setting of 2 output max voltage thresholds, and the two current and voltage limits can be selected also by 2 external NIM/TTL signals. A NIM/TTL signal is also available for the KILL function. There is also the possibility of an autocalibration of the module by an appropriate menu. The High Voltage is present only on the female HV-LEMO output connectors.

4.2 SY 127 40 CHANNEL HIGH VOLTAGE POWER SUPPLY

Top-of-the-range High Voltage System, featuring modularity and high flexibility. It consists of one std 19" Euro Crate that houses a Control Unit at the front, and HV Output Channels (**Mods. A 300 to A 400 , A 600**, see below) at the rear.
The SY 127 features a powerful yet friendly software user interface, and sophisticated over-voltage and over-current protections. It can be locally monitored and controlled via on board alpha-numeric keypad and display. Remote control is possible via: the RS-232-C port and the following H.V. CAENET controllers: the CAMAC Mod. C 139, the G 64 Bus Mod. A 199, or the VME Bus Mod. A 200.
Up to 4000 channels can be controlled from a single point. Non-volatile memory of HV values and all operational parameters. Access is password protected.

4.2.1 A300/ A 400/ A 600 SY 127 PLUG-IN CHANNELS

The series A300-A400 of HV Plug-in Modules for the SY 127 covers the full voltage range from 200 V to 15 KV (positive or negative polarity) with current limits from 200 μA to 3 mA. The A329-A429-A 629, 15 KV modules, have two output channels and HV-LEMO connectors. Each channel features:
- an LED indicator, ON when active,
- VMAX protection (hardware protection of max output voltage) set by front-panel trimmer and read by test point,
- TRIP Status/Control feature (channel trip detection and switch-off control).

Model	V	I	ΔV	ΔI
A329P/N	± 15 KV	1 mA	4 V	1 μA
A429P/N	± 15 KV	200.0 μA	4 V	100 nA
A629P/N	± 15 KV	40.0 μA	4 V	10 nA

The authors would like to thank the following persons for their collaboration in the development of this system: R.Santonico, R.Cardarelli (INFN Roma 2); M.Bonori, F.Massa, U.Contino (INFN Roma 1); M.Ambrosio, G.Barbarino (INFN Napoli); G.Liguori, A.Lanza (INFN Pavia); O.Catalano, G.Agnetta (CNR Palermo).